HAL open science

Sedimentary recycling and chemical weathering: a silicon and lithium isotopes perspective

Xu (Yvon) Zhang

▶ **To cite this version:**

Xu (Yvon) Zhang. Sedimentary recycling and chemical weathering: a silicon and lithium isotopes perspective. Geochemistry. Institut de Physique du Globe de Paris, 2018. English. NNT : . tel-03070776

HAL Id: tel-03070776

https://insu.hal.science/tel-03070776

Submitted on 12 Apr 2021

HAL is a multi-disciplinary open access archive for the deposit and dissemination of scientific research documents, whether they are published or not. The documents may come from teaching and research institutions in France or abroad, or from public or private research centers.

L'archive ouverte pluridisciplinaire **HAL**, est destinée au dépôt et à la diffusion de documents scientifiques de niveau recherche, publiés ou non, émanant des établissements d'enseignement et de recherche français ou étrangers, des laboratoires publics ou privés.

UNIVERSITÉ SORBONNE PARIS CITÉ

Thèse préparée
à l'INSTITUT DU PHYSIQUE DU GLOBE DE PARIS
École doctorale STEP'UP-ED N°560
IPGP - Équipe Géochimie des enveloppes externes

Sedimentary recycling and chemical weathering: a silicon and lithium isotopes perspective

Par
Xu Zhang

Présentée et soutenue publiquement le
28 Septembre 2018

Thèse de doctorat de Sciences de la Terre et de l'environnement
Dirigée par Jérôme Gaillardet

Devant un jury composé de :

Rachael James Professeure (Université de Southampton, UK)	Rapportrice
Sophie Opfergelt Professeure (Université catholique de Louvain, Belgique)	Rapportrice
Christian France-Lanord Directeur de recherche (CRPG, Nancy)	Membre
Jiubin Chen Professeur (Université de Tianjin, Chine)	Membre
Marc Benedetti Professeur (Université Paris Diderot, IPGP)	Membre
Julien Bouchez Chargé de recherches (IPGP)	Co-encadrant
Jérôme Gaillardet Professeur (Université Paris Diderot, IPGP)	Directeur de thèse

Résumé

Les actions combinées du cycle de l'eau et le cycle des roches résultent en un transport de sédiments des continents aux océans. Il a été proposé que dans l'océan, les sédiments détritiques réagissent avec l'eau de mer lors de processus encore mal compris, connus sous le terme d'« altération inverse », consommant des cations, formant des minéraux authigènes et libérant du CO_2. Sur de longues échelles de temps, les sédiments détritiques sont convertis en roches sédimentaire et « recyclées », sous l'effet de la surrection tectonique, c'est-à-dire ramenées à la surface de la Terre.

Cette thèse étudie ces processus au travers (1) d'expériences en laboratoire (2) d'une étude de terrain sur des sédiments d'un delta d'âge Éocène, déposés dans des conditions continentale et marine, et (3) sur la base d'analyses des sédiments de 42 fleuves mondiaux. Notre approche est en particulier basée sur des systèmes isotopiques "non traditionnels" : Si et Li. Les résultats expérimentaux montrent que les argiles adsorbent le Li marin en occasionnant un important fractionnement isotopique ($\Delta^7Li_{min/solution} \sim 20‰$). L'étude terrain indique que le δ^7Li enregistre l'interaction entre l'eau de mer et les sédiments détritiques et de ce fait signe l'« altération inverse » se produisant dans les environnements deltaïques et y couplant les cycles du Li, du Si, et du Fe. Enfin, les isotopes du Si suggèrent que les roches sédimentaires exercent une influence majeure sur la composition des particules actuellement transportées à la mer, et que ceci pourrait sur le long terme affaiblir la capacité d'absorption du CO_2 atmosphérique par l'altération des silicates sur les continents.

Mots clés : Silicium, Lithium, isotopes, altération chimique, altération inverse, cycle sédimentaire

Abstract

At the Earth surface, the interplay between the water cycle and the rock cycle leads to transport of materials from the continents to the sea. In the ocean, detrital sediments are thought to react with seawater through a set of hypothesized, but yet-under constrained, processes called “reverse weathering” which consume cations, form authigenic clays, and liberate CO_2. Over long-time scales, sediments are transformed into sedimentary rocks. Under the action of tectonic uplift these sedimentary rocks are "recycled" back to the Earth surface.

This thesis investigates these processes through (1) a set of laboratory experiments; (2) the close examination of detrital sediments deposited in environments varying from alluvial to marine at an Eocene delta; and (3) the role of sedimentary rocks in erosion and weathering, using the geochemistry of river sediments from 42 world rivers. These objectives have been achieved using "non-traditional" isotope systems: Si and Li. First, our experiments show that detrital clays exhibit a strong capacity to adsorb Li and fractionate seawater Li isotopes ($\Delta^7Li_{min/fluid} \sim 20‰$). Second, the field data show that seawater composition (especially δ^7Li) can be modified by interacting with detrital sediments over geological time scales, and that deltaic “reverse weathering"-type processes result in a coupling between the Li, Si, and Fe cycles. Third, Si isotopes suggest that the recycling of sedimentary rocks has a major influence on the composition of sediments currently transported to the ocean, and that this possibly results in a long-term weakening of the capacity of continental silicate weathering to consume atmospheric CO_2.

Key words: Silicon, Lithium, Isotopes, Chemical weathering, Reverse weathering, Sedimentary cycle

Acknowledgements

As you may know, authors who often write acknowledgements at the end of their masterpieces, although it appears at the beginning. This is the same case here, I start writing this part after realizing that I have finished ~300 pages for this thesis and knowing that there are so many people involved in this thesis. To begin with, I sincerely appreciate the equal opportunity offered by the Initial Training Networks, project ISONOSE, under Marie Skłodowska-Curie Actions from European commission, which was granted to me, a non-European citizen, and made this thesis possible. Among me and my European colleagues and supervisors, our cultural backgrounds and histories separate us; however, our pursuit of truth, our insistence on ethics, our values on equality, and our passion in science unite us.

Next, I would like to thank my supervisors, Jérôme Gaillardet and Julien Bouchez, because they chose me in the first place and babysat me for almost four years. I still remember the Skype interview I had with these two gentlemen, during which I was so pretentious that I did not even smile. I am truly grateful that they had faith in me even after have met me in person after my arrival at IPGP. Jérôme has always been supporting my free thinking, either in daily work or on Twitter, and casually sharing his expertise and thoughts based on decades of experience with me, a junior who is standing at the entrance level of his career. I am also equivalently thankful to Julien, who has spent a lot of time, energies, and tolerance on me at IPGP rather than with his new born children. He is always accessible and insightful, for example, during my writing Julien has offered me massive corrections and criticisms like a true hater or an intelligent senior who is trying his best to guide me in my academic journey.

Also, I want to thank Rachel James, Marc Benedetti, Sophie Opfergelt, Jiubin Chen, Christian France-Lanord, Jerome Gaillardet, Julien Bouchez, and Laure Barrier for being members of my jury.

Next, I would share my gratitude to my colleagues. Pascale Louvat, Julien Moureau, Jessica Dallas, thank you for your help and instruction on measurements on Neptune, the core analysis of this thesis. Laurie Barrier and Amandine Laborde, thank you for the wonderful field trip in Spain and thoughtful guidance in sedimentology. Frédéric Monier, Emily Pringle, Alkis Gourgiotis, Emile Bolou, Soufian Henchiri, Jean-louis Birck, Laëticia Faure, Pierre Burckel, Samia Hidalgo, Laure Cordier, Agnès Michel, Hassiba Lazar, Delphine Limmois, and Caroline Gorge thank you for helping me to accomplish my analysis, without you this project won't be accomplished. Also Wafa Abouchami, Catherine Chauvel, Louis Derry, and Vincent Busigny, thank you for sharing your time and wonderful discussions with me. Moreover, Inma Lopez, Irina Shilobreeva, Martine Rodier, and Lydie Guillerot, thank you for helping me sort out my issues with finance, visa, and health care in France, the champion of the World Cup of Paperwork. Also, I want to thank my group members at GEE, Matthieu Buisson, Claire Rollion-Bard, Laure Meynadier, Fatim Hankard, Eric Gayer, Antoine Cogez, Damien Guinoiseau, Hongming Cai, Johanna Noireaux, Mathieu Dellinger, Nicole Fernandez, and Damien Calmels, thank you for sharing your great time with me, it was four solid wonderful years.

I would also thank for my colleagues in Toulouse, in particular, for the experiment study of this thesis. Giuseppe Saldi, you deserve a huge credit for all the help, work, and intelligence you have devoted into this project. Jacques Schott, thank you for your confidence on this project and your wise direction of me to finish our experiments. Although I have invited you two to restaurants twice, I still believe that you deserve more acknowledgements. Also, I thank Franziska Stamm and

Maria Cristina Castillo Alvarez for your help when I was in Toulouse, and all those researchers who have helped this project.

Now I would share my thanks for the isonosers. Maja Tesmer, thank you for all your organization and all your efforts, I understand it was challenging to deal with all the professors, students, and EU office at the same time, and you have done your best to keep the success of the project. All the PIs, Friedhelm von Blanckenburg, Balz Kamber, Seán McClenaghan, Emma Tomlinson, Rachael James, Anna Gorbushina, Eric Oelkers, Jacques Schott, Claudia Bouman, and Joachim Albrecht, thank you for sharing your ideas, your experience, and your suggestions. My Isonose-mates, Rasesh Pokharel, Daniel Frick, Marie Küßner, Ann-Kristin Kalveram, Nils Suhr, Carolina Rosca, David Fries, Jens Krüger, Cristina Castillo, Franziska Stamm, Grant Craig, Danijela Mavrić and Ruben Gerrits, all those meetings at Prague, Potsdam, Dublin, Zandvoort, and Sorèze have became memorable experiences and there will always a connection among us in the future.

I thank for all my friends for have supported me in various forms during my time in Paris. The little group among Paul Floury, Sara Milner Garcia, Marie Kuessner, Quentin Charbonnier (occasional group member 1), Rene Kapannusch (occasional group member 2), thank you for all those great memories of my PhD. My friends who traveled all the way to Paris just to hang out with me: 钱霓，江瑜，陈立果，曾向南，李皑，Will Matthews, Catherine You, Michael Henry, Ansis Rosmanis, Lauren Kotecki, Liam Buller, Serge Bidon, and Charles Paillet, thank you, it was cool.

At the end, I thank for my family back in China, especially 张弢 and 曾庆碧, who happened to be my parents.

Table of contents

Résumé i
Abstract ii
Acknowledgements iii
Table of contents vii
Figure List xi
Table list xiv
Chapter 1: Introduction 1
1.1 Weathering: a pivotal process for the evolution of the Earth surface compartments 3
1.1.1 Weathering and the hydrosphere 4
1.1.2 Weathering and lithosphere 9
1.1.3 Weathering, the atmosphere, and the biosphere 14
1.2 Reverse weathering: the missing link between river sediments and sedimentary rocks 17
1.3 The Si and Li isotope systems 19
1.3.1 Si isotope system 21
1.3.2 Li isotope system 24
1.3.3 A Si-Li paradox in sedimentary cannibalistic recycling 27
1.4 Objectives of this dissertation 29
Bibliography 35
Chapter 2: Methods and techniques 43
2.1 Samples and reagents 44
2.1.1 Depth-profile sampling 44
2.1.2 Laboratory protocols 44
2.2 Major and trace elements 46
2.3 Purification of Si and Li 47
2.3.1 Alkaline fusion 47
2.3.2 Si separation 48
2.3.3 Li separation 50
2.4 Isotope measurements by MC-ICP-MS (Neptune/Neptune *Plus*) 63
2.4.1 Sample introduction system 63

2.4.2 Ionisation system ... 68
2.4.3 Interface ... 69
2.4.4 Mass analysis ... 70
2.4.5 Analytical sessions on a MC-ICP-MS ... 72
2.4.6 δ^{30}Si measurements ... 73
2.4.7 δ^{7}Li measurements ... 77
Bibliography ... 82
Chapter 3: Experimental investigation of the possible impact of reverse weathering on Lithium isotope composition in seawater ... 87
3.1 Introduction ... 88
3.2 Materials and experimental methods ... 91
3.3 Analytical protocol ... 95
3.4 Thermodynamic calculations ... 99
3.5 Results ... 99
3.6 Discussion ... 112
3.6.1 Kaolinite dissolution in acidic seawater (experiment (1)) ... 112
3.6.2 Interaction between basaltic glass and seawater (experiment (2)) ... 116
3.6.3 Interaction between kaolinite and seawater (experiment (3)) ... 120
3.7 Conclusion ... 130
Bibliography ... 132
Chapter 4. “Reverse weathering” reactions: insights from Si and Li isotopes at a paleo-detaic environment ... 136
4.1 Introduction ... 137
4.2 Sample material ... 142
4.2.1 The Ainsa Basin and its mid-Eocene deltaic system ... 142
4.2.2 Sample description ... 143
4.3 Analytical methods ... 147
4.3.1 Sample preparation and major and trace element concentrations ... 147
4.3.2 Selective extraction of Li pools ... 147
4.3.3 Lithium isotope measurements ... 148
4.3.4 Silicon isotope measurement ... 149
4.3.5 Neodymium isotope measurement ... 150
4.4 Results ... 151

4.4.1 Thin section ... 151
4.4.2 Major and trace elements ... 154
4.4.3 Li isotope system ... 164
4.4.4 Silicon isotope system ... 164
4.4.5 Neodymium isotopes system ... 166
4.4.6 Water rinsing and HCl leaching experiments ... 167
4.5 Discussion ... 168
4.5.1 Impact of reverse weathering on the chemical and isotope composition of sediments ... 169
4.5.2 Coupling between Si, Li, and Fe cycles in deltas ... 176
4.5.3 Contribution of deltaic processes to the oceanic cycles of Si and Li ... 183
4.6 Conclusion ... 185
Bibliography ... 188
Appendix i: ... 195
1. Water rinsing experiments ... 195
2. Leaching experiments ... 197
Chapter 5: "Source-to-sink-to-source" effects on the Si isotope composition of detrital sediments ... 205
5.1 Introduction ... 206
5.2 Sample material ... 211
5.2.1 River depth profiles: Amazon and Mackenzie rivers ... 214
5.2.2 Sediments from other large rivers ... 222
5.3 Analytical methods ... 225
5.4 Results ... 226
5.5 Discussion ... 231
5.5.1 Negligible biological effects on the δ^{30}Si of river sediments ... 231
5.5.2 δ^{30}Si and δ^{7}Li variations in large river bed sands ... 232
5.5.3 Mineralogical controls on the δ^{30}Si of large river sediments ... 233
5.5.4 Interpretation of large river sediment δ^{30}Si in terms of the geological context ... 243
5.5.5 Contribution of bedload transport to total sedimentary fluxes of large rivers from Si isotopes 244
5.5.6 The evolution of the river sediment Si isotope composition through continental recycling ... 247

5.5.7 Can we still use the $\delta^{30}Si$ composition of detrital sediments to trace weathering regimes? 260
5.6 Conclusion and implications 262
Bibliography 264
Appendix ii 275
Chapter 6: Conclusions and perspectives 283

Figure List

Figure 1.1 Ocean residence time against seawater – UCC partition coefficient 6
Figure 1.2 Secular variation of seawater Li isotope 8
Figure 1.3 REE diagram (normalized to chondrites) 10
Figure 1.4 Nd model age vs. depositional age of sedimentary rocks 13
Figure 1.5 The global mass-age distribution of the sedimentary mass at the Earth surface 14
Figure 1.6 Simplified schematic of the silicate-carbonate feedback 16
Figure 1.7 Schematic of the present-day global Si cycle 22
Figure 1.8 Silicon isotopic signature of Earth surface material 23
Figure 1.9 Present-day geochemical cycle of Li at Earth surface 25
Figure 1.10 Lithium isotopic signature of Earth surface materials 26
Figure 1.11 Sedimentary rock δ^{30}Si and δ^{7}Li signatures against their Al/Si ratios 29
Figure 1.12 Schematic of sedimentary cannibalism 30
Figure 2.1 Calibration curve for diluted seawater Li purification 56
Figure 2.2 Examples of unsuccessful Li purification of seawater 57
Figure 2.3 Separation of Li using column chromatography protocol 59
Figure 2.4 Calibration curves of two-step Li separation 59
Figure 2.5 Example of resin matrix tinting eluting out and tinting the frits 62
Figure 2.6 Schematic of a MC-ICP-MS 65
Figure 2.7 Photograph of a quartz-made "Stable Introduction System" 66
Figure 2.8 Schematic of the APEX sample introduction system 68
Figure 2.9 Schematic of two types of nickel-made skimmer cones 70
Figure 2.10 Example of a "mass scan" of Si isotope peaks 75
Figure 2.11 δ^{29}Si vs. δ^{30}Si throughout this study 76
Figure 2.12 Summary of δ^{30}Si analyses for the basalt reference material BHVO-2 76
Figure 2.13 Example of a "mass scan" around Li isotope peaks 79
Figure 2.14 Summary of δ^{7}Li analyses for the pure Li solutions 79
Figure 2.15 Summary of δ^{7}Li analyses for the reference materials 81
Figure 3.1 Schematic of the experimental system 94
Figure 3.2 Protocol of Li separation 98
Figure 3.3 SEM images of fresh and reacted kaolinite recovered from experiment (1) 105

Figure 3.4 SEM images of kaolinite for experiment (3) 108
Figure 3.5 ^{7}Li NMR spectra of kaolinite in experiments (d) 110
Figure 3.6 Thermodynamic calculation (PHREEQC) of saturation index 111
Figure 3.7 Results of experiment (1) 113
Figure 3.8 Preferential release of Li over Si during the dissolution of kaolinite 114
Figure 3.9 Results of experiment (2) 119
Figure 3.10 Results of experiment (3) 122
Figure 3.11 Two scenarios explaining the Li isotope fractionation in the system 125
Figure 3.12 Evolution of seawater δ^{7}Li and sea-level from the late-Cretaceous 128
Figure 3.13 Schematic for the impact of the variation of sea-level on the seawater δ^{7}Li 129
Figure 4.1 Schematic of mixing between detrital sediments and authigenic clays 138
Figure 4.2 Maps of the sampling area 144
Figure 4.3 Optical microscopy images of the thin sections 153
Figure 4.4 Relationship between Li concentration and the sum of Al and Fe concentrations 155
Figure 4.5 Frequency distribution of Li/Al and Li/Fe ratios. 155
Figure 4.6 Relationship between the Na/(Al+Fe) and Li/(Al+Fe) ratios 156
Figure 4.7 Relationship between Li isotope composition and grain size 165
Figure 4.8 Relationship between Si isotope composition and grain size 166
Figure 4.9 δ^{7}Li composition of the bulk sample, the first step of the HCl leaching, and the third step of the HCl leaching 168
Figure 4.10 δ^{7}Li vs. Al/Si ratios for alluvial sediments from the Ainsa basin and for sediments from modern large rivers 175
Figure 4.11 Relationship between δ^{30}Si and the Si/Fe in Ainsa sediments. 178
Figure 4.12 Relationship between δ^{7}Li and the Li/(Al+Fe), Li/Al, and Li/Fe ratios in Ainsa sediments. 180
Figure 4.13 Relationship between δ^{7}Li and Li/Fe 182
Figure 5.1 Map of large rivers studied for Si isotope composition 213
Figure 5.2 "Three-isotope plot" (δ^{29}Si against δ^{30}Si) 226
Figure 5.3 Relationship between the δ^{30}Si and δ^{7}Li in river sediments 230
Figure 5.4 Relationship between feldspar content and grain size 235
Figure 5.5 Relationship between δ^{30}Si and grain size 236

Figure 5.6 Compilation of δ^{30}Si in world's river waters _____ 250
Figure 5.7 Large river sediment δ^{30}Si as a function of grain size _____ 252
Figure 5.8 Schematic evolution of the mineralogical composition of large river sediment __ 258
Figure 5.9 Relationship between weathering intensity (W/D) and difference in silicon isotope composition between coarse and fine large river sediments_____ 261

Table list

Table 2.1 Protocol for Si separation 49
Table 2.2 Single-step procedure for Li separation 54
Table 2.3 Li separation protocol using 1-ml resin columns 60
Table 2.4 Typical performing conditions of Neptune plus for δ^{30}Si measurements 74
Table 2.5 Literature values of δ^{30}Si for BHVO-2 77
Table 2.6 Typical analytical conditions of the Neptune Plus for δ^{7}Li measurements 78
Table 2.7 Literature values of δ^{7}Li seawater and basalt reference materials. 80
Table 1.1 Protocol of making artificial seawater (ASW) solution 92
Table 1.2 Li separation protocol using the 1 ml resin method 97
Table 1.3 Experiment (1): Dissolution of kaolinite (KGa-2) powder in artificial seawater 100
Table 1.4 Experiment (2): Interaction between basaltic glass and Li-doped artificial seawater 101
Table 1.5 Experiment (3): Interaction between kaolinite and Li-doped artificial seawater 102
Table 1.6 Summary of adsorption experiment 103
Table 1.7 Reported Li isotope fractionation factor (α) from experimental studies 124
Table 4.1 Sample depositional environment, location, δ^{7}Li and δ^{30}Si compositions (in ‰), εNd, and Al/Si ratios result 145
Table 4.2 Summary of thin section examinations 152
Table 4.3 Summary of major elements expressed as oxides (%) 157
Table 4.4 Summary of trace elements concentrations (in ppm) 160
Table 5.1 Silicon isotope composition of river sediments from the Amazon Basin 216
Table 5.2 Silicon isotope composition river sediments from the Mackenzie Basin 219
Table 5.3 Silicon isotope composition of river sediments across the world 223
Table 5.4 Si isotope composition and Al/Si ratio in primary minerals 240
Table 5.5 Dissolved and particulate Si fluxes to the ocean 245
Table 5.6 Calculation of relative flux of sediments (RBS and SPM) 247

Chapter 1: Introduction

Weathering: Making the earth of the Earth

It is surprising how compatible human beings from different cultures can be when talking about planets. When looking at a flaming planet in the night sky, our ancestors from western cultures named it after the god of war from Roman mythology, Mars, and our ancestors from eastern cultures simply called this planet as *"火星"*, meaning the planet of fire. When talking about the planet where we live, there is no cultural diversity. In French, a beautiful language which I am still learning, it is called "*la Terre"*. The French name is not substantially different from how it is called in my scientific working language, English, the Earth. In my mother tongue, Chinese, it is called *"地球"* which literally means "the sphere of earth". In the etymologies of these languages, the word "earth" shares a same origin, soil.

If we consider the beginning of our modern life style as being early as the industrial revolution around 18th century (although many important inventions such as electricity, internet, etc., occurred later), the current course of human society only occupies an insignificant fraction of human history, as our ancestors can be dated back as old as 4.4 million years ago (Gibbons, 2009). For a long period of history, and even today, our lives are very much dependent on soils over which fruit-bearing trees and crops grow. Without soils, many forms of life would not exist on the Earth surface and civilizations would never have appeared.

Although soils are everywhere nowadays, they do not just "appear". As for any other geological feature, the formation of soils requires certain processes at specific time scales. It is precisely weathering, in particular silicate weathering, which exerts a major control on soil formation through rock dissolution and secondary mineral precipitation. Atmospheric CO_2 is dissolved in meteoric water and slightly acidifies the fluids, which leads to mineral dissolution.

Once released, the aqueous constituents can be re-precipitated, and consequentially secondary minerals are formed. These reactions, involving water, gases, and rocks, can only occur at the very surface of the Earth's surface, defined by many scientists as the "Critical Zone"(Brantley et al., 2007).

Although, we had astronauts landed on the Moon; the movie director of *Titanic* and *Avatar* James Cameron reached the bottom of Mariana trench; great men and women working in the International Space Station, the vast majority of human beings and our civilization are still dependent on this thin layer of the Earth surface. Therefore, it is of importance to understand weathering, which is a key process modifying and shaping the Earth surface. This dissertation is about expanding our knowledge of weathering by exploring several questions such as the fate of dissolved constituents when they are transported into the ocean, and by addressing the importance of the weathering of "already-weathered" rocks.

1.1 Weathering: a pivotal process for the evolution of the Earth surface compartments

Weathering is a natural process occurring on the Earth surface, which breaks up rocks and transforms them into sediments. Once the rocks are relocated via tectonics from the depth of the crust to the Earth surface, they are subjected to weathering. Decompression via the removal of overburden and cooling triggers *physical weathering* which allows the rocks to break. Meanwhile, *chemical weathering* takes place when water in the form of rain, groundwater flow, or stream interacts with rocks. Both physical weathering and chemical weathering break rocks into debris, but only chemical weathering is able to substantially alter the nature of rocks. Carbon dioxide gas (CO_2) in the atmosphere dissolved in water produces carbonic acid, which in turn lowers the pH. Protons offered by the carbonic acid enables the dissolution of primary minerals constituting the

solid rocks and the formation of pedogenic secondary minerals, which can be simplified as (for example of weathering K-feldspar into kaolinite; Bouchez and Gaillardet, 2014):

$$CO_2 + H_2O \leftrightarrow H_2CO_3$$

$$KAlSi_3O_8\ \textit{(k-feldspar)} + H_2CO_3 + \frac{9}{2}H_2O \rightarrow \frac{1}{2}Al_2Si_2O_5(OH)_4\ \textit{(kaolinite)} + 2H_4SiO_4 + K^+ + HCO_3^-$$

Therefore, weathering produces minerals dissolved in water and precipitated in soils (and the sediments transported by rivers, corresponding to eroded debris of soils and rocks). From the point view of the water cycle, weathering determines the composition of river water and the dissolved fluxes to the ocean. From a point view of the rock cycle, river sediments are then transported to deposition sites to form sedimentary bodies, which with time, through processes such as diagenesis or metamorphism, consolidate to form sedimentary rocks. As a consequence, weathering transforms all types of rocks (igneous, metamorphic, and sedimentary) into sedimentary rocks. For all these reasons, it is thus also critical to comprehend the impact of weathering as it connects the various layers of the Earth surface: hydrosphere, lithosphere, atmosphere and biosphere. Additionally, as our planet is a dynamic system, these spheres have been evolving through geological times. For instance, the onset of tectonics fundamentally changed the nature of the lithosphere, the atmosphere has been evolving from anoxic to oxic, and life appeared. All these changes have induced modifications and regulations on the style of the weathering at the Earth surface. In turn, weathering processes have affected the evolution of the Earth compartments.

1.1.1 Weathering and the hydrosphere

At first order, the ocean is the ultimate destination of materials dissolved through the weathering of continental crust. The flux of riverine dissolved material derived from continental

weathering is also one of the main inputs determining the aqueous chemistry of the ocean. As shown by the pioneering studies (Turner and Whitfield, 1979; Whitfield and Turner, 1979; Whitfield, 1979), it is informative to examine the relationship between oceanic residence time (τ) and the water-rock partition coefficient (K_y^{SW}) of a given element. The water-rock partition coefficient for an element *y* quantifies the distribution of this element between seawater and the upper continental crust (UCC), and it is defined as:

$$\mathrm{K}_y^{SW} = \frac{X_y^{SW}}{X_y^{UCC}}$$

where X_y^{SW} is the concentration of *y* in seawater and X_y^{UCC} is the concentration of *y* in UCC. The plot of τ against K_y^{SW} results in a positive relationship (Fig 1.1), suggesting a long-term effect of weathering on the hydrosphere (Taylor and McLennan, 1985; Rudnick and Gao, 2014).

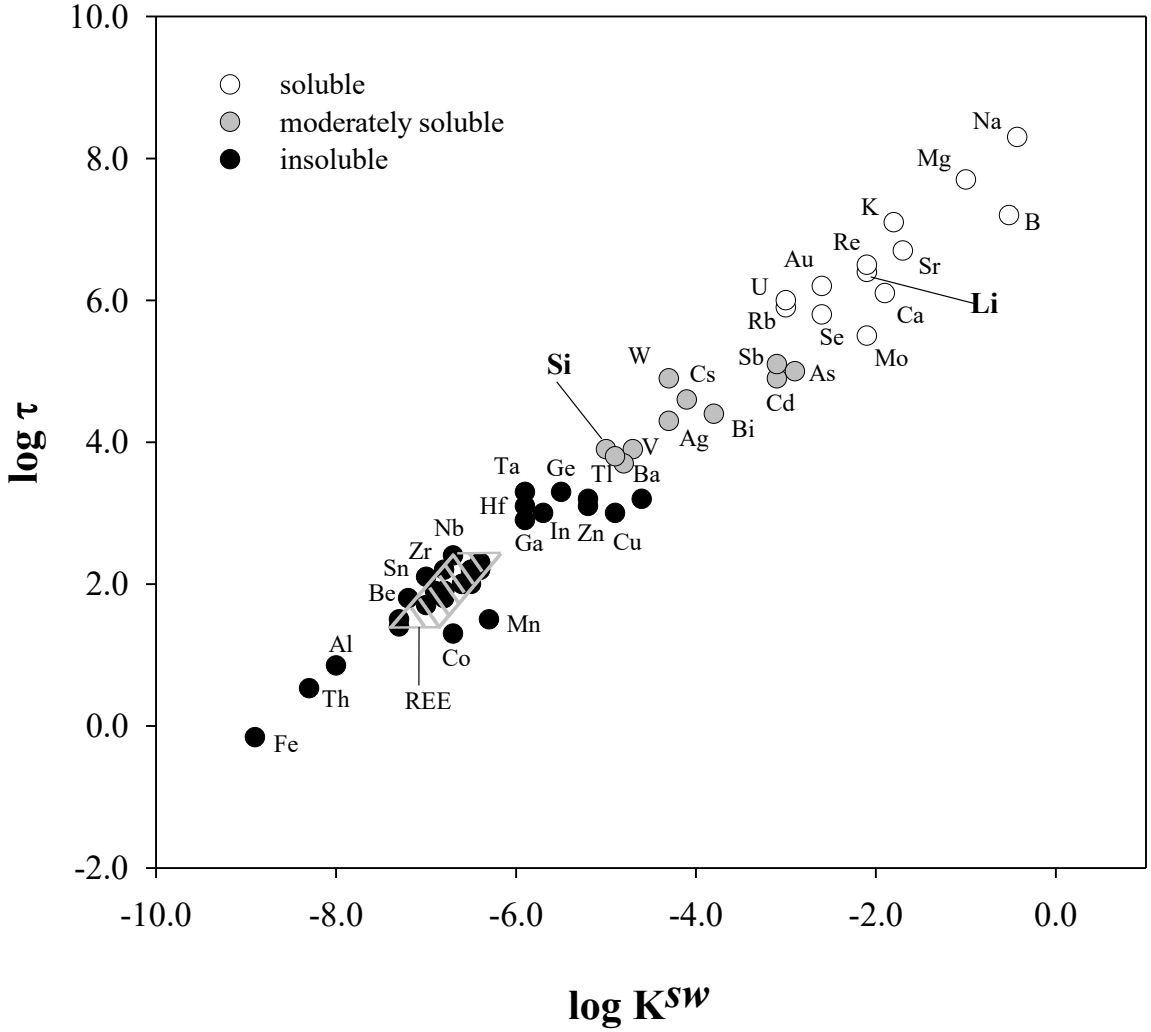

Figure 1.1 Plot of ocean residence time (expressed as log τ) against seawater − UCC partition coefficient (expressed as log K^{SW}) for various elements. Data from Taylor and McLennan (1985).

For a given element, the longer the residence time in the ocean, the greater the partition coefficient is. The elements located in the upper-right corner of Figure 1.1 are considered as soluble elements. These elements include alkali elements such as lithium (Li), alkaline-earth elements, and some other elements like boron (B), rhenium, molybdenum, gold and uranium. Those elements located in the lower-left corner of Figure 1.1 have short residence time in the ocean and are considered insoluble elements. The insoluble elements include rare earth elements (REE),

transition metals such as zinc and copper, post-transitional metals such as aluminum and gallium. Some of these "insoluble-in-seawater" elements may actually not be immobile during continental weathering. Pointed out by Taylor and McLennan (1985), some elements are subjected to changes of solubility with oxidation state variation, for example manganese and iron. The remaining elements in Figure 1.1 are considered as moderately soluble as they have intermediate residence time. These elements include some transitional metals, barium, cadmium, and silicon (Si).

The soluble elements tend to enter the hydrosphere, hence the ocean, during weathering. For these elements, the seawater chemical and isotope compositions can be greatly controlled by weathering parameters: source rocks, rates, and intensity. This is shown in particular for the past Li isotope composition of the ocean, one of the foci of the current dissertation. The study of Misra and Froelich (2012) reports the evolution of oceanic Li isotopes composition over the Cenozoic. Such record is preserved in the calcium carbonate of planktonic foraminifera, as trace amount of Li is incorporated from ambient seawater during growth (Hathorne and James, 2006; Misra and Froelich, 2012). The record shows secular variation of seawater in terms of Li isotopes (Fig 1.2). Briefly, the results from Misra and Froelich (2012) show a rapid decrease of seawater Li isotope composition (expressed as δ^7Li) at the K-T boundary (ca. 66 Ma) where the late Cretaceous seawater has a δ^7Li of ~29 ‰, which is close to the value of the modern ocean (31 ‰). Within a short period of time (a few Myr), the seawater Li isotope signature drops by ~5 ‰. Thereafter, the seawater δ^7Li gradually increases to the level of today. Such variation of seawater Li isotopes was interpreted by the authors as largely due to changes in continental silicate weathering. Increased denudation and lower weathering intensity were suggested to cause the increase in the δ^7Li of the riverine dissolved flux, which in turn elevated the seawater δ^7Li.

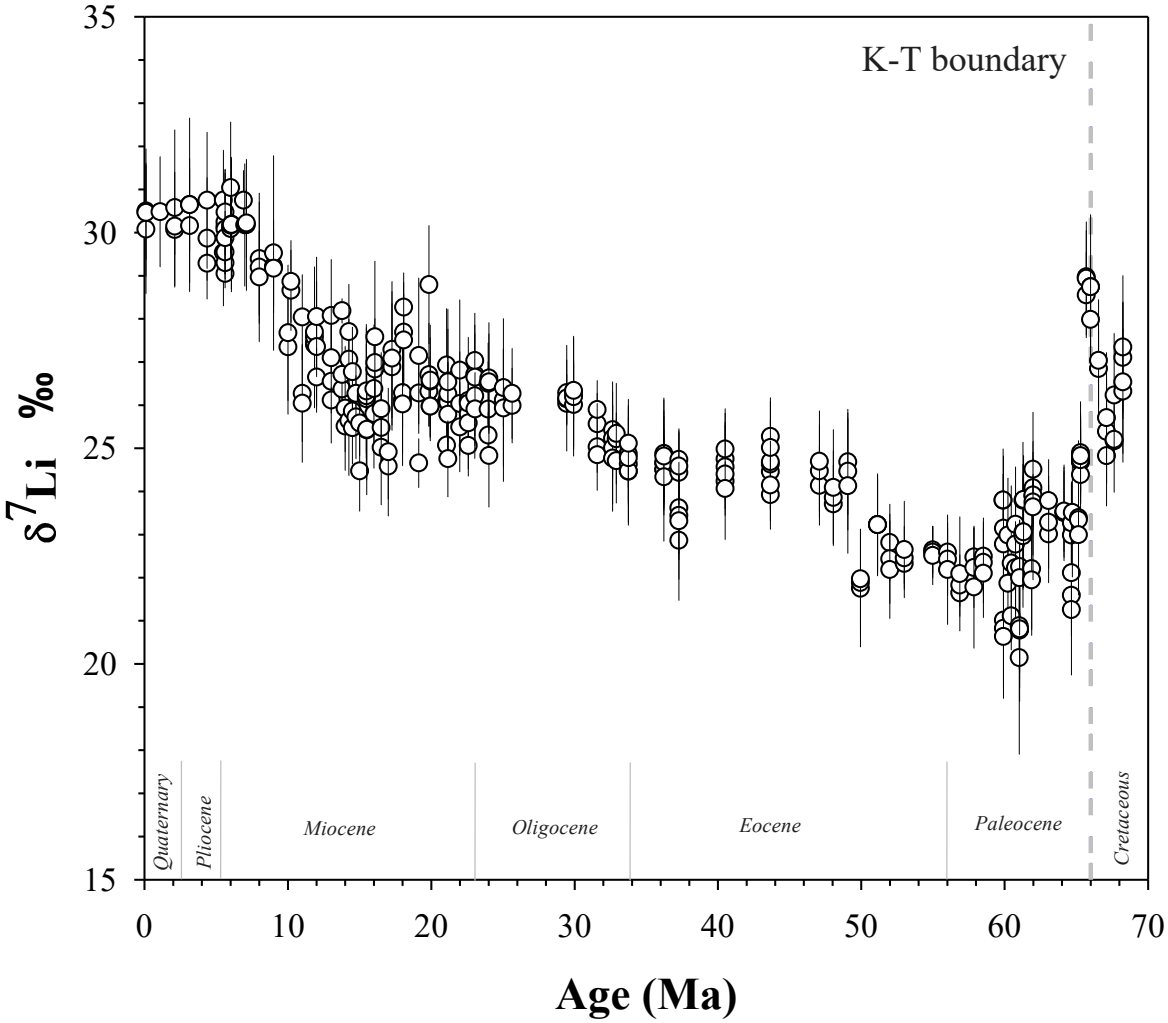

Figure 1.2 Secular variation of seawater Li isotope (δ^7Li) from the late Cretaceous to present (Holocene). Data from the Misra and Froelich (2012).

Another soluble element, boron (B), also shows similar characteristics. The seawater B isotope evolution records were retrieved from foraminifera deposited at different ages (Pearson and Palmer, 2000) as well as directly measured from evaporites formed through geological times (Paris et al., 2010). Both B isotope archives show that there was an evolution of increasing seawater B isotopes for the past 40 Myr, although the reported increase rates are different between the different studies. The seawater B isotope record, is also suggested to be influenced by

continental weathering (Lemarchand et al., 2002), and to serve as a proxy for past variations in continental weathering (Paris et al., 2010).

Overall, the Earth hydrosphere is sensitive to the changes of continental weathering. In particular, the seawater archives of certain soluble elements such as Li and B are able to reveal the history of continental weathering.

1.1.2 Weathering and lithosphere

The earth lithosphere consists of three major rock types: igneous, metamorphic, and sedimentary rocks. Today, sedimentary rocks occupy nearly two thirds of the exposed rocks on the Earths' surface (Blatt and Jones, 1975) and are thus a major contributor to the rock cycle. In particular, clastic sedimentary rocks (originated from the Greek word *klastós*, meaning "broken") are cemented sediments that have therefore undergone weathering reactions in the distant past. As such, clastic sediments keep some of the oldest secret about the Earth surface dynamics. Little variation is expected for insoluble elements (lower-left corner of Figure 1.1) during weathering as they preferentially remain in the solids. Therefore, for these elements, clastic sediments are representative of the source rock, such that if any major change occurred in the Earth's lithosphere such information could potentially be preserved in the insoluble element composition of clastic sediments.

One of the most important contributions of Geochemistry to Earth Sciences was to reveal the remarkable crustal change at the Archean−Proterozoic boundary, when the continental crust was largely produced. This was achieved through a series of studies of late Archean and post-Archean sedimentary rocks (Taylor and McLennan, 1985, 1995; McLennan, 2001). Comparing the fine clastic sedimentary rocks from Archean and post-Archean times, a remarkable difference exists between their REE patterns (Fig 1.3).

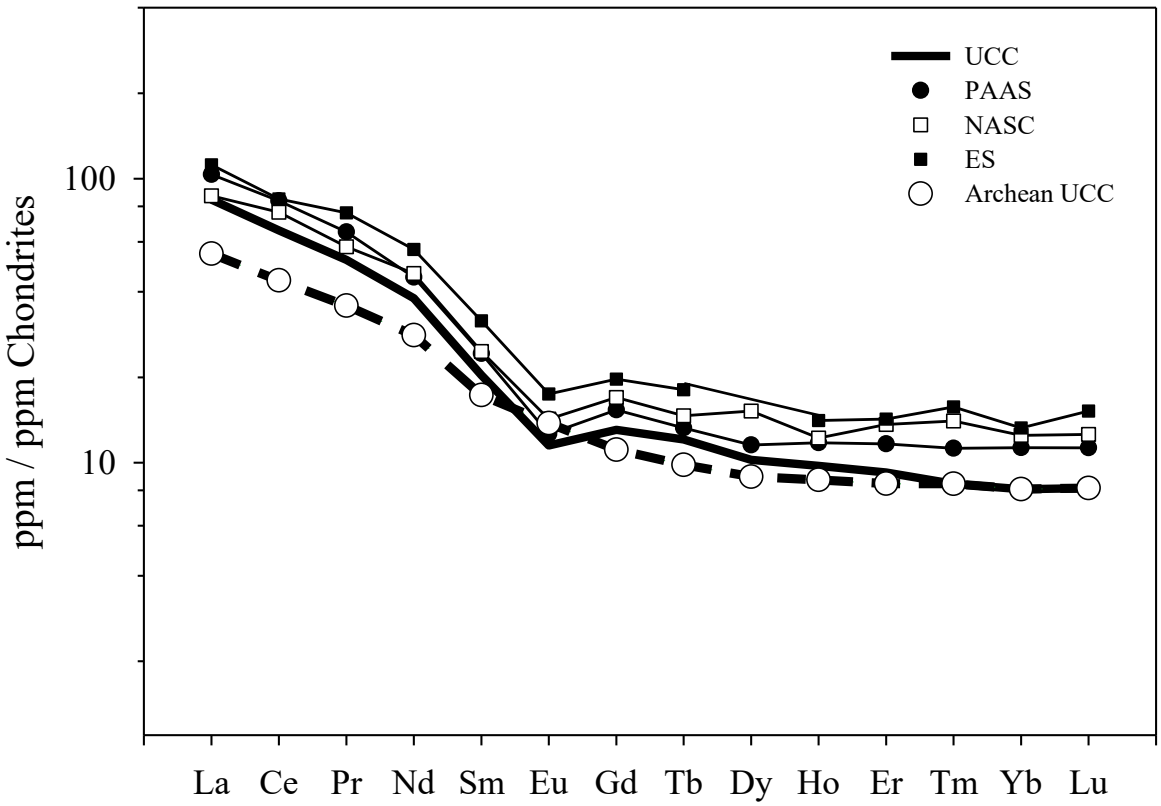

Figure 1.3 REE diagram (normalized to chondrites) showing the negative Eu anomaly characteristic of post-Archean sedimentary rocks. The data of UCC is from Rudnick and Gao (2014). The data of PAAS (post-archean Austrilian shale), NASC (North American shale composite), ES (European shale composite), and Archean UCC are from Taylor and McLennan (1985) and Taylor and McLennan (1995).

In the post-Archean sedimentary rocks, there is a global depletion of Eu, whereas such depletion does not exist in Archean sedimentary rocks. This Eu depletion is suggested to be a proxy of igneous events, as Eu is incorporated in plagioclase during intracrustal melting.

This implies that the crustal composition evolved from a basaltic (*i.e.* Tonalite–Trondhjemite–Granodiorite, TTG) to a granitic nature. Therefore, comparing the insoluble elements in the clastic sedimentary record provide a direct way to investigate the history of crustal rocks. Nevertheless, such techniques are complexified for post-Archean samples due to the onset

of tectonics and the so-called “sedimentary recycling” (Mackenzie and Garrels, 1971; Veizer and Jansen, 1979; McLennan and Taylor, 1980; Taylor and McLennan, 1985). The first hint of the recycling of crustal sediments is the discrepancy between the “model ages” based on Nd isotopes and the depositional ages of sedimentary rocks (Fig 1.4). The Nd model age dates the event of igneous differentiation from the mantle (e.g. McCulloch and Wasserburg, 1978; Allègre and Rousseau, 1984), and it gives insight into the formation of the source materials of sedimentary rocks. As shown in Figure 1.4, sedimentary rocks, in particular post-Archean sedimentary rocks, have younger stratigraphic (or deposition) ages than the Nd model ages. Additionally, the excess time ($T_{\text{Nd Model age}} - T_{\text{Stratigraphic age}}$) increases, in general, with younger deposition. Such pattern is a result of the preservation and the recycling of sediments on the continental crust. The excess age is an indication of the efficient "cannibalistic" recycling of sediments (Veizer and Jansen, 1979; Veizer and Mackenzie, 2013). Sometimes, this excess time is referred as the “crustal residence age” (Allègre and Rousseau, 1984). However, this terminology may not be fully accurate to express the actual residence time of the sediment at the Earth surface, which in principle starts at the rock formation from magma partial melting and ends at the subduction of sedimentary rock.

It is difficult to predict when exactly an existing sedimentary formation will be reaching a subduction zone and be subjected to recycling to the mantle, and it is impossible to date for sedimentary formations that have already undergone subduction. However, in general, sediments reaching the oceanic floor have greater chances to enter subduction zones than which those do not even reach the ocean. For example, one can also expect a sedimentary basin is suited in a continental platform has a greater post-sedimentation preservation potential than those sediments located in a trench (Busby and Ingersoll, 1995). This tectonic control on the preservation of sedimentary mass is well illustrated in Figure 1.5. At first sight, the preservation of sediments

seems to be exponentially declining with increasing depositional age. However, closer look shows that such feature does not exist when only the sediments preserved on continents are considered. This implies that the amount of continental sediments is relatively stable and compared to "short-lived" sediments deposited in active settings like oceanic floors, continental sediments are able to remain "alive" for a long time.

Regardless, today it is estimated nearly 90 ± 5 % of the sedimentary rocks are cannibalistic (Veizer and Jansen, 1985; Veizer and Mackenzie, 2013), meaning that the vast majority of sedimentary rocks are composed of residuals from even older sediments, and that only a small fraction of juvenile crust is added during each weathering cycle. Therefore, at the geological time scale, an evolution of the chemical composition of sedimentary rocks is expected.

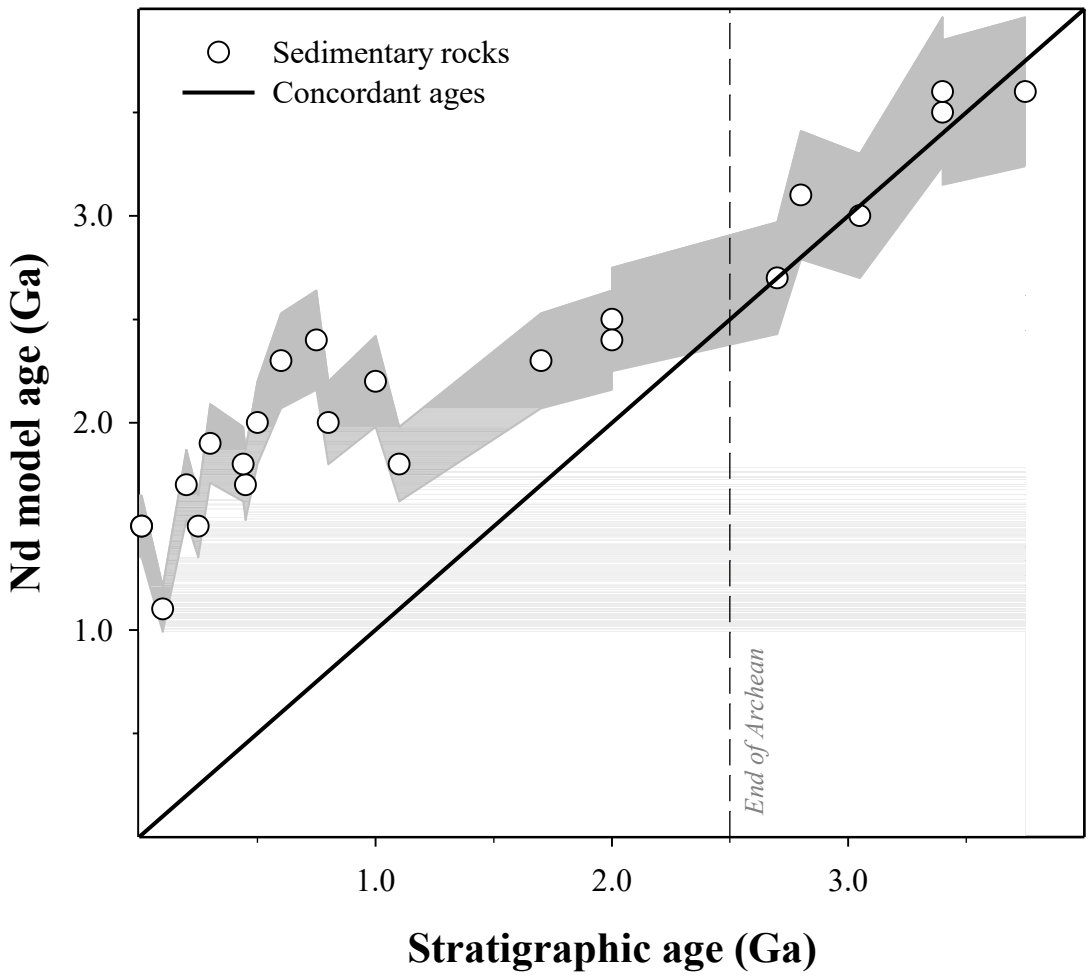

Figure 1.4 Nd model age *vs.* depositional age of sedimentary rocks. Post-Archean sedimentary samples have older Nd model ages than their stratigraphic ages. The excess ages are due to the recycling and the preservation of sediments. Data from Taylor and McLennan (1985).

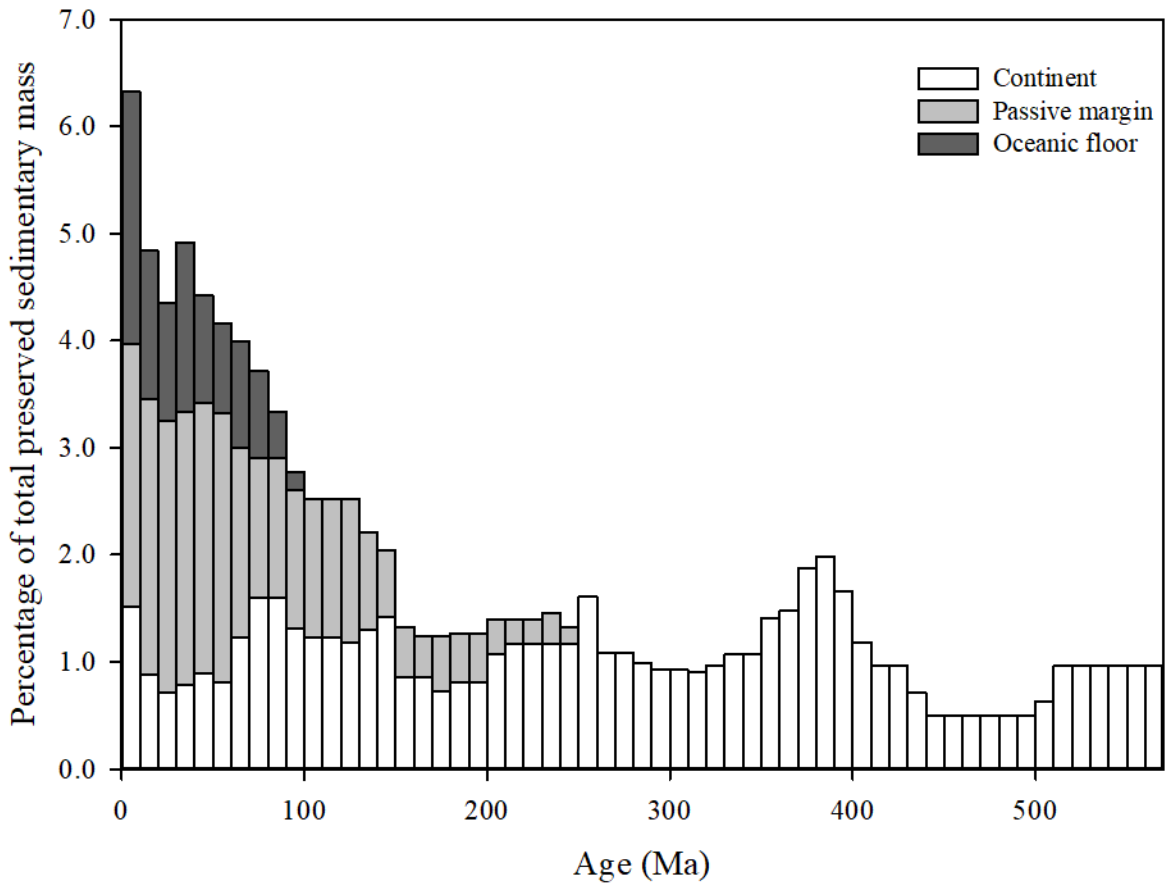

Figure 1.5 The global mass-age distribution of the sedimentary mass at the Earth surface. Modified and reproduced from Veizer and Mackenzie (2013). The white bars represent sedimentary mass deposited and preserved on the continents, data from Ronov (1993). Light grey bars represent sediments on passive margins, data from Gregor (1985). Dark grey bars represent sediments on oceanic floors, data from Hay et al. (1988)

1.1.3 Weathering, the atmosphere, and the biosphere

One of the most important roles of weathering on the Earth atmosphere is, at geological time scales, the regulation of atmospheric CO_2. It has been long speculated that air can be "fixed" into rocks. Lavoisier (1801) first suggested that the phenomenon of air fixation could be similar to calcination. Later, after the identification of carbon (C), Lavoisier (1892) pointed out that atmospheric C can be sequestrated in carbonate rocks (note that Lavoisier was beheaded in 1794,

and some of his worknotes were published much after). These pioneering works fertilize the embryo of the present-day understanding of climate-atmosphere feedbacks (*e.g.* Walker et al., 1981; Berner et al., 1983). Silicate weathering is a key factor in this feedback system (Fig 1.6): As shown in section 1.1, CO_2 in the atmosphere is consumed to form carbonic acid dissolved in meteoric and surface waters, which further provides to protons react with silicate minerals.

The relationship between weathering biosphere is unable to be easily summarized due to the inherent complexity of biological systems, and the long-term dynamics of the biosphere (*e.g.* evolution and mass extinctions). It is, however, necessary to point out the most salient roles of the biosphere on the operation of weathering at the Earth surface. In the terrestrial biosphere, living beings are dependent on nutrient and bio-essential elements released into soil waters and/or surficial waters by weathering reactions except for a very small number of microbes who survive from direct digestion of rock minerals (*e.g.* Pokharel et al., 2017). The development of marine biota also largely relies upon the delivery of dissolved materials to the oceans via rivers except for those biological communities who habit in deep sea environments and are supported by the dissolved substances from vent fluids.

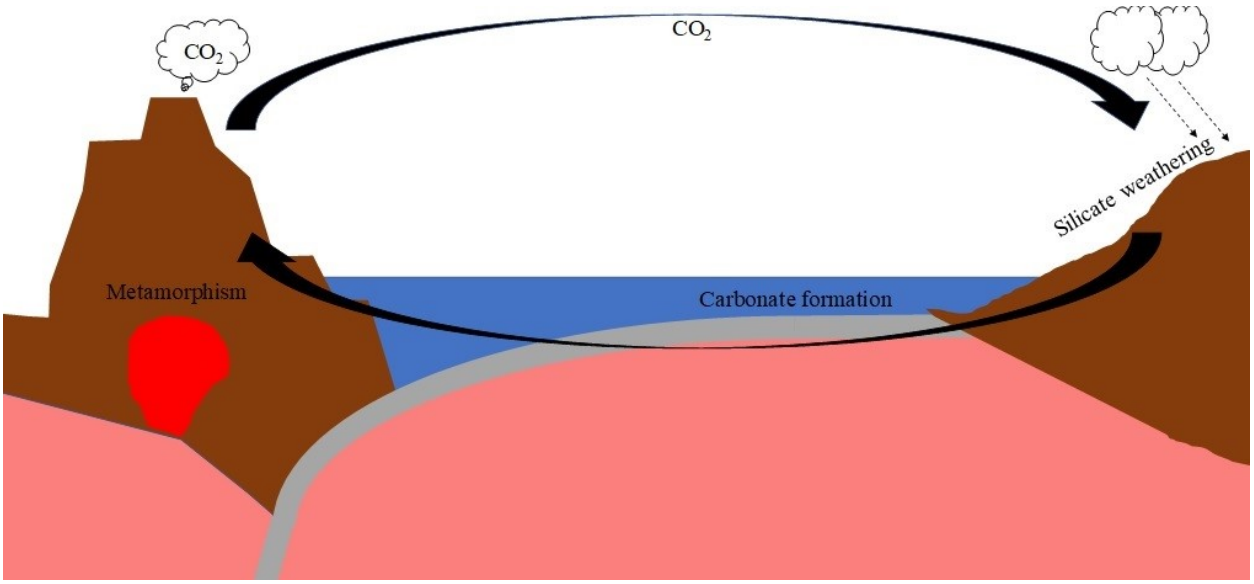

Figure 1.6 Simplified schematic of the silicate-carbonate feedback. In this feed back, carbon cycle is incorporated into rock cycle. Atmospheric C is consumed by silicate weathering, and this carbon is later sequestrated into carbonate rocks. Once carbonate rocks are subjected to metamorphism, C is liberated and re-enters into the atmosphere in the form of CO_2.

Regarding the effect of biota onto weathering processes, the picture is more complex. On one hand, some compartments of the biosphere, such as forest, are able stabilize slopes subjected to erosion. On the other hand, other actors such as humans, can greatly promote erosion (Milliman and Farnsworth, 2013). In addition, carbon sequestration via photosynthesis is the main channel through which CO_2 reaches surficial waters, leading to water-rock interactions of silicate weathering. Lastly, life leads to the formation of carbonate rocks, which temporally store C before they are subjected to metamorphism. Carbonate rocks can be easily weathered; however, if debris of carbonate rocks can survive one weathering cycle and are deposited and re-involved in the formation of sedimentary rocks, then they can also be considered as cannibalistic.

1.2 Reverse weathering: the missing link between river sediments and sedimentary rocks

A full weathering cycle of sediments includes weathering of source material, deposition in the sedimentary basin, diagenesis and lithification, and eventually uplift and recycling. It is essential to know the impact of each step on clastic sediments to fully comprehend the cannibalistic nature of sedimentary rocks. Here, we focus on the process of "reverse weathering".

Since the birth of modern chemistry, seawater chemistry has always been at the center of interests. Lavoisier (1772) first published the chemical analysis of seawater. The simple interpretation of the "salty" seawater composition was that ocean was due to the dissolution of the Earth's materials by rain water and the transportation of the resulting solution to the ocean. This idea gave a hint about the origin of the ocean; however it can not be completely correct when considering the age of the ocean and the annual influx from rivers. In fact, this is one of the most famous arguments from creationists claiming that the Earth is young: it would not take long to reach the level of the present-day seawater composition from the transportation of dissolved weathered materials by rivers (Morris, 1974).

While some think that God created Heaven and Earth in 6 days and other stuff like Wi-Fi and vegan ice-creams on the 7th day, earth scientists, who hold alternative opinions on how the universe functions, have been working on finding explanations to this mystery of seawater composition. The key paradox is the geochemical balance between the inputs to and outputs from the ocean. Initial attempts to understand the the continental processes were made by pioneer geoscientist (*e.g*. Ebelmen, 1845; Bischof, 1847; Vernadsky, 1926). The most famous geochemist Goldschmidt (1933) considered the sea–land interaction as the following reaction:

$$\text{Igneous rocks} + \text{Volatiles} \rightarrow \text{Seawater} + \text{Sediments} + \text{Air}$$

Establishing the geochemical balance in the ocean requires reliable constraints on inputs to and outputs from the ocean. Because of relative easiness of observation, historically the input fluxes have been receiving more attentions than the removal fluxes. The concept proposed by Mackenzie and Garrels (1966) aiming to address the issue of chemical sinks was referred to as *reverse weathering*. These authors noticed that in the modern ocean Si is depleted and pH is low, both compared to what is expected from a geochemical mass balance based on river fluxes. Hence an efficient mechanism should exist to take up cations into authigenic clays and liberating carbon dioxide consumed via weathering. Sillen (1967) in particularly pointed out that clay formation in the ocean should be accountable for this purported reaction. Although this idea was proposed relatively early, little progress was made in the following decades. One of the reason lies in the discoveries around the studies on hydrothermal activity (*e.g*. Edmond et al., 1979), which took some attention away from scientists working on marine geochemical sinks. But most importantly, the challenge was to obtain *in situ* evidence of reverse weathering, as (1) authigenic clay formation was traditionally considered as a slow process, which takes place at a time scale of 10^3—10^6 yrs (Odin and Fröhlich, 1988) and (2) it is difficult to distinguish authigenic and detrital clays in marine deposits.

The breakthrough from the work of Michalopoulos and Aller (1995) re-opened the Pandora box of reverse weathering. In their experiments, not only did they prove that reverse weathering can be a rapid process in a highly active sedimentary system such as the Amazon delta, but also they showed that it can be an efficient sink of major cations in the ocean. Based these results, Mackenzie and Kump (1995) generalized reverse weathering as:

Silica + degraded aluminous clays + iron oxide + organic carbon + soluble cations + bicarbonate

→ new clay minerals + water + carbon dioxide

Since then, the concept of reverse weathering returned to front of the stage. One of the well-studied aspects of this topic is the potential impact of reverse weathering on Si cycle. As pointed out by Mackenzie and Garrels (1966), seawater contains less Si than expected from the geochemical mass balance and the amount of siliceous cherts in sedimentary records is unable to account for such an imbalance. On the contrary, reverse weathering is a viable candidate for the missing Si sink. To date, the main Si source to the authigenic clays is considered to be the dissolution of biogenic silica (Van Cappellen and Qiu, 1997; Michalopoulos and Aller, 2004; Aller, 2014; Rahman et al., 2016), and reverse weathering is deemed accountable for removing up to 25% of the total Si from the ocean (Frings et a., 2016). Although a number of studies have been applying the reverse weathering concept to explain a diversity of geochemical observations (Bastian et al., 2017; Dunlea et al., 2017) or to achieve element budget (Misra and Froelich, 2012), few *in situ* studies (Rahman et al., 2016; Dunlea et al., 2017; Ramos et al., 2018) have been made to constrain the magnitude and the nature of reverse weathering.

In this dissertation, reverse weathering is investigated for its potential to further alter sediments deposited during the sedimentary cycle. Our approach relies in particular on the Si and Li isotopic systems.

1.3 The Si and Li isotope systems

In the human history, some archeological periods were named after by the remarkable materials that were employed to shape societies, such as the “bronze age” or the “iron age”. What are the most significant materials representing our current society? Silicon (Si) and Lithium (Li) are good candidates. Because our modern society has a strong demand for calculation, computing, and tele-communication, Si is largely used in semi-conductors by high-tech enterprises to produce

electronic devices. Si-based chips are everywhere in computing industries. Today, the geographical area sheltering some of the largest high-technology companies, in the San Francisco bay area, is referred to as *Silicon Valley*. Meanwhile, another challenge of the current human society is the balance between the energy demands for everyday life and environmental sustainability. Due to the chemical property of Li ions, Li is used in batteries, and rechargeable Li-ion batteries are widely applied from electronic devices to transportation, to the point that the National Aeronautics and Space Administration (NASA) of the United States launched a mission to send an electric car powered by rechargeable Li-ion battery to space in February 2018.

Not only testifying for the stage of development of the current society, Si and Li are also powerful archives of the geochemical history of the Earth. Both Si (^{28}Si, ^{29}Si, and ^{30}Si) and Li (^{6}Li and ^{7}Li) have more than one stable isotope. In brief, the stable isotope Geochemistry takes advantage of isotope fractionation which occurs when a chemical reaction system minimizes energy (equilibrium fractionation) or in an incomplete, or unidirectional process preferentially uses lighter isotopes (kinetic fractionation) (White, 2013). Measured in different geochemical reservoirs, distinct isotopic fingerprints reveal the information about the source of the element and/or the history of process that have affected the elements on its way to the measured reservoirs. For a given element X, the absolute ratio of two isotopes (with molar masses of m and n) is:

$$R = \frac{^{m}X}{^{n}X}$$

The isotope signature for many elements are often reported relative to a standard reference material, expressed as:

$$\delta\,^{m}X = \left(\frac{R_{sample}}{R_{standard}} - 1\right)\times 1000$$

The isotope fractionation factor between two phases (A and B) is defined as:

$$\alpha_{A\text{-}B} = \frac{R_A}{R_B}$$

Sometimes the isotope fractionation factor between two phases are also reported as:

$$\varepsilon_{A\text{-}B} = \delta_A - \delta_B, \text{ where } \varepsilon_{A\text{-}B} \approx 10^3 (\alpha_{A\text{-}B} - 1).$$

Next the Si and Li isotope cycles will be briefly introduced.

1.3.1 Si isotope system

Si is a metalloid element and has 14 protons. It has 3 naturally occurring stable isotopes: ^{28}Si, ^{29}Si, and ^{30}Si, and respectively they have natural abundances of 92.23%, 4.67%, and 3.10%. On the Earth surface, Si is almost exclusively present in the oxidation state +4 (Poitrasson, 2017). Meanwhile, Si is the second most abundant element in the Earth crust (Taylor, 1964). It is therefore one of the most important mineral-forming elements. Si contained in minerals can be released into water through weathering (Fig 1.7). According to Figure 1.1, Si is moderately soluble during continental weathering. The ultimate destination of the dissolved Si (DSi) derived from weathering is the ocean. Before reaching the ocean, part of DSi can be either taken up by secondary mineral formation to produce clays or be consumed by biological activity. In the ocean, the riverine DSi flux is the main source of marine DSi. Biogenic Si (BSi) in the marine environment holds a large Si reservoir and the deposition of BSi is a major sink of Si in the ocean. Noteworthy, the combined magnitude of the "directly measurable" sinks of Si, such as BSi formation, can not balance the Si inputs to the ocean. Therefore, reverse weathering is widely considered as the "missing Si sink" (Tréguer et al., 1995; DeMaster, 2002; Holland, 2005; Tréguer and De La Rocha, 2013; Frings et al., 2016).

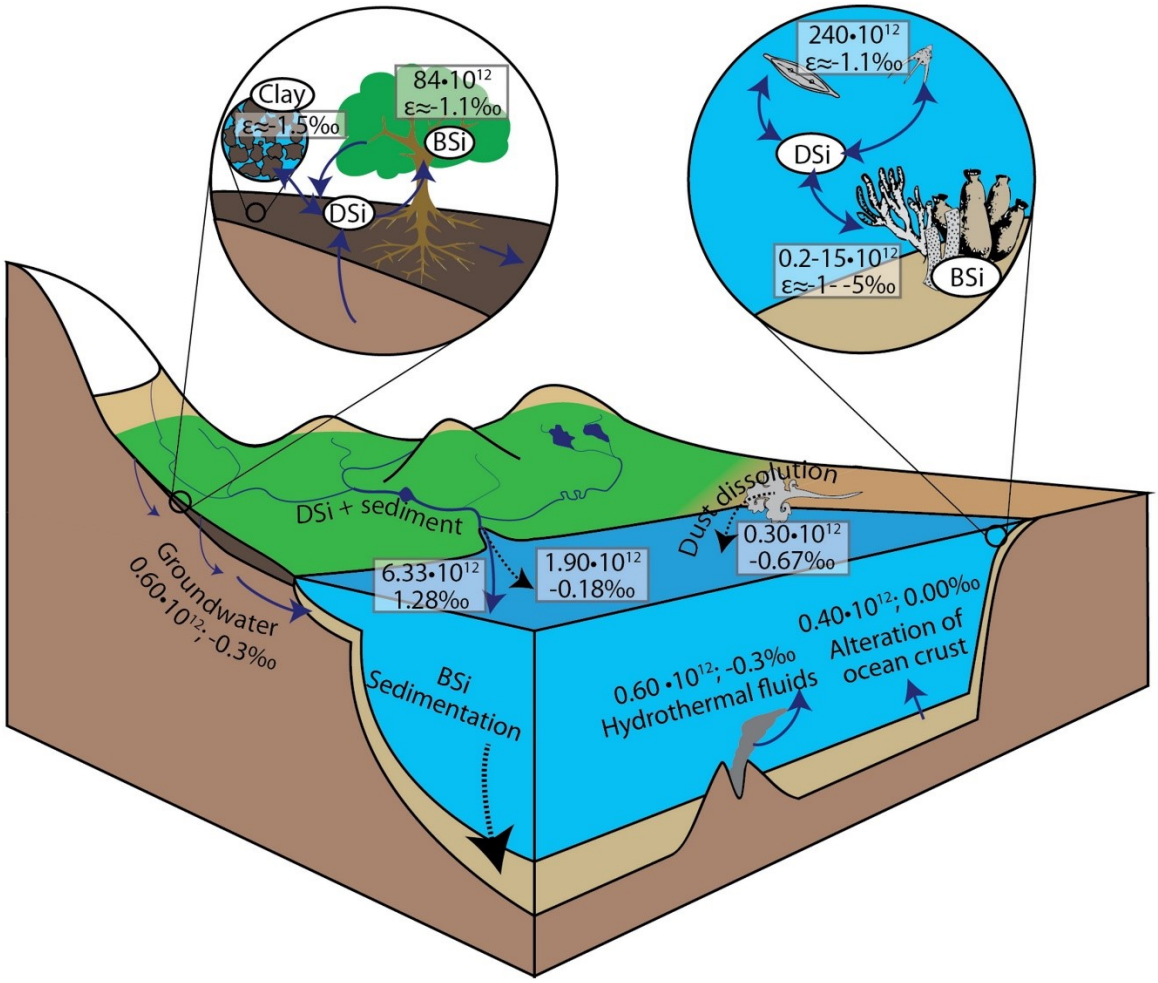

Figure 1.7 Schematic of the present-day global Si cycle. All Si fluxes are in the unit of mol/yr. Solid lines represent DSi fluxes or transformation and dotted lines represent Si carried by solids. Figure is reproduced from Frings et al., (2016) under Creative Commons user license (http://creativecommons.org/licenses/by-nc-nd/4.0/).

Although sometimes referred to as a "non-traditional" isotope system, the study of Si isotope system has in fact a long history. Initial efforts for measuring Si isotope signatures (δ^{30}Si) in natural samples were made by Reynolds and Verhoogen (1953) and Allenby (1954) using Gas-Source Mass-Spectrometry (GS-MS); the knowledge on Si isotope compositions and potential fractionation was later expanded by large surveys of δ^{30}Si in Earth's materials (Douthitt, 1982; Ding and Tang, 1996). With the advent of Multi Collector-Inductively Coupled Plasma-Mass Spectrometer (MC-ICP-MS) and the improvement of Si purification method (Georg et al., 2006),

measurement precision reached a level of ±0.1 ‰, allowing for a plethora of δ^{30}Si studies on Earth's materials. The δ^{30}Si signature of common materials on the Earth's surface is displayed in Figure 1.8:

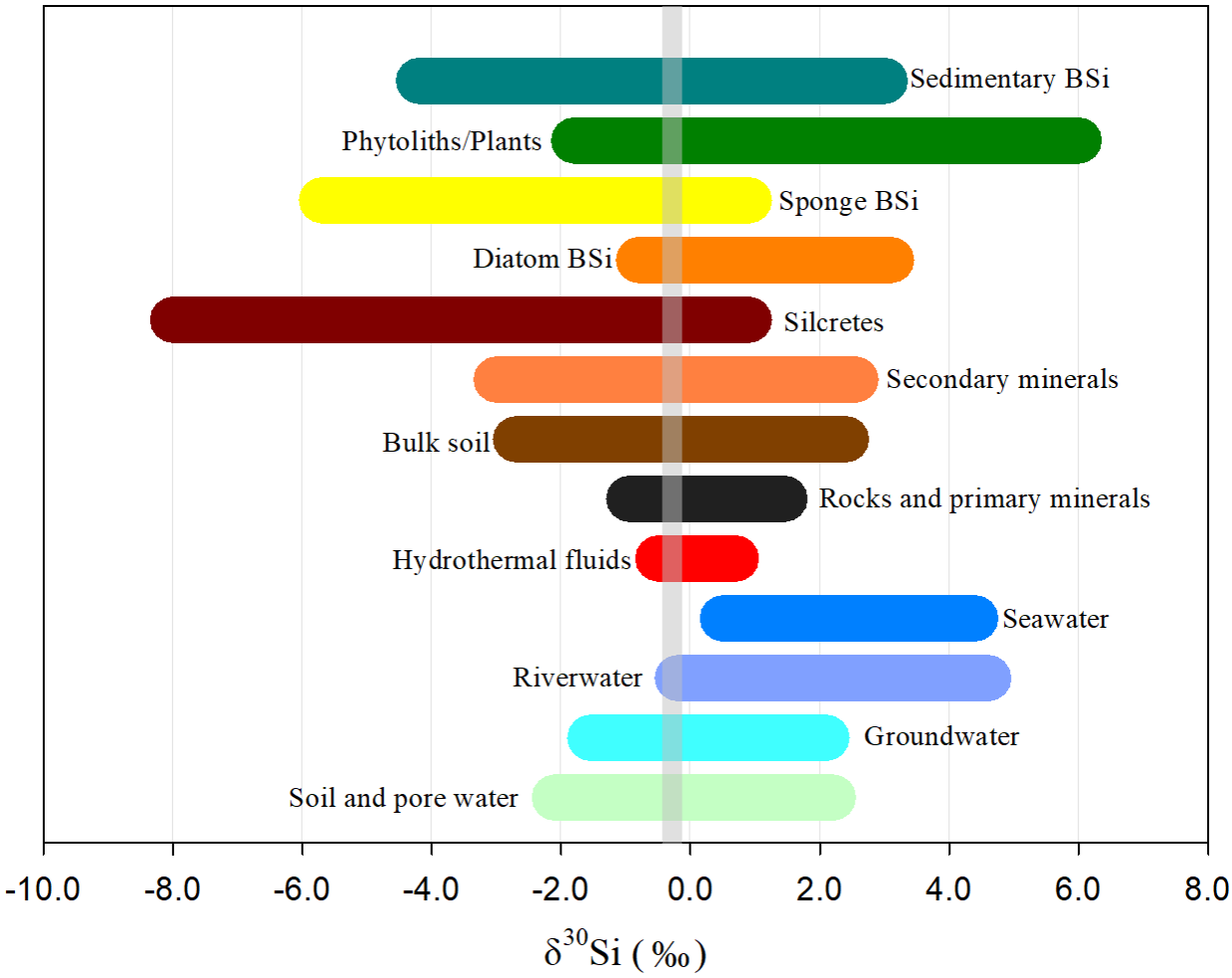

Figure 1.8 Silicon isotopic signature of Earth surface materials. Data from Frings et al. (2016) and references therein. The vertical grey bar marks the average UCC δ^{30}Si value at −0.25±0.16‰ (Savage et al., 2013).

The most important isotope fractionation related to weathering occurs during the formation of secondary minerals, which leads to the preferential uptake of the light Si isotopes, resulting in clays that have lower δ^{30}Si values and a DSi pool with higher δ^{30}Si than source rock (e.g. Ziegler et al., 2005a, 2005b; Opfergelt et al., 2008, 2009; Bern et al., 2010). As a result of weathering,

sedimentary rocks exhibit a shift towards lower values compared to UCC (Savage et al., 2013). To date, few investigations have been made to understand the impact of reverse weathering on δ^{30}Si, although it is assumed that such a process would preferentially remove light Si from seawater into solids (Frings et al., 2016).

1.3.2 Li isotope system

Li is the first metal element in periodic table with only 3 protons. Lithium has two stable isotopes:^{6}Li (7.6%) and ^{7}Li (92.4%) (Penniston-Dorland et al., 2017). Li is an alkali element, and like other elements in the same group, Li loses 1 electron from its outer orbit to form an electronic configuration of noble gas element. Therefore, Li is always found in the oxidation state of +1 in the nature. During weathering, it is readily dissolved in the water (Fig 1.1). Its isotope fractionation follows the same pattern as that of Si during weathering: lighter Li isotopes are preferentially retained into solids, leaving the dissolved phase with heavy δ^{7}Li. On the Earth's surface, its geochemical cycle is relatively simple as it is not an essential nutrient for biological activities (Fig 1.9). The δ^{7}Li has been used as a proxy to trace the past style and magnitude of Earth surficial processes, especially from its seawater record (Fig. 1.2) (Hathorne and James, 2006; Misra and Froelich, 2012; Li and West, 2014; Vigier and Godderis, 2014). The ocean receives Li fluxes from continental weathering, hydrothermal fluids, and subduction reflux (Fig. 1.9). In the recent years, the application of δ^{7}Li has become widespread in the studies of continental weathering (e.g. Dellinger et al., 2014, 2017; Pogge Von Strandmann and Henderson, 2015; Henchiri et al., 2016). Nevertheless, other major fluxes to the ocean, such as the subduction reflux, are much less well constrained. Finally, at steady state, an annual sink of 29×10^{9} moles is required to balance the combined inputs to the ocean.

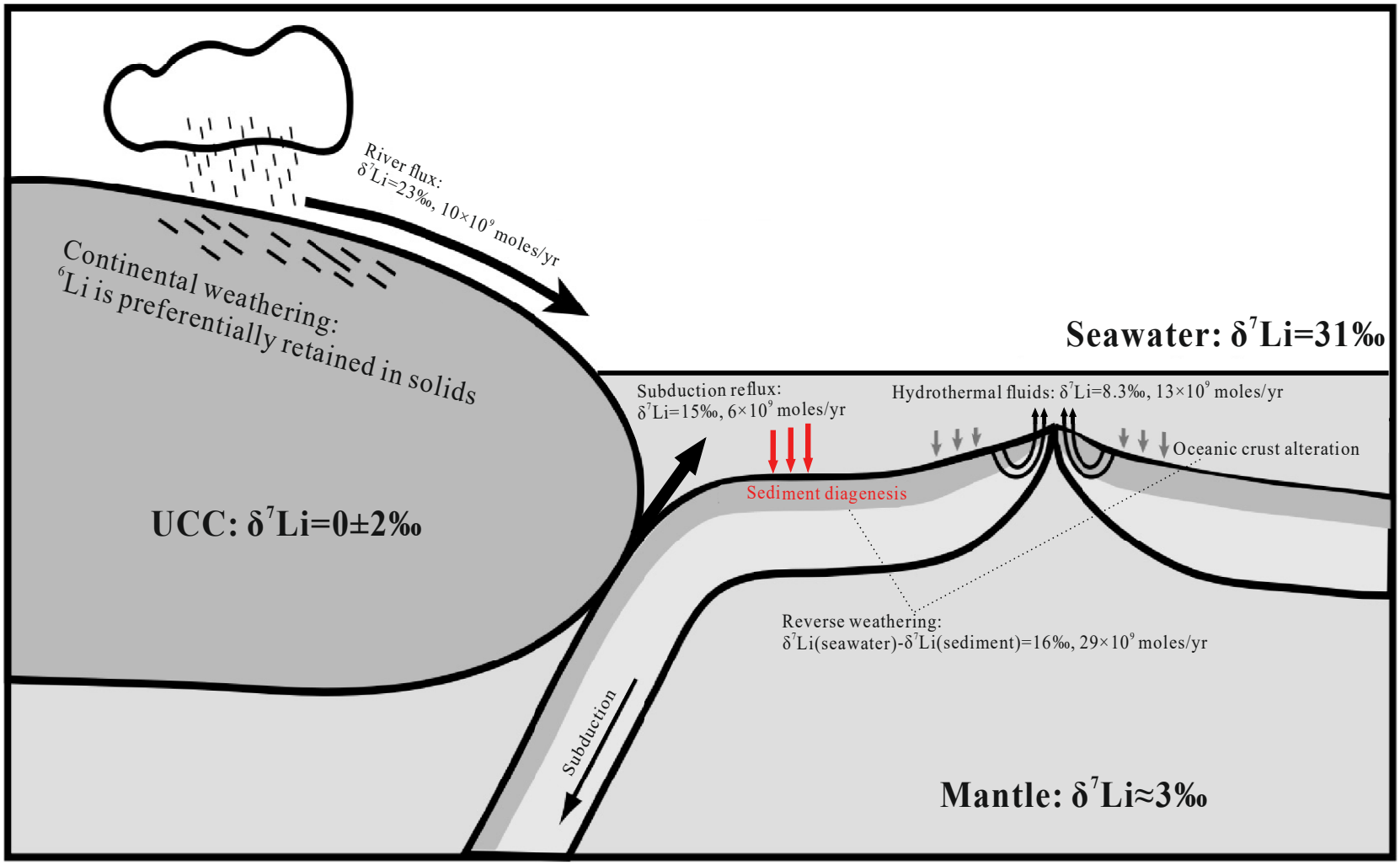

Figure 1.9 Present-day geochemical cycle of Li at Earth surface. Figure is reprinted and modified from Elliott et al. (2004) with permission from Elsevier. Data of Li fluxes are updated using values from Misra and Froelich (2012). The UCC δ^7Li value is from Teng et al. (2004).

The δ^7Li distribution across Earth surface materials (Fig. 1.10) shows that the Li isotope variation range (~70‰) is large and is significantly greater than that of Si isotopes (~14‰, Fig. 1.8). Such characteristic allows Li for being a robust tracer of the Earth surface processes. Secondly, despite the large range of δ^7Li values in nature, its seawater composition has one of the highest values (~31‰).

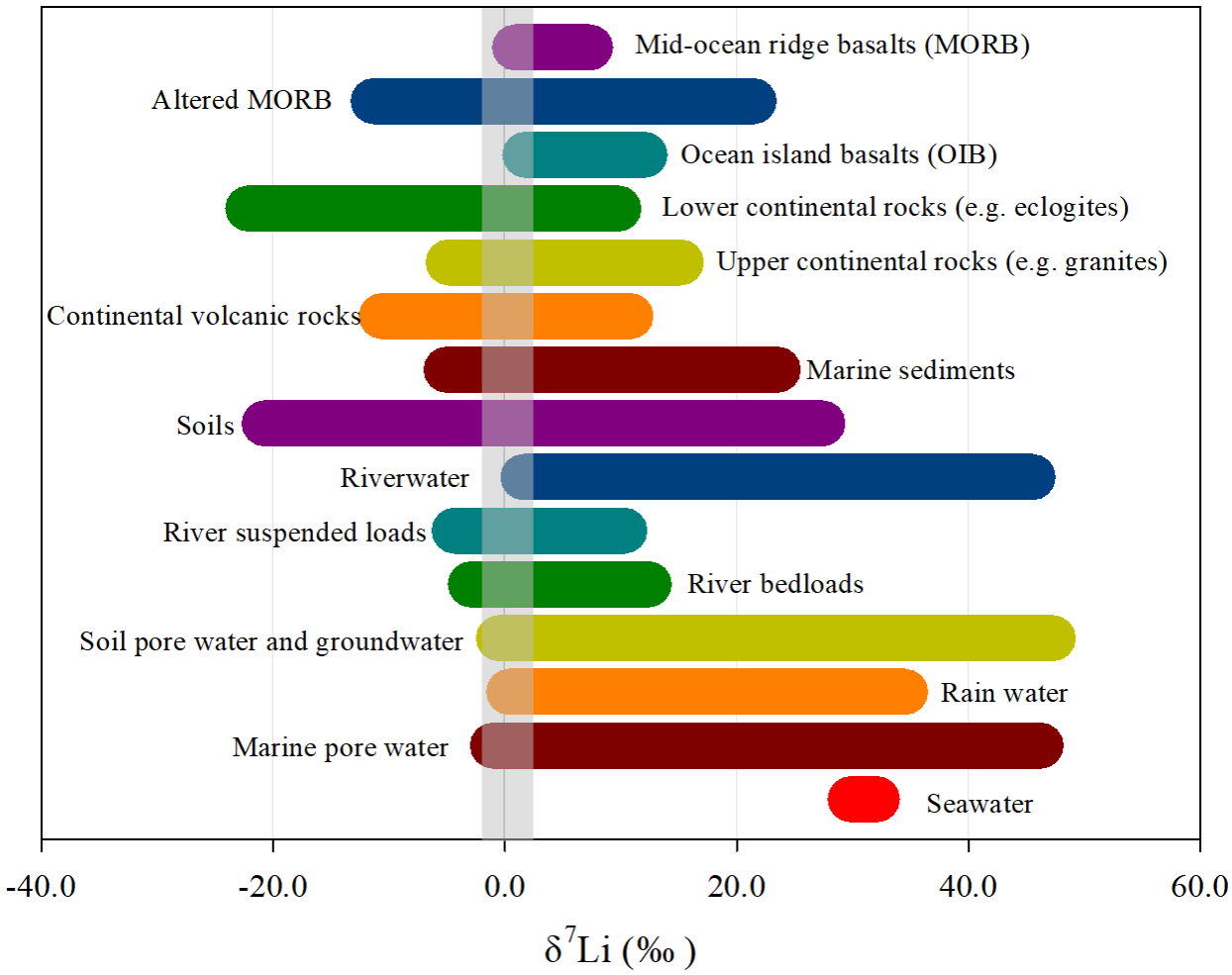

Figure 1.10 Lithium isotopic signature of Earth surface materials. Reproduced from Tomascak et al. (2016).

Continental weathering certainly played a crucial role on the seawater evolution at the geological time scale (Hathorne and James, 2006; Misra and Froelich, 2012); however this process alone is

unable to explain why seawater is isotopically heavier than the influxes including river, subduction reflux, and hydrothermal activities. The investigation of the alteration of oceanic crust showed that such a process is indeed able to take up light Li via clay formation at lower temperatures (*e.g.* Chan et al., 1994; James et al., 2003; Chan et al., 2006). This process, however, is not well constrained and quantified. Additionally, in marine sediments, the vast majority of clays are of terrigenous origin (Drever, 1971). A role of detrital clays in regulating the seawater Li content and isotope signature has been suspected (Misra and Froelich, 2012), since some of clays such as smectite are chemically identical to the clays formed during oceanic basalt alteration. Overall, Li uptake by detrital clays via reverse weathering has been suggested as a major sink of seawater Li, whilst *in situ* investigations are still sparse.

1.3.3 A Si-Li paradox in sedimentary cannibalistic recycling

In general, Si and Li isotopes behave similarly at the Earth surface: both elements are almost exclusively borne by silicate minerals; during continental weathering, light isotopes are preferentially retained in solids due to secondary formation, and aqueous phase is enriched with heavy isotopes; according to mass balance arguments, the anticipated reverse weathering processes should also preferentially take up light Si and Li from seawater into marine sediments; the only major difference between these two elements is that Si is utilised by the biota as a nutrient, while Li is not.

Despite of these similarities, a Si-Li paradox exists when comparing the δ^{30}Si and δ^{7}Li signatures in sedimentary rocks. In Figure 1.11, sedimentary rock δ^{30}Si and δ^{7}Li values are plotted against the corresponding Al/Si ratio, which can be seen as a grain size proxy (*e.g.* Bouchez et al., 2011; Dellinger et al., 2014) or a weathering index (Savage et al., 2013). Lower Al/Si values indicate coarser grain sizes and lower weathering intensities (quartz-rich sediments), whereas

higher Al/Si values indicate finer grain sizes and higher weathering intensities (higher clay contents). Sedimentary δ^{30}Si decreases with increasing Al/Si, whereas δ^{7}Li increases with Al/Si. Such observation, at first order, is a paradox with respect to the similar behavior of the two elements during weathering and reverse weathering. The negative trend (as observed for Si) is actually expected as weathering preferentially takes up lighter Si and Li isotopes in secondary minerals. To obtain a positive relationship between δ^{7}Li and Al/Si ratio, the only possible explanation is that in the marine environment, reverse weathering affecting mostly the fine portion of sediments, takes up seawater Li, which has a high δ^{7}Li value. In other words, a strong source effects would exist on the Li signature of reverse weathering products, whereas it is not for Si. The reason for the observed trends lies therefore in the high δ^{7}Li value of seawater, which deserves to be explained. In this dissertation, we will provide experimental and field evidence for processes allowing to build up this specific signature of the ocean.

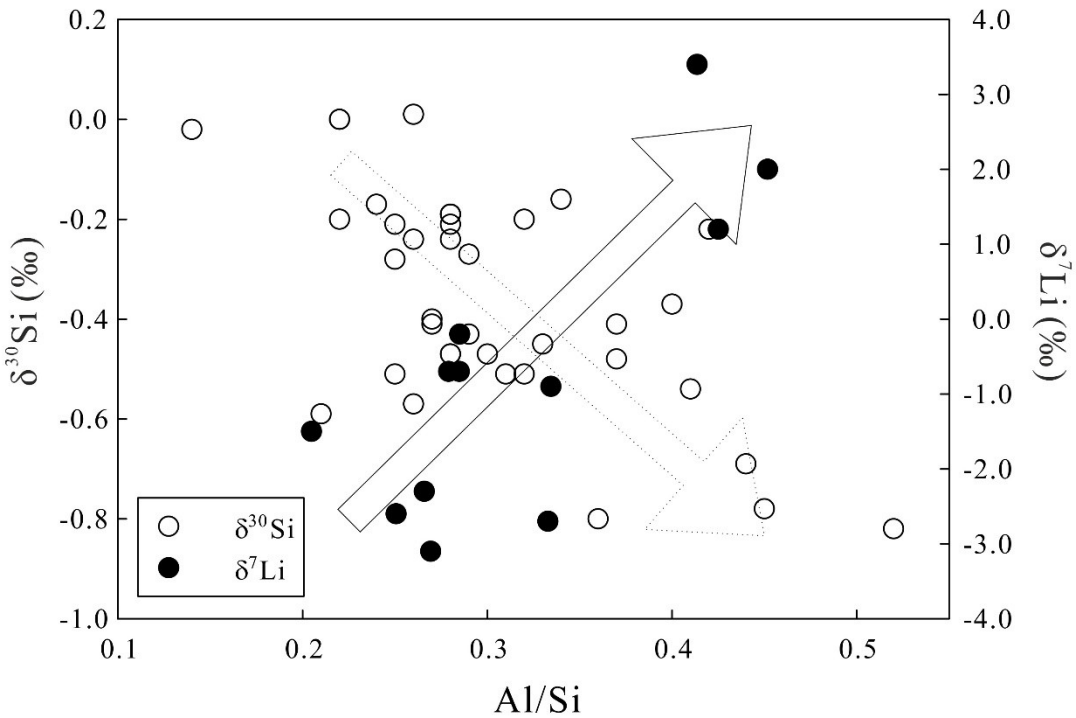

Figure 1.11 Sedimentary rock δ^{30}Si and δ^{7}Li signatures against their Al/Si ratios. δ^{30}Si data is from Savage et al. (2013), and δ^{7}Li data is from Teng et al. (2004). δ^{30}Si is negatively correlated with Al/Si ratio, which is consistent with the effect of weathering. δ^{7}Li is, however, positively correlated with Al/Si ratio.

1.4 Objectives of this dissertation

The main aim of this dissertation is to investigate the cannibalistic nature of sedimentary recycling, and how such a process is impacting the chemical and isotope composition of the Earth surface materials over geological time scales. To explain our conceptual framework, a schematic of intra-continental sedimentary recycling is given in Figure 1.12, featuring three main steps:

1. Continental weathering and sediment deposition
2. Post-depositional diagenesis with seawater interaction

3. Secondary-cycle weathering of re-uplifted (via tectonics) sedimentary rocks

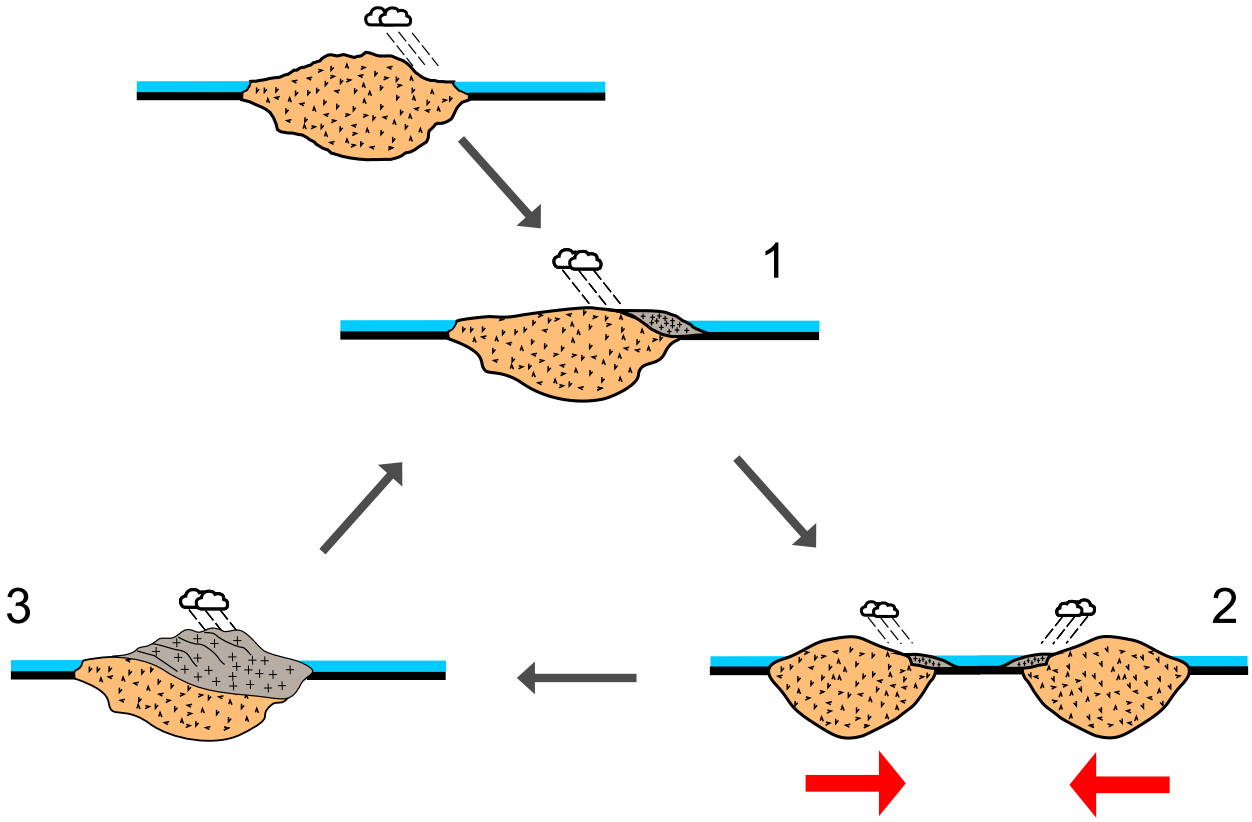

Figure 1.12 Schematic of sedimentary cannibalism. The recycling of sedimentary rocks involves three mains steps: 1. Sediment production; 2. Post-depositional diagenesis; 3. Secondary weathering of sedimentary rocks.

To better constrain the characteristics of each step in the cannibalistic cycle, we use a selection of sample materials of rock and sediment samples from different environments. First of all, it is necessary to know the nature of source rocks. Secondly, large river suspended particulate materials (SPM) and river bed sands (RBS) are of preferential interest as those materials carry the information of continental weathering at the scale of their vast drainage basins (Gaillardet, Dupré and Allègre, 1999; Dellinger et al., 2014). The vast majority of the present-day Earth surface is covered by sedimentary rocks (Wilkinson et al., 2009). Therefore, the investigation of SPM not only reveals information about the weathering of igneous rocks, but also about cannibalistic

weathering. Lastly, marine sediments and marine sedimentary rocks are key objects to investigate reverse weathering.

The benefits of using δ^{30}Si and δ^{7}Li as geochemical tracers of sedimentary recycling are two folds. Firstly, the two isotopic systems show great potential in tracing low-temperature Earth surface processes due to their geochemical properties as introduced in section 1.3. Secondly, an initial understanding of δ^{30}Si and δ^{7}Li signatures has been established from past studies. For instance, Savage et al. (2013) and Teng et al. (2004) respectively conducted extensive studies on the δ^{30}Si and δ^{7}Li systems in igneous and sedimentary rocks, which benefits to the understanding of the step 1 (Fig 1.12) in the cannibalistic cycle. In particular, the study of δ^{7}Li of the Amazon, Mackenzie, and Ganga-Brahmaputra rivers sediments by Dellinger et al. (2014) showed that the current river sedimentary load is largely composed by materials sourced from sedimentary rocks. Although few direct *in situ* efforts were made to better understand reverse weathering, the mass balance models for δ^{7}Li (Misra and Froelich, 2012) and δ^{30}Si (Tréguer and De La Rocha, 2013; Frings et al., 2016) provided preliminary guidance on this subject.

In this dissertation, the less constrained aspects of the sedimentary and weathering cycles on the Si and Li isotope systems are explored. As such, the first objective for us was to precisely measure δ^{30}Si and δ^{7}Li compositions using well-established techniques of analyses by MC-ICP-MS at the Institut de Physique de Globe a Paris. The pre-treatment of samples for δ^{30}Si measurement was adopted from a widely applied separation method (Georg et al., 2006). Conversely, due to the challenge associated with the separation of Li from the sample matrix, a new pre-treatment method was developed for δ^{7}Li analysis. Additionally, to better understand the grain-size effects on the δ^{30}Si signature of clastic sediments, river sediments collected along depth profiles were used. The detailed descriptions of the depth-profile sampling, sample pre-treatment,

separation, and mass-spectrometry techniques used for the precise measurements of δ^{30}Si and δ^{7}Li are provided in Chapter 2.

After confirming the feasibility of precisely measuring δ^{30}Si and δ^{7}Li in solid samples, our objectives were accomplished through 3 studies. These studies aimed at placing better constraints on reverse weathering (step 2, Fig 1.12) and secondary-cycle weathering (step 3, Fig 1.12) processes, and they form Chapter 3 to 5 in this dissertation. These 3 studies are organized following an increase in the relevant time scales from short (experimental work in Chapter 3) to long (sedimentary cycles from large river studies, Chapter 5). Each of these studies is briefly introduced next.

In Chapter 3, using an experimental approach we aim at investigating the processes by which detrital sediments can sequestrate seawater Li and cause isotopic fractionation through reverse weathering. As such, laboratory experiments were performed allowing primary minerals (basalt glass) and secondary minerals (kaolinite) for reacting with artificial seawater "doped" with Li (with known concentration and δ^{7}Li composition). The experiments lasted for ~170 days. Significant Li removal from seawater accompanied by remarkable δ^{7}Li fractionation in residual solution were observed in the experiment where kaolinite was added to artificial seawater. Such finding confirms that detrital secondary minerals have the ability to lead to reverse-weathering-style reactions in marine environments.

In Chapter 4, a field study of reverse weathering was conducted. Marine and alluvial sedimentary rocks deposited on a paleo-delta system (Ainsa, Spain) were carefully studied using a variety of geochemical tools: major and trace elements, thin section mineralogy, neodymium (Nd) isotopes, δ^{30}Si, and δ^{7}Li. Samples were collected from a field trip (May, 2015) in southern Pyrenees, Spain where tectonic induced transgression-regression in mid-Eocene caused sediments

to be deposited in different environments ranging from marine to alluvial. Although both marine and alluvial sediments share the same source, as indicated by the Nd data, the interaction with seawater generated different δ^{30}Si and δ^{7}Li signatures: marine sediments are depleted in heavy isotopes for both isotope systems. Such behavior indicates that reverse weathering can consume light Li isotopes in deltaic environments (and thus could be a reason for the elevated δ^{7}Li in seawater). We suggest that this process is coupled with the scavenging of iron (Fe) in the same environment.

In Chapter 5, an extensive survey of δ^{30}Si in the world largest rivers was conducted. Surface SPM and RBS from 42 rivers, along with SPM river depth-profiles from the Mackenzie and the Amazon rivers, were analyzed. The results of δ^{30}Si in SPM and RBS confirm that all river sediments are enriched with lighter δ^{30}Si isotopes compared to dissolved load. Moreover, together with the considerations of Si minerology, the results also suggest that significant δ^{30}Si fractionation across the river sediment grain size range can be attributed to "first-cycle" weathering, in which feldspars can be transformed to clays by weathering. At long geological times scales, the recycling of sedimentary rocks separates Si into two main reservoirs: quartz-rich sandstones and clay-rich shales. During secondary weathering of the sedimentary rocks, Si is confined in minerals unsensitive to weathering, such as quartz. This again hints at the importance of igneous rocks such as basalts (and therefore of geological settings such as volcanic islands and large igneous provinces) in regulating atmospheric CO_2.

In Chapter 6, the significant findings of this dissertation are summarized: 1. Detrital clay minerals transported to ocean are able to preferentially take up light Li isotopes from the ocean after their chemical interaction with seawater; 2. Reverse weathering at deltaic environments consumes light Si and Li isotopes, resulting in elevated seawater δ^{30}Si and δ^{7}Li; 3. Seawater Li

uptake by sediments via reverse weathering does not necessarily make the δ^7Li of sedimentary rocks elevated; 4. Lithology plays a primary role on the δ^{30}Si signature of river sediments; 5. "First-cycle" weathering is the most important contributor to the overall δ^{30}Si variation in river sediments, as weathering-sensitive minerals such as feldspars are most available during this step; 6. In secondary weathering cycles, although Si is still abundant, it is carried by inactive minerals barely involved in CO_2 consumption by silicate weathering.

Bibliography

Allègre, C.J., Rousseau, D., 1984. The growth of the continent through geological time studied by Nd isotope analysis of shales. Earth and Planetary Science Letters 67 (1), 19-34.

Allenby, R., 1954. Determination of the isotopic ratios of silicon in rocks. Geochimica et Cosmochimica Acta 5 (1), 40-48.

Aller, R.C., 2014. 8.11 - Sedimentary Diagenesis, Depositional Environments, and Benthic Fluxes. In: Holland, H.D. and Turekian, K.K., (Eds.). Treatise on Geochemistry (Second Edition). Elsevier, Oxford.

Bastian, L., Revel, M., Bayon, G., Dufour, A., Vigier, N., 2017. Abrupt response of chemical weathering to Late Quaternary hydroclimate changes in northeast Africa. Scientific reports 7, 44231.

Bern, C.R., Brzezinski, M.A., Beucher, C., Ziegler, K., Chadwick, O.A., 2010. Weathering, dust, and biocycling effects on soil silicon isotope ratios. Geochimica et Cosmochimica Acta 74 (3), 876-889.

Berner, R.A., Lasaga, A.C., Garrels, R.M., 1983. The carbonate-silicate geochemical cycle and its effect on atmospheric carbon dioxide over the past 100 million years. American Journal of Science 283 (7), 641-683.

Bischof, G., 1847. Lehrbuch Der Chemischen Und Physikalischen Geologie. A. Marcus.

Blatt, H., Jones, R.L., 1975. Proportions of exposed igneous, metamorphic, and sedimentary rocks. Geological Society of America Bulletin 86 (8), 1085-1088.

Bouchez, J., Gaillardet, J., 2014. How accurate are rivers as gauges of chemical denudation of the Earth surface? Geology 42 (2), 171-174.

Bouchez, J., Gaillardet, J., France-Lanord, C., Maurice, L., Dutra-Maia, P., 2011. Grain size control of river suspended sediment geochemistry: Clues from Amazon River depth profiles. Geochemistry Geophysics Geosystems 12, Q03008.

Brantley, S.L., Goldhaber, M.B., Ragnarsdottir, K.V., 2007. Crossing disciplines and scales to understand the critical zone. Elements 3 (5), 307-314.

Busby, C., Ingersoll, R., 1995. Tectonics of Sedimentary Basins.

Chan, L., Leeman, W.P., Plank, T., 2006. Lithium isotopic composition of marine sediments. Geochemistry, Geophysics, Geosystems 7 (6).

Chan, L., Gieskes, J.M., You, C., Edmond, J.M., 1994. Lithium isotope geochemistry of sediments and hydrothermal fluids of the Guaymas Basin, Gulf of California. Geochimica et Cosmochimica Acta 58 (20), 4443-4454.

Dellinger, M., Bouchez, J., Gaillardet, J., Faure, L., Moureau, J., 2017. Tracing weathering regimes using the lithium isotope composition of detrital sediments. Geology 45 (5), 411-414.

Dellinger, M., Gaillardet, J., Bouchez, J., Calmels, D., Galy, V., Hilton, R.G., Louvat, P., France-Lanord, C., 2014. Lithium isotopes in large rivers reveal the cannibalistic nature of modern continental weathering and erosion. Earth and Planetary Science Letters 401, 359-372.

DeMaster, D.J., 2002. The accumulation and cycling of biogenic silica in the Southern Ocean: revisiting the marine silica budget. Deep Sea Research Part II: Topical Studies in Oceanography 49 (16), 3155-3167.

Ding, T., Tang, L., 1996. Silicon Isotope Geochemistry. Geological Publishing House.

Douthitt, C., 1982. The geochemistry of the stable isotopes of silicon. Geochimica et Cosmochimica Acta 46 (8), 1449-1458.

Drever, J.I., 1971. Early diagenesis of clay minerals, Rio Ameca basin, Mexico. Journal of Sedimentary Research 41 (4).

Dunlea, A.G., Murray, R.W., Ramos, D.P.S., Higgins, J.A., 2017. Cenozoic global cooling and increased seawater Mg/Ca via reduced reverse weathering. Nature Communications 8 (1), 844.

Ebelmen, J., Sur les produits de la décomposition des espèces minérales de la famille des silicates. 7, 66391.

Edmond, J.M., McDuff, R., Chan, L., Collier, R., Grant, B., Gordon, L., Corliss, J., 1979. Ridge crest hydrothermal activity and the balances of the major and minor elements in the ocean: the Galapagos data. Earth and Planetary Science Letters 46 (1), 1-18.

Elliott, T., Jeffcoate, A., Bouman, C., 2004. The terrestrial Li isotope cycle: light-weight constraints on mantle convection. Earth and Planetary Science Letters 220 (3-4), 231-245.

Frings, P.J., Clymans, W., Fontorbe, G., De La Rocha, C.L., Conley, D.J., 2016. The continental Si cycle and its impact on the ocean Si isotope budget. Chemical Geology 425, 12-36.

Gaillardet, J., Dupré, B., Allègre, C.J., Geochemistry of large river suspended sediments: silicate weathering or recycling tracer? 63, 4037-405172.

Georg, R.B., Reynolds, B.C., Frank, M., Halliday, A.N., 2006. New sample preparation techniques for the determination of Si isotopic compositions using MC-ICPMS. Chemical Geology 235 (3–4), 95-104.

Gibbons, A., 2009. Ardipithecus ramidus. A new kind of ancestor: Ardipithecus unveiled. Science (New York, N.Y.) 326 (5949), 36-40.

Goldschmidt, V., 1933. Grundlagen der quantitativen Geochemie. Fortschr.Mienral.Kirst.Petrogr 17, 112.

Gregor, C., 1985. The mass-age distribution of Phanerozoic sediments. Geological Society, London, Memoirs 10 (1), 284-289.

Hathorne, E.C., James, R.H., 2006. Temporal record of lithium in seawater: A tracer for silicate weathering? Earth and Planetary Science Letters 246 (3-4), 393-406.

Hay, W.W., Sloan, J.L., Wold, C.N., 1988. Mass/age distribution and composition of sediments on the ocean floor and the global rate of sediment subduction. Journal of Geophysical Research: Solid Earth 93 (B12), 14933-14940.

Henchiri, S., Gaillardet, J., Dellinger, M., Bouchez, J., Spencer, R.G.M., 2016. Riverine dissolved lithium isotopic signatures in low-relief central Africa and their link to weathering regimes. Geophysical Research Letters 43 (9), 4391-4399.

Holland, H.D., 2005. Sea level, sediments and the composition of seawater. American Journal of Science 305 (3), 220-239.

James, R.H., Allen, D.E., Seyfried, W., 2003. An experimental study of alteration of oceanic crust and terrigenous sediments at moderate temperatures (51 to 350 C): Insights as to chemical processes in near-shore ridge-flank hydrothermal systems. Geochimica et Cosmochimica Acta 67 (4), 681-691.

Lavoisier, A., 1772. Mémoire sur l'usage de l'esprit-de-vin dans l'analyse des eaux minérales. Mem.Acad.Roy.Sci.(Paris) , 555-563.

Lavoisier, A.L., 1892. Oeuvres. Impr. imperiale.

Lavoisier, A.L., 1801. Opuscules Physiques Et Chimiques. Deterville.

Lemarchand, D., Gaillardet, J., Lewin, E., Allegre, C., 2002. Boron isotope systematics in large rivers: implications for the marine boron budget and paleo-pH reconstruction over the Cenozoic. Chemical Geology 190 (1-4), 123-140.

Li, G., West, A.J., 2014. Evolution of Cenozoic seawater lithium isotopes: Coupling of global denudation regime and shifting seawater sinks. Earth and Planetary Science Letters 401, 284-293.

Mackenzie, F.T., Kump, L.R., 1995. Reverse weathering, clay mineral formation, and oceanic element cycles. Science 270 (5236), 586.

Mackenzie, F.T., Garrels, R., 1971. Evolution of Sedimentary Rocks. Norton.

Mackenzie, F.T., Garrels, R.M., 1966. Chemical mass balance between rivers and oceans. American Journal of Science 264 (7), 507-525.

McCulloch, M.T., Wasserburg, G.J., 1978. Sm-nd and rb-sr chronology of continental crust formation. Science (New York, N.Y.) 200 (4345), 1003-1011.

McLennan, S.M., 2001. Relationships between the trace element composition of sedimentary rocks and upper continental crust. Geochemistry, Geophysics, Geosystems 2 (4).

McLennan, S.M., Taylor, S., 1980. Th and U in sedimentary rocks: crustal evolution and sedimentary recycling. Nature 285 (5767), 621.

Michalopoulos, P., Aller, R.C., 1995. Rapid clay mineral formation in Amazon delta sediments: reverse weathering and oceanic elemental cycles. Science, 270 (5236), 614-617.

Michalopoulos, P., Aller, R.C., 2004. Early diagenesis of biogenic silica in the Amazon delta: alteration, authigenic clay formation, and storage. Geochimica et Cosmochimica Acta 68 (5), 1061-1085.

Milliman, J.D., Farnsworth, K.L., 2013. River Discharge to the Coastal Ocean: A Global Synthesis. Cambridge University Press.

Misra, S., Froelich, P.N., 2012. Lithium Isotope History of Cenozoic Seawater: Changes in Silicate Weathering and Reverse Weathering. Science 335 (6070), 818-823.

Morris, H.M., 1974. Scientific Creationism. New Leaf Publishing Group.

Odin, G., Fröhlich, F., 1988. Chapter C3 Glaucony from the Kerguelen Plateau (Southern Indian Ocean). In: Anonymous Developments in Sedimentology. Elsevier.

Opfergelt, S., Delvaux, B., André, L., Cardinal, D., 2008. Plant silicon isotopic signature might reflect soil weathering degree. Biogeochemistry 91 (2-3), 163-175.

Opfergelt, S., De Bournonville, G., Cardinal, D., André, L., Delstanche, S., Delvaux, B., 2009. Impact of soil weathering degree on silicon isotopic fractionation during adsorption onto iron oxides in basaltic ash soils, Cameroon. Geochimica et Cosmochimica Acta 73 (24), 7226-7240.

Paris, G., Gaillardet, J., Louvat, P., 2010. Geological evolution of seawater boron isotopic composition recorded in evaporites. Geology 38 (11), 1035-1038.

Pearson, P.N., Palmer, M.R., 2000. Atmospheric carbon dioxide concentrations over the past 60 million years. Nature 406 (6797), 695.

Penniston-Dorland, S., Liu, X., Rudnick, R.L., 2017. Lithium isotope geochemistry. Reviews in Mineralogy and Geochemistry 82 (1), 165-217.

Pogge von Strandmann, Philip AE, Henderson, G.M., 2015. The Li isotope response to mountain uplift. Geology 43 (1), 67-70.

Poitrasson, F., 2017. Silicon Isotope Geochemistry. Reviews in Mineralogy and Geochemistry 82 (1), 289-344.

Pokharel, R., Gerrits, R., Schuessler, J.A., Floor, G.H., Gorbushina, A.A., von Blanckenburg, F., 2017. Mg Isotope Fractionation during Uptake by a Rock-Inhabiting, Model Microcolonial Fungus Knufia petricola at Acidic and Neutral pH. Environmental science & technology 51 (17), 9691-9699.

Rahman, S., Aller, R., Cochran, J., 2016. Cosmogenic 32Si as a tracer of biogenic silica burial and diagenesis: Major deltaic sinks in the silica cycle. Geophysical Research Letters 43 (13), 7124-7132.

Ramos, D.P.S., Morgan, L.E., Lloyd, N.S., Higgins, J.A., 2018. Reverse weathering in marine sediments and the geochemical cycle of potassium in seawater: Insights from the K isotopic composition (41K/39K) of deep-sea pore-fluids. Geochimica et Cosmochimica Acta .

Reynolds, J.H., Verhoogen, J., 1953. Natural variations in the isotopic constitution of silicon. Geochimica et Cosmochimica Acta 3 (5), 224-234.

Ronov, A.B. (Ed.), 1993. Stratisfera – Ili Osadochnaya Obolochka Zemli (Kolichestvennoe Issledovanie). Nauka, Moscow, USSR.

Rudnick, R., Gao, S., 2014. Composition of the continental crust.

Savage, P.S., Georg, R.B., Williams, H.M., Halliday, A.N., 2013. The silicon isotope composition of the upper continental crust. Geochimica et Cosmochimica Acta 109, 384-399.

Sillen, L.G., 1967. The ocean as a chemical system. Science (New York, N.Y.) 156 (3779), 1189-1197.

Taylor, S., McLennan, S., 1985. The continental crust: its composition and evolution. Oxford: Blackwell Press 1, 312.

Taylor, S.R., McLennan, S.M., 1995. The geochemical evolution of the continental crust. Reviews of Geophysics 33 (2), 241-265.

Taylor SR., 1964, Abundance of chemical elements in the continental crust: a new table. Geochimica et cosmochimica acta. 28 (8),1273-1285.

Teng, F., McDonough, W.F., Rudnick, R., Dalpé, C., Tomascak, P., Chappell, B.W., Gao, S., 2004. Lithium isotopic composition and concentration of the upper continental crust. Geochimica et Cosmochimica Acta 68 (20), 4167-4178.

Tomascak, P.B., Magna, T., Dohmen, R., 2016. Advances in Lithium Isotope Geochemistry. Springer International Publishing, Springer International Publishing Switzerland.

Tréguer, P., Nelson, D.M., Van Bennekom, A.J., DeMaster, D.J., Leynaert, A., Quéguiner, B., 1995. The Silica Balance in the World Ocean: A Reestimate. Science 268 (5209), 375-379.

Tréguer, P., De La Rocha, C., 2013. The world ocean silica cycle. Annual review of marine science 5, 477-501.

Turner, D., Whitfield, M., 1979. Control of seawater composition. Nature 281 (5731), 468.

Van Cappellen, P., Qiu, L., 1997. Biogenic silica dissolution in sediments of the Southern Ocean. II. Kinetics. Deep Sea Research Part II: Topical Studies in Oceanography 44 (5), 1129-1149.

Veizer, J., Jansen, S.L., 1979. Basement and sedimentary recycling and continental evolution. The Journal of geology 87 (4), 341-370.

Veizer, J., Jansen, S.L., 1985. Basement and sedimentary recycling-2: time dimension to global tectonics. The Journal of geology 93 (6), 625-643.

Veizer, J., Mackenzie, F., 2013. Evolution of Sedimentary Rocks.

Vernadsky, V., 1926. Biosfera, Leningrad, Nauchno-techn. Izd., 146p .

Vigier, N., Godderis, Y., 2014. A new approach for modeling Cenozoic oceanic lithium isotope paleo-variations: the key role of climate. Climate of the Past Discussions 11 (4), 635-645.

Walker, J.C.G., Hays, P.B., Kasting, J.F., 1981. A negative feedback mechanism for the long-term stabilization of Earth's surface temperature. Journal of Geophysical Research: Oceans 86 (C10), 9776-9782.

White, W.M., 2013. Geochemistry. John Wiley & Sons.

Whitfield, M., 1979. The mean oceanic residence time (MORT) concept-a rationalisation. Marine Chemistry 8 (2), 101-123.

Whitfield, M., Turner, D., 1979. Water–rock partition coefficients and the composition of seawater and river water. Nature 278 (5700), 132-137.

Wilkinson, B.H., McElroy, B.J., Kesler, S.E., Peters, S.E., Rothman, E.D., 2009. Global geologic maps are tectonic speedometers—Rates of rock cycling from area-age frequencies. Geological Society of America Bulletin 121 (5-6), 760-779.

Ziegler, K., Chadwick, O.A., White, A.F., Brzezinski, M.A., 2005a. d30Si systematics in a granitic saprolite, Puerto Rico. Geology 33 (10), 817-820.

Ziegler, K., Chadwick, O.A., Brzezinski, M.A., Kelly, E.F., 2005b. Natural variations of δ30Si ratios during progressive basalt weathering, Hawaiian Islands. Geochimica et Cosmochimica Acta 69 (19), 4597-4610.

Chapter 2: Methods and techniques

2.1 Samples and reagents

2.1.1 Depth-profile sampling

For our study of large river sediments (Chapter 5), surface SPM and RBS samples were selected from the sample repository at IPGP. River depth-profile samples of the Mackenzie and the Amazon rivers were respectively the same as in the studies of Dellinger et al. (2014) and Bouchez et al. (2011). In order to collect river depth sample profiles, Acoustic Doppler Current Profiler (ADCP) had been employed in the field, to retrieve channel depth, water velocity profiles, and instantaneous discharge.

Vertical depth-profile of sediment samples were then collected at targeted depths using a point-sampler fixed on a boat. The sampler consists of a cylinder tube, one stopper attached at each outlet of the two sides of the cylinder tube, and a weight of ~30kg stabilizing the sampler attached at the bottom of the tube. The sampler is attached to a reel fixed on a boat through a wire. The length of the wire is known, such that the depth of sampler can be measured. Samples are filtered within one or two days after collection and kept in prewashed plastic containers. Once the sediment samples have been transported back to the laboratory, the samples are dried for further analysis.

2.1.2 Laboratory protocols

A main requirement of this dissertation is to precisely measure δ^{30}Si and δ^{7}Li compositions. Except for the experimental study of Chapter 3, all samples were received as solids, and thus had to be crushed into powders in order to guarantee complete dissolution of minerals during digestion. Sediments from large rivers were in the form of powders and were directly used for the following analysis. Samples collected from the Ainsa field site (Spain, see Chapter 4) were in the form of rocks, and therefore were first crushed in an agate mortar. Although contamination from the agate mortar for δ^{30}Si analysis could in theory be possible, such an effect has been shown to be undetectable (Zambardi and Poitrasson, 2011).

To precisely measure the isotopic compositions, it is crucial to avoid contaminations during the manipulation of samples. In particular, Li is a trace element and the presence of the major element Na in the analyzed solution can affect the results obtained on the MC-ICP-MS. As Si is a major element (*e.g.* the average SiO_2 content in UCC is about 66%; Taylor and McLennan, 1985; Rudnick and Gao, 2003), the contamination issue is less important. All manipulations were conducted in a clean lab facility at IPGP except for the alkaline fusion of solid samples before Si purification. All acids used (HF, HCl, and HNO_3, electronic industry grade, VASL, BASF) were purified by distillation in the laboratory (DST1000, Savillex, USA). Water used in this dissertation was Milli-Q (MQ) water (resistivity of 18.2 MΩ cm^{-1}). Analytical grade chemical reagents were used. Ultra-pure NaOH was used for alkaline fusion (99.99% purity, Sigma-Aldrich). All labware was cleaned following standard protocols. A "hot wash" method was used for Teflon containers, in which Teflon containers were first cleaned 3 times with water, then were boiled with concentrated acid (HNO_3 or HCl) on a hot plate at least over night, and finally rinsed 3 times with MQ-water and dried. All other labware (pipette tips, PP bottles, tubes, etc.,) was washed using a "cold wash" method which requires the labware being rinsed 3 times by water, then submerged in 1 N HNO_3 solution, and finally rinsed by MQ water and dried.

Procedural blanks of Li and Si were analyzed by both Inductively Coupled Plasma Quadrupole Mass Spectrometer (ICP-Q-MS) and MC-ICP-MS, showing that they were unresolvable from instrumental background baselines, indicating that the possible contaminations were minimized and would not contribute further to the results.

2.2 Major and trace elements

Large river sediments' geochemical characteristics such as major and trace elements are already available (e.g. Bouchez et al., 2011; Dellinger et al., 2014). Within this work, major and trace elements were analyzed for Ainsa samples. The major elements were measured at the SARM (Le Service d'Analyse des Roches et des Minéraux, Vandoeuvre-les-Nancy, France). The details of sample preparation and analyzing methods are provided at http://helium.crpg.cnrs-nancy.fr/SARM/pages/roches.html, and the typical error bars are less than 5%.

Powdered samples first had to be dissolved to be used for the trace element analyse and Li isotope measurements. A standard acid attack method was applied. Here a brief description of this method is provided. Approximately 0.1 g of sample materials was weighed in a Teflon bomb. Then 1 ml HF (27 N) was carefully pipetted onto the sample. Then the sample was sonicated for 1 hour with Teflon cap firmly tightened. Next, 1 ml HNO_3 (16 N) was added into the solution and the Teflon bomb was boiled at ~110°C for 24 hours. Then the sample was allowed to evaporate until dryness. In this step, silicates can be effectively dissolved by HF acid and Si is removed into gaseous phase in the form of H_2SiF_6. The remaining residuals were then repeatedly taken up using HCl (6 N) and evaporated, until the sample was completely dissolved. Finally, the sample was evaporated and re-dissolved in ~2 ml HNO_3, and then transferred in to a Falcon tube and diluted to 10 ml with MQ-water.

Trace elements were analyzed using ICP-Q-MS at IPGP. The benefit of ICP-Q-MS is the possible measurement of the concentrations of multiple elements in the same analytical session. A dilution factor from 1:5000 to 1:10000 (g/ml) was used for solid samples, and the measurements of ICP-Q-MS were conducted in 0.5 N HNO_3 solution. Therefore, aliquots of digested rock samples stored in the Falcon tubes were further evaporated and diluted ~50 to 100 times in 0.5 N

HNO_3 solutions. Instrument was calibrated with a series of multi-element standards of concentration between 0.1 ppb and 200 ppb. Internal standards were routinely measured at each measurement session to monitor the drift of the instrument sensitivity. The well-constrained basalt reference materials BHVO-2 and JB-2 were also routinely analyzed to determine the accuracy and precision of the measurements. Depending on the instrumental conditions, and depending on the elements, the precision was often within a level of ±5% and occasionally could reach ±10%.

2.3 Purification of Si and Li

The precise measurement of δ^{30}Si and δ^{7}Li compositions requires an efficient purification of Si and Li from the sample matrix. This was achieved from chromatographic separation based on ion exchange resins.

2.3.1 Alkaline fusion

During rock sample digestion using HF, Si is removed into the gaseous phase in the form of SiF_4. Therefore, samples used for δ^{30}Si analyse were digested using an alkaline fusion method (Georg et al., 2006). When a mixture of silicate minerals and an "alkaline flux" is heated to a high temperature, the melt can completely dissolve the silicate minerals (Potts, 2012). A "fusion cake", in which elements were at metastable states, forms when the melt cools down. This fusion cake can be readily dissolved in a weakly acidified solution. In this study, ~200 mg NaOH were added into ~10 mg sample in a silver crucible. In principle, other alkaline fluxes can also be used for the digestion of Si, such as $LiBO_2$ (Abraham et al., 2008). As Li was also studied in this dissertation, in order to avoid any potential cross lab contamination, NaOH was chosen as an alkaline flux. The samples were then heated in a pre-heated furnace at 720°C for 12 minutes. Next, crucibles were removed from the furnace and were allowed for cooling at ambient temperature. Then they were

carefully transferred and submerged in ~15ml MQ water contained in 30 ml Teflon beakers. After 24 hours, the crucibles contained in the Teflon beakers were placed in an ultrasonic bath for ~1 hour, and then the samples were carefully transferred into 125-ml pre-cleaned PE bottles. Crucibles were rinsed by MQ water for several times to ensure complete transfer of the sample. Sample solutions were diluted by MQ water to ~100 g, and then acidified to 1% HNO_3 v/v. After acidification, the solution should be completely transparent. The Si concentrations of sample solutions were measured using ICP-Q-MS at IPGP.

2.3.2 Si separation

The purification of Si from the sample matrix and Na added during the alkaline fusion step was achieved via a single-step column chromatography protocol. This method is directly adopted from a widely-used Si separation (*e.g.* Pringle et al., 2013, 2014, 2016), which had been in turn a modified version from the well-established method from Georg et al. (2006). The BioRad AG50-X12 (200-400 mesh) cation exchange resin was employed as the stationary phase. BioRad Poly-Prep columns with a 2-ml volume of resin reservoir and a 10-ml volume of mobile phase reservoir were used. Precleaned columns were first bedded with 1.8 ml of wet resin. The resins from the batch storage was first pre-cleaned and stored in water before loading into columns. At the beginning of each purification session, resins bedded in columns were washed and conditioned. The purification of Si can be achieved in a single-step chromatography protocol with cationic resin due to its speciation in acidified solutions, either as neutral orthosilicic acid (H_4SiO_4) or its dissociated anionic specie $H_3SiO_4^-$. Meanwhile most matrix elements such as Na are in the cationic forms and will be selectively retained on the cationic exchange resin while Si passes through the column (see section 2.3.3 for details about the theory of column chromatography).

During the protocol, 0.2 mg of Si (of the sample solution in 1% HNO_3) were loaded on the top of column, followed by 5 ml elution by MQ. Sample eluates were directly collected in a 10-ml vial. At the end, 125 µl HNO_3 were added to acidify the sample, which were adjusted to 10 ml with MQ, reaching a medium of 0.2 N HNO_3 in the final solution. The detailed steps of resin cleaning, column conditioning, and separation (with an example) are provided in table 2.1. At each purification session, the well-constrained basalt reference material BHVO-2 was routinely processed in order to determine the quality of column chemistry. Meanwhile, the reference standard NBS-28 (by definition at $\delta^{30}Si$=0‰) was also routinely processed with samples. As the NBS-28 solution is used as a bracketing standard, its use during the MC-ICP-MS is large. In general, at each chemistry session, a NBS-28 standard is prepared every third sample through the separation protocol.

Table 2.1 Protocol for Si separation by column chromatography and resin cleaning procedures

<table>
<tr><th>1. Batch resin cleaning</th><th>2. Column cleaning</th><th>3. Purification (Principle)</th><th>Purification example (with an NBS-28 solution having [Si] of 25 ppm)</th></tr>
<tr><td>MQ</td><td>10 ml 3 N HNO_3</td><td>0.2 mg Si (in solution)</td><td rowspan="3">0.8 ml sample solution on top of column</td></tr>
<tr><td>HCl (6N)</td><td>6 ml 6 N HNO_3</td><td>2 ml MQ</td></tr>
<tr><td>MQ</td><td>5 ml 6 N HCl</td><td>3 ml MQ</td></tr>
<tr><td>HCl (6N)</td><td>3 ml 6 N HNO_3</td><td rowspan="9">0.125 ml 16 N HNO_3 added into the collected sample, and further diluted to 10 ml with MQ</td><td>2 ml MQ</td></tr>
<tr><td>MQ</td><td>3 ml 3 N HNO_3</td><td>2 ml MQ</td></tr>
<tr><td>HCl (6N)</td><td>10 ml MQ</td><td rowspan="9">0.125 ml HNO_3 and 4.075 ml MQ in collecting vial. The final solution has a [Si] of 2 ppm in 0.2 N HNO_3</td></tr>
<tr><td>MQ</td><td>3 ml MQ</td></tr>
<tr><td>HCl (6N)</td><td rowspan="7">3 ml MQ (the pH of the eluate solution needs to be neutral after this step)</td></tr>
<tr><td>MQ</td></tr>
<tr><td>HCl (6N)</td></tr>
<tr><td>MQ</td></tr>
<tr><td>HCl (6N)</td></tr>
<tr><td>MQ (until pH=7)</td></tr>
<tr><td>Resin stored in solution in dark</td></tr>
</table>

In order to avoid amorphous silica polymerization and silica precipitation, which causes undesired fractionation of Si isotopes in the solution, samples have to be analyzed within 24 hours after separation.

2.3.3 Li separation

The separation of Li from the matrix in natural samples is challenging due to: 1. the low abundance of Li as a trace element, for example in seawater Li concentration is approximately 180 ppb whereas Na concentration is about ~1%; 2. The fact that during cation exchange Li shares similarities with some major matrix elements such as Na. Although a previous method was well established at IPGP (*e.g.* Dellinger et al., 2014; Henchiri et al., 2016), the shortage of column materials and resin aging issues made the separation of Li challenging. A new method was then developed for purifying Li. As the difficulties encountered for separating Li were a major problem in this study, this method development will be addressed next.

The resin used for Li separation is the same resin employed for Si purification, the BioRad AG50-X12 (200-400 mesh) cation exchange resin (section 2.3.2). As for any stable isotope system, in the Li separation procedure there are two main objectives: complete Li recovery (~100% yield) and effective separation of Li from the sample matrix (Na for example). During cation exchange, the principle is that when a sample solution (mobile phase) is added onto a resin bed (stationary phase), the cation X will be interacting with the resin functional groups and be redistributed across both phases until a local chemical equilibrium is reached. The equilibrium distribution coefficient (K_d) is defined as:

$$K_d = \frac{\text{Amount of component per gram of dry exchanger}}{\text{Amount of component per milligram of mobile phease}} = \frac{C_{\text{Solid}}}{C_{\text{liquid}}} \quad \text{(Equation 2-1)}$$

where C_{solid} is the concentration of the solute in the dry ion exchange resin and C_{liquid} is the solute X concentration in liquid in equilibrium with the resin (*e.g.* Peters et al., 1974; Schönbächler and Fehr, 2013). The K_d value is dependent on the element, as well as the exchanging ions (H^+ for cation exchange). During the exchange of Li with the resin used in this study (BioRad AG50-X12), the reaction occurs as:

$$R\text{-}SO^-,_3H^+_{resin} + Li^+_{solution} \rightleftharpoons R\text{-}SO^-,_3Li^+_{resin} + H^+_{solution} \quad \text{(Equation 2-2)}$$

where $R\text{-}SO^-,_3H^+$ is the functional group (sulfonic) of the resin, Li^+ is the mobile form of Li in the solution, $R\text{-}SO_3^-\ Li^+$ is the exchanged Li in the resin, and H^+ is the free H^+ in the solution, the equilibrium constant for this reaction is:

$$K_e = \frac{[R\text{-}SO^-,_3Li^+]_{resin} \times [H^+]_{solution}}{[R\text{-}SO^-,_3H^+_{resin}] \times [Li^+]_{solution}} \quad \text{(Equation 2-3)}$$

Since we have $K_d = [R\text{-}SO^-,_3Li^+]_{resin} / [Li^+_{solution}]$ (equation 2-1), and $[R\text{-}SO^-,_3H^+_{resin}]$ is considered as a constant (≈ 1), then the K_d can expressed as a function of K_e:

$$K_d = \frac{K_e}{[H^+]_{solution}} \quad \text{(Equation 2-4)}$$

When a sample solution is added onto a column, the solution will pass through the resins, with the flow driven by gravity for manual chromatography. The desorption of the solute X retained in the resins is significant when an eluent containing no X is added. As a result of both the flow and the ion exchange, a peak of X is produced at the column outlet when integrating the concentration of

X in the eluate with the eluent volume. As shown in equation 2-4, K_d is inversely proportional with H^+ concentration in the solution hence lower concentration of H^+ can exchange with Li^+ slower and better separate it with matrix cations. Meanwhile, the elution volume can be expressed as a function of K_d:

$$V_{elu} = m \times K_d + V_i \quad \text{(Equation 2-5)}$$

where V_{elu} is the elution volume, m is the mass of the resin and V_i is the initial volume in the resin. The lower K_d (hence higher $[H^+]$ in the eluting solution) would result smaller elution volume and hence a faster separation. Therefore, the choice of the concentration of eluting acids need to be compensated in order to achieve a good and relatively fast separation. Elements with higher K_d values show greater affinity to the resin therefore they will be eluted more slowly than those elements having smaller K_d values. Such difference does not only exist among elements, but also between isotopes of a given element. The effect on Li isotopes has been well recorded long ago (Taylor and Urey, 1938) that ^{6}Li has a greater affinity to resins than ^{7}Li. If the sample collection at the column outlet during elution starts too late, then the foremost fraction of the Li eluate, in which ^{7}Li is enriched compared to the loaded sample, will be missed. As a result, the collected Li will be drifted to a lower δ^7Li composition. Conversely, if the sample collection ends too early, the fraction containing more ^{6}Li will be missed. Those effects have been well documented (Moriguti and Nakamura, 1998; Košler et al., 2001; Tomascak et al., 2016). A second challenge of the determination the Li eluate collection is that the elution of Li varies with sample types (*e.g.* river water *vs.* basalts). For example, Li can be eluted faster when a large amount of Fe is present in the matrix (James and Palmer, 2000). Lastly, the collection volume cannot be extended too much, as other matrix elements would be introduced and would affect the accuracy of δ^7Li measurements (Tomascak et al., 2016, and references therein). In particular, if the collection ends

too late (often this "too much" unwanted volumes can be as small as 0.5 ml ~ 1 ml), a significant amount of Na will be introduced to the sample collection.

At the beginning of this study, the first attempts were made to purify Li following the same method used by previous researchers at IPGP (Dellinger et al., 2014; Henchiri et al., 2016). This method was modified from the initial protocol established by James and Palmer (2000). In this method, Li purification was achieved by a single-step chemistry. Dry resin from a batch bottle was washed in the same protocol as described in table 2.2, and it was stored in water before usage. Historically at IPGP, home-made columns were used for this protocol, and were composed of three parts: a funnel-shaped reservoir at the column top, a PP tube for resin bedding, and an outlet plugged with frits connected to the bottom of column. Due to the shortage of the PP tubes and to the imperfection of this column structure in which elution solutions or resins occasionally seeped out at the connections between the different column parts, initial efforts were made to build one-piece style columns with Teflon heat shrink tubes (4 – 1"). The advantage of such a column would be that the entire column is made in one piece, avoiding seeping of the solution/resin. A Teflon tube was first coated on a column mould made of steel. The column mould is shaped of a solution reservoir at the top (~10 ml) and a resin reservoir (~10 cm, ø≈7mm) at the bottom. Then the heat shrink tube was placed into pre-heated furnace at 340°C until it shrank completely (usually this took about ~20 minutes). Once cooled, the column was taken off from the iron mould, and a PTFE frit (ø≈8mm) was placed to the end of column. Finally, the outlet was coated using a piece of 2-cm polyolefin tube and heated again using a heat gun to ensure that the frit was firmly enclosed, and the outlet was well sealed. There were, however, a few drawbacks of this approach. First, the part of column devoted to resin bedding tends to bend, and the degree of bending was observed to vary at between columns. Second, it was excessively difficult to take the column off from the iron

mould after shrinking as it was tightly attached onto the mould. Lastly, due to the difficulties to take the column off the mould, sometimes the column would break during this operation.

The home-made one-piece columns were then calibrated and tested for Li purification using the traditional method. In this method, 2.7-ml pre-cleaned wet resin was bedded into the column. Columns were first rinsed and conditioned before loading the sample. Then 1 ml of sample containing 20 ng Li in a 0.2 N HCl solution was introduced. Then the reservoir was rinsed with 1.5 ml MQ. Finally, the column was eluted with 40 ml 0.2 N HCl, with the first 16 ml of the eluate being discarded and the final 24 ml of the eluate being collected (Li fraction). The detailed procedure is provided in Table 2.2.

Table 2.2 Single-step procedure for Li separation using column in 0.2 N HCl

Column cleaning	Column conditioning	Li separation	
10 ml 6 N HCl	5 ml 0.2 N HCl	1 ml sample solution (20 ppb Li in 0.2 N HCl)	**Discard**
10 ml MQ			
10 ml 6 N HCl			
10 ml MQ		Reservoir rinse with 1.5 ml MQ	
		2 ml 0.2 N HCl	
		2 ml 0.2 N HCl	
		6 ml 0.2 N HCl	
		6 ml 0.2 N HCl	
		6 ml 0.2 N HCl	**Collection**
		6 ml 0.2 N HCl	
		6 ml 0.2 N HCl	
		6 ml 0.2 N HCl	

The one-piece columns were calibrated by collecting eluate solutions at small volume intervals, starting from the sample loading. The calibration curve using old columns (three-pieced) was used as a reference to decide what the volume intervals should be. At the head and the tail of the Li elution peak, based on the old calibration curve, several intervals of 1 ml were taken to

precisely determine the start and the end of Li elution. Samples collected were then evaporated and re-dissolved in 0.5 N HNO_3. The concentrations of Li and matrix elements were measured using ICP-Q-MS at IPGP. Although the geometry of the columns made from Teflon heat shrink tubes is different from the traditional columns used at IPGP, the calibration curve showed no resolvable difference between these two types of columns (Dellinger, 2013). A sample calibration curve is provided as an example in Figure 2.1.

Then, several well-studied geological reference materials including seawater (NASS-5 and NASS-6), basalts (BHVO-2 and JB-2), and the isotope standard solution (Li-SVEC) were used to test the accuracy of Li purification using the single-pieced columns made from Teflon shrink tubes and the single-step column chemistry. Eluate solutions were evaporated at 95°C to dryness and stored in Teflon beakers with caps firmly closed until analysis on the MC-ICP-MS (details in section 2.4). The results showed an unexpected ~1‰ shift towards lower δ^7Li compared to literature values. The measured BHVO-2 had a value of 3.63±0.05‰ whereas literature values vary from 4.3 to 4.9‰; JB-2 (3.89±0.06‰ vs. ~4.5‰), seawater (30.12±0.19‰ vs. ~31‰), and Li-SVEC (-0.60±0.24‰ vs. 0‰) showed similar patterns. The "internal standards" (pure Li solutions IRMM-016 and SPEC) used during measurement on the MC-ICP-MS showed there was little instrumental error. Therefore, the apparent fractionation was attributed to the performance of the column chemistry.

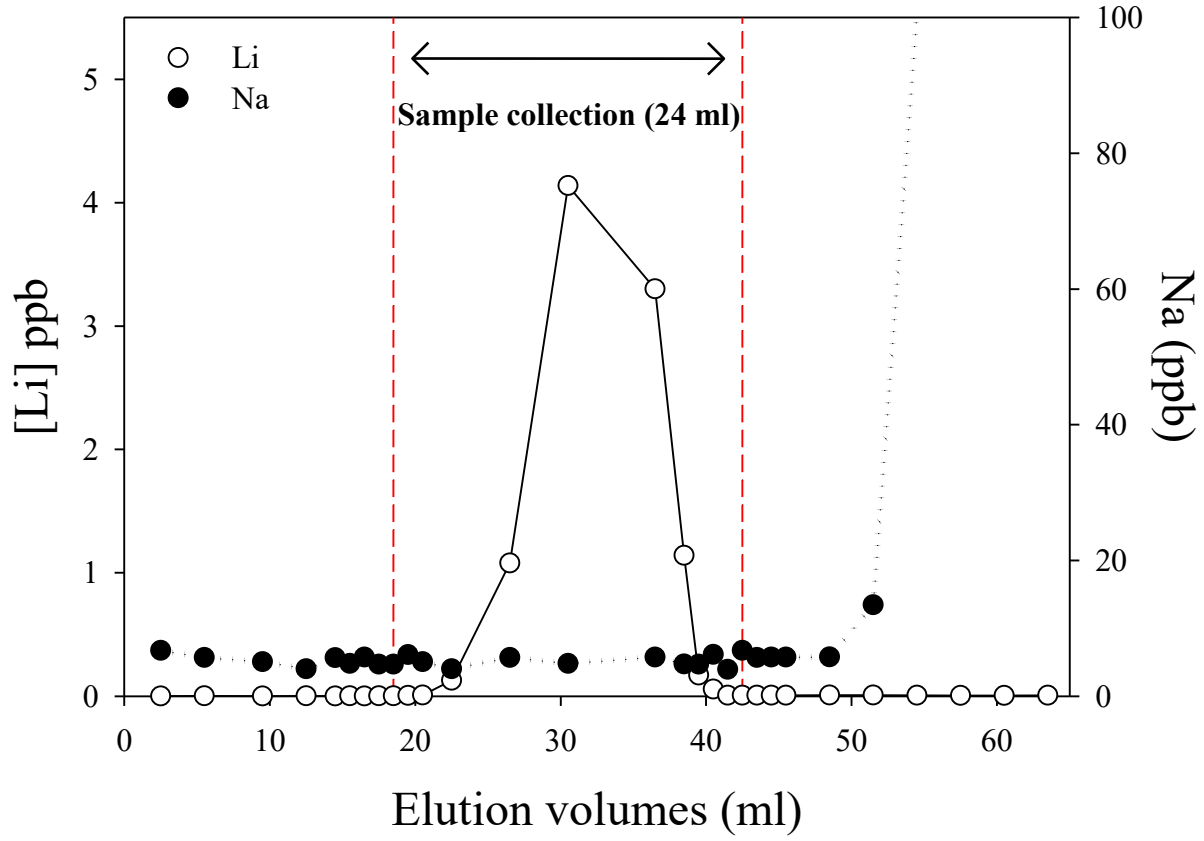

Figure 2.1 Calibration curve for diluted seawater Li purification using the method adopted from Dellinger et al. (2014) in single-pieced columns made from Teflon heat shrink tubes. Column chemistry was conducted using 0.2 N HCl as the eluting solution. The fraction of eluate from 18.5 to 42.5 (starting from the beginning of sample loading) had to be collected in order to completely recover Li from the sample solution.

Several attempts were made to solve this problem. First, all the experimental materials were carefully washed to avoid contaminations. Second, the eluate volumes before and after the Li peak were collected and measured for Li concentration, such that any Li loss during column chemistry could be traced. Moreover, the resin used was thoroughly washed using HCl or ethanol. Lastly, evaporated samples were boiled with H_2O_2 or concentrated HNO_3 in order to eliminate any organic matters that could have been released by the resin and cause cryptic matrix effects during measurements. In spite of all these efforts, obtaining accurate δ^7Li values was unsuccessful (Fig. 2.2). However, hope was brought from the boiling of eluates in concentrated HNO_3. For this test,

the measured δ^7Li values were slightly higher than for the other tests. This suggests that the shift of δ^7Li towards lower values was highly possibly caused by matrix effects triggered by the presence of organic matter released from the resin.

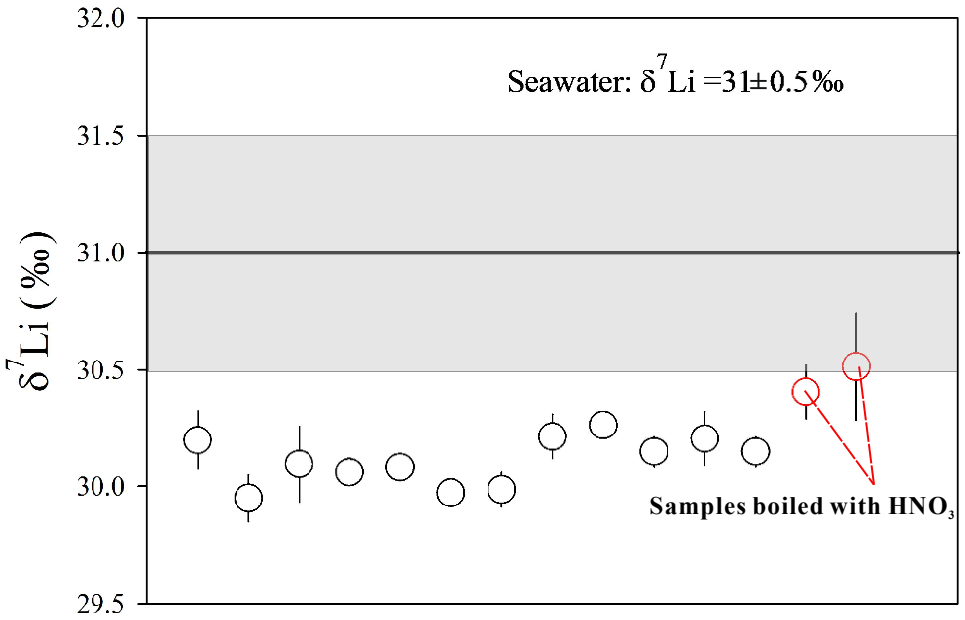

Figure 2.2 Examples of unsuccessful Li purification of seawater. Seawater has a well-known δ^7Li value of 31‰, whereas the measured values were ~1‰ lower. The average δ^7Li from these tests is 30.12±0.19‰ (n=12). δ^7Li values from the two tests where eluates were boiled with concentrated HNO_3 were slightly higher (30.46±0.10‰), still lower than the literature values but closer to them.

As soon as the fractionation was identified as due to resin-derived substances, a new batch of resin was purchased. Due to the urgency of obtaining reliable data and no confidence in the one step separation protocol, a new Li purification method was developed. In some studies, short columns were used to get rid of the sample matrix (Moriguti and Nakamura, 1998; Hall et al., 2005; Magna et al., 2006). For example, to purify Li, Magna et al. (2006) used a multi-step recipe in which samples were cleaned using a short column (0.6 ml resin) in 0.5 M HNO_3. Following this approach, a multi-step protocol was developed using 1-ml resin columns.

In this protocol, the Li separation was achieved in two steps. In the first step, samples were eluted using 1 N HNO_3, which removes the majority of matrix. In the second step, the elution acid was changed to 0.2 N HNO_3. Because of the lower concentration of acid, finer separation between Li and Na could be accomplished. The same 1-ml resin column was used for both steps. The detailed description is provided next.

Commercially available PP+PE column (AC-142-TK, TRISKEM) were used for the new protocol. The columns contain a 5-ml reservoir at the top and a 2-ml resin reservoir (internal ø=7mm) at the bottom. PE frits attached to the columns with a pore size of 20 µm were placed to the column bottom. Then the column was first bedded with 1 ml of pre-cleaned wet BioRad AG50-X12 (200-400 mesh) resin. Considering the issues encountered during Li chemistry using previous method and observing that the top of the resin sometimes re-suspended and stick to the walls of the reservoirs, another frit was placed onto the top of the resin bed. A schematic of the new column is shown in Figure 2.3.

The new chemistry protocol was first calibrated using standard reference materials with various matrix including basalt (BHVO-2 and JB-2), seawater (NASS-6), pure Li_2CO_3 solution (Li-SVEC). A sample calibration curve using JB-2 is provided next in Figure 2.4.

Based on these calibration curve, the following protocol was established. In the first step, 0.5 ml of sample (20 ppb Li in 0.2 N HNO_3) were first loaded and eluted with 4 ml 1 N HNO_3. The entire eluate (4.5 ml) was collected, evaporated, and re-dissolved in 0.5 ml 0.2 N HNO_3. After the column was thoroughly washed and conditioned, the re-dissolved sample was then loaded on the column in the second step. Then it was eluted with 16 ml 0.2 N HNO_3 solution. The last 8 ml were collected. In this step, Na could be successfully eliminated. The details of this two-step protocol are provided in Table 2.3.

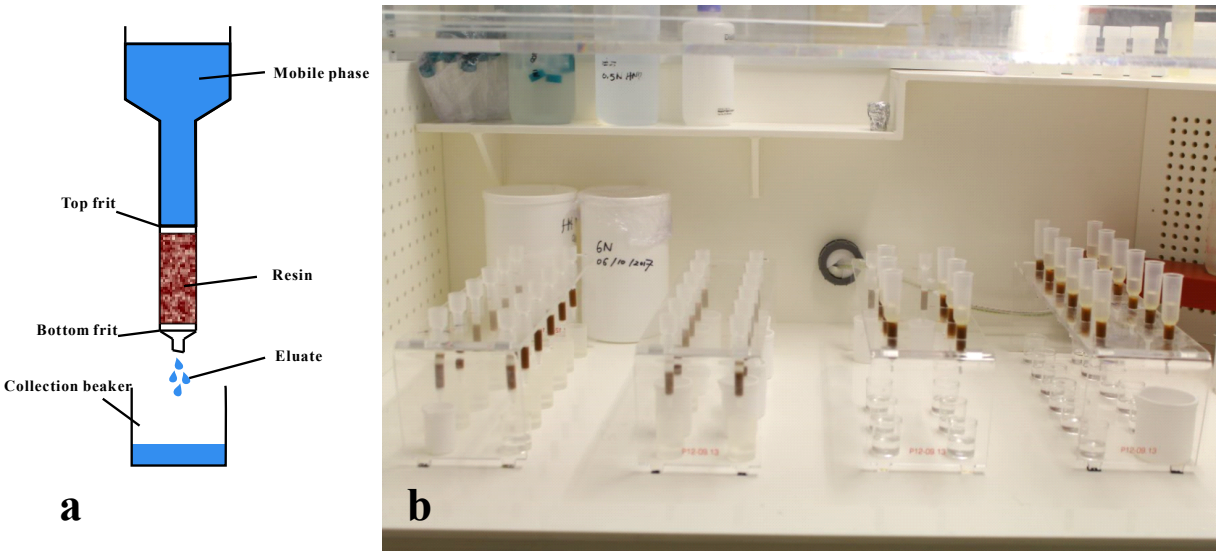

Figure 2.3 Separation of Li using column chromatography protocol established for this study (a) schematic of the column using 1 ml BioRad AG50-X12 (200-400) mesh resins. (b) Photographs of the columns (first two rows to the left, the two rows to the right are columns used for Si chemistry).

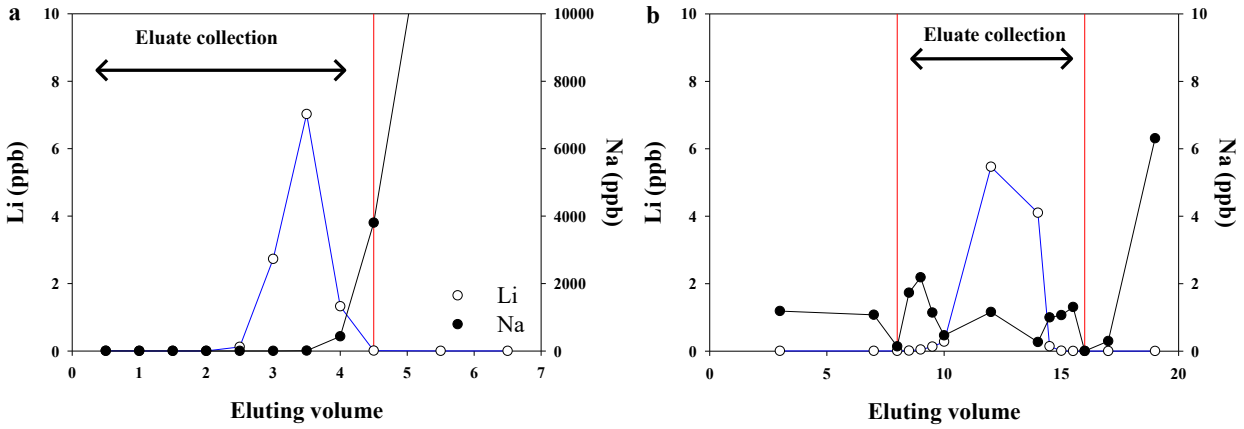

Figure 2.4 Calibration curves of two-step Li separation. (a) In the first step, the sample was eluted using 1 N HNO_3. An efficient Li enrichment over matrix elements was achieved in this step. (b) In the second step, the sample was eluted using a weak acid (0.2 N HNO_3), which allowed for a fine separation between Li and Na.

This protocol was tested for a number of times to determine its ability to separate Li from Na. It was observed that when the Li/matrix ratio is too low, such as seawater, some Na may remain in the sample. To precisely measure δ^7Li, it is crucial to isolate Li from Na. Although there is a certain degree of freedom to tolerate Na during measurement using MC-ICP-MS, it was suggested the Na:Li ratio should be controlled to be lower than 3:1 (Dellinger, 2013). Therefore, our new protocol constitutes an improvement: sample with a large amount of matrix cations compared to Li can be broadly purified in step 1 twice, before the final separation between Li and Na in step 2. Since most the samples analyzed in this dissertation were solid samples, any sample with a Li concentration lower than 10 ppm was passed through the first column twice. With the application of this extra elution, Li is completely isolated from Na.

Table 2.3 Li separation protocol using 1-ml resin columns

Step 1	Step 2
Column cleaning	Column cleaning
5 ml 6 N HCl 3 ml MQ 3 ml MQ	5 ml 6 N HCl 3 ml MQ 3 ml MQ
Column conditioning	Column conditioning
2 ml 1 N HNO_3	2 ml 1 N HNO_3
Li separation	Li separation
0.5 ml sample solution (20 ppb Li in 1 N HNO_3, collected) 4 ml 1 N HNO_3 (collected)	0.5 ml sample solution (20 ppb Li in 0.2 N HNO_3) 4 ml 0.2 N HNO_3 4 ml 0.2 N HNO_3 4 ml 1 N HNO_3 (collected) 4 ml 1 N HNO3 (collected)

Both the new protocol and the “traditional” method were tested with seawater using fresh resin. All samples collected at the end of the procedure were evaporated and boiled with

concentrated HNO_3. Both methods generated results well matched with literature values. However, the multi-step method was chosen as the chemistry recipe for this dissertation. This protocol indeed has some drawbacks in which it requires transfer, evaporation, and re-dissolution of the samples between the steps, and it cannot be accomplished in a single day. Nevertheless, it has its own outstanding advantages:

1. The time cost of the new recipe is lower. The older single-step protocol is based on a resin volume of 2.7 ml and requires an elution of 86.5 ml of 0.2N HCl. To achieve a separation session of 12 samples, this method takes at least 18 hours in a working day. Conversely, the new two-step protocol, only uses 1 ml of resin, and has an elution of 17.5 ml (first step) or 29.5 ml (second step). Each step can be readily achieved within 4 hours. In practice the two-step method is more suitable for manual separation. If a robot assistant system is available, the single-step method would become the better option (to reduce the use of beakers and the consumption of acids for cleaning purpose).
2. The two-step protocol enriches Li in the first step, which can be used as a sample pre-treatment. The calibration of Li-SVEC (pure Li) showed that the peak position was within the first 4 ml elution, which puts a boundary on the peak of the Li elution peak whatever the matrix is (because the peak position can be affected by the matrix effect, theoretically, high matrix content should "push" the Li peak in front of the other peaks, leading to an even earlier elution of Li). This advantage has been applied in our experimental study (Chapter 3), where some samples had very high Na:Li ratios (10 times higher than for seawater, for example).

A few additional notes need to be made regarding the Li separation procedure. First, the concentration of the eluting acid needs to be accurate, as any change of concentration will shift

the Li peak position. Thus, the 0.2 N HNO_3 solution must be titrated before use. Second, attention needs to be paid all the time about matters that could be released from the resin during elution. The resin was systematically changed after 6 separation sessions, to avoid effects due to resin aging. Before the isotope measurements, all samples were boiled with concentrated acid (either 16 N HNO_3 or 6 N HCl) for a few days, evaporated to dryness, and stored in Teflon beakers with caps firmly closed. It has been noticed that an isotopic shift towards lower values could re-appear (as in the initial test with the single-pieced columns, see above), and this was solved by prolonging the duration of the acid boiling step. Although the exact reason for this shift is still unknown, we suggest that matters released by the resin (probably organic matters) are the cause. For example, as shown in Figure 2.5, the frits located at the bottom of a column can exhibit a pink color (instead of the original white) if the column was not used for a few weeks.

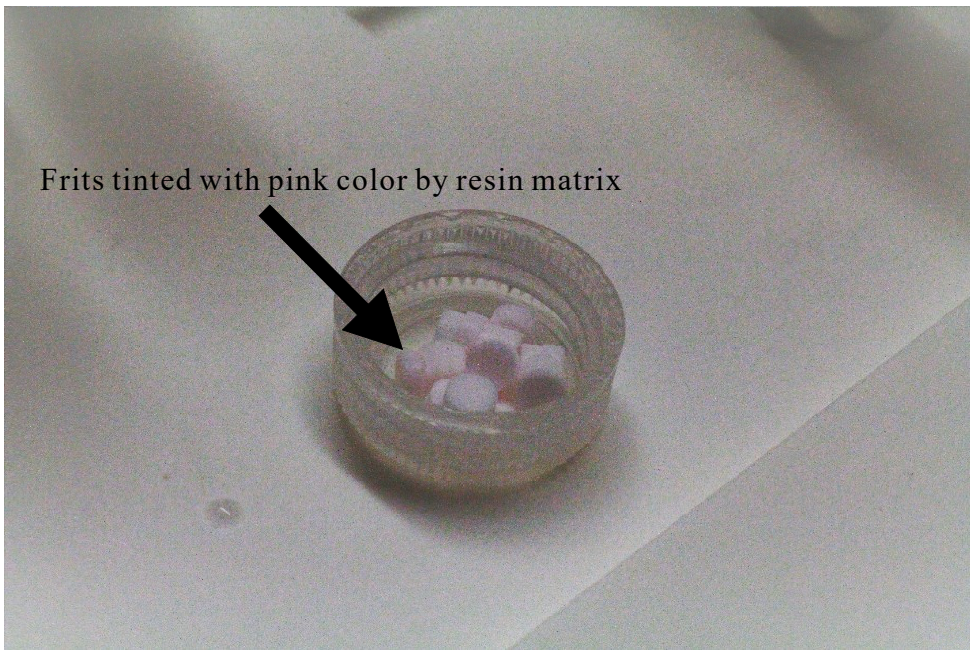

Figure 2.5 Example of resin matrix tinting eluting out and tinting the frits.

2.4 Isotope measurements by MC-ICP-MS (Neptune/Neptune *Plus*)

Throughout the study, all the isotopic measurements were performed using two MC-ICP-MS instruments (Neptune/Neptune *Plus*) at IPGP (note that the Neptune at IPGP has been upgraded to the level of a Neptune *Plus*). In brief, the instrument consists of 3 parts: the sample introduction system; the ionisation system; and the mass analyser (Fig 2.6). The Neptune *plus* MC-ICP-MS is an updated generation of Neptune MC-ICP-MS with a number of new features including improved pumping capacity at the interface (between the skimmer and sample cones).

2.4.1 Sample introduction system

In order to be ionised in the plasma, it is necessary to deliver samples as a mist (fine aerosol). For this purpose, throughout this study we used PFA-ST type microflow self-aspiring nebulizers (ESI), in which the spray was formed through a mixture of argon (Ar) at a rate of ~1 L/min (sample gas), and to which samples were carried using a probe connected to a PFA capillary. The stability and the intensity of the signal are positively related to the size of capillary, and sample consumption is correlated to the size of capillary. In order to achieve the best signal, larger sized capillaries are recommended. In some case, the sample volume was limited, therefore smaller capillaries were used. In this study, 0.25 mm i.d. (~100 µl/min sample consumptions rate) capillaries (ESI) were used for the measurement for the δ^{30}Si measurements (2 ppm Si in 10 ml 0.2 N HNO_3 solution), whereas 0.2 mm i.d. (~50 µl/min sample consumption rate) capillaries (ESI) were used for the measurement for the δ^{7}Li measurements (20 ppb Li in 1 ml 0.5 N HNO_3 solution).

Plasma formation and stability are critical in MC-ICP-MS techniques, in terms of ionisation efficiency, signal sensitivity, instrumental fractionation, and interferences (for example through the formation of oxides). In principle, to enhance plasma performance, only the finest aerosols are

wanted to be introduced to the plasma. Different techniques are available including “wet” plasma, where a spray chamber filters out all the large droplets (so-called “Stable Introduction System SIS), or “dry” plasma which uses a desolvating system APEX (ESI) or Aridus (Cetac). Sometimes, this can also be achieved by using a “Direct Injection Nebulisation” system (*e.g.* d-DIHEN, Louvat et al., 2011).

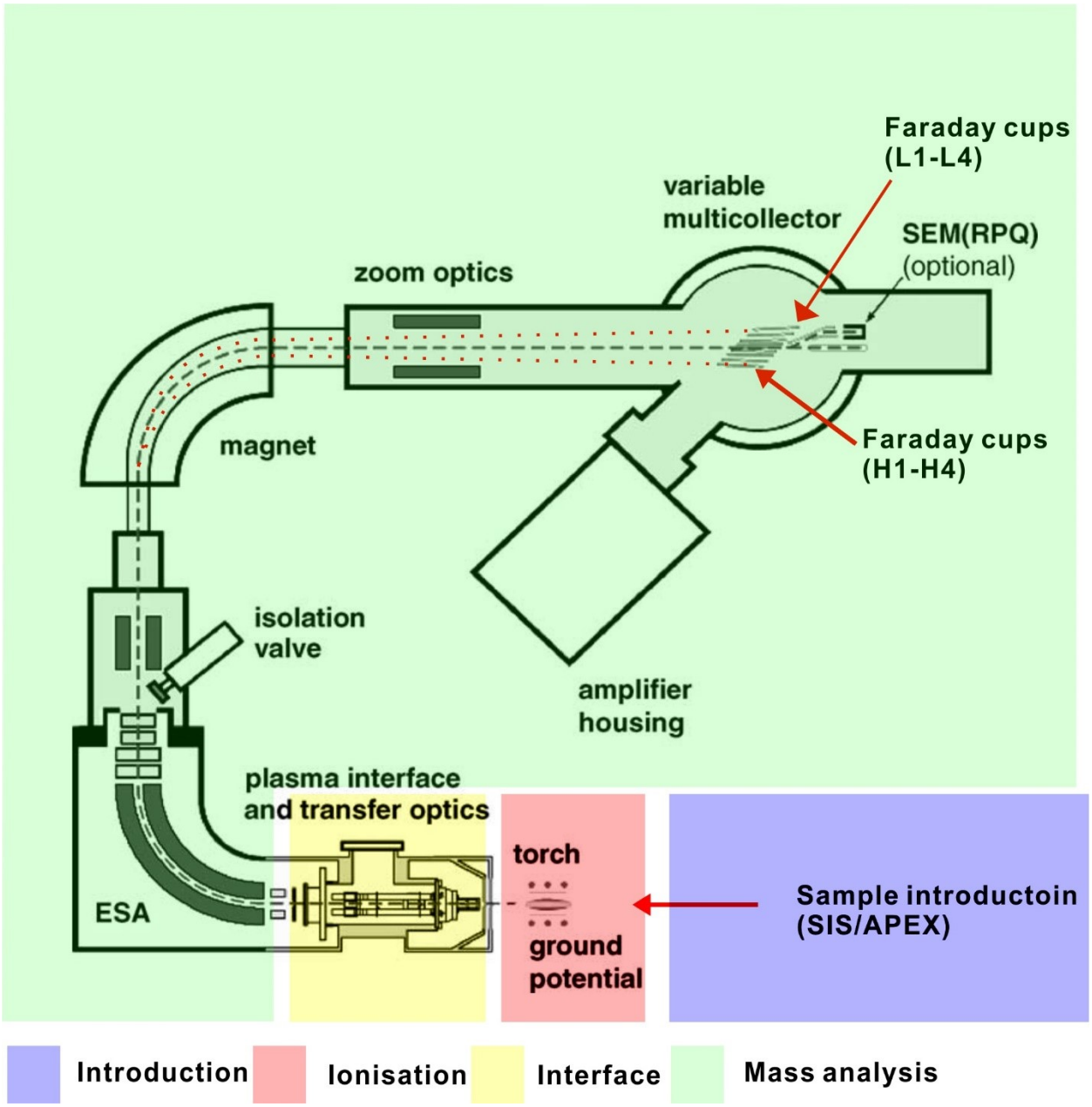

Figure 2.6 Schematic of a MC-ICP-MS. Modified from Weyer and Schwieters (2003), under the Creative Commons user license (http://creativecommons.org/licenses/by-nc-nd/4.0/).

In this dissertation, an SIS was used for the analysis of δ^{30}Si and an APEX (ESI) was used for the analysis of δ^{7}Li. The quartz-made SIS consists of two parts: a cyclonic spray chamber at the bottom and a "Scott" spray chamber at the top (Fig 2.7).

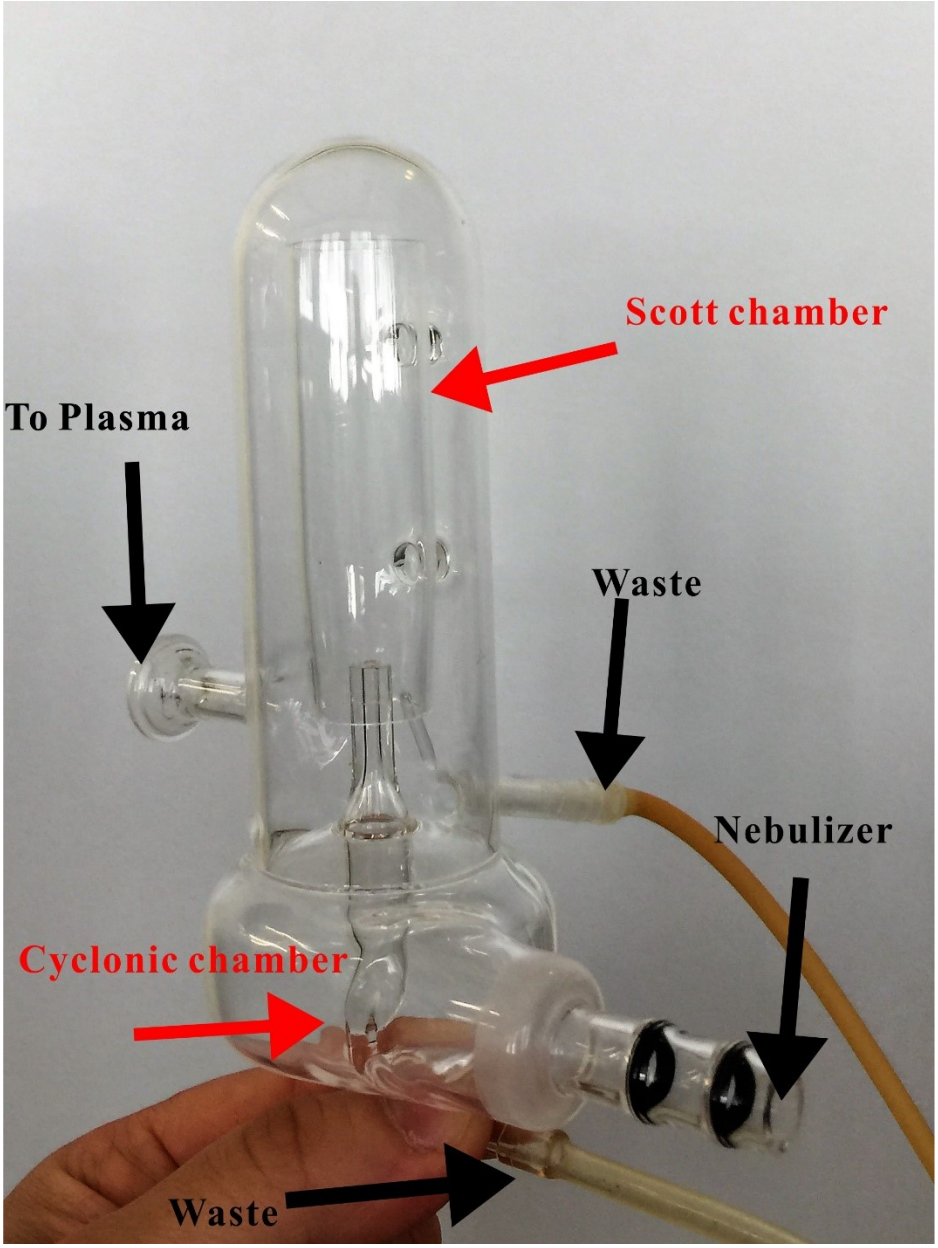

Figure 2.7 Photograph of a quartz-made "Stable Introduction System" SIS, used in this study for Si isotope measurements.

Once the sample is introduced into the SIS, it first enters the cyclonic chamber. With the presence of the Ar flow and the cyclonic structure of the chamber itself, a vortex is produced. With the centrifugation, large droplets condense on the glass walls of the chamber and drain out at the bottom of the chamber with the waste outlet. On the other hand, smaller droplets in the center are

carried into the double pass Scott spray chamber, where finer aerosols are further "filtered" and injected into plasma. An SIS offers stable and sensitive signals.

The purified Li samples (20 ng) were introduced in the form of 1 ml 0.5 N HNO_3 solutions. Because of their low concentrations, the desolvating system APEX (ESI) was employed to enhance the sensitivity of the Li signal as this introduction system provides the best signal sensitivity for Li (Louvat et al., 2011). With the APEX, samples are first nebulized and introduced into a heated cyclonic spray chamber at 120°C, and then subsequently cooled to 2°C with a Peltier-cooled multi-pass condenser. As such, the large aerosols were eliminated and the interferences from solvent molecules (0.5 N HNO_3 solution) were then reduced. As a result, an improved sensitivity is obtained.

After the sample introduction system, samples were converted from solutions to fine aerosols, and were introduced to the plasma.

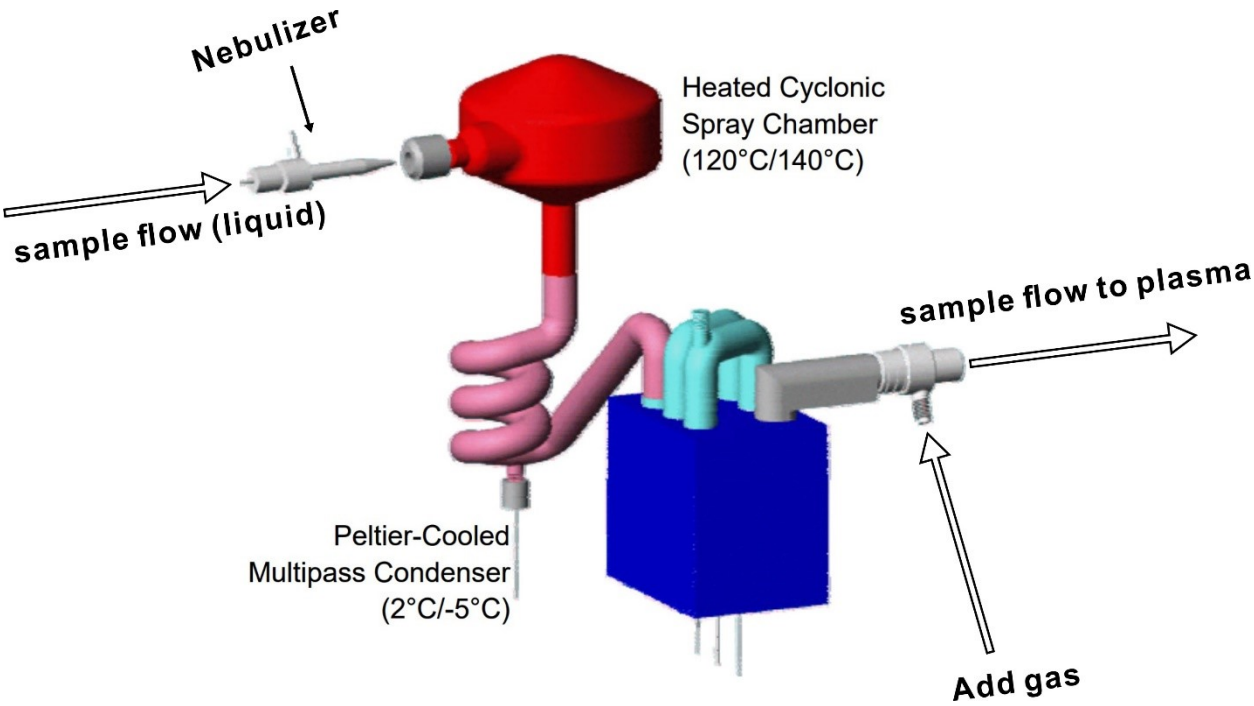

Figure 2.8 Schematic of the APEX sample introduction system, used in this study for Li isotope measurements. An "Add Gas" at a rate of ~ 1 L/min was used in this study for Li isotopes. Modified from Elemental scientific Inc.

2.4.2 Ionisation system

Once samples are introduced to the Ar-operating plasma, aerosols are atomized and ionised before further mass analysis. In brief, the ionisation system consists of three main parts: the radio frequency (RF) coil, the RF generator, and the plasma torch itself.

The quartz-made plasma torch is composed of three concentric tubes. The "Sample Gas" (~1 L/min) flows through the inner-most tube, which is connected with the sample introduction systems (SIS or APEX) and delivers the sample aerosol to the center of the plasma. The "Auxiliary Gas" (~1 L/min) passes through the middle tube to controls the position of plasma to avoid it being too close to the coils. The "Cool Gas" (~16 L/min) flows through the outermost tube and isolates the plasma from the walls of the torch.

To form the Ar plasma, the RF generator provides a power of 1200W to the coil wrapped around the torch, which induces a strong electromagnetic RF field (27 Mhz). The plasma is a partially ionized gas (with temperature of ~10,000 K at the center), is ignited through a spark, and is maintained because of sustained Ar flows and RF fields. The interest of an Ar hosted plasma is that it is able to ionise most other elements to a +1 state, as Ar has a high first ionisation energy (15.8 eV), higher than that of most other elements (but lower than the second ionization energy of most other elements, thus preventing the formation of most doubly charged ions). In particular for this study, both Li (5.39 eV) and Si (8.15 eV) have lower first ionisation energies than Ar, such that they can be readily ionised before mass analysis. In particular, Li, as most alkaline elements, has a low first ionization energy, and is thus easily ionized allowing for high sensitivity and low detection limit.

2.4.3 Interface

The plasma is formed under atmospheric pressure, while in the magnetic field and in the multicollector areas (see below) the operating pressure is at a level of ~10^{-7} mbar. The transition between these two-contrast pressures is achieved through the "interface" (and its pieced cones and interface pump) followed by a series of four turbo pumps. The lowest pressure of the analyzer part of the instrument is maintained by two ionic pumps. At the interface, first, the "Sampler Cone" samples the center of the plasma and expands it (a "Jet" cone was used for both Si and Li). Then the smaller "Skimmer Cone" selectively permits the entry of the central portion of the ionised samples that has passed through the sampler cone orifice. Two types of nickel-made skimmers cones are available (Fig 2.9): the standard "H" cone which has a cylindrical entrance; and the "X" cone whose orifice is more "trumpet-shaped". An X cone provides more space for particle transfer, which ultimately improves signal sensitivity (He et al., 2016), especially for low mass elements.

In this study, δ^{30}Si measurements were performed using an H cone, whereas all δ^{7}Li measurements were conducted using an X cone. The space between the two cones is pumped to an intermediate vacuum of a few mbars using the "interface pump", which is efficiently improved in Neptune-*Plus* type instruments compared to the older generation of Neptune.

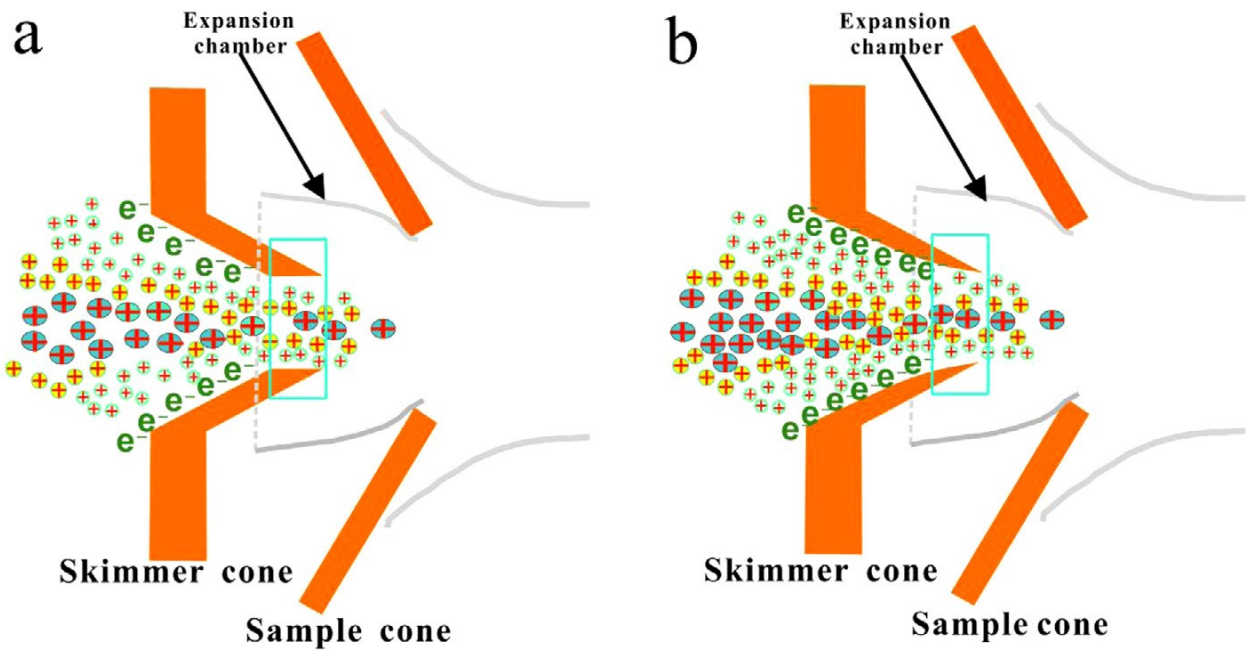

Figure 2.9 Schematic of two types of nickel-made skimmer cones: (a) "H" skimmer cone which has a cylindrical orifice. (b) "X" skimmer cone with a "trumpet-shaped" entrance. Reprinted from He et al. (2016), under the Creative Commons user license (http://creativecommons.org/licenses/by-nc-nd/4.0/)

2.4.4 Mass analysis

After the interface, ions are accelerated through a series of lenses to -10 kV (the negative electric field accelerates the positively charged ions formed in the plasma), such that a cation beam is formed and transported to the analyzer part. Through this series of lenses, the shape and density of the beam can be optimized. The beam also passes through the "entrance slit", which determines the mass resolution of the analyse. Despite all the efforts made to eliminate potential isobaric atomic interference (*e.g.* through chemical separation by eliminating matrix elements), other

interferences are common in ICP because of the formation of molecules in the plasma. This is the case for the analysis of $\delta^{30}Si$. One of the Si isotopes, ^{30}Si, shares a similar mass with a major polyatomic interference $^{14}N^{16}O^{+}$. As a result, at low mass resolution the beams of ^{30}Si and $^{14}N^{16}O^{+}$ are barely be separated on the focal plane where the collection of beams is made (see below). Narrowing the slit width allows to reach the so-called "medium-resolution" (MR) or even "high-resolution" (HR), such that a smaller image of the ion beams is permitted on the focal plane and molecular interferences can be separated. One of the drawbacks of employing higher resolution modes is the significant reduction of signal sensitivity (by a factor of 3 for MR and 10 for HR) because of the narrowing of entrance. Therefore, a compromise needs to be made between signal intensity and mass resolution. Therefore, the medium resolution mode was employed for the analysis of $\delta^{30}Si$ and a low-resolution mode was selected for the measurements of $\delta^{7}Li$.

The MC-ICP-MS has a double focalisation system. After ion acceleration, the ion beam is first "filtered" in the "ESA" (Electro Static Analyzer), where an electric field is applied to the ion beams (angular focusing), such that ions with different energies (in particular due to scatter in the plasma energy distribution) are focused on marginally different spots of the intermediate slit located between the ESA and the mass analyzer. After the intermediate slit, ion beam enters a large magnet where a magnetic field sorts the beams with respect to their mass/charge ratio.

For collecting and measuring the ion beams, the MC-ICP-MS is equipped with one fixed and eight movable detector platforms where Faraday cups are assigned. Each Faraday cup is connected to an amplifier which converts and amplifies the current intensity into voltage (10^{11}-ohm resistors were used for all signals in this study). The Faraday cups are precisely positioned at distances proportional the relative mass difference between the isotopes of interests. Therefore, for the analysis of $\delta^{7}Li$ the Faraday cups were assigned to the most extreme cup positions with the

outer cups L4 (^{6}Li) and H4 (^{7}Li), as the relative mass different between the two Li isotopes is very large.

2.4.5 Analytical sessions on a MC-ICP-MS

On a measuring day, the plasma of the Neptune MC-ICP-MS was first ignited. For the δ^{7}Li measurement, the APEX heating/cooling systems were also switched on. Usually, it took 30 minutes to 1 hour to allow the plasma to stabilize. After proper Faraday cup positioning, the instrument was tuned to reach an optimized signal using standard solutions. The NBS-28 (NIST) solution and the standard Li-SVEC (NIST) solution and were respectively used for Si and Li. To optimize the signal, three points need to be taken into consideration: signal intensity and stability, peak shape, and peak center (for Li)/central cup position (for Si). The signal intensity can be modified by tuning parameters such as gas flows, torch position, and lenses voltages. Noteworthy, optimizing for signal intensity may also lead to an increase of background noise. Thus, a compromise needs to be made to achieve the lowest background/sample signal ratio. Then, it is of importance to ensure that the peak of "mass scans" (obtained by varying the magnet current) plateaus are as flat as possible. The peak shape can be tuned using the "zoom lenses" feature. Two quadruples located before and after the magnet allows for a refined alignment of the different ion beams in the Faraday cups (Dispersion Quad) and a better peak shape (Focus Quad). Lastly, the peak plateau needs to be centered around the mass of interest for Li so that correct signals can be read for both ^{6}Li and ^{7}Li signals; while the central cup position needs to be correctly chosen for δ^{30}Si measurements in order to avoid the interference of the $^{14}N^{16}O^{+}$, which generates a shoulder on the peak plateau of ^{30}Si (Fig 2.10). Once the optimized signal is obtained, the secondary standard solutions were measured relative to the reference standard solutions to ensure the instrument was performing under reliable conditions. The IRMM-016 (~0.12‰ vs. Li-SVEC) and

Li-SPEC (~94.3‰ vs. Li-SVEC) solutions were used for Li measurements. As a lack of a secondary pure standard solution of known Si isotope composition, the digested and purified BHVO-2 reference material solution was used for Si measurements.

During the measurement, a sample standard bracketing (SSB) method was used for both isotope systems. As the Neptune MC-ICP-MS has a relatively large but stable instrumental mass bias (measured isotopic ratios *vs*. true isotopic ratios due to isotope fractionation within the instrument, especially in the plasma), samples are bracketed by the reference standard solution at same Si or Li concentrations as the sample solutions, which averages out the effect of this bias when the δ-values are calculated. To determine the sample concentration, before the isotope ratio measurement a quick mass scan around the mass of the element of interest was performed for each sample and the signal intensity was read and compared with the signal intensity of the bracketing standards. Concentrations were adjusted if necessary.

2.4.6 δ^{30}Si measurements

The typical analytical conditions of the Neptune *Plus* for the δ^{30}Si measurements are listed below in Table 2.4.

Table 2.4 Typical performing conditions of Neptune plus for δ^{30}Si measurements

RF power	1200 W
Cool gas	15-16 l/min
Auxiliary gas	~1 l/min
Sample gas	~1 l/min
Resolution mode	Medium resolution
Sample uptake	100 µl/min
Introduction system	SIS
Nebulizer	PFA (ESI)
cones	Jet + H
Cup configuration	L4 (^{28}Si), L1(^{29}Si), and H2(^{30}Si)
Method	25 cycles for samples and standards, and 12 cycles for blanks. Each cycle takes an integration time of 4.194 seconds, and blank correction was performed.

As Si is a major element, the purified Si samples have a relatively high concentration (2 ppm), and the signal intensities (note that the Si isotope measurement were made at medium resolution; see below about the resolution) generally vary from 5 to 8 V/ppm at ~100 µl/min uptake rate, depending on session instrumental performance. An example of a Si peak shape in medium resolution mode is provided in Figure. 2.10. As shown in the figure, the ^{30}Si peak shares a "shoulder" of the signal formed by the isobaric molecule $^{14}N^{16}O^{+}$ ion. In order to avoid this interference, the center of the peak needs to be defined "away" from this $^{14}N^{16}O^{+}$ + ^{30}Si peak. The precise position of the measurement of the center of the ^{30}Si "plateau" is determined for the best stability of the ^{30}Si/^{28}Si ratio measurement.

Another important issue needs to be monitored during the δ^{30}Si measurements is the mass-dependent relationship between measured δ^{29}Si and δ^{30}Si values. As shown in Figure. 2.11,

throughout this study, all measured values (standards and samples) follow a linear relationship between the measured δ^{29}Si and δ^{30}Si values, which attests for mass-dependent fractionation, and therefore lack of interference. The slope (δ^{29}Si vs. δ^{30}Si) generated from this study has a value of k=0.5050, which is unresolvable between kinetic fractionation (k=0.5092) and equilibrium fractionation (k=0.5178) (Young et al., 2002; Opfergelt and Delmelle, 2012).

Over the course of the study, for the reference material BHVO-2, we have obtained a δ^{30}Si value of -0.29±0.07‰ (2σ, n=72, Figure 2.12), which is well matched with literature values (Table 2.5)

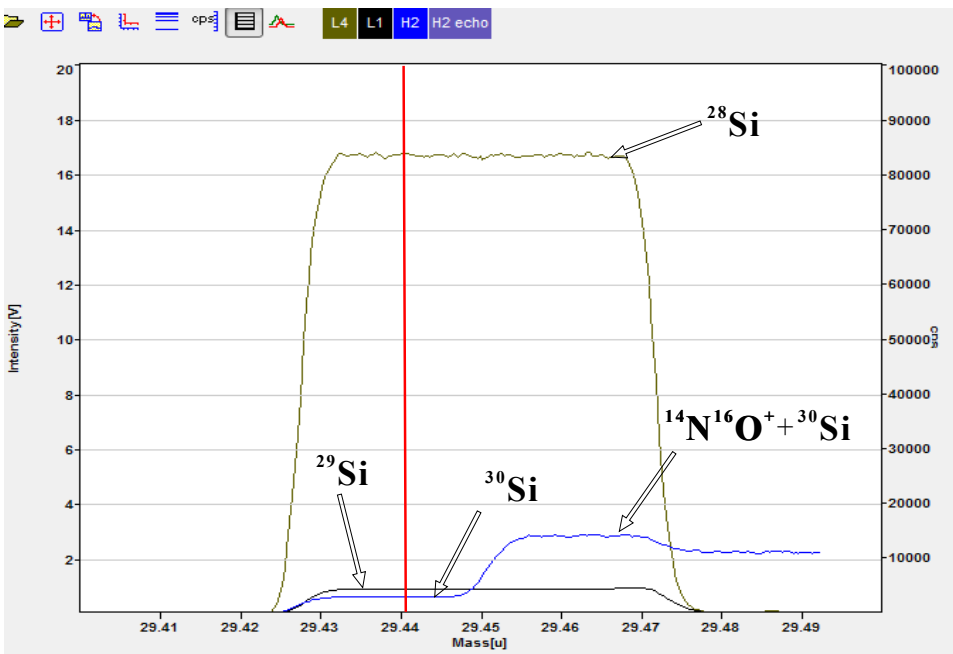

Figure 2.10 Example of a "mass scan" of Si isotope peaks, in medium resolution mode. The central cup position is here set as 29.441.

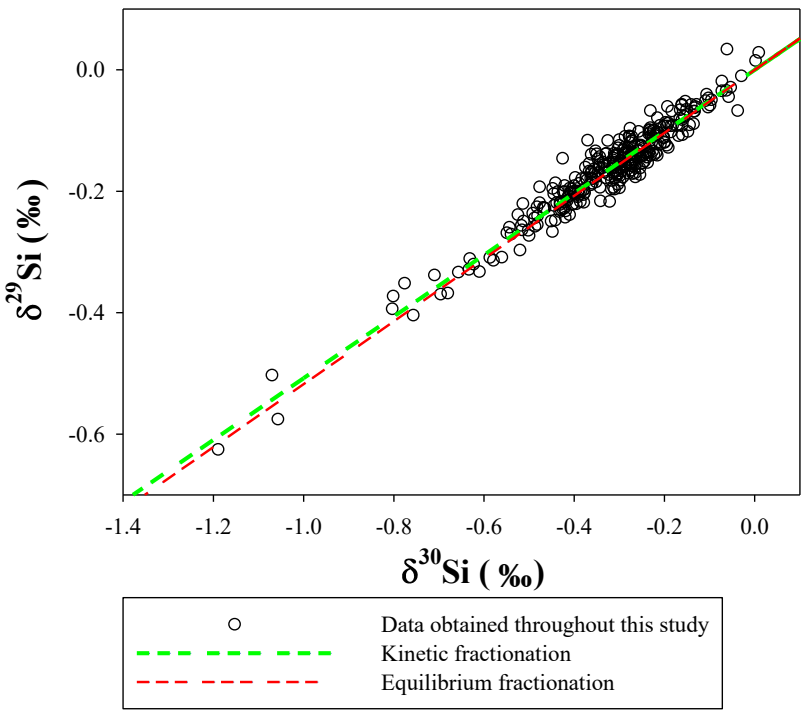

Figure 2.11 δ^{29}Si *vs.* δ^{30}Si throughout this study. The linear relationship, with a slope of 0.5050, indicates mass-dependent fractionation of silicon isotopes and thus the absence of interference during measurements.

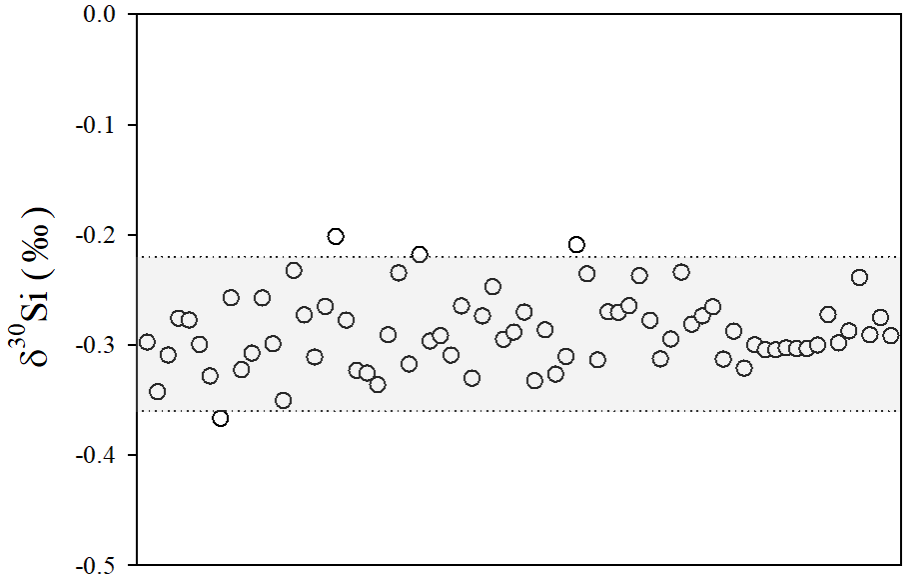

Figure 2.12 Summary of δ^{30}Si analyses for the basalt reference material BHVO-2 made throughout this study. $\delta^{30}Si_{BHVO\text{-}2}$=−0.29±0.07 (2 s.d., n=72) The gray area represents 2 s.d..

Table 2.5 Literature values of δ^{30}Si for BHVO-2

BHVO-2	δ^{30}Si	2 s.d.
This study	-0.29	0.07
Savage et al. (2011)	-0.29	0.09
Abraham et al. (2008)	-0.29	0.11
Zambardi and Poitrasson, (2011)	-0.27	0.08
Savage et al. (2013)	-0.30	0.04
Pringle et al. (2014)	-0.31	0.12
Pringle et al. (2016)	-0.30	0.12

2.4.7 δ^{7}Li measurements

The typical analytical conditions of the Neptune/Neptune *Plus* for the δ^{7}Li measurements are listed below in Table 2.6. As no significant interference is likely to contribute to the Li signals, the low-resolution mode was deemed suitable for the analysis of δ^{7}Li. However, due to the challenges associated to Li purification (see section 2.3.3), some matrix cations, in particular Na, can still be present in samples introduced in the plasma, which can cause so-called "cryptic" matrix effects can thus introduce additional instrumental fractionation that is not corrected for by normalization to a pure standard solution during SSB procedure (Tomascak et al., 2016, and references therein). Therefore, it is necessary to check the Na content of each sample before an isotope measurement. By experience a small amount of Na can be tolerated allowed, as long as the Na:Li ratio in the sample remains under 3:1 (Dellinger, 2013). Therefore, the samples were routinely scanned over Li and Na mass regions before measurements. Any sample with Na:Li ratios higher than 3:1 was either discarded or kept aside for further separations. Because of the low mass of Li and possible magnet field drift (as by experience) through time, it was also critical to repeat peak centering at peak-center at the middle of both ^{6}Li and ^{7}Li plateaus (Figure 2.13). With

such conditions, the Li signals (note that the Li signals were made at low resolution and with the APEX) usually varied from 250 to 5 V/ppm at ~50 µl/min uptake rate.

Table 2.6 Typical analytical conditions of the Neptune *Plus* for δ^7Li measurements

RF power	1200 W
Cool gas	15-16 l/min
Auxiliary gas	~1 l/min
Sample gas	~1 l/min
Add gas	0.2–0.4 l/min
Resolution mode	Low resolution
Sample uptake	50 µl/min
Introduction system	APEX
Nebulizer	PFA (ESI)
cones	Jet + X
Cup configuration	L4/L5 (^{6}Li) and H4(^{7}Li)
Method	12 cycles for samples and standards, and 5 cycles for blanks. Each cycle takes an integration time of 8.389 seconds, and blank correction was performed.

Secondary standards IRMM-016 and SPEC solutions were regularly measured to ensure measurements were accurate. In this study, IRMM-016 and SPEC respectively have values of 0.13±0.17‰ (2σ, n=63) and 94.32±0.19‰ (2σ, n=26), which are both unresolvable from previous results δ^7Li_{IRMM}=0.14±0.25‰ and δ^7Li_{SPEC}=94.39±0.27‰ (2σ, n=73) (Dellinger, 2013).

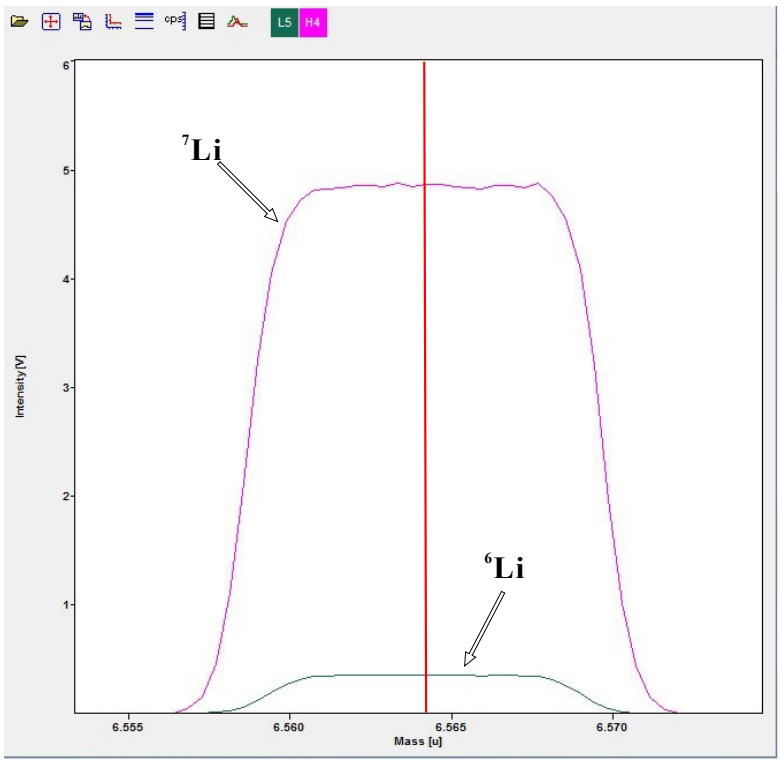

Figure 2.13 Example of a "mass scan" of Li isotope peaks, in low resolution mode.

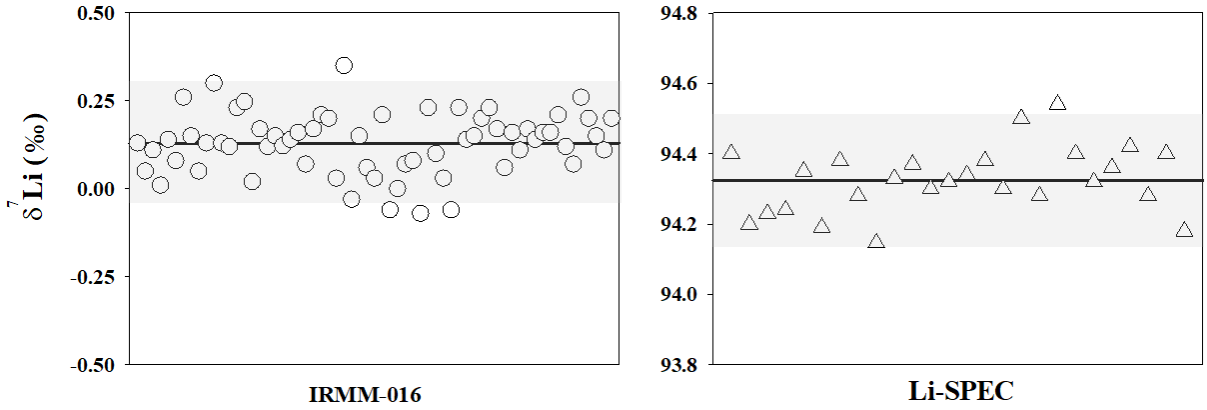

Figure 2.14 Summary of δ^7Li analyses for the pure solutions IRMM-016 and Li-SPEC. The black lines represent the average values ($\delta^7Li_{Li\text{-}IRMM}$=0.13±0.17‰ and $\delta^7Li_{Li\text{-}SPEC}$=94.32±0.19‰) and the grey areas represent the average ± 2 s.d.

The values obtained for the reference materials BHVO-2 and JB-2 (basalts), and NASS-5 and NASS-6 (seawater) are listed in Table 2.7 and are in good agreement with literature values. We also report the δ^7Li values of two reference soil materials, TILL-1 (δ^7Li=6.61±0.66‰, 2 s.d., n=20) and NIST-2709a (δ^7Li=-0.36±0.67‰, 2 s.d., n=18). The long-term reproducibility of each standard is also shown in Figure 2.15. It is important to note that the standard deviations (Table 2.7) is slightly greater than reported values. This could be partially due to the change of instruments during this study. The measurement of δ^7Li was operated on a Neptune MC-ICP-MS from 2015 to the middle of 2016, then the signal stability became poor. Since then δ^7Li was measured on a a Neptune *plus* MC-ICP-MS.

Table 2.7 Literature values of δ^7Li seawater and basalt reference materials.

Seawater	δ^7Li (‰)	2 s.d.
This study (n=19)	30.92	0.44
Clergue et al. (2015)	30.73	0.35
Dellinger et al. (2015)	30.91	0.26
Rosner et al. (2007)	30.63	0.44
Huang et al. (2010)	30.73	0.15
Misra and Froelich (2009)	30.75	0.41

BHVO-2	δ^7Li (‰)	2 s.d.
This study (n=15)	4.57	0.71
Clergue et al. (2015)	4.33	0.43
Dellinger et al. (2015)	4.34	0.41
Liu et al. (2018)	4.84	0.35
Magna et al. (2004)	4.55	0.29
Jeffcoate et al. (2007)	4.70	0.20

JB-2	δ^7Li (‰)	2 s.d.
This study (n=20)	4.62	0.78
Dellinger et al. (2015)	4.47	0.53
Liu et al. (2018)	4.77	0.53
Millot et al. (2010b)	4.90	0.60
Magna et al. (2004)	4.70	0.29
Nishio and Nakai (2002)	4.29	0.34

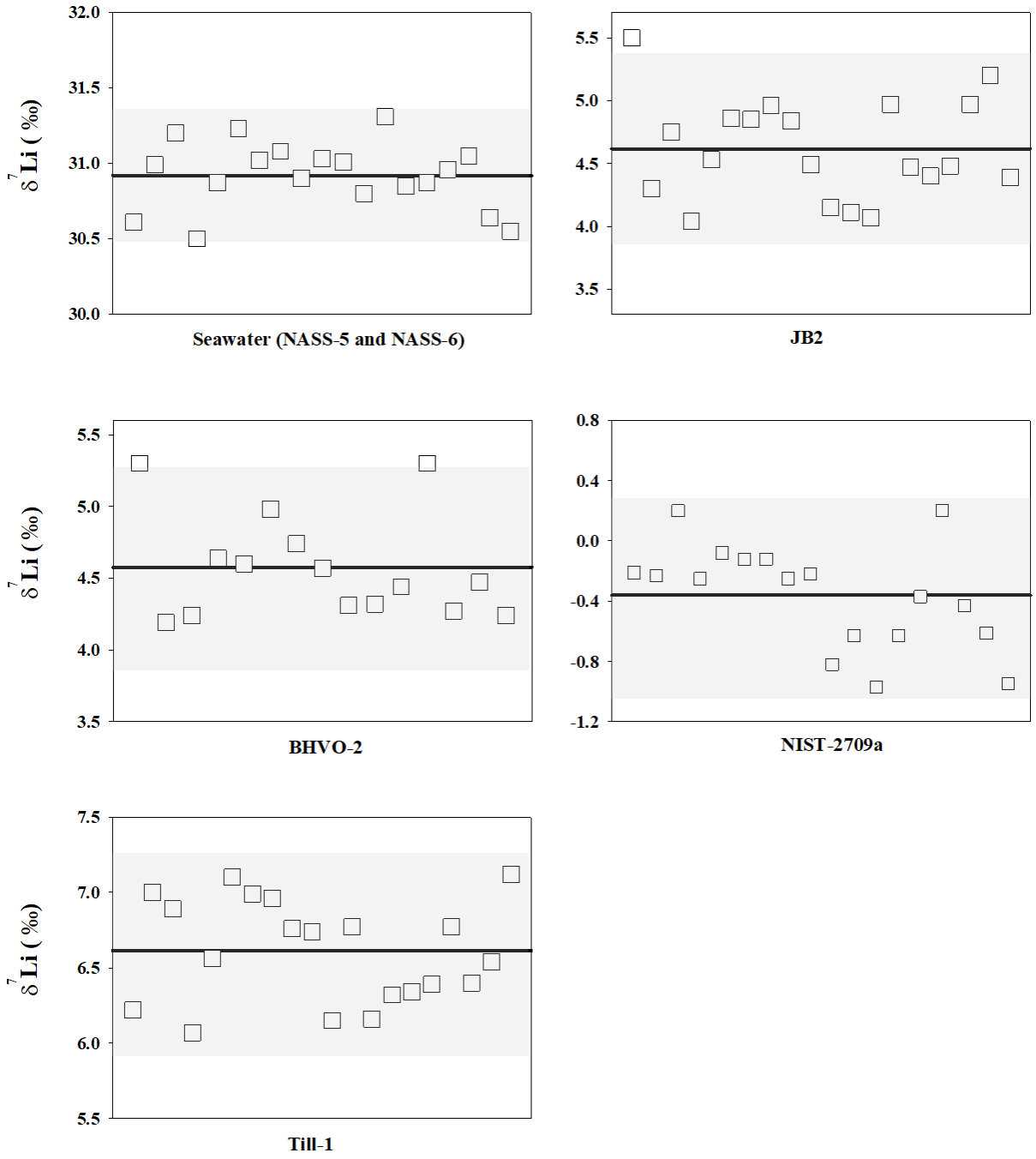

Figure 2.15 Summary of δ^7Li analyses for the reference materials NASS-5/NASS-6 (seawater), JB-2 and BHVO-2 (basalts), NIST-2709a and Till-1 (soils). The black lines represent the average values and the grey areas represent the average ± 2 s.d.

Bibliography

Abraham, K., Opfergelt, S., Fripiat, F., Cavagna, A., De Jong, J., Foley, S.F., André, L., Cardinal, D., 2008. δ30Si and δ29Si Determinations on USGS BHVO-1 and BHVO-2 Reference Materials with a New Configuration on a Nu Plasma Multi-Collector ICP-MS. Geostandards and Geoanalytical Research 32 (2), 193-202.

Bouchez, J., Gaillardet, J., France-Lanord, C., Maurice, L., Dutra-Maia, P., 2011. Grain size control of river suspended sediment geochemistry: Clues from Amazon River depth profiles. Geochemistry Geophysics Geosystems 12, Q03008.

Clergue, C., Dellinger, M., Buss, H., Gaillardet, J., Benedetti, M., Dessert, C., 2015. Influence of atmospheric deposits and secondary minerals on Li isotopes budget in a highly weathered catchment, Guadeloupe (Lesser Antilles). Chemical Geology 414, 28-41.

Dellinger, M., 2013. Apport des isotopes du lithium et des éléments alcalins à la compréhension des processus d'altération chimique et de recyclage sédimentaire, PhD thesis at IPGP.

Dellinger, M., Gaillardet, J., Bouchez, J., Calmels, D., Galy, V., Hilton, R.G., Louvat, P., France-Lanord, C., 2014. Lithium isotopes in large rivers reveal the cannibalistic nature of modern continental weathering and erosion. Earth and Planetary Science Letters 401, 359-372.

Dellinger, M., Gaillardet, J., Bouchez, J., Calmels, D., Louvat, P., Dosseto, A., Gorge, C., Alanoca, L., Maurice, L., 2015. Riverine Li isotope fractionation in the Amazon River basin controlled by the weathering regimes. Geochimica et Cosmochimica Acta 164, 71-93.

Georg, R.B., Reynolds, B.C., Frank, M., Halliday, A.N., 2006. New sample preparation techniques for the determination of Si isotopic compositions using MC-ICPMS. Chemical Geology 235 (3–4), 95-104.

Hall, J.M., Chan, L.H, McDonough, W.F., Turekian, K.K., 2005. Determination of the lithium isotopic composition of planktic foraminifera and its application as a paleo-seawater proxy. Marine Geology, 217(3-4), 255-265.

He, M., Jin, Z., Lu, H., Deng, L., Luo, C., 2016. The different cones combination enhanced sensitivity on MC-ICP-MS: The results from boron isotope analysis. International Journal of Mass Spectrometry 408, 33-37.

Henchiri, S., Gaillardet, J., Dellinger, M., Bouchez, J., Spencer, R.G.M., 2016. Riverine dissolved lithium isotopic signatures in low-relief central Africa and their link to weathering regimes. Geophysical Research Letters 43 (9), 4391-4399.

Huang, K., You, C., Liu, Y., Wang, R., Lin, P., Chung, C., 2010. Low-memory, small sample size, accurate and high-precision determinations of lithium isotopic ratios in natural materials by MC-ICP-MS. Journal of Analytical Atomic Spectrometry 25 (7), 1019-1024.

James, R.H., Palmer, M.R., 2000. The lithium isotope composition of international rock standards. Chemical Geology 166 (3-4), 319-326.

Jeffcoate, A., Elliott, T., Kasemann, S., Ionov, D., Cooper, K., Brooker, R., 2007. Li isotope fractionation in peridotites and mafic melts. Geochimica et Cosmochimica Acta 71 (1), 202-218.

Košler, J., Kučera, M., Sylvester, P., 2001. Precise measurement of Li isotopes in planktonic foraminiferal tests by quadrupole ICPMS. Chemical Geology 181 (1-4), 169-179.

Liu, Y., Huang, K., Lee, D., 2018. Precise and accurate boron and lithium isotope determinations for small sample-size geological materials by MC-ICP-MS. Journal of Analytical Atomic Spectrometry 33 (5), 846-855.

Louvat, P., Bouchez, J., Paris, G., 2011. MC-ICP-MS Isotope Measurements with Direct Injection Nebulisation (d-DIHEN): Optimisation and Application to Boron in Seawater and Carbonate Samples. Geostandards and Geoanalytical Research 35 (1), 75-88.

Magna, T., Wiechert, U.H., Halliday, A.N., 2004. Low-blank isotope ratio measurement of small samples of lithium using multiple-collector ICPMS. International Journal of Mass Spectrometry 239 (1), 67-76.

Magna, T., Wiechert, U., Halliday, A.N., 2006. New constraints on the lithium isotope compositions of the Moon and terrestrial planets. Earth and Planetary Science Letters, 243 (3-4), 336-353.

Millot, R., Vigier, N., Gaillardet, J., 2010. Behaviour of lithium and its isotopes during weathering in the Mackenzie Basin, Canada. Geochimica et Cosmochimica Acta. 74 (14), 3897-3912.

Misra, S., Froelich, P.N., 2009. Measurement of lithium isotope ratios by quadrupole-ICP-MS: application to seawater and natural carbonates. Journal of Analytical Atomic Spectrometry 24 (11), 1524-1533.

Moriguti, T., Nakamura, E., 1998. High-yield lithium separation and the precise isotopic analysis for natural rock and aqueous samples. Chemical Geology, 145(1-2), 91-104.

Nishio, Y., Nakai, S., 2002. Accurate and precise lithium isotopic determinations of igneous rock samples using multi-collector inductively coupled plasma mass spectrometry. Analytica Chimica Acta 456 (2), 271-281.

Opfergelt, S., Delmelle, P., 2012. Silicon isotopes and continental weathering processes: Assessing controls on Si transfer to the ocean. Comptes Rendus Geoscience 344 (11–12), 723-738.

Peters, D. G., Hayes, J. M., & Hieftje, G. M., 1974. Chemical separations and measurements: theory and practice of analytical chemistry. WB Saunders Company.

Potts, P.J., 2012. A Handbook of Silicate Rock Analysis. Springer Science & Business Media.

Pringle, E.A., Savage, P.S., Jackson, M.G., Barrat, J., Moynier, F., 2013. Si Isotope Homogeneity of the Solar Nebula. The Astrophysical Journal 779 (2), 123.

Pringle, E.A., Moynier, F., Savage, P.S., Badro, J., Barrat, J., 2014. Silicon isotopes in angrites and volatile loss in planetesimals. Proceedings of the National Academy of Sciences 111 (48), 17029-17032.

Pringle, E.A., Moynier, F., Savage, P.S., Jackson, M.G., Moreira, M., Day, J.M.D., 2016. Silicon isotopes reveal recycled altered oceanic crust in the mantle sources of Ocean Island Basalts. Geochimica et Cosmochimica Acta 189, 282-295.

Rosner, M., Ball, L., Peucker-Ehrenbrink, B., Blusztajn, J., Bach, W., Erzinger, J., 2007. A simplified, accurate and fast method for lithium isotope analysis of rocks and fluids, and δ7Li values of seawater and rock reference materials. Geostandards and Geoanalytical Research 31 (2), 77-88.

Rudnick, R.L., Gao, S., 2003. 3.01 - Composition of the Continental Crust. In: Holland, H.D. and Turekian, K.K., (Eds.). Treatise on Geochemistry. Pergamon, Oxford.

Savage, P.S., Georg, R.B., Williams, H.M., Burton, K.W., Halliday, A.N., 2011. Silicon isotope fractionation during magmatic differentiation. Geochimica et Cosmochimica Acta 75 (20), 6124-6139.

Savage, P.S., Georg, R.B., Williams, H.M., Halliday, A.N., 2013. The silicon isotope composition of the upper continental crust. Geochimica et Cosmochimica Acta 109, 384-399.

Schönbächler, M., Fehr, M.A., 2013. Basics of ion exchange chromatography for selected geological applications. In: Anonymous Treatise on Geochemistry. Vol. 15: Analytical Geochemistry/Inorganic Instrument Analysis. Elsevier.

Taylor, S., McLennan, S., 1985. The continental crust: its composition and evolution. Oxford: Blackwell Press 1, 312.

Taylor, T.I., Urey, H.C., 1938. Fractionation of the lithium and potassium isotopes by chemical exchange with zeolites. The Journal of chemical physics 6 (8), 429-438.

Tomascak, P.B., Magna, T., Dohmen, R., 2016. Advances in Lithium Isotope Geochemistry. Springer International Publishing, Springer International Publishing Switzerland.

Weyer, S., Schwieters, J., 2003. High precision Fe isotope measurements with high mass resolution MC-ICPMS. International Journal of Mass Spectrometry 226 (3), 355-368.

Young, E.D., Galy, A., Nagahara, H., 2002. Kinetic and equilibrium mass-dependent isotope fractionation laws in nature and their geochemical and cosmochemical significance. Geochimica et Cosmochimica Acta 66 (6), 1095-1104.

Zambardi, T., Poitrasson, F., 2011. Precise Determination of Silicon Isotopes in Silicate Rock Reference Materials by MC-ICP-MS. Geostandards and Geoanalytical Research 35 (1), 89-99.

Chapter 3: Experimental investigation of the possible impact of “reverse weathering” on the Lithium isotope composition of seawater

3.1 Introduction

Noticing the unbalanced oceanic mass budget of some of the major elements such as Na and Si, Mackenzie and Garrels (1966) proposed the existence of a process taking up cations from seawater into authigenic sediments and liberating carbon dioxide, termed as "reverse weathering". Sillen (1967) later suggested that clay formation would be accountable for this reaction between sediments and seawater. More than half a century later, only a limited number of studies have attempted to characterize or quantify the global role of reverse weathering. The challenges include, but are not limited to, the slow reaction rates of this processes, and the fact that continental weathering products are mineralogically and chemically similar to the authigenic clays which would be produced by reverse weathering. However, Michalopoulos and Aller (1995) showed the possibility of such a process based on laboratory experiments involving the incubation in seawater of different seed materials (kaolinite, quartz grains, iron oxide-hydroxide coated quartz grains, and glass beads) with sediment samples from the delta of Amazon River. They observed the formation of aluminosilicates when incubating quartz grains, and the decomposition of seed materials when incubating kaolinite and glass beads. Based on this work, Mackenzie and Kump (1995) generalized reverse weathering as the following reaction:

Silica + aluminous clays + iron oxides + organic carbon + soluble cations + bicarbonate → new clay minerals + water + carbon dioxide

The limiting factor of such a reaction in the marine environment (seawater column or sediment pore water) is the supply of silicon (Si), rather than that of aluminium (Al). Although Al is an immobile element during silicate weathering, the demand of Al for authigenic clay formation in marine environments can be satisfied by the simultaneous dissolution of Al-oxides or highly weathered aluminosilicates (Michalopoulos and Aller, 1995). It has been shown that the diagenesis

of biological silica could provide the necessary silica source (Van Cappellen and Qiu, 1997; Michalopoulos and Aller, 2004; Aller, 2014). More recently, three studies have investigated reverse weathering based on isotope methods. Rahman et al. (2016) reported the presence of cosmogenic radioactive ^{32}Si (half-life ~140 years) in sediments as a witness of the significant impact of reverse weathering on the Si cycle in deltaic environments. Based on the Mg isotopes of deep sea floor sediments from the South Pacific gyre, Dunlea et al. (2017) suggested that the clays contained in these sediments are authigenic and proposed a relationship between reverse weathering and climate evolution during the Cenozoic. Ramos et al. (2018) used K isotopes in deep-sea sediment pore waters to suggest that reverse weathering contributes to regulate the isotopic signature of seawater potassium.

Additionally, reverse weathering and the associated lithium (Li) chemical and isotopic fractionation are likely to significantly contribute to the isotope mass balance of Li in the ocean (Misra and Froelich, 2012). Lithium has two stable isotopes (^{6}Li and ^{7}Li), with a relative large mass difference (~1/6) enabling strong fractionation and consequentially a large variability of the Li isotope composition in nature. The Li isotopic composition of a sample is expressed in δ-notation in the unit of ‰, defined as the deviation of the $^{7}Li/^{6}Li$ ratio compared to a reference material from the National Institute of Standards and Technology (NIST RM-8545), commonly referred as L-SVEC:

$$\delta^{7}Li=\left[\frac{(^{7}Li/^{6}Li)_{sample}}{(^{7}Li/^{6}Li)_{L\text{-}SVEC}}-1\right]\times 1000$$

The span of $\delta^{7}Li$ in geological materials is greater than 50‰, making Li one of the most isotopically fractionated metals. A number of experimental studies have addressed the behaviour

of Li and its isotopes during the weathering of igneous rocks/minerals to strengthen our understanding of (1) the effect of the alteration of oceanic basalts in various environments including low-temperature seafloor and high-temperature hydrothermal vents (Seyfried et al., 1984; Berger et al., 1987, 1988; James et al., 2003; Millot et al., 2010a) and (2) Li partitioning between fluids and solids during silicate weathering on the continents (Pistiner and Henderson, 2003; Vigier et al., 2008; Wimpenny et al., 2010, 2015; Verney-Carron et al., 2011). These studies have shown that in low temperature environments, clay minerals are capable to take up Li from the fluid with a preference for ^{6}Li. Solutions are enriched in ^{7}Li as a result of the preferential uptake of ^{6}Li into secondary minerals (such as clays or oxides) during weathering processes. Today, the average global riverine dissolved δ^{7}Li has a value of 23‰ (Huh et al., 1998), much higher than that of the upper continental crust (UCC, $\delta^{7}Li_{UCC}$=0±2‰; Teng et al., 2004), showing the potential of δ^{7}Li as a robust tracer of continental weathering. In the present-day Li cycle, seawater is the Li reservoir exhibiting the heaviest δ^{7}Li (~31‰), a value higher than those of the main Li influxes to the ocean, *i.e.* hydrothermal and riverine inputs. At steady state, for the ocean to achieve such a high δ^{7}Li value, either an additional, yet unknown heavy δ^{7}Li input, or a light δ^{7}Li output is needed. Reverse weathering is a viable candidate for such an isotopically light output. The mass balance model from Misra and Froelich (2012) suggests that a Δ^{7}Li fractionation factor of 16‰ ($\Delta^{7}Li = \delta^{7}Li_{seawater} - \delta^{7}Li_{authigenic\text{-}sediments}$) is associated to reverse weathering in the ocean. In this chapter, in order to better characterize the impact of reverse weathering on the Li isotope composition of the ocean, we report the results of an experimental study of Li isotope fractionation during the interaction of seawater with detrital sediments. We focus on two solid products: kaolinite and basalt glass, each representing a fraction of the detrital inputs to the ocean (clays and an unweathered primary material).

3.2 Materials and experimental methods

In this study, we used synthetic "artificial seawater" (ASW) rather than natural seawater to control the chemistry of the reactive solution and to minimize the effect of biological activity. To synthesize the ASW solution, we followed a modified version of the protocol from Kester et al. (1967) (Table 3.1). The solids used were a basaltic glass and kaolinite, thus representing an unweathered silicate and a secondary mineral. The basaltic glass (reference BG-001) was obtained from the volcanic ash of Stapafell Mountain, southwestern Iceland; its chemical composition is reported in Oelkers and Gislason (2001). Poorly crystallized kaolinite (reference KGa-2), from Washington County (Georgia, USA), was supplied by the Source Clay Repository of the Clay Minerals Society (surface properties are described in Schroth and Sposito, 1997). The Li contents of the BG-001 basaltic glass (4.04 ppm) and the KGa-2 kaolinite (95.94 ppm) were determined at the Institut de Physique du Globe de Paris (IPGP) using an Inductively coupled plasma-Quadruple-Mass spectrometer (ICP-Q-MS) after acid digestion (HF-HNO_3) of powdered aliquots of the solids.

Four sets of experiments were conducted at Géosciences Environnement Toulouse (GET). Each type of experiment aimed at investigating: (1) the dissolution of kaolinite in "acidic" seawater (and potential associated Li release); (2) the interaction between basalt glass and seawater Li (the Li release/uptake); (3) the interaction between kaolinite and seawater Li (the Li release/uptake); and (4) the specific sites on which Li adsorbed onto kaolinite.

Table 3.1 Protocol for making the "artificial seawater" (ASW) solution

Salt	Weight (g)	Concentration (g/kg)
NaCl	119.63	23.926
KCl	3.39	0.678
$SrCl_2 \bullet 6H_2O$	0.12	0.024
$MgCl_2 \bullet 6H_2O$	54.16	10.832
$CaCl_2 \bullet 2H_2O$	7.59	1.518
Na_2SO_4	20.04	4.008
$NaHCO_3$	0.98	0.196
Dilute in Milli-Q water to 5000 g		
Li was doped in the solution for experiments (2) and (3), to [Li]=180.32 ppb (δ^7Li=52.83 ±0.28‰)		

For experiment (1), 20.5 g of the KGa-2 powder was immersed in 501.5 ml of the ASW solution. To enhance the dissolution of kaolinite, which is the process we wanted to isolate with this experiment, the fluid pH was set to around 2.7 and maintained at this level throughout the experiment. Over the course of the reaction (~28 days), 7 solution samples were taken. The concentration of Li, Al, and Si, as well as the δ^7Li composition of these solutions were measured, and the details are listed in Table 3.3.

In experiments (2) and (3), the ASW solution used was first doped with Li using an ICP standard solution (whose δ^7Li was measured as δ^7Li_i=52.83±0.28 ‰, 2σ, n=2), to a level close to seawater [Li] (~25.9 μmol/kg, or ~180 ppb), and its pH was adjusted using NaOH and HCl to pH=8.32. For the experiment (2), 1.2 g of BG-001 powder was immersed in 949.1 ml of Li-doped

and pH-adjusted ASW solution. For the experiment (3), 20.0 g of KGa-2 powder was immersed in 500.4 ml of Li-doped and pH adjusted ASW solution. Sampling started 1 day after the immersions. In total, 16 samples were collected for each of experiment (2) and (3) (Tables 3.4 and 3.5). After each sample collection, the pH was measured and if needed re-adjusted to pH~8.4 using NaOH or HCl. The concentration of Al, Si, Li, as well as Li isotope composition of each sample solution were measured.

Experiments (1-3) were conducted in polypropylene (PP) beakers hermetically sealed with PVC lids and rubber O-rings. The solutions were continuously mixed using either a Teflon propeller driven by an overhead stirrer or a suspended Teflon-coated magnetic bar attached to a fish-clip (Figure 3.1). For experiment (3), solid samples (before and after the experiment) were analyzed using a JSM 7800F Prime-EDS (JEOL, Ltd.) scanning electron microscope (SEM) at the Castaing Micro-characterization Center in Toulouse to detect any mineralogical change due to solid-solution interactions.

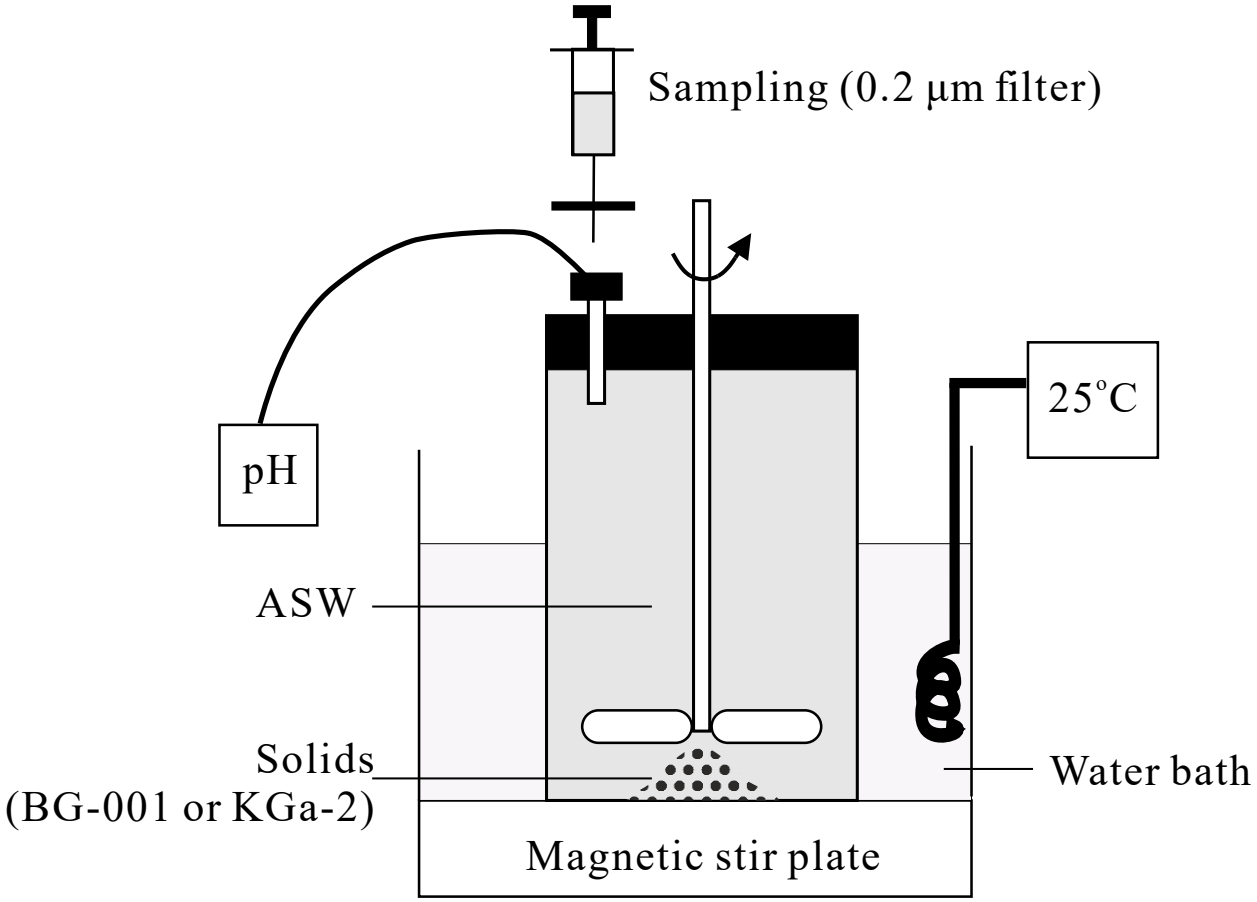

Figure 3.1 Schematic of the experimental system used to study the interaction between artificial seawater (ASW) solution and selected solids BG-001 (basaltic glass) or KGa-2 (kaolinite).

In clay minerals, such as smectite, Li is often bonded in two types of sites: structural octahedral site and interlayer exchangeable site (Vigier et al., 2008). In order to better understand the behaviour of Li during the dissolution of kaolinite and investigate whether the observed Li isotope fractionation is site-dependent, experiments (4) were conducted (Table 3.6). In this set of experiments, an aliquot of KGa-2 sample was first carefully rinsed with double deionized (DDI) water for 12 times, leading to the removal (at least partially) of Li located at the exchangeable sites. Adsorption experiments were conducted with these rinsed samples at 20°C in 50 ml PP centrifuge tubes. A suspension made of about 1g of kaolinite and 30 ml of aqueous solution pre-equilibrated

with the same kaolinite powder was mixed with a tube rotator for several hours before Li addition. The aqueous solutions consisted of either the ASW or a NaCl solution with the same molarity as ASW (0.41 M). Between 0.5 and ~19 ppm of dissolved Li was added to the suspension from Li stock solutions at 15-600 ppm prepared in the same matrix, while the pH was adjusted by the addition of small amounts of NaOH (1 M). The suspensions were then mixed for 30 minutes to 6 days and at last centrifuged at a speed of 6500 rpm to separate the aqueous solution from the solid. Sample solutions were collected for chemical analyses and the measurement of pH. The partition coefficient K_d was calculated as:

$$K_d = \frac{(m_{Li\text{-}ads}/m_{kaol})}{(m_{Li\text{-}aq}/m_{Li\text{-}sol})} \qquad \text{(Equation 3-1)}$$

Where $m_{Li\text{-}ads}$ and $m_{Li\text{-}aq}$ correspond to the mass of Li adsorbed on the solid surface and the mass of Li in soluition, and m_{kaol} and m_{sol} designate the corresponding mass of kaolinite and aqueous solution, respectively. The solid samples from two of the runs with the highest amount of Li adsorbed after the expdriments, KL-17 (78.3 µg/g; NaCl solution) and KL-18 (44.3 µg/g; ASW), were analyzed together with a sample of fresh KGa-2 powder and of unreacted but washed KGa-2 using Nuclear Magnetic Resonance (NMR) at the research unit of CEMHTI (Conditions Extrêmes et Matériaux: Haute Température et Irradiation; CNRS, Orléans) to examine the potential structural variation in kaolinite caused by the Li release. ^{7}Li Magic Angle Spinning (MAS) NMR spectra were acquired on a bruker AVANCE III spectrometer (750 MHz – 17.6 T) at a Larmor frequency of 291.5 MHz and a spinning speed of 30 kHz. Around 2000 scans were accumulated with a recycling delay of 10s, insuring complete relaxation of the signal. ^{7}Li chemical shift were referenced relative to a 1 M LiCl solution.

3.3 Analytical protocol

During the experiments (1−3), fluid aliquots ranging from 3 to 25 ml were sampled using a

weighed, clean syringe attached to a 0.2-µm porosity filter. The sampled volume was determined via the mass difference of the syringe before and after sampling. Part of the sampled volume was acidified by adding 1 drop of concentrated HNO_3 and was stored for the measurements of dissolved Al, Si, and Li concentrations. Additionally, Ca, K, and Mg concentrations were also monitored during the experiment (3) for the calculation of the aqueous solution speciation and the degree of saturation with respect to the possible formation of secondary minerals. The pH of the aqueous solution was measured *in situ* by inserting a glass combination electrode, calibrated against NIST-certified buffers, inside the reactor through an opening made on the lid for this purpose. The concentrations of Al and Si were measured using Inductively Coupled Plasma Optical Emission Spectrometry (ICP-OES), whereas the concentrations of the other cations (K, Mg, and Ca) were determined by Atomic Absorption Spectroscopy (AAS) at GET. The measurements of Li concentration and isotope composition were conducted at IPGP, where dissolved Li was measured by ICP-Q-MS.

Li separation was performed prior to the measurement of δ^7Li. A protocol based on the use of small volume columns for Li separation (Table 3.2), modified from previously published multi-step Li separation methods (Moriguti and Nakamura, 1998; Hall et al., 2005; Magna et al., 2006), was employed. In brief, this protocol involves a first step of rough separation of Li and a second step of Li purification. For both steps 1 ml of cation exchange resin (Biorad AG50W-X12, 200-400 mesh) was used.

Table 3.2 Li separation protocol using the 1 ml resin method

Step 1	Step 2
Column cleaning	Column cleaning
5 ml 6 N HCl 3 ml MQ 3 ml MQ	5 ml 6 N HCl 3 ml MQ 3 ml MQ
Column conditioning	Column conditioning
2 ml 1 N HNO_3	2 ml 0.2 N HNO_3
Li separation	Li separation
0.5 ml sample solution (20 ppb Li in 1 N HNO_3, collected) 4 ml 1 N HNO_3 (collected)	0.5 ml sample solution (20 ppb Li in 0.2 N HNO_3) 4 ml 0.2 N HNO_3 4 ml 0.2 N HNO_3 4 ml 1 N HNO_3 (collected) 4 ml 1 N HNO_3 (collected)

For the first step, 0.5 ml of sample solution in 1 N HNO_3 at a Li concentration of 40 ppb were loaded onto the column and followed by elution using 1 N HNO_3. Lithium was collected from the start of the sample loading and across the first 4 ml of the elution volume, and the collected solution was evaporated to dryness and then re-dissolved in 0.5 ml 0.2 N HNO_3. For the second step, the elution of sample from the previous step was carried in a less acidic medium (0.2 N HNO_3), allowing for a better separation between Li and Na. The fraction between 8 ml and 16 ml after the beginning of the elution was collected for the measurement of δ^7Li.

The first step was repeated multiple times in parallel for samples with high matrix/Li ratios, such as those collected from experiment (1), whose Na/Li ratios are approximately ~40 times greater than that of seawater. To obtain the Li amount required for isotope analysis (20 ng), each of these sample was first diluted and split into 12 sub-samples, and then processed in parallel

through 12 separation columns (equivalent to those used in the first step described above). Eluted fractions from these 12 columns were collected, combined, evaporated, redissolved, and split into 6 aliquots loaded onto 6 parallel columns. This procedure was repeated with 3 parallel columns, 2 parallel columns, and finally 1 column (Figure 3.2). Then the second step of Li purification (as for other samples) was performed for the final elution fraction. Such a separation procedure was tested using seawater, and no matrix effect was observed.

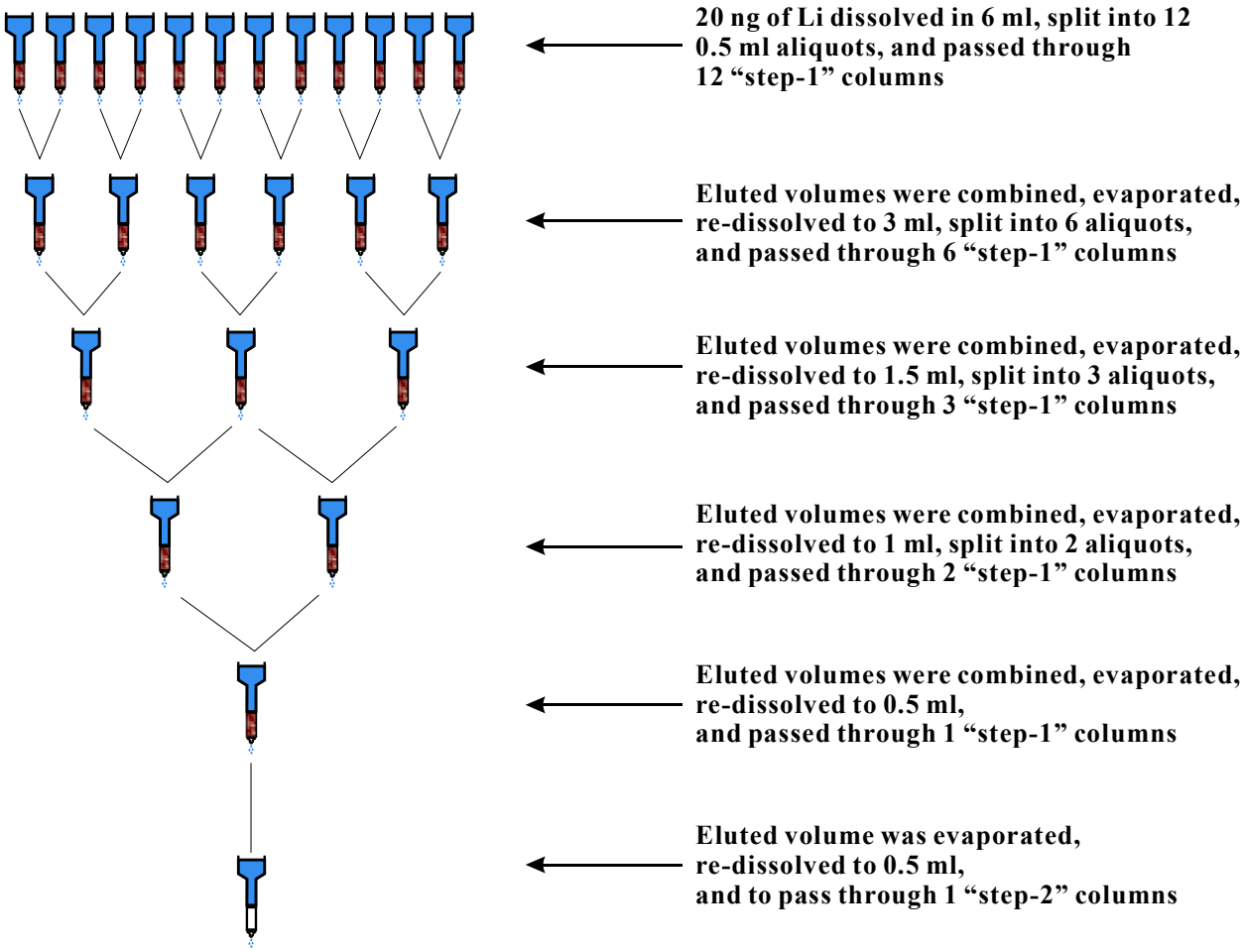

Figure 3.2 Protocol for Li separation for samples collected in experiment (1). Those samples had high Na/Li ratios.

The initial δ^7Li composition of the Li-doped solution was also analysed, and the solid materials used in the experiments, BG-001 and KGa-2, were digested and processed to measure

their δ^7Li composition following the same protocols. Five reference materials (basalts: BHVO-2 and JB-2; seawater: NASS-6; soils: NIST-2709a and Till-1) were systematically processed for each chemistry session to determine the quality of the protocol.

The Li fraction obtained from the separation protocol was diluted to a Li concentration of 20 ppb and acidified to 0.5 N HNO_3 for isotope analyses on a Thermo Fisher Neptune Plus MC-ICP-MS at IPGP. The long-term reproducibility of the instrument was checked by regular measurements of standards IRMM-016 (δ^7Li=0.17±0.13‰, ±2σ, n=20). The overall accuracy of the procedure was checked using the results of the reference materials BHVO-2 (δ^7Li=4.34±0.23‰, ±2σ, n=7), JB-2 (δ^7Li=4.33±0.67‰, ±2σ, n=7), and NASS-6 (δ^7Li=30.98±0.35‰, ±2σ, n=7) for which δ^7Li have been reported in previous studies (Dellinger et al., 2014; Dellinger et al., 2015). Here we also report the δ^7Li composition of two additional reference materials including a soil standard NIST-2709a (δ^7Li= -0.62±0.53 ‰, ±2σ, n=7), and a till standard Till-1 (δ^7Li= 6.42±0.38‰, ±2σ, n=7).

3.4 Thermodynamic calculations

Authigenic clays are formed during reverse weathering process. For the experiment (3), theoretical calculations were performed in order to detect the formation of secondary phases as a complement of SEM analyses of solids. All speciation and solubility calculations with respect to all relevant solid phases were performed using the geochemical code PHREEQC v. 3.3 (Parkhurst and Appelo, 2013) and its "LLNL" thermodynamic database. Activity coefficients for dissolved species were calculated using the extended Debye–Huckel and Davies equations.

3.5 Results

Results from experiment (1-4) are listed below in Table 3.3, 3.4, 3.5, and 3.6.

Table 3.3 Experiment (1): dissolution of kaolinite (KGa-2) powder in "artificial seawater" solution

Sample	elapsed time (days)	pH	Sampled Vol (g)	Fluid Vol (g)	[Al] (mmol/kg)	[Si] (mmol/kg)	[Li] (µmol/kg)	Al/Si	δ^7Li	2 s.d.
G2-1	1.09	2.68	12.1944	489.31	0.29	0.090		3.1		
G2-2	2.25		9.1662	480.14	0.32	0.132		2.4		
G2-3	7.35		18.1016	462.04	0.41	0.212	0.609422	1.8	-16.61	0.11
G2-4	10.34		19.8286	442.21	0.43	0.238	0.692552	1.7	-16.56	0.13
G2-5	14.31	2.79	17.3749	424.83	0.47	0.278	0.799597	1.6	-17.77	0.25
G2-6	21.35	2.78	14.9089	409.93	0.53	0.322	0.909811	1.6	-18.32	0.25
G2-7	28.17	2.82	17.0449	392.88	0.57	0.365	1.030831	1.5	-19.03	0.20

δ^7Li (KGa-2) = −0.38±0.72 ‰ (2 s.d., n=12)

Table 3.4 Experiment (2): interaction between basaltic glass and Li-doped "artificial seawater" solution

Sample	elapsed time (days)	pH	Sampled (g)	Fluid Vol (g)	[Al] (mmol/kg)	[Si] (mmol/kg)	[Li] (µmol/kg)	Al/Si	δ^7Li	2 s.d.
BG1-1	1.03	8.19	3.8302	945.27	1.31E-03	1.15E-02	26.0	0.11		
BG1-2	3.80	8.22	5.8837	939.39	8.65E-04	2.09E-02	26.9	0.04	53.45	0.09
BG1-3	6.80	8.18	6.3109	933.08	3.21E-03	2.86E-02	26.6	0.11	53.13	0.09
BG1-4	10.87	8.15	5.5988	927.48	2.03E-03	3.51E-02	26.4	0.06	52.15	0.19
BG1-5	19.91	8.10	9.2528	918.22	1.76E-03	6.29E-02	24.9	0.03	52.78	0.22
BG1-6	31.98	8.17	7.5317	910.69	1.72E-03	8.08E-02	25.4	0.02	51.81	0.08
*	33.75	8.41	-0.15	910.84						
BG1-7	39.04	7.91	9.1172	901.72	1.58E-03	8.85E-02	24.9	0.02	52.90	0.30
*	39.08	8.39	-0.16	901.88						
BG1-8	46.92	7.91	8.8123	893.07	1.53E-03	9.34E-02	24.8	0.02	53.91	0.19
*	47.03	8.41	-0.17	893.24						
*	54.87	8.41	-0.16	893.40						
BG1-9	61.06	8.00	11.442	881.96	1.60E-03	8.19E-02	24.2	0.02	53.35	0.08
*	61.88	8.49	-0.16	882.12						
*	70.00	8.45	-0.15	882.27						
BG1-10	74.90	8.12	9.1036	873.17	1.46E-03	9.19E-02	23.9	0.02	53.79	0.09
*	83.98	8.54	-0.16	873.33						
BG1-11	90.03	8.15	12.75	860.58	2.71E-03	9.83E-02	24.5	0.03	53.44	0.09
BG1-12	105.03	8.08	9.935	850.64	1.91E-04	1.03E-01	23.4	0.00		
BG1-13	119.02	7.92	12.8825	837.76	1.19E-03	1.07E-01	23.0	0.01		
BG1-14	140.07	8.04	12.404	825.36	1.32E-03	1.09E-01	23.1	0.01	53.14	0.09
BG1-15	158.93	7.95	12.2292	813.13	6.27E-04	1.15E-01	23.0	0.01	52.20	0.02
BG1-16	165.98	7.94	25	788.13	1.43E-03	1.17E-01				

* addition of 1M NaOH to adjust the pH to ~8.4

δ^7Li (BG-001) = 5.15 ± 0.09 ‰ (n=2)

Table 3.5 Experiment (3): interaction between kaolinite and Li-doped "artificial seawater" solution

Sample	Time (days)	pH	Sample Vol (g)	Fluid Vol (g)	[Al] (mmol/kg)	[Si] (mmol/kg)	[Ca] (mmol/kg)	[Mg] (mmol/kg)	[Li] (µmol/kg)	Al/Si	δ^7Li (‰)	2 s.d.
W1-1	1.03	6.48	4.226	496.15	n.d.	1.17E-02			19.37	0		
*	1.1	8.2	0.74	496.89								
W1-2	3.86	7.99	5.68	491.21	n.d.	7.21E-03	10.76	52.65	15.66	0	64.02	0.10
*	4.8	8.46	0.3	491.51								
W1-3	6.88	8.25	5.713	485.8	7.90E-04	1.03E-02			12.61	0.1	67.72	0.14
*	7.03	8.42	0.15	485.95								
W1-4	10.92	8.27	4.809	481.14	1.56E-03	1.28E-02	10.93	50.33	11.27	0.1	70.57	0.06
W1-5	19.91	8.28	9.386	471.76	4.20E-04	1.74E-02			9.53	0	72.68	0.25
W1-6	32.04	8.18	7.896	463.86	1.71E-04	1.98E-02	10.70	50.19	8.98	0	74.08	0.16
*	33.76	8.39	-0.1	463.96								
W1-7	39.04	8.25	8.198	455.77	1.67E-04	2.08E-02			7.95	0	75.44	0.3
W1-8	46.92	8.22	8.11	447.66	n.d.	2.24E-02	10.83	51.24	7.85	0	76.45	0.23
W1-9	61.06	8.17	11.1	436.56	1.75E-04	2.21E-02			7.47	0	76.38	0.09
W1-10	74.9	8.09	10.93	425.63	9.17E-05	2.35E-02			7.27	0	78.54	0.07
W1-11	90.02	8.07	12.82	412.81	4.38E-04	2.47E-02			6.86	0	78.79	0.15
W1-12	105.03	8.07	9.961	402.84	n.d.	2.61E-02	10.8	51.69	6.34	0		
W1-13	119.02	8.08	10.05	392.79	1.02E-03	2.73E-02	10.96	51.82	6.09	0		
W1-14	140.06	8.09	12.75	380.04	n.d.	2.46E-02	10.81	51.73	5.53	0	78.29	0.08
W1-15	158.93	8.09	12.14	367.9	n.d.	2.70E-02			5.46	0	80.23	0.21
W1-16	165.97	8.08	25	342.9	7.68E-04	2.81E-02				0		

* addition of 1M NaOH to adjust the pH to ~8.4

δ^7Li (KGa-2) = -0.38±0.72 ‰ (n=12)

Table 3.6 Experiments (4): adsorption of Li onto kaolinite

Sample	pH	Solution	Water/Solid	Exposure time (hrs)	$[Li]_i$ (ppm)	Δ[Li] (ppm)	Li (ads) (µg/g)	K_d	Al (mmol/kg)	Si (mmol/kg)
KLT-02	10.12	NaCl	20.6	17.3	0.49	-0.29	5.9	28.2	2.8E-02	1.1E-02
KL-01	7.03	NaCl	30	0.6	4.95	-0.25	7.5	1.6	2.5E-04	1.1E-02
KL-02	6.92	NaCl	29.9	1.5	4.93	-0.33	10	2.2	7.6E-05	1.2E-02
KL-03	6.91	NaCl	30	3	4.94	-0.3	9.1	2	3.4E-04	1.2E-02
KL-04	6.9	NaCl	30	6	4.96	-0.24	7.1	1.5	<DL	1.2E-02
KL-05	6.94	NaCl	29.6	8	4.94	-0.22	6.4	1.4	<DL	1.2E-02
KL-06	9.95	NaCl	28.2	20.7	5.01	-0.84	23.6	5.7	1.3E-02	1.4E-02
KL-07	7.42	NaCl	27.7	21.4	3.6	-0.26	7.1	2.1	1.3E-04	8.0E-03
KL-08	8.54	NaCl	28.7	26.1	3.6	-0.38	11.1	3.4	9.3E-04	5.3E-03
KL-09	6.96	ASW	28.9	24	3.74	-0.18	5.2	1.5	<DL	1.2E-02
KL-10	7.59	ASW	29.1	24	3.74	-0.25	7.2	2.1	<DL	1.0E-02
KL-11	7.84	ASW	28.2	148.7	3.64	-0.01	0.2	0.05	4.4E-04	1.2E-02
KL-12	8.29	ASW	29.4	148.7	3.66	-0.15	4.4	1.3	2.8E-04	2.3E-02
KL-13	8.45	NaCl	28.5	148.6	3.47	-0.3	8.6	2.7	5.9E-04	6.8E-03
KL-14	9.65	NaCl	29.2	148.6	3.46	-0.49	14.4	4.9	6.8E-03	9.4E-03
KL-15	10.95	NaCl	27.9	90.6	18.75	-2.29	63.9	3.9	8.3E-03	6.8E-02
KL-16	8.79	ASW	28	90.6	3.42	-0.54	15.1	5.2	3.5E-04	1.3E-02
KL-17	11.58	NaCl	30	90.5	18.3	-2.61	78.3	5	2.7E-04	1.9E-01
KL-18	8.77	ASW	26.9	90.5	18.81	-1.65	44.3	2.6	3.7E-04	1.4E-02
Experiment (3)	8.1-8.3	ASW	~17-25	4006	0.18	-0.142	3.4*	89.6*	2.2E-04	2.8E-02

*Value corrected for the change of solution volume and [Li] during experiment (3)

In experiment (1), dissolved Li, Al, and Si concentrations ([Li], [Al], and [Si]) all increase with time (Fig 3.7; Table 3.3). [Al] and [Si] respectively reached 0.57 mmol/kg and 0.365 mmol/kg at the end of the experiment. These concentrations are significantly higher than those attained during the experiments (2) and (3) (Fig 3.8, Table 3.4; Fig 3.9, Table 3.5). [Li] started from below the detection limit in the ASW solution and reached 1.03 µmol/kg at the end of experiment (after 28 days). Light Li isotopes enters the solution first. Whereas the bulk KGa-2 solid has a δ^7Li value of δ^7Li_{KGa-2}=−0.38‰, the dissolved Li in the first sample (after ~7 days of experiment) analysed had a δ^7Li value of −16.61±0.11‰, and the δ^7Li gradually decreased to a final value of −19.03±0.20‰ (Table 3.3). It is important to note that, according to our thermodynamic calculations, the aqueous solution was always undersaturated with respect to any Al-Si secondary phase, whose presence could potentially incorporate part of the Li dissolved during the course of the reaction. This observation suggests that the large Li isotope fractionation observed is only due to the preferential release of ^{6}Li from kaolinite. The absence of newly formed secondary phases is also confirmed by SEM observations on both fresh and reacted solid powders. Indeed, the reacted sample recovered at the end of the experiment does not show any significant difference compared to the fresh KGa-2 sample (Figure 3.3).

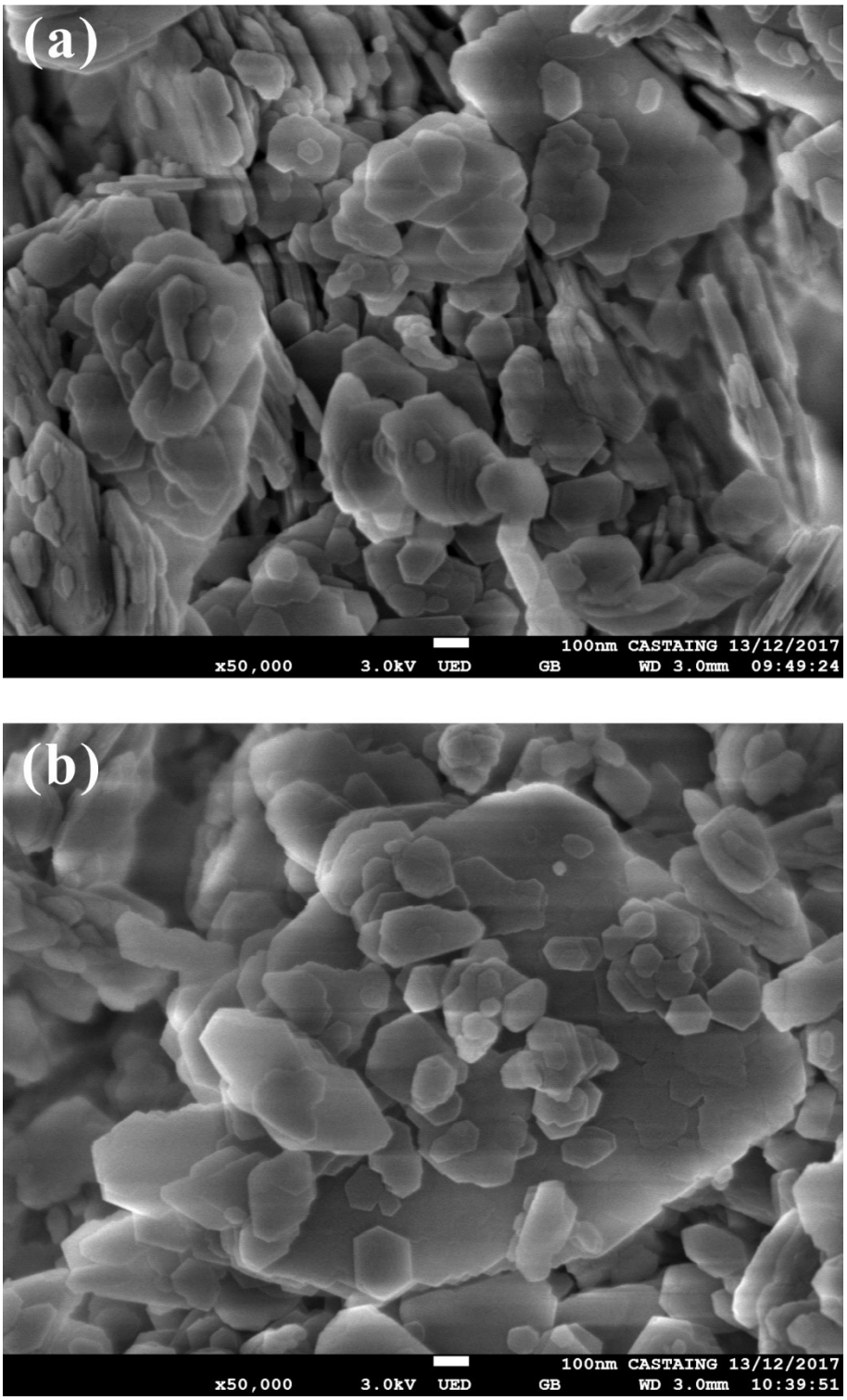

Figure 3.3 SEM images of "fresh" and reacted kaolinite powders recovered from experiment (1) conducted at pH~2.5. (a) "fresh" KGa-2 sample; (b) KGa-2 recovered at the end of experiment (1).

During the experiment (2), [Si] in the solution increased from below the detection limit at the start to 116.5 µmol/kg at the end of experiment (Figure 3.8; Table 3.3). [Al] in the solution shows little variation and remained at low level (~10^{-3} mmol/kg) compared to [Si] (~10^{-2} to ~10^{-3} mmol/kg). A slight increase of [Li] in the solution was observed in the first 6.8 days of experiment from the initial concentration of 26.0 µmol/kg to 26.6 µmol/kg, corresponding to about 2% increase. Afterwards, [Li] gradually decreased. The [Li] was 23.0 µmol/kg at the end of the experiment, representing approximately 10% of Li removal from the solution. A small range of δ^7Li variation in the solution was observed. The δ^7Li composition of the solution between the initial and final stage were close ($\Delta = \delta^7Li_{terminal} - \delta^7Li_{initial} = 0.63‰$). The δ^7Li of the basaltic glass was measured as $\delta^7Li_{BG} = 5.15 \pm 0.09$ ‰ (n=2). Although small fluctuations were observed during the experiment, most solution samples were within 1‰ variation of the initial δ^7Li composition of the solution.

Experiment (3) was conducted on kaolinite with the same aqueous solution as experiment (2): ASW solution at pH~8.4 with an initial Li concentration of 26 µmol/kg (~180 ppb). The silicon concentration in the solution increased during the experiment (Figure 3.9; Table 3.4). At the end of the experiment [Si] reached 28.1 µmol/kg, while [Al] remained almost unchanged, at a very low level (close or under detection limit). [Li] in the solution rapidly decreased during the course of the reaction, attaining a final concentration of 5.5 µmol/kg. About 80% of the Li initially dissolved in the synthetic seawater was removed during the experiment. The [Li] decrease was accompanied by an increase of δ^7Li in the solution. During the first 39 days, δ^7Li increased rapidly ($\Delta = 22.61‰$), and then it increased at a lower rate ($\Delta = 4.79‰$ over the following ~120 days). At the end of the experiment the fluid became highly enriched in ^{7}Li with $\delta^7Li=80.23 \pm 0.21‰$. The δ^7Li composition of the initial kaolinite powder was $-0.38 \pm 0.72‰$ (2σ, n=12). As for the

experiment (2), the solid recovered from the reactor at the end of the experiment was analysed by SEM and EDX spot analyses. The comparison of this sample with its unreacted counterpart did not allow us to observe remarkable differences in terms of morphological characteristics and chemical composition (Figure 3.4).

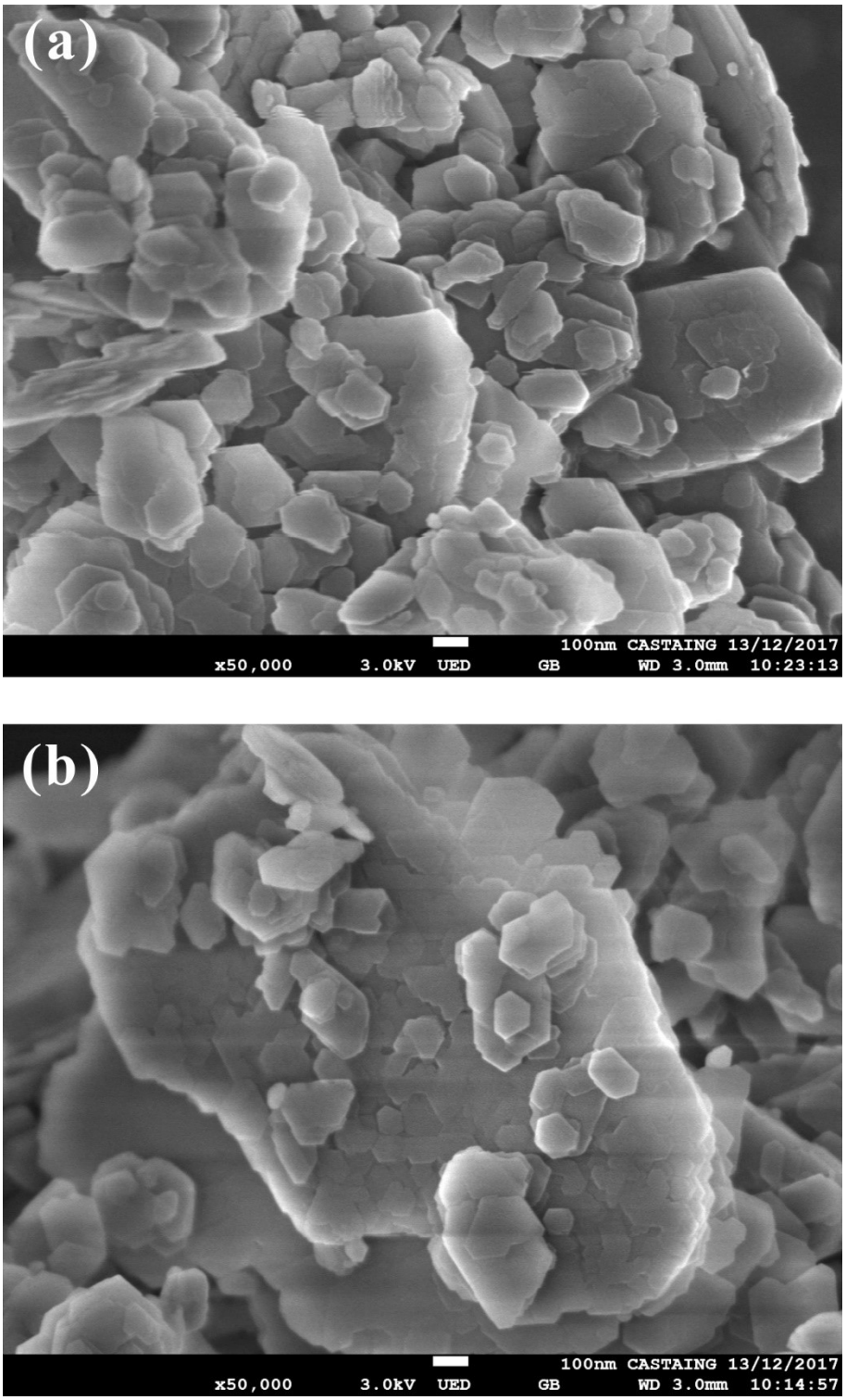

Figure 3.4 SEM images of "fresh" and reacted kaolinite powders recovered from experiment (3) conducted at pH~8.4: (a) "fresh" KGa-2; (b) KGa-2 recovered at the end of experiment (3).

A single peak in the NMR spectra is displayed for all solid samples analyzed after experiment (4) (Fig 3.5). The original kaolinite powder, without any treatments, has a peak centered at δ_{iso}=−0.10 ppm. After the DDI rinsing step, the ^{7}Li peak is slightly shifted to a more negative value (δ_{iso}=−0.17 ppm, δ_{rinse}− δ_{fresh}= −0.07 ppm). After adsorption of Li, these DDI rinsed samples exhibit a distinct inversed shift of the Li peak towards more positive values (δ_{iso}=−0.08 ppm, δ_{ads}− δ_{rinse}= 0.09 ppm).

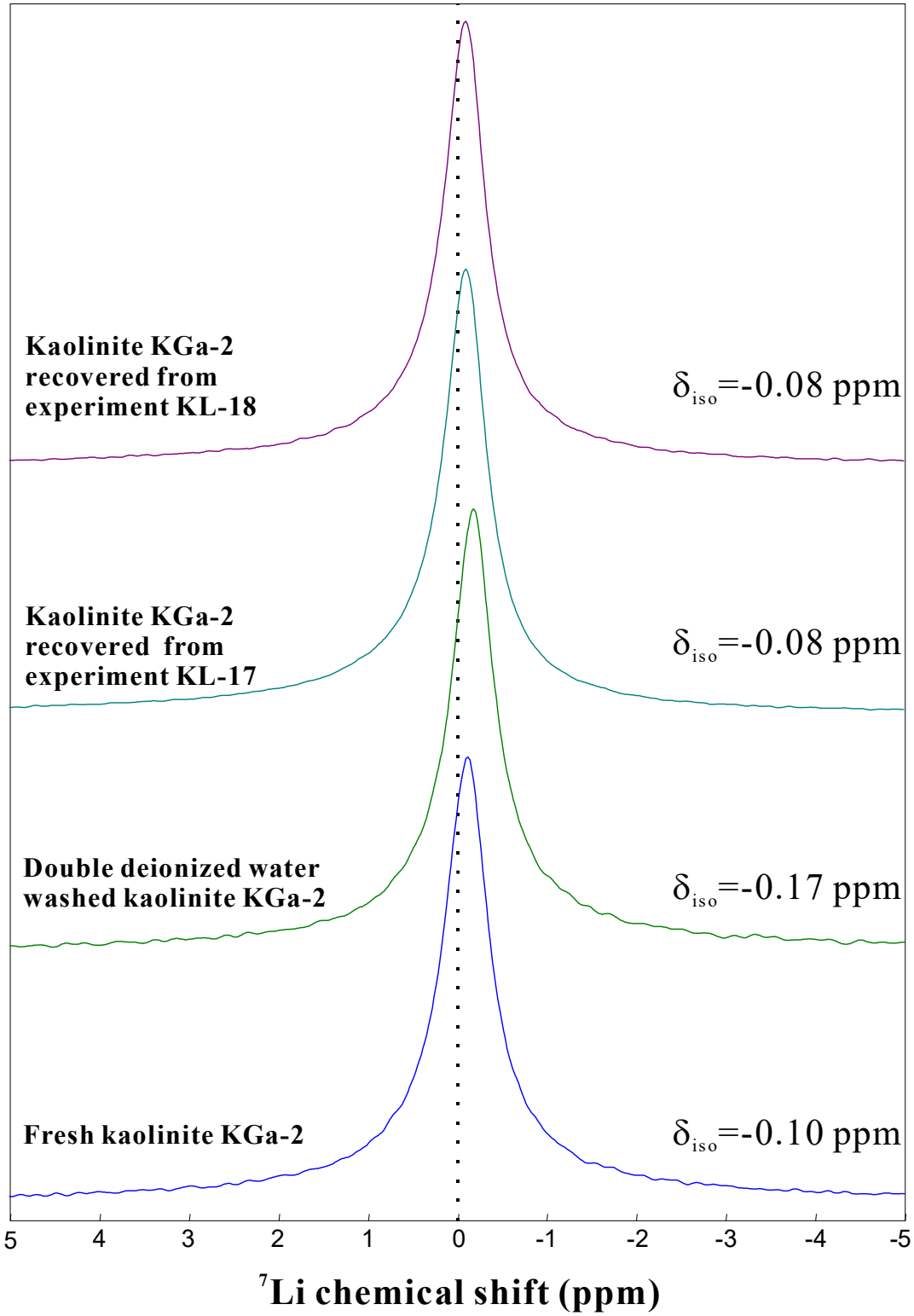

Figure 3.5 ^{7}Li NMR spectra of "fresh" KGa-2, double-deionized water washed KGa-2, and KGa-2 collected after Li-adsorption (exposed to Li-rich fluids) in experiments (4).

As a complement to SEM observations, the calculations of the saturation index of the aqueous solutions with respect to relevant secondary phases were performed using PHREEQC v. 3.3 with its LLNL database. The saturation index (SI) is defined as the logarithm of the saturation ratio Ω, which is the ratio between the ion activity product (IAP) of the aqueous species involved in the dissolution reaction of the solid phase of interest and the solubility product of that phase (K_{sp}): SI = Log Ω = Log (IAP/K_{sp}). The results of these calculations are illustrated in the plot of Figure 3.6 for the experiment (3). The plot shows that the solution is supersaturated (Log Ω > 0) with respect to several Al-bearing phases like aluminum hydroxides (boehmite and gibbsite) and aluminosilicate clay minerals. In particular, the aqueous solution is highly supersaturated (Ω > 10000) with respect to Mg-saponite for most of the duration of the experiment, suggesting the formation of this phase during the reaction.

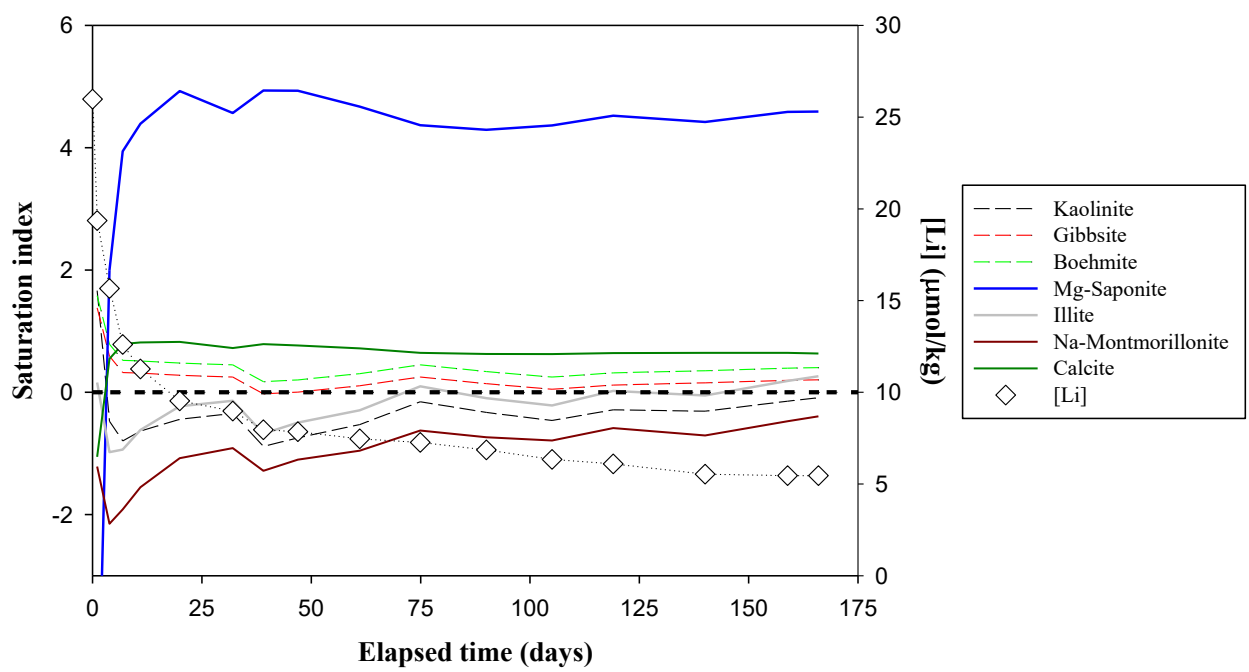

Figure 3.6 Thermodynamic calculation (PHREEQC) of saturation index of the solution of experiment (3) with respect to various phases including gibbsite, boehmite, Mg-saponite, illite, Na-Montmorillonite, and calcite.

3.6 Discussion

3.6.1 Kaolinite dissolution in acidic seawater (experiment (1))

Significant kaolinite dissolution occurred in this experiment as shown by the [Al] and [Si] increases (Figure 3.7). First the dissolution was significant as [Si] reached 364.8 µmol/kg after only 28 days of experiment, which is almost 13 times of the [Si] released in experiment (2) after 166 days. Second, [Al] reached 568.2 µmol/kg in the solution, which is not only significantly greater than in experiments (2) and (3), but even larger than the [Si] in the same solution. The dissolution of kaolinite was also accompanied by a preferential release of [Li] in the solution (Fig 3.7b) compared to the corresponding amount of Al and Si.

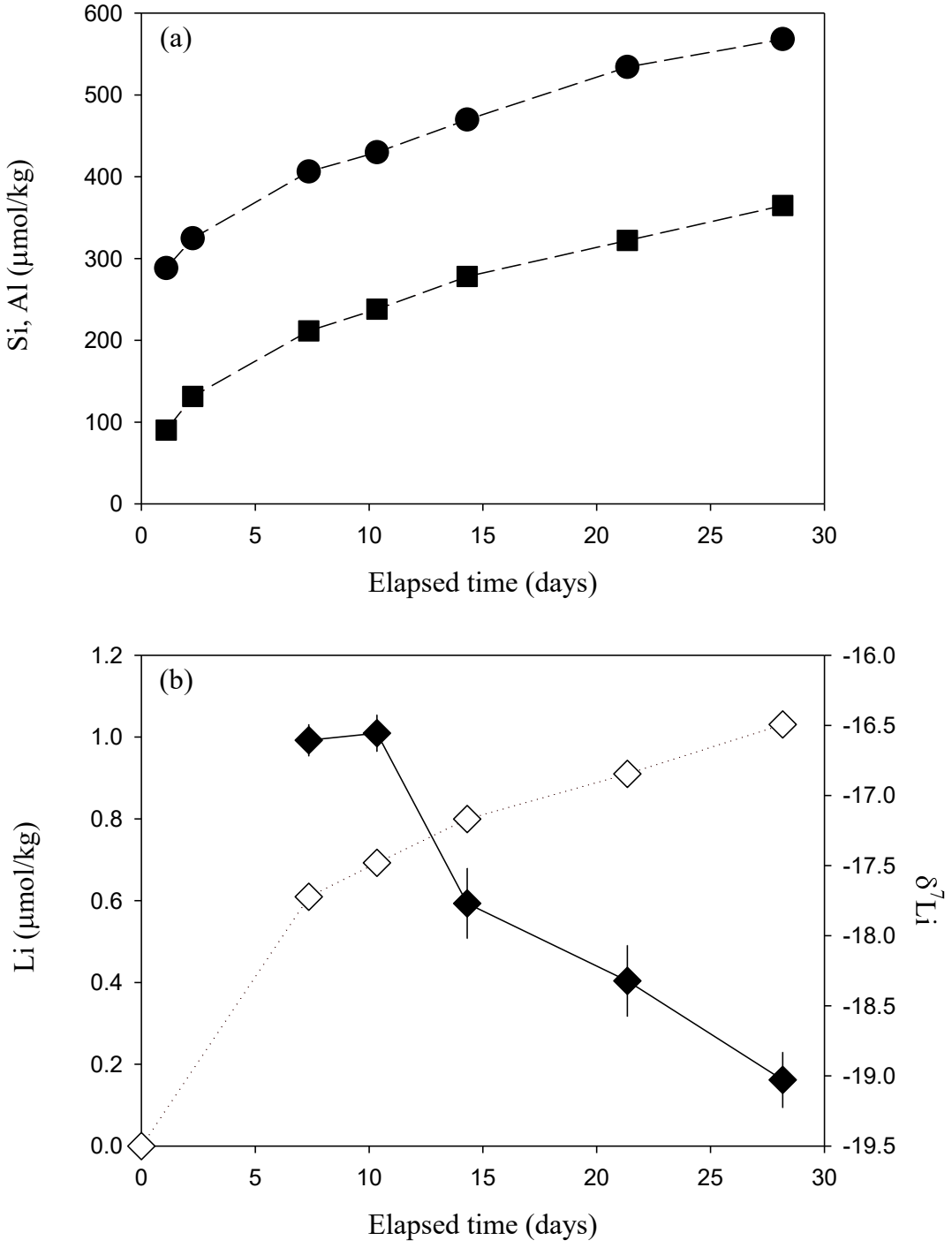

Figure 3.7 Results of experiment (1): kaolinite dissolution in artificial seawater: (a) dissolved Si (represented by squares) and Al (represented by circles) concentrations; (b) dissolved Li concentration (represented by open diamonds) and isotope composition (represented by diamonds, with error bars corresponding to 2 s.d.).

In this experiment, a preferential release of Li over Si is observed (Fig 3.8). According to mass balance calculations, 0.16% of the Li contained in kaolinite is released whereas the released Si corresponds to only 0.11% of the total Si of the solid. A large difference in isotope composition between the solid and the released Li in this experiment was also observed. Although it is commonly thought that mineral dissolution results in little Li isotope fractionation, we observe here that ^{6}Li was preferentially released from solids. The bulk KGa-2 has a δ^{7}Li composition of −0.38‰, while the δ^{7}Li of the first released portion had a value of −16.61‰ and it decreased to −19.03‰ with the progress of experiment.

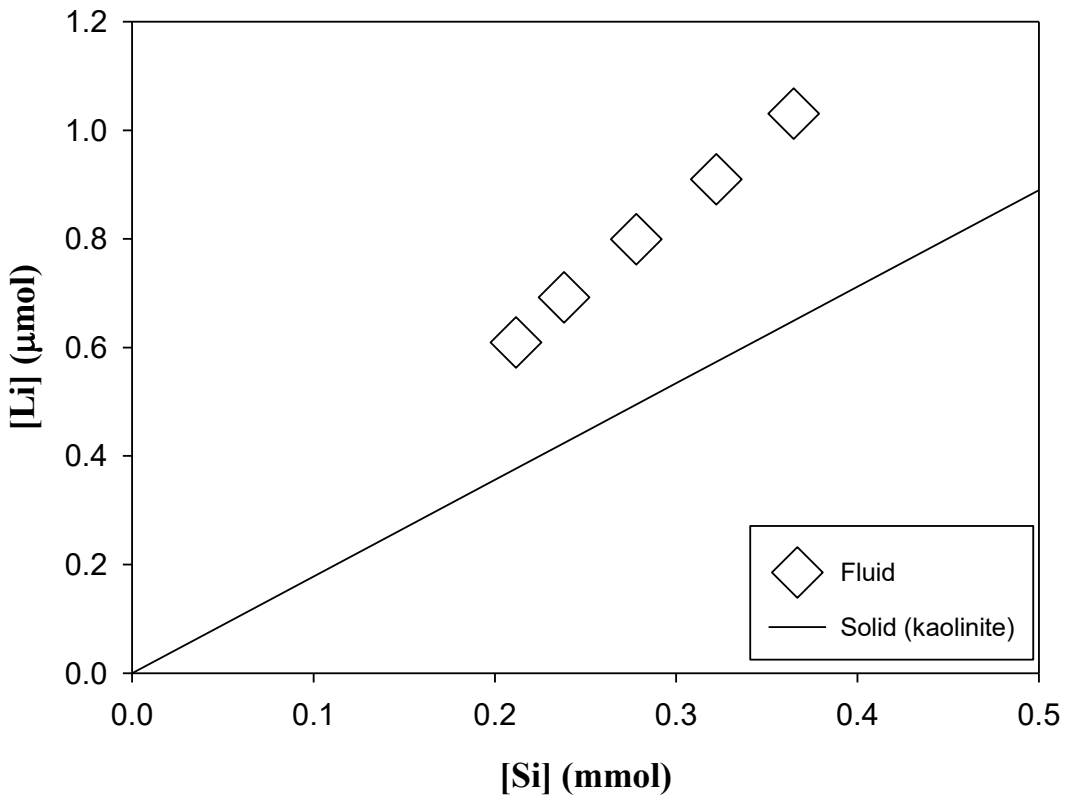

Figure 3.8 Preferential release of Li over Si during the dissolution of kaolinite (KGa-2, $Al_2Si_2O_5(OH)_4$) in acidic seawater (pH~2.7). Diamonds represent the data for Si and Li concentrations in the solution, and the solid line represents the relationship between Si and Li in "fresh" KGa-2.

We can first dismiss the effect of the formation of new phases as this acidic aqueous solution is constantly undersaturated with respect to secondary minerals based on thermodynamic calculations. Hence, the largely negative δ^7Li value in the solution may result from the preferential release of ^{6}Li in solution and/or the preferential release of Li from kaolinite sites where Li is enriched in light isotopes. Our observation agrees with the findings from the study of dissolution of basalt glass by Verney-Carron et al. (2011), where secondary mineral precipitation did not occur, and who witnessed that ^{6}Li was preferentially dissolved into solution during the early stage of basalt glass dissolution. These authors also observed that at later stage of dissolution, δ^7Li in the solution increased back towards the glass δ^7Li composition. This was interpreted as a result of different diffusivity of ^{6}Li and ^{7}Li. At the mineral surface ^{6}Li is preferentially moved to the solution from the solid phase, resulting in a lower δ^7Li in the fluid and a higher δ^7Li in the remaining solid. With ongoing dissolution, the remaining Li in the leached layer would be further dissolved, thus causing an increase of δ^7Li in the solution. If this mechanism is valid for our experiment, with further dissolution of the remaining solid, the δ^7Li in the solution should increase back to the composition of KGa-2.

A second explanation of our observation could be that during the dissolution in the acidic solution Li located at interlayer sites ("exchangeable" Li) is released first. As shown in Figure 3.5, a removal of exchangeable Li by rinsing the KGa-2 powder in DDI led to a small shift (−0.07 ppm) in the ^{7}Li NMR spectra. The dissolution using an acidic solution could also remove a portion of Li on exchangeable sites from the clay. In natural systems, the clays could possibly undergo exchange reactions with cations in ambient solutions (*e.g.* NH_4^+) and essentially favour the light Li in the exchangeable sites (Zhang et al., 1998). Therefore, either a more rapid departure of ^{6}Li from the altered mineral surface or a preferential release of ^{6}Li from exchangeable sites can result in the

low δ^7Li measured in the solution compared to the bulk solid.

Although we have detected a significant fractionation during the early-stage dissolution of kaolinite, we can speculate that such an effect is limited in natural environments as an aqueous environment with pH ~2.7 is rather uncommon, and also because Li isotope release is expected to become stoichiometric for longer water residence times. However, the sudden supply of water to "fresh" kaolinite could potentially imprint a transient, marked ^{6}Li signature of the released Li; this could occur, for example, during rain storms in catchments, where transient incongruent dissolution of soil-hosted kaolinite could result in low-δ^7Li composition of the river outflow over short time scales.

3.6.2 Interaction between basaltic glass and seawater (experiment (2))

Studies on hydrothermal systems show that the Li isotope behavior during basalt-fluid interactions is temperature-dependent. Pioneer studies (Seyfried et al., 1984; Berger et al., 1987, 1988) showed that at low temperatures (below 150°C) Li is leached from basalt and then removed from the solution by the secondary mineral phases, whereas at higher temperatures the dissolution of basalt is controlling the Li content in the fluid and little Li is incorporated by secondary phases. The isotope variations linked to the temperature-dependent behavior of Li during the dissolution of basalt was also observed later in the study of James et al. (2003), which again showed that ^{6}Li is preferentially incorporated into secondary minerals at low temperature. In the marine environment, as seawater has a high δ^7Li value (31‰) and basalts have lower δ^7Li values (usually <10‰), if isotope fractionation during dissolution can be neglected (see above), the dissolution of basalt will lower the δ^7Li of seawater; but as ^{6}Li is preferentially incorporated into secondary phases in the altered basalts, the Li uptake by secondary minerals will increase the δ^7Li in the solution. Therefore, as suggested by Millot et al. (2010), fluid δ^7Li during alteration of the seafloor

is controlled by the relative magnitudes of these two processes.

During silicate weathering, the effect of dissolution on δ^7Li is considered to be small. As shown by Pistiner and Henderson (2003), the partial dissolution of basalts causes no fractionation of δ^7Li while a significant fractionation effect was observed during the partial dissolution of granite ($\Delta=\delta^7Li_{dissolved}-\delta^7Li_{Bulk\text{-}granite}=7.4‰$) which was interpreted as a "mineralogical" effect due to the preferential dissolution of some minerals with heavy δ^7Li compositions such as chlorite and calcite. No fractionation of δ^7Li was observed during the dissolution of basalt by Wimpenny et al. (2010). However, Verney-Carron et al. (2011) shows that ^{6}Li is leached out faster during early-stage dissolution of Li-rich synthetic basalt. In spite of the possibility of δ^7Li fractionation during the early-stage dissolution of silicate minerals, as shown by our experiment (1), field observations suggest that secondary phase formation exerts a dominant control on dissolved δ^7Li during silicate weathering (e.g. Dellinger et al., 2014, 2015), as in low-temperature marine environments.

In our experiment (2), the dissolution of the basalt glass is shown by the increasing [Si] (Fig 3.9a). Basaltic rocks are relatively reactive and can react in the ocean (Pokrovsky and Schott, 2000; Oelkers, 2001; Montserrat et al., 2017). Compared to Si, Al was mostly retained in the solids. In terms of Li, the experimental results are also consistent with the initial effect of basalt dissolution observed in other studies: we first observe an increase of [Li] in the solution in the first 11 days of reaction (Fig 3.9b). Later in the experiment, [Li] decreases, and by the end of the experiment (166 days) a total amount of approximately 10% Li initially present in the solution has been removed. Based on the evidence of Li dissolution at the early stage of the experiment and Li removal at the later stage of the experiment, we could argue that secondary mineral phases produced and took up Li from the solution. At the same time, the δ^7Li fluctuated throughout the experiment, and the overall δ^7Li fluctuation in the fluid is relatively small compared to previous studies on basalt

dissolution. We obtain an average value of 52.99 ± 1.27 ‰ (2σ) for all measured samples in this experiment (Fig 3.9b). This small δ^7Li variation could be explained by the fact that the water/rock ratio in this experiment was high (~790), hence less "interaction sites" were available and the fractionation effect induced during the experiment was weaker than in the studies at lower water/rock ratios such as experiment (3).

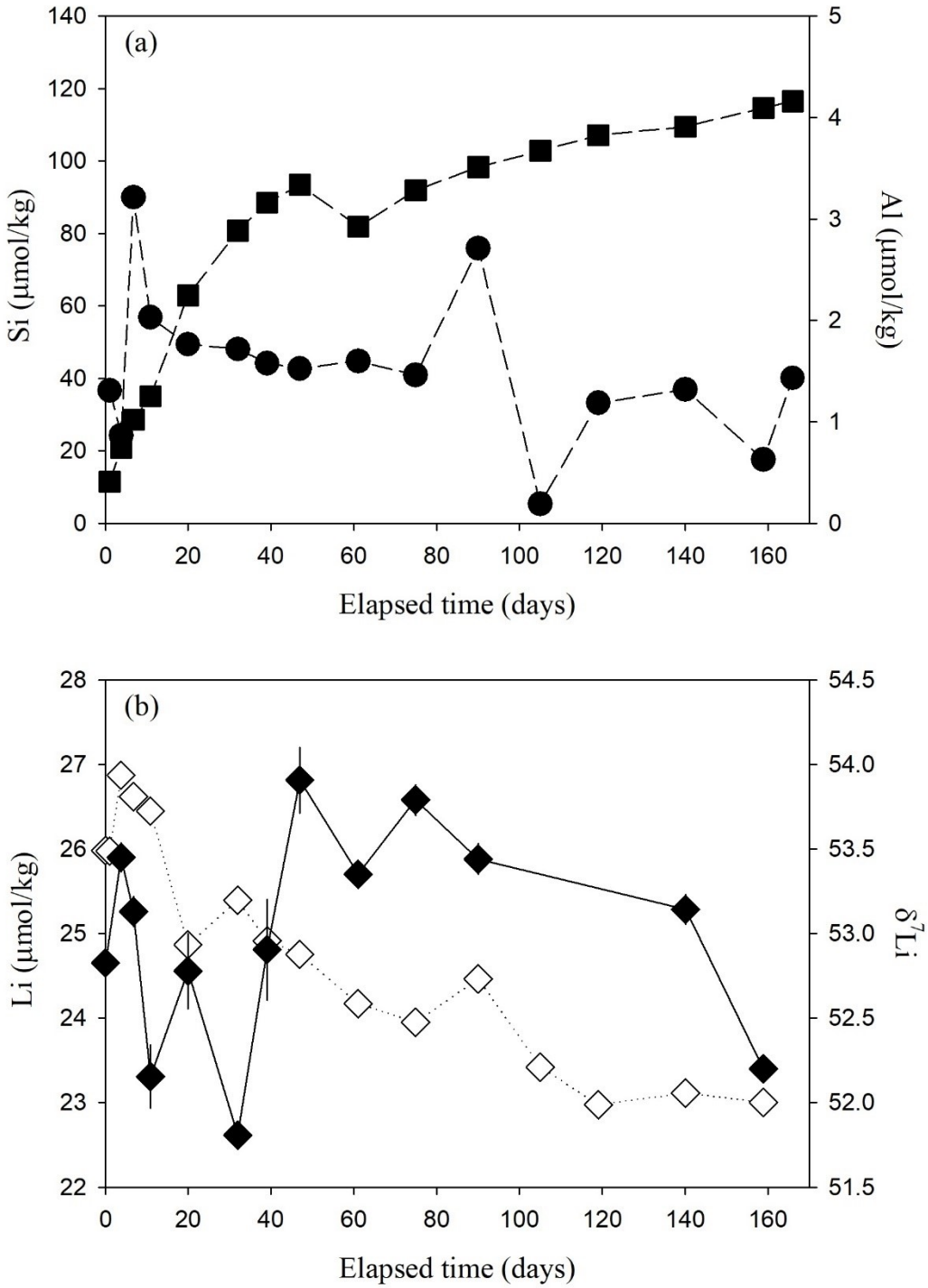

Figure 3.9 Results of experiment (b): basalt glass interaction with artificial seawater: (a) dissolved Si (represented by squares) and Al (represented by circles) concentrations; (b) dissolved Li concentration (represented by open diamonds) and isotope composition (represented by diamonds, with error bars corresponding to 2 s.d.).

3.6.3 Interaction between kaolinite and seawater (experiment (3))

Only few studies have investigated the Li isotope behaviour during rock-fluid interaction using detrital sediments or (natural or synthetic) secondary minerals (Chan et al., 1994; Zhang et al., 1998; You and Gieskes, 2001; Pistiner and Henderson, 2003; James et al., 2003; Vigier et al., 2008; Wimpenny et al., 2015). Consistent with findings on the alteration of seafloor, Li behavior during the alteration of sediments is temperature-dependent with more efficient Li uptake at lower temperatures and more efficient Li dissolution at higher temperatures. The accompanying isotope fractionation during the alteration of sediments favors the presence of ^{7}Li in the fluid at low temperatures (Chan et al., 1994; You and Gieskes, 2001; James et al., 2003). The change in δ^{7}Li in the fluid at low temperature can be explained by the preferential uptake of ^{6}Li by secondary phases, especially clay minerals, from the fluid (Zhang et al., 1998; Pistiner and Henderson, 2003; Vigier et al., 2008; Wimpenny et al., 2015). The Li incorporated into clays could be physically located at exchangeable sites or chemically bonded into the structural sites. This incorporation in structural sites is assumed to be the one causing the enrichment of ^{6}Li in the solid, as a significant fractionation of Li between the solution and exchangeable sites was not observed in literature (e.g. Vigier et al., 2008; Wimpenny et al., 2015). Zhang et al. (1998) performed experiments similar to this study to determine the effect of Li adsorption using kaolinite, vermiculite, and Mississippi river sediment reacting with the surface water from the Gulf of Mexico. This study showed that kaolinite has the greatest capacity to remove Li from seawater (after ~200 days 43% of Li was removed) compared to vermiculite (34%) and Mississippi river sediments (23%), resulting in δ^{7}Li increase in the solution by 10‰ (kaolinite), 13‰ (vermiculite), and 6‰ (Mississippi sediments).

As for the experiment (2), we also observe in the experiment (3) the dissolution of kaolinite through the increasing [Si] through time. The formation of authigenic clays in marine

environments requires a supply of Al. The dissolution of detrital clays such as illite or kaolinite could possibly be a source of Al (Mackin, 1989; Moran and Moore, 1991). In the experiment (3), we have not observed any significant release of Al from the kaolinite, which shows that released Al was rapidly consumed by the neo-formed secondary mineral phases. Note that Michalopoulos and Aller, (1995) stated that at certain environments such as the Amazon delta, Al used for reverse weathering can be supplied by the dissolution of amorphous unstable Al oxides, whereas the Si source is limited. Little evidence for the formation of secondary phases has been found from the SEM observations (Fig 3.4), whereas the thermodynamic calculations (Fig 3.6) showed that secondary phases could be produced during the experiment, in particular saponite and calcite.

As shown in Figure 3.10, we observe significant removal of Li (~80%) from the initial solution, accompanied by a strong enrichment of ^{7}Li in fluid (~25 ‰ change in dissolved δ^{7}Li). This is in agreement with previously published results (Zhang et al., 1998; Millot and Girard, 2007; Vigier et al., 2008) that clays preferentially incorporate light Li isotopes. Two mechanisms could explain the observed Li uptake and isotopic fractionation. They could be due to (1) the adsorption of Li at kaolinite edge sites eventually followed by its incorporation in octahedral sites and (2) Li incorporation in newly formed secondary phases such as saponites.

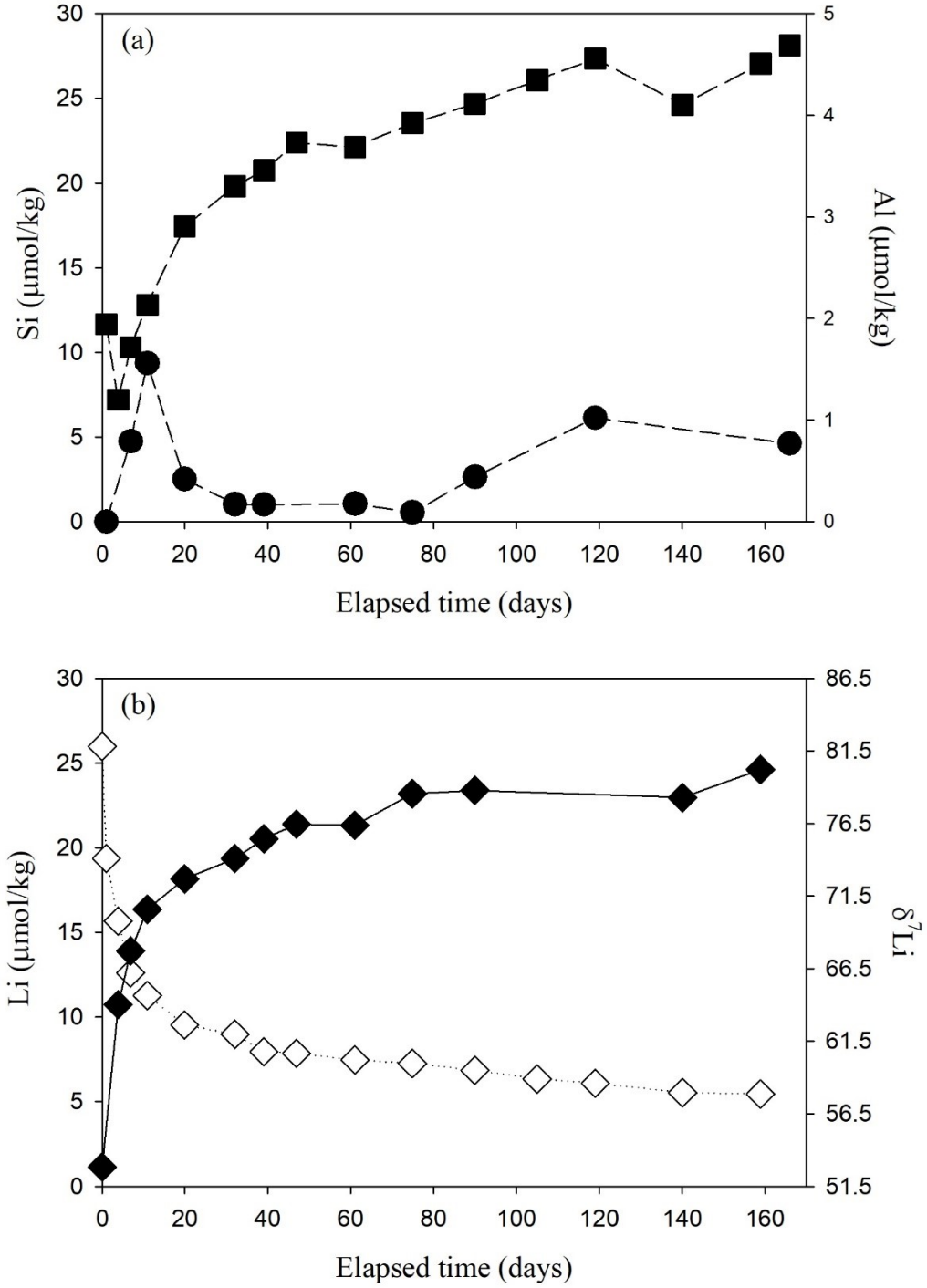

Figure 3.10 Results of experiment (3): kaolinite interaction with artificial seawater at 25°C and pH 8.3: (a): dissolved Si (filled squares) and Al (filled circles) concentrations; (b): dissolved Li concentration (filled diamonds) and isotope composition (empty diamonds) with error bars corresponding to 2 s.d..

Regardless of the process controlling the Li isotopic fractionation, Li aqueous isotopic composition can be described by (a) Rayleigh fractionation mass balance in which Li adsorbed at the solid surface or incorporated in the precipitating solid is isolated from isotopic exchange with the solution immediately upon the adsorption/precipitation or (b) a "closed system" mass balance, in which Li adsorbed to or incorporated in the solids remains available to isotopic exchange during the all reaction. Depending on the mass balance, the Li isotope composition of the remaining solution can be expressed as:

(a) Rayleigh fractionation: $\delta^7Li_t = \delta^7Li_i - 1000\times\ln\alpha\times F$ (Equation 3-2)

(b) Closed system equilibrium: $\delta^7Li_t = \delta^7Li_i + 1000\times\ln\alpha\times\ln(1-F)$ (Equation 3-3)

where δ^7Li_i and δ^7Li_t are the initial isotopic composition of the solution and the composition at time t, respectively t; α is the fractionation factor between the solid and the solution; and F stands for the fraction of Li removed from the solution. Examining our results, two possible scenarios could take place. In the first scenario, as shown in Figure 3.11a, a closed-system mass balance model with a fractionation factor of 0.968 ($\Delta^7Li_{sol\text{-}fluid} = -32‰$) can reasonably explain the whole experiment. The second scenario consists of two stages (Fig 3.11b). At the early stage the removal of Li follows a Rayleigh fractionation mass balance with a fractionation factor of 0.979 ($\Delta^7Li_{sol\text{-}fluid} = -21‰$), indicating that Li is irreversibly removed from the solution. The rest of the experiment may be explained using the closed-system mass balance with a fractionation factor of 0.981 ($\Delta^7Li_{sol\text{-}fluid} = -19‰$). The two steps (Rayleigh + closed-system) scenario seems the most plausible because 1) it yields very similar Li isotope fractionation factors for the Rayleigh and closed-system steps, equal to 0.979 and 0.981, respectively; 2) the inferred α value is in good agreement with the values reported for Li sorption onto kaolinite and vermiculite by Zhang et al. (1998) and for Li co-precipitation with smectite by Vigier et al. (2008) (see Table 3.7); and 3) the

fractionation yielded by the first scenario (only closed-system mass balance) is much larger (α = 0.968; $\Delta^7Li_{sol\text{-}fluid}$ = −32‰) than any yet-reported isotope fractionation factor for Li. Note also that the very fast kinetics of Li removal from the solution observed during the first 10 days of reaction prevents isotopic equilibrium from being achieved between the solution and the scavenged Li, consistent with a Rayleigh mass balance. In contrast the much slower kinetics of Li removal after 10 days should allow for attaining isotopic equilibrium between aqueous Li and adsorbed/co-precipitated Li.

Table 3.7 Reported Li isotope fractionation factor (α) from experimental studies

Mineral	α	Temperature (°C)	Solution	Reference
smectite	0.99 0.989	90 25	LiCl	Vigier et al. (2008)
smectite gibbsite	1 0.986	22 22	L-SVEC	Pistiner and Henderson (2003) (2003)(2003)
calcite aragonite	0.997 0.989	25 25	ASW	Marriott et al. (2004)
zeolite	0.978	25	LiCl	Taylor and Urey (1938)
basalt	0.981	25	diluted seawater	Millot et al. (2010)
kaolinite vermiculite	0.979 0.972	25	seawater	Zhang et al. (1998)
kaolinite	0.979-0.981	25	ASW	This study

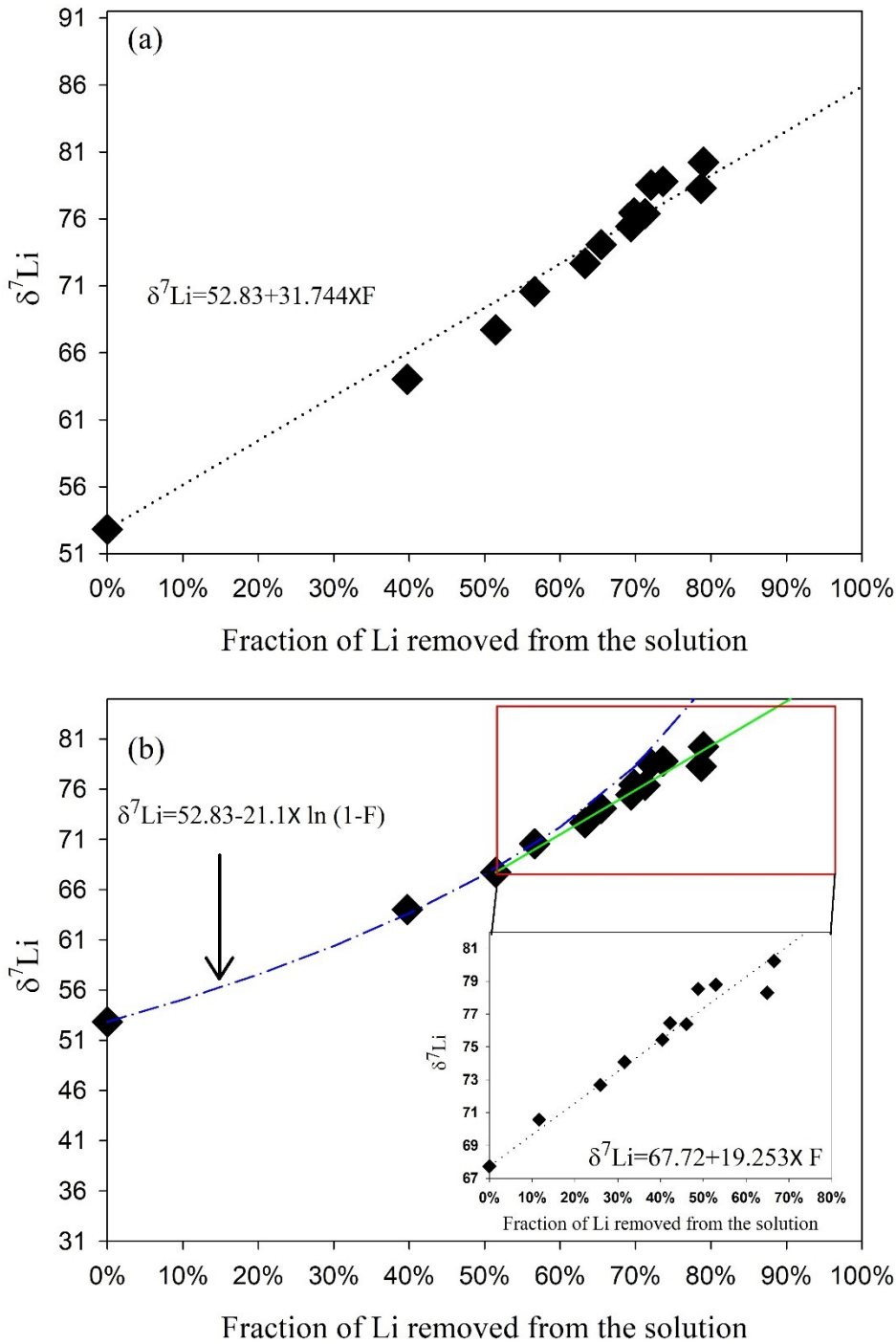

Figure 3.11 Two scenarios explaining the observed Li isotope fractionation in experiment (4): (a) a closed system mass balance in which Li removed from the solution is allowed to further equilibrate with the remaining dissolved Li; (b) a two-step scenario where a Rayleigh mass balance step at early stage is followed by a closed system mass balance at the later stage.

The results of our experiment on the interaction of KGa-2 kaolinite with seawater at pH=8.4 suggest that the detrital sediments transported to the ocean by rivers may have a significant impact on the Li chemical and isotopic composition in the ocean. This is shown by the following simple mass balance calculation. With a total flux of suspended matter transported annually by the world rivers to the ocean of 19 Gt (Milliman and Farnsworth, 2013) and assuming that 1% (which we believe to be a conservative estimate for the global kaolinite content of the continental detrital flux to the oceans) of this flux is composed of clay minerals exhibiting a Li partition coefficient similar to that measured in this study, K_{Li}=89 (Table 3.6), the amount of aqueous Li which can be removed from the ocean through adsorption onto this terrestrial solids is equal to 4.62×10^{8} moles. In comparison the annual flux of dissolved Li brought to the ocean by rivers is equal to 10×10^{9} moles (Huh et al., 1998; Gaillardet et al., 2003; Misra and Froelich, 2012). The impact of Li scavenging by river suspended matter on the ocean Li isotopic composition could be approximated from:

$$\delta^7\mathrm{Li(sw)}_{\mathrm{initial}} = f\times\delta^7\mathrm{Li(sw)}_{\mathrm{scav}} + (1-f)\times\delta^7\mathrm{Li(sw)}_{\mathrm{end}} \quad \text{(Equation 3-4)}$$

where $\delta^7\mathrm{Li(sw)}_{\mathrm{initial}}$ and $\delta^7\mathrm{Li(sw)}_{\mathrm{end}}$ stand for seawater Li isotopic composition before and after Li scavenging by clay minerals, respectively, and f and $\delta^7\mathrm{Li(sw)}_{\mathrm{scav}}$ represents the Li fraction and Li isotope composition of seawater Li scavenged by clay minerals, respectively. With a mass of the ocean of 1.359×10^{21} kg, the total amount of Li in seawater Li is equal to 3.53×10^{16} moles, an annual flux of Li removed from the ocean by suspended matter equal to 4.62×10^{8} moles (hence f=1.3×10^{-8}) and $\Delta^7\mathrm{Li}_{\mathrm{kaol\text{-}sw}}\sim-20$‰, it is found that the Li isotopic composition of the ocean could be enriched by this process by about 2.6‰ per 10 Myr. In comparison, Froelich and Mistra (2014) reported that the present seawater Li isotopic composition is about 9‰ heavier that during the late Paleocene (-60 Ma). The effect caused by detrital clays on seawater δ^7Li is of the same magnitude

as their observation, showing that the effect of the interaction between detrital clay and seawater Li on the seawater Li isotope composition cannot be neglected at geological times scales (Li and West, 2014).

More generally, in their study of the seawater δ^7Li evolution from Cenozoic, Misra and Froelich (2012) the suggested changes in riverine δ^7Li, due to variations in the style of continental weathering, as the main contributor to the elevation of δ^7Li in seawater. Our results support additional effects caused by the variation in detrital sediment supply, as proposed by Li and West (2014). We note that a co-variation exists between the seawater δ^7Li (Misra and Froelich, 2012) and the sea-level (Miller et al., 2005) evolution over the Cenozoic (Fig 3.12). From this observation, we can propose a new hypothesis to explain the Cenozoic seawater δ^7Li curve. The falling of the global sea-level over the Cenozoic (Haq et al., 1987; Miller et al., 2005) might have exposed a fraction of previously flooded areas. Examples of these events are represented by the closure of Tethyan seaway in Europe and the Western Interior seaway in North America. As a result, newly exposed areas could have been important sites for continental weathering and for the Li isotope signal delivered to the ocean. In general, such areas can provide new sites for continental weathering (hence soil formation) and potentially for floodplain development (Fig 3.13). Under these circumstances, secondary mineral formation could be enhanced as the residence time of continental weathering is prolonged. This would have led to an elevated δ^7Li of the global riverine dissolved load (Dellinger et al., 2015; Pogge von Strandmann and Henderson, 2015); additionally, the fraction of clays in the sediments load transported to the ocean should have increased as well, as the increased residence time of solid matter on the continents would allow for the maturation of secondary minerals (to be more kaolinite like). Therefore, the increased delivery of detrital clays to the ocean could then significantly lead to Li incorporation into authigenic clays, and further

modify the δ^7Li of seawater. Although our hypothesis is highly speculative, the impact of detrital clay input on the evolution of seawater δ^7Li should not be neglected.

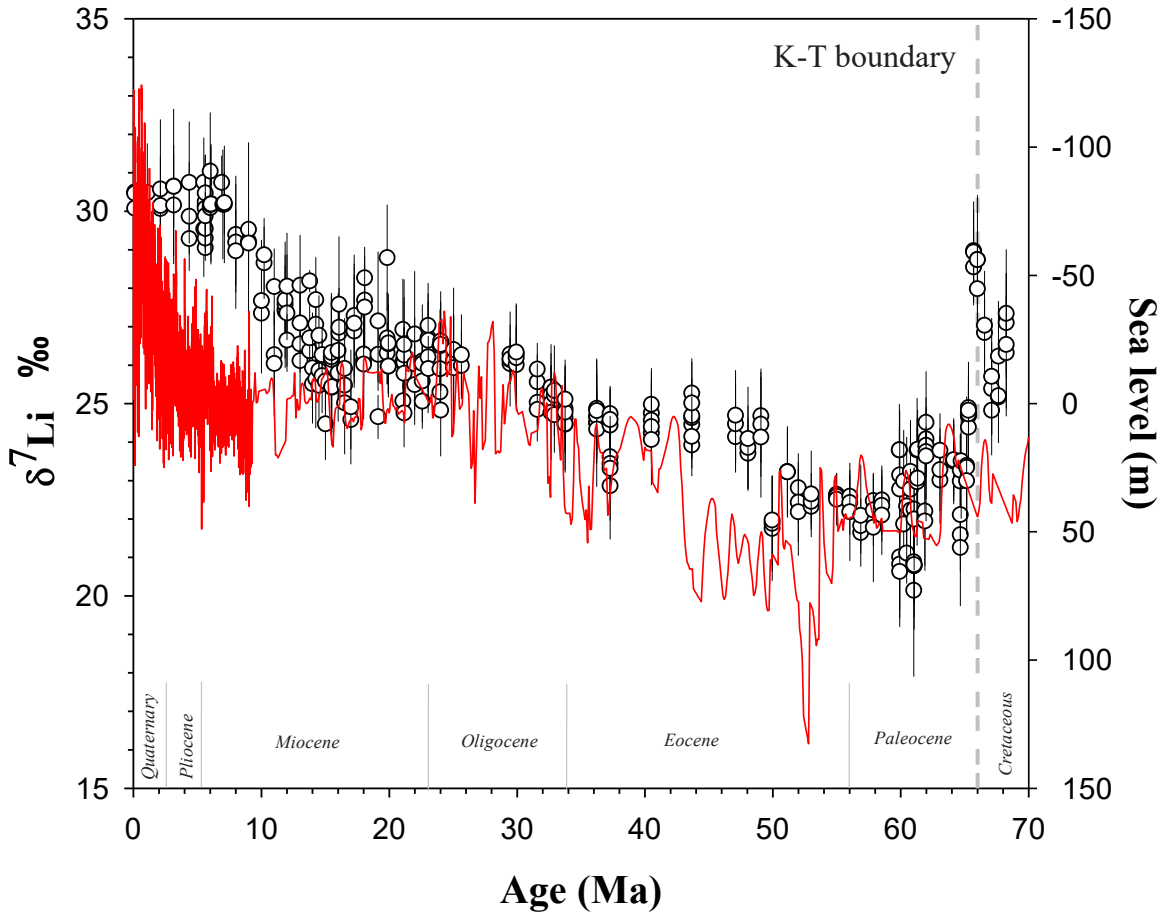

Figure 3.12 Evolution of seawater δ^7Li and sea-level from the late-Cretaceous to present-day.

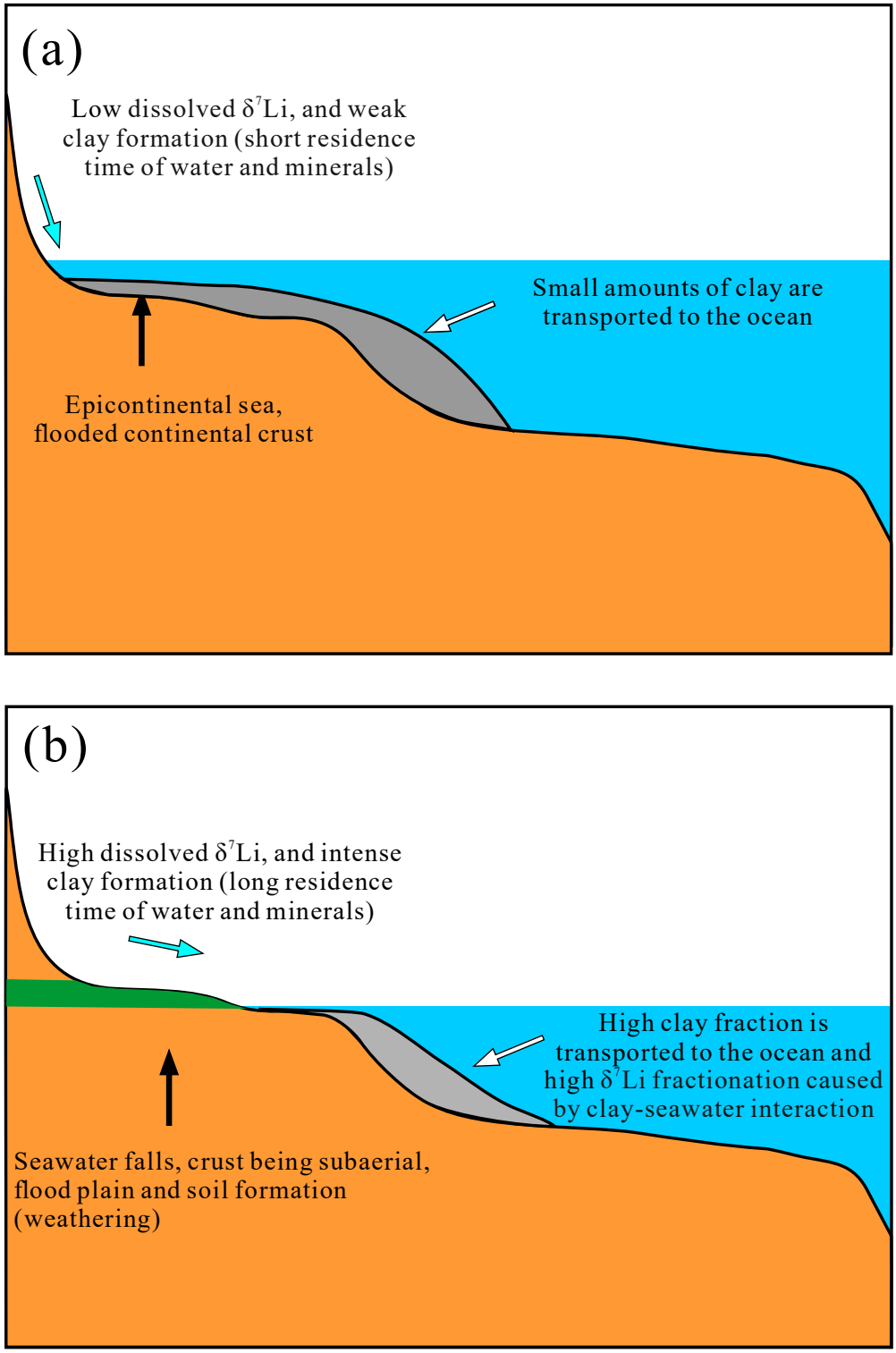

Figure 3.13 Schematic for the impact of the variation of sea-level on the seawater δ^7Li: (a) when sea-level is high, the δ^7Li of continental dissolved inputs and the extent of clay-seawater interaction is low; (b) when sea-level is low, the δ^7Li of continental dissolved inputs and the extent of clay-seawater interaction is high.

3.7 Conclusion

The experiments carried out in this study on the interaction of kaolinite with seawater provide preliminary information on Li isotope fractionation induced by clay mineral-seawater interactions. The dissolution of kaolinite in Li-free seawater in acidic conditions shows a strong preferential release of light Li isotopes with $\Delta^7Li_{fluid\text{-}kaol}$ ~19‰. This likely reflects the preferential breaking of ^{6}Li-O bonds over ^{7}Li-O bonds in kaolinite octahedral sites. However, the presence in kaolinite of Li in different sites with different isotopic composition may contribute to this unexpected very strong isotopic composition. This result suggests that far-from equilibrium kaolinite (and more generally clays)/fluid interactions, for example during flood events in catchments, may imprint a strong and transient ^{6}Li signature in river waters.

Kaolinite dissolution in seawater at pH 8.3 results in a strong increase of ca. 25‰ of seawater δ^7Li. This fractionation, induced by Li sorption on kaolinite and the formation of secondary clays such as Mg-saponites, can be described by a Rayleigh fractionation model at the early stage of the experiment (and fast scavenging of Li from solution) followed by a closed-system behaviour during the later stage of reaction (and slow removal of Li from the solution). Our data are consistent with a fractionation between the solid and the solution equal to ~ −20‰.

The results of this study suggest that clays alone have the ability to remove Li from seawater and to raise the δ^7Li composition of oceans. These clays can be produced at various locations including hydrothermal alteration of seafloors, authigenic formation, and continental weathering products transported by the rivers into the ocean. In lower temperature environments such as estuary and continental margins, with the ability of clays to remove Li during "reverse weathering"-type processes, the presence of clays produced by weathering on lands can possibly be a key in regulating the Li ocean cycle. Therefore, regarding the seawater δ^7Li evolution at

geological time scales, it is important to consider the variations on the global clay production. A key parameter is the residence time of the solid particles during continental weathering, and hence any effect that could change particles residence time, such as mean sea-level fluctuations, should be taken into account for reconstrucing the long-term evolution of seawater δ^7Li.

Bibliography

Aller, R.C., 2014. 8.11 - Sedimentary Diagenesis, Depositional Environments, and Benthic Fluxes. In: Holland, H.D. and Turekian, K.K., (Eds.). Treatise on Geochemistry (Second Edition). Elsevier, Oxford.

Berger, G., Schott, J., Loubet, M., 1987. Fundamental processes controlling the first stage of alteration of a basalt glass by seawater: an experimental study between 200 and 320 C. Earth and Planetary Science Letters 84 (4), 431-445.

Berger, G., Schott, J., Guy, C., 1988. Behavior of Li, Rb and Cs during basalt glass and olivine dissolution and chlorite, smectite and zeolite precipitation from seawater: experimental investigations and modelization between 50 and 300 C. Chemical Geology 71 (4), 297-312.

Chan, L., Gieskes, J.M., You, C., Edmond, J.M., 1994. Lithium isotope geochemistry of sediments and hydrothermal fluids of the Guaymas Basin, Gulf of California. Geochimica et Cosmochimica Acta 58 (20), 4443-4454.

Dellinger, M., Gaillardet, J., Bouchez, J., Calmels, D., Galy, V., Hilton, R.G., Louvat, P., France-Lanord, C., 2014. Lithium isotopes in large rivers reveal the cannibalistic nature of modern continental weathering and erosion. Earth and Planetary Science Letters 401, 359-372.

Dellinger, M., Gaillardet, J., Bouchez, J., Calmels, D., Louvat, P., Dosseto, A., Gorge, C., Alanoca, L., Maurice, L., 2015. Riverine Li isotope fractionation in the Amazon River basin controlled by the weathering regimes. Geochimica et Cosmochimica Acta 164, 71-93.

Dunlea, A.G., Murray, R.W., Ramos, D.P.S., Higgins, J.A., 2017. Cenozoic global cooling and increased seawater Mg/Ca via reduced reverse weathering. Nature Communications 8 (1), 844.

Gaillardet, J., Viers, J., Dupré, B., 2003. Trace elements in river waters. Treatise on geochemistry 5, 605.

Hall, J.M., Chan, L.H, McDonough, W.F., Turekian, K.K., 2005. Determination of the lithium isotopic composition of planktic foraminifera and its application as a paleo-seawater proxy. Marine Geology, 217(3-4), 255-265.

Haq, B.U., Hardenbol, J., Vail, P.R., 1987. Chronology of fluctuating sea levels since the triassic. Science (New York, N.Y.) 235 (4793), 1156-1167.

Huh, Y., Chan, L., Zhang, L., Edmond, J.M., 1998. Lithium and its isotopes in major world rivers: implications for weathering and the oceanic budget. Geochimica et Cosmochimica Acta 62 (12), 2039-2051.

James, R.H., Allen, D.E., Seyfried, W., 2003. An experimental study of alteration of oceanic crust and terrigenous sediments at moderate temperatures (51 to 350 C): Insights as to chemical processes in near-shore ridge-flank hydrothermal systems. Geochimica et Cosmochimica Acta 67 (4), 681-691.

Kester, D.R., Duedall, I.W., Connors, D.N., Pytkowicz, R.M., 1967. Preparation of artificial seawater. Limnology and Oceanography 12 (1), 176-179.

Li, G., West, A.J., 2014. Evolution of Cenozoic seawater lithium isotopes: Coupling of global denudation regime and shifting seawater sinks. Earth and Planetary Science Letters 401, 284-293.

Mackenzie, F.T., Kump, L.R., 1995. Reverse weathering, clay mineral formation, and oceanic element cycles. Science 270 (5236), 586.

Mackenzie, F.T., Garrels, R.M., 1966. Chemical mass balance between rivers and oceans. American Journal of Science 264 (7), 507-525.

Mackin, J., 1989. The nearshore marine and estuarine chemistry of dissolved aluminum and rapid authigenic mineral precipitation. Rev Aquat Sci 1, 537-554.

Magna, T., Wiechert, U., Halliday, A.N., 2006. New constraints on the lithium isotope compositions of the Moon and terrestrial planets. Earth and Planetary Science Letters, 243 (3-4), 336-353

Marriott, C.S., Henderson, G.M., Crompton, R., Staubwasser, M., Shaw, S., 2004. Effect of mineralogy, salinity, and temperature on Li/Ca and Li isotope composition of calcium carbonate. Chemical Geology 212 (1-2), 5-15.

Michalopoulos, P., Aller, R.C., 2004. Early diagenesis of biogenic silica in the Amazon delta: alteration, authigenic clay formation, and storage. Geochimica et Cosmochimica Acta 68 (5), 1061-1085.

Michalopoulos, P., Aller, R.C., 1995. Rapid clay mineral formation in Amazon delta sediments: reverse weathering and oceanic elemental cycles. Science, 270 (5236), 614-617.

Miller, K.G., Kominz, M.A., Browning, J.V., Wright, J.D., Mountain, G.S., Katz, M.E., Sugarman, P.J., Cramer, B.S., Christie-Blick, N., Pekar, S.F., 2005. The Phanerozoic record of global sea-level change. Science (New York, N.Y.) 310 (5752), 1293-1298.

Milliman, J.D., Farnsworth, K.L., 2013. River Discharge to the Coastal Ocean: A Global Synthesis. Cambridge University Press.

Millot, R. and Girard, J.P., 2007. Lithium isotope fractionation during adsorption onto mineral surfaces. In International Meeting on Clays in Natural & Engineered Barriers for Radioactive Waste Confinement, Lille, France.

Millot, R., Scaillet, B., Sanjuan, B., 2010. Lithium isotopes in island arc geothermal systems: Guadeloupe, Martinique (French West Indies) and experimental approach. Geochimica et Cosmochimica Acta 74 (6), 1852-1871.

Misra, S., Froelich, P.N., 2012. Lithium Isotope History of Cenozoic Seawater: Changes in Silicate Weathering and Reverse Weathering. Science 335 (6070), 818-823.

Montserrat, F., Renforth, P., Hartmann, J., Leermakers, M., Knops, P., Meysman, F.J.R., 2017. Olivine Dissolution in Seawater: Implications for CO(2) Sequestration through Enhanced Weathering in Coastal Environments. Environmental science & technology 51 (7), 3960-3972.

Moran, S.B., Moore, R.M., 1991. The potential source of dissolved aluminum from resuspended sediments to the North Atlantic Deep Water. Geochimica et Cosmochimica Acta, 55(10), 2745-2751.

Moriguti, T., Nakamura, E., 1998. High-yield lithium separation and the precise isotopic analysis for natural rock and aqueous samples. Chemical Geology, 145(1-2), 91-104.

Oelkers, E.H., Gislason, S.R., 2001. The mechanism, rates and consequences of basaltic glass dissolution: I. An experimental study of the dissolution rates of basaltic glass as a function of aqueous Al, Si and oxalic acid concentration at 25 C and pH= 3 and 11. Geochimica et Cosmochimica Acta 65 (21), 3671-3681.

Oelkers, E.H., 2001. An experimental study of forsterite dissolution rates as a function of temperature and aqueous Mg and Si concentrations. Chemical Geology, 175(3-4), 485-494.

Parkhurst, D.L., Appelo, C., 2013. Description of input and examples for PHREEQC version 3--A computer program for speciation, batch-reaction, one-dimensional transport, and inverse geochemical calculations. US Geological Survey.

Pistiner, J.S., Henderson, G.M., 2003. Lithium-isotope fractionation during continental weathering processes. Earth and Planetary Science Letters 214 (1), 327-339.

Pogge von Strandmann, Philip AE, Henderson, G.M., 2015. The Li isotope response to mountain uplift. Geology 43 (1), 67-70.

Pokrovsky, O.S. and Schott, J., 2000. Kinetics and mechanism of forsterite dissolution at 25 C and pH from 1 to 12. Geochimica et Cosmochimica Acta, 64(19), 3313-3325.

Rahman, S., Aller, R., Cochran, J., 2016. Cosmogenic 32Si as a tracer of biogenic silica burial and diagenesis: Major deltaic sinks in the silica cycle. Geophysical Research Letters 43 (13), 7124-7132.

Ramos, D.P.S., Morgan, L.E., Lloyd, N.S., Higgins, J.A., 2018. Reverse weathering in marine sediments and the geochemical cycle of potassium in seawater: Insights from the K isotopic composition (41K/39K) of deep-sea pore-fluids. Geochimica et Cosmochimica Acta .

Schroth, B.K., Sposito, G., 1997. Surface charge properties of kaolinite. Clays and Clay Minerals 45 (1), 85-91.

Seyfried, W., Janecky, D., Mottl, M., 1984. Alteration of the oceanic crust: implications for geochemical cycles of lithium and boron. Geochimica et Cosmochimica Acta 48 (3), 557-569.

Sillen, L.G., 1967. The ocean as a chemical system. Science (New York, N.Y.) 156 (3779), 1189-1197.

Taylor, T.I., Urey, H.C., 1938. Fractionation of the lithium and potassium isotopes by chemical exchange with zeolites. The Journal of chemical physics 6 (8), 429-438.

Teng, F., McDonough, W.F., Rudnick, R., Dalpé, C., Tomascak, P., Chappell, B.W., Gao, S., 2004. Lithium isotopic composition and concentration of the upper continental crust. Geochimica et Cosmochimica Acta 68 (20), 4167-4178.

Van Cappellen, P., Qiu, L., 1997. Biogenic silica dissolution in sediments of the Southern Ocean. II. Kinetics. Deep Sea Research Part II: Topical Studies in Oceanography 44 (5), 1129-1149.

Verney-Carron, A., Vigier, N., Millot, R., 2011. Experimental determination of the role of diffusion on Li isotope fractionation during basaltic glass weathering. Geochimica et Cosmochimica Acta 75 (12), 3452-3468.

Vigier, N., Decarreau, A., Millot, R., Carignan, J., Petit, S., France-Lanord, C., 2008. Quantifying Li isotope fractionation during smectite formation and implications for the Li cycle. Geochimica et Cosmochimica Acta 72 (3), 780-792.

Wimpenny, J., Colla, C.A., Yu, P., Yin, Q., Rustad, J.R., Casey, W.H., 2015. Lithium isotope fractionation during uptake by gibbsite. Geochimica et Cosmochimica Acta 168, 133-150.

Wimpenny, J., Gíslason, S.R., James, R.H., Gannoun, A., Von Strandmann, Philip AE Pogge, Burton, K.W., 2010. The behaviour of Li and Mg isotopes during primary phase dissolution and secondary mineral formation in basalt. Geochimica et Cosmochimica Acta 74 (18), 5259-5279.

You, C., Gieskes, J.M., 2001. Hydrothermal alteration of hemi-pelagic sediments: experimental evaluation of geochemical processes in shallow subduction zones. Applied Geochemistry 16 (9), 1055-1066.

Zhang, L., Chan, L., Gieskes, J.M., 1998. Lithium isotope geochemistry of pore waters from Ocean Drilling Program Sites 918 and 919, Irminger Basin. Geochimica et Cosmochimica Acta 62 (14), 2437-2450.

Chapter 4. “Reverse weathering” reactions: insights from Si and Li isotopes at a paleo-detaic environment

Jérôme: “how do you feel when you look at a paleo-river from 40 million years ago?”

Me: “I’m infinitely small.”

— 42°16'57.1"N 0°09'01.5"E, Ainsa, Spain
20/05/2015

4.1 Introduction

The evolution of the chemical composition of seawater is defined by inputs such as river fluxes, and by outputs such as carbonate precipitation. Historically, better constraints have been obtained on the input fluxes as they are more readily monitored, for example by gauging and sampling at river mouths. Several studies have shown that for some cations (*e.g.* potassium; Holland, 2005) the current oceanic budget does not appear to be at steady state. In particular, a “cation sink” seems to be missing. This imbalance is unsustainable over long time-scales (*i.e.* several times the element oceanic residence time), as it would make present-day seawater much more concentrated in cations. Mackenzie and Garrels (1966) proposed a process taking up cations from seawater into authigenic sediments. This process was termed “reverse weathering”, as it would in turn consume alkalinity and release carbon dioxide to the ocean-atmosphere system. Sillen (1967) then pointed out that clay formation in the ocean would be accountable for this reaction (Fig 4.1). Experiments performed by Michalopoulos and Aller (1995) confirmed the possibility of such a process, and Mackenzie and Kump (1995) generalized the reverse weathering reaction as:

Silica + degraded terrestrial aluminous clays + iron oxide + organic carbon + soluble cations + bicarbonate → new authigenic clay minerals + water + carbon dioxide (Equation 4-1)

However, field evidence of the reverse weathering process is still scarce (Rahman et al., 2016; Dunlea et al., 2017; Ramos et al., 2018). One of the challenges is that the nature of authigenic clays are not substantially different from detrital clays. In this chapter, we use silicon (Si) and lithium (Li) isotopes to investigate the relevance of reverse weathering at the scale of deltas, through a field study corresponding to a test of the experimental results from Chapter 3, and further explore the post-depositional diagenesis effects on sediment.

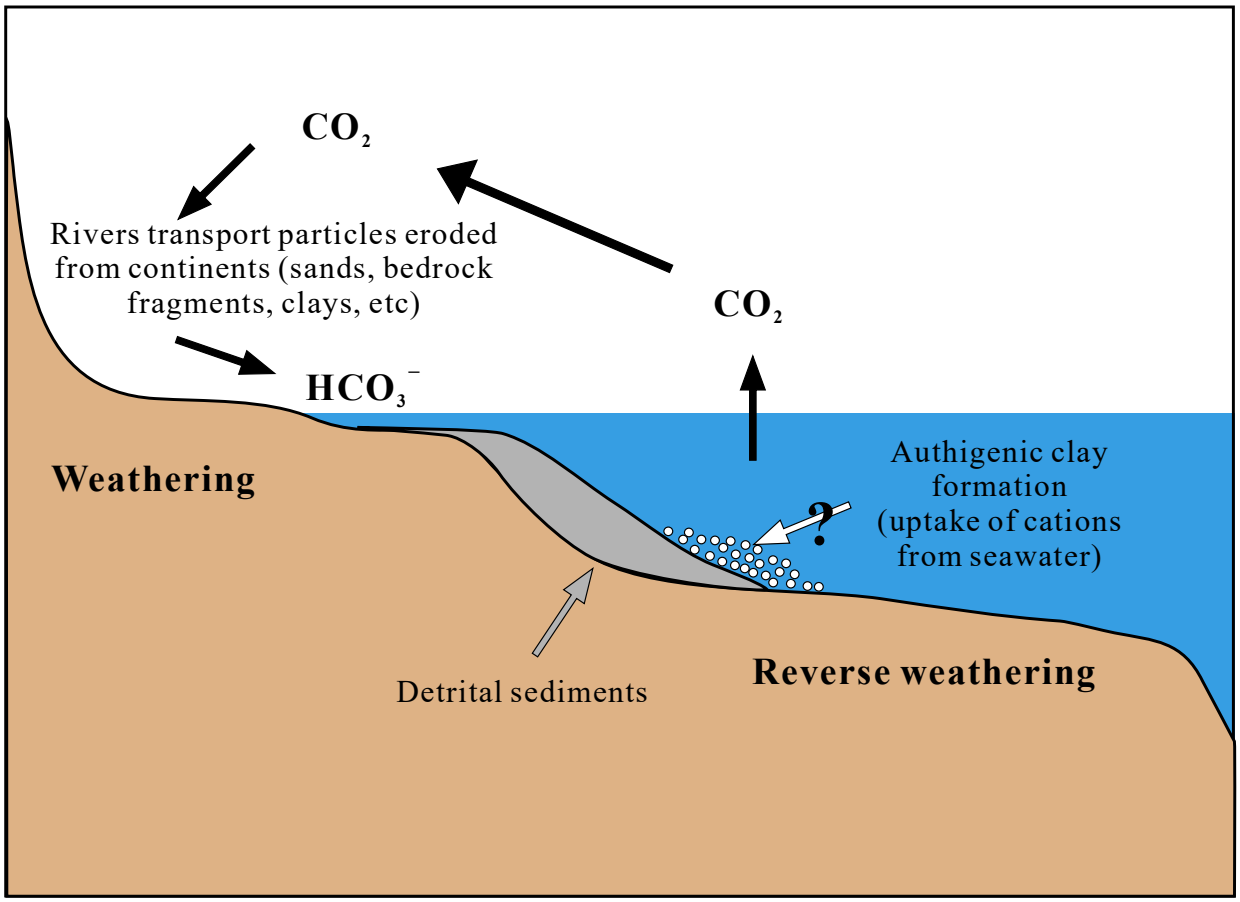

Figure 4.1 Schematic of mixing between detrital sediments and authigenic clays produced from "reverse weathering".

On the continents, dissolved Si is released by silicate weathering, and its isotope composition is heavy compared to crustal material as light Si isotopes are preferentially taken up in the particulates during secondary mineral formation (Opfergelt and Delmelle, 2012; Frings et al., 2016; Poitrasson, 2017). The Si isotope composition is expressed in δ-notation in the unit of ‰, related to a reference material, the National Bureau of Standards 28 Sand Quartz (NBS-28, or also called NIST RM-8546):

$$\delta^{x}Si=\left[\frac{(^{x}Si/^{28}Si)_{Sample}}{(^{x}Si/^{28}Si)_{NBS\text{-}28}}-1\right]\times 1000\text{ , where x=29 or 30.}$$

Mackenzie and Garrels (1966) initially pointed out that the scavenging of dissolved Si (DSi) from the ocean is required to maintain the steady state of oceanic DSi and suggested that this could be only achieved by clay formation, as other plausible means such as chert formation are of minor magnitude according to the sedimentary record. As deltaic environments feature a high biogenic productivity and sedimentation rates, these environments can serve as Si sinks. Approximately up to 10% riverine DSi is estimated to be removed when river water passes through estuaries (Tréguer et al., 1995; DeMaster, 2002; Tréguer and De La Rocha, 2013; Frings et al., 2016). The removal of DSi at deltas can be attributed to the uptake by living organisms, and to authigenic clay formation. In particular, the formation of authigenic clays can result from the diagenesis of biogenic silica (BSi) followed by reprecipitation of phyllosilicates (Van Cappellen and Qiu, 1997; Michalopoulos and Aller, 2004; Aller, 2014; Rahman et al., 2016). Therefore, BSi might be of importance for the sink of Si at deltas, such that the silicon isotope signature of sediments in the deltaic environments are controlled by both weathering processes on land and the fate of BSi in the sea.

On the other hand, the advantage of using Li as a geochemical tracer is that it is readily released to solution during silicate weathering on the continents. Following the same logics as Si, the heavy Li (^{7}Li) are enriched in the fluid, whereas the lighter one (^{6}Li) is preferentially incorporated into secondary phases such as clays or oxides during weathering. The Li isotope composition is expressed in δ-notation in the unit of ‰, related to the reference material LSVEC (lithium carbonate):

$$\delta^{7}\mathrm{Li}=\left[\frac{(^{7}\mathrm{Li}/^{6}\mathrm{Li})_{\mathrm{Sample}}}{(^{7}\mathrm{Li}/^{6}\mathrm{Li})_{\mathrm{LSVEC}}}-1\right]\times 1000$$

In the recent years, the Li isotope system has been widely used to improve our understanding of

weathering at the Earth's surface (Huh et al., 1998, 2001, 2004; Dellinger et al., 2014; Henchiri et al., 2016, etc.). Nevertheless, the ocean Li cycle is still poorly understood. The modern ocean is characterised by a δ^7Li of 31‰, which is heavier than the two main influxes of rivers (23‰) and hydrothermal fluids (8.3‰) (Chan et al., 1994; Huh et al., 1998; Misra and Froelich, 2012). Hence in the marine environment, light Li is expected to be removed from the ocean into sediments, and such effect would cause isotopic fractionation of Li, leaving seawater being 16 ‰ higher than authigenic clays (Misra and Froelich, 2012).

The mass balance of seawater chemistry points that cations need to be removed from seawater to authigenic sediments (Fig 4.1), and the box model of Li budget in the ocean suggests the authigenic sediments formation acts as the sink for oceanic dissolved Li. Nevertheless, there is still a big gap which needs to be filled between the prediction from mass balance calculation and field observations. A first set of questions is where can we find the evidence in the natural system to prove the Li sink estimated based on mass balance? The compilation made by Teng et al. (2004) shows that the δ^7Li of shales increases with clay content (indexed by Al_2O_3/SiO_2 ratio), which is opposite to the behaviour of Si isotopes in shales (Savage et al., 2013). The authors attributed such relationship to the sorption of seawater Li onto the clay-rich end-member of shale. However, to date, this positive relationship between δ^7Li and clay contents observed in shales by Teng et al. (2004) has not been confirmed in marine sedimentary rocks (Romer et al., 2014), metamorphosed marine sediments (Qiu et al., 2009), marine sediments (Bouman et al., 2004; Chan et al., 2006), or other shale samples (Pogge von Strandmann et al., 2017). The only data that support such a relationship are those related to sediments from the Banda Arc in Indonesia (Bouman et al., 2004), which are mostly terrestrially derived. In fact, most of the available data show a trend opposite to that of Teng et al. (2004), in line with the δ^7Li behaviour observed from solids during continental

weathering, for which δ^7Li is negatively correlated with Al/Si ratios (Dellinger et al., 2014). In general, detrital particulates are enriched in light Li owing to secondary clay formation during continental weathering (Huh et al., 2001; Dellinger et al., 2014; Tomascak et al., 2016). Romer et al. (2014) indeed observed that fluvial sediments have δ^7Li lighter than marine sediments. Nevertheless, source effects could also explain such differences between those samples.

A second set of questions concerning reverse weathering and the oceanic chemistry evolution is the behaviour of Si and Li in deltaic environments. River deltas have been considered as viable candidates for the sites permitting the reverse weathering reactions (*e.g.* Michalopoulos and Aller, 1995). In the case of Si, models have suggested 10% riverine DSi is captured at deltas in the form of BSi (DeMaster, 2002), such that DSi eventually transported to open ocean will be further fractionated to heavier δ^{30}Si compositions. Such a phenomenon of removing DSi at estuaries/deltas and increasing δ^{30}Si in remaining DSi have indeed been observed in some rivers (Delvaux et al., 2013; Weiss et al., 2015), but not everywhere (*e.g.* Hughes et al., 2012). Similarly, the behaviour of Li at estuaries/deltas is still enigmatic. Previous studies indicate that despite the fact that dissolved Li is conservative in such environments (Stoffyn-Egli, 1982; Brunskill et al., 2003; Pogge von Strandmann et al., 2008; Murphy et al., 2014), Li concentration in river transported particulate materials can increase during the transfer through the estuary (Pogge von Strandmann et al., 2008) and dissolved δ^7Li can be elevated off from the conservative mixing line (Murphy et al., 2014). These contradictory findings warrant further research to refine our understanding of processes occurring in these environments.

The main goal of this chapter is thus to test the ability of reverse weathering to change the chemical and isotope composition of detrital shallow marine sediments in deltas by mixing with authigenic clays (Fig 4.1). To this aim, we investigated alluvial and marine sediments derived from

the same source and deposited in a well-known paleo-delta (of Eocene age), extensively studied by sedimentologists (*e.g.* De Federico, 1981; Dreyer et al., 1999; Pickering and Bayliss, 2009). Our results enable a direct observation of the effect of deltaic processes on detrital sediments entering the ocean.

4.2 Sample material

In order to observe whether reverse weathering has an impact at the scale of a field setting representative of same contexts of the land-ocean interface, we collected sedimentary rock samples from a paleo-deltaic system (the Sobrarbe Delta complex) in the Ainsa Bain in the Spanish Pyrenees. This well-studied area allows us to compare samples from a continental environment (alluvial plain) where the sediments have never interacted with seawater, besides sediments, which have reached to seawater, recovered from marine environments (delta plain, delta front, and pro-delta).

4.2.1 The Ainsa Basin and its mid-Eocene deltaic system

The Ainsa Basin is part of the Southern Pyrenees foreland basin system (Fig 4.2a). This sub-basin is bordered by two N-S anticlines, the Mediano and Boltaña anticlines, located to the east and west respectively. To the south, the basin is also bordered by with the Sierras Marginales, at the top of a thrust, which was active during the Eocene-Oligocene. The basin formation begun approximately at the Cuisian/Lutetian transition (c.a. 48.9 Ma ago) and ended around the early Oligocene. The relative seawater level varies during the basin filling due to the local tectonic activity as the primary driver, as well as glacio-eustatic seawater level changes associated with the onset of the Antarctic ice sheet formation (Pickering and Bayliss, 2009). Sediments within the basin therefore range from lower Eocene limestones and sandstones (Guara Formation) to

Oligocene alluvial fan conglomerates (Collegats Formation) (De Federico, 1981; Dreyer et al., 1999).

In between, the San Vicente, Sobrarbe and Escanilla formations preserve the progradation of a paleo-delta formation developed over the Ainsa Basin. The lower strata of this complex is defined by lower slope with marls and turbidite sandstones (San Vicente Formation, lower Lutetian), which represents a pro-delta environment. In contrary, the top strata are characterized by alluvial deposits (Escanilla Formation, upper Lutetian to lower Priabonian), which represents the most proximal part of the delta. Between the alluvial plain and the pro-delta, the Sobrarbe Formation (mid Lutetian to lower Bartonian) consists of marginal-marine to shallow and slope deposits representing the delta plain and delta front (De Federico, 1981; Dreyer et al., 1999).

4.2.2 Sample description

In order to investigate the occurrence of reverse weathering and the impact of seawater on terrigenous sediments, we have selected sampling sites (Fig 4.2 b and c) representing different parts of the Ainsa delta system: alluvial plain (samples with prefix SA), the delta plain (landwards from the shoreline but influenced by seawater, salt marshes for example; samples with prefix SC), marine deposition including the delta front (samples with prefix SD) and the pro-delta (turbidite; samples with prefix ST). It is noticeable that in the field, the colors of the different outcrops are distinctive: alluvial deposits generally exhibit a red color whereas marine deposits are of a greyish color. One or several sites were chosen for each part of the delta. At each site, about 5 to 10 unweathered rock samples of different grain sizes were collected, generally in road cuts. During the sampling, the outermost part of each sample was discarded to eliminate any potential effects of present-day weathering. Detailed information on each sample is listed in Table 4.1.

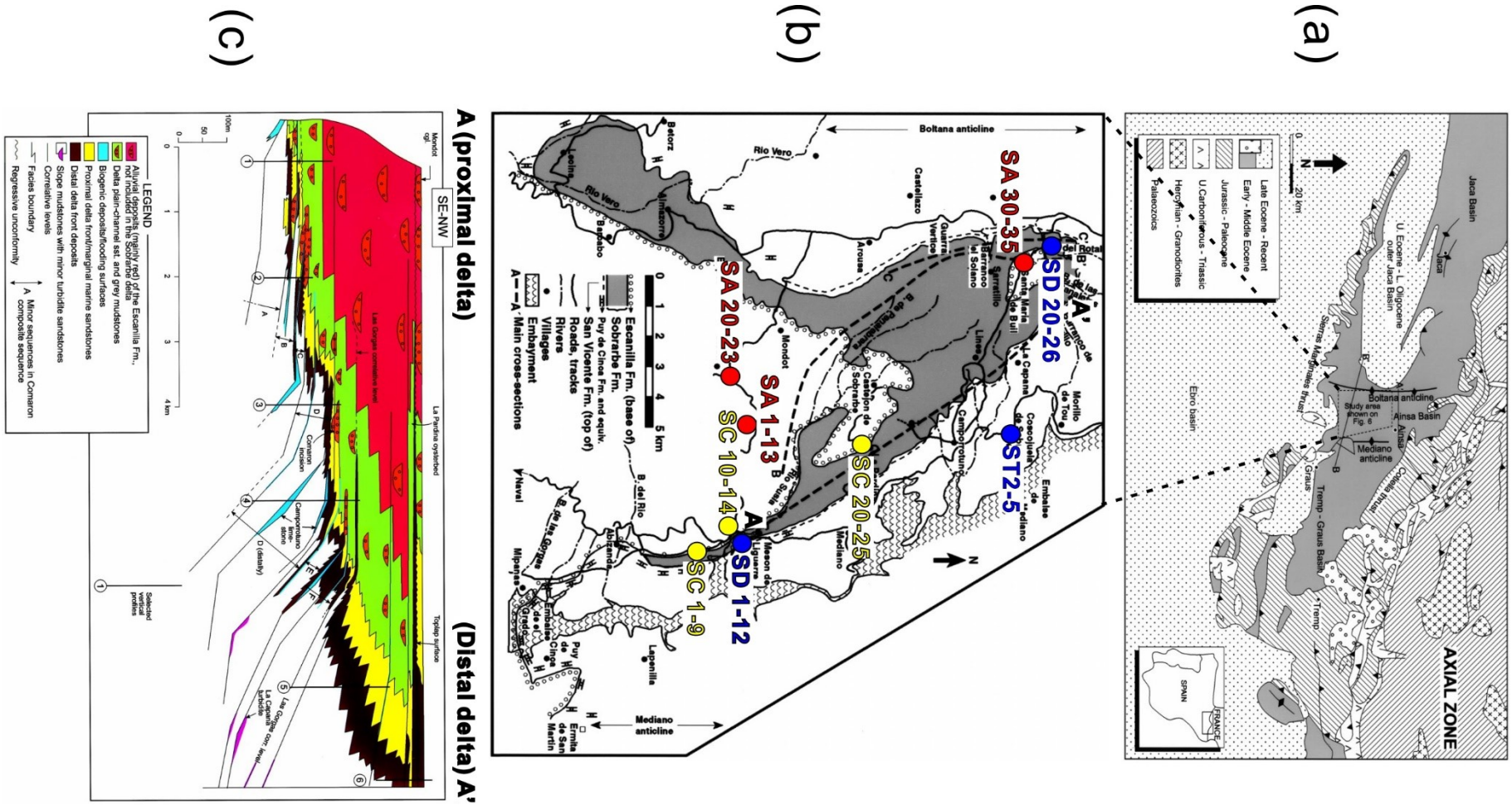

Figure 4.2 Maps of the sampling area. (a) Location of the Ainsa basin within the Southern Pyrenees. (b) Geological map of the sampling area with the shallow marine part of the Sobrarbe deltaic complex highlighted in gray color. The sampled areas are in the different sediment environments, colored by blue (marine deposits), yellow (delta plain), and red (alluvial plain) dots. (c) Cross section of the transect A-A’ (located in figure 4.2b). The depositional environments evolves from alluvial (proximal delta) to deep-marine (distal delta) deposits. Figures reprinted and modified from Dreyer et al. (1999) with permission from Elsevier.

Table 4.1 Sample depositional environment, location, δ^7Li and δ^{30}Si compositions (in ‰), εNd, and Al/Si ratios result

Sample	*Location*	*Depositional type*	*Al/Si*	*δ^7Li*	*2 s.d.*	*δ^{30}Si*	*2 s.d.*	*δ^{29}Si*	*2 s.d.*	*εNd*
SA 1	42°16'57.1"N 0°09'01.5"E	Alluvial plain	0.21	3.10	0.29	-0.19	0.07	-0.09	0.03	
SA 2	42°16'57.1"N 0°09'01.5"E	Alluvial plain	0.22	3.58	0.29	-0.16	0.08	-0.06	0.05	-11.0
SA 3	42°16'57.1"N 0°09'01.5"E	Alluvial plain	0.24	1.70	0.43	-0.17	0.08	-0.09	0.04	
SA 4	42°16'57.1"N 0°09'01.5"E	Alluvial plain	0.42	1.70	0.29	-0.37	0.04	-0.16	0.05	-11.2
SA 5	42°16'57.1"N 0°09'01.5"E	Alluvial plain	0.30	2.45	0.11	-0.22	0.01	-0.10	0.05	
SA 6	42°16'57.1"N 0°09'01.5"E	Alluvial plain	0.10	6.92	0.13	-0.07	0.08	-0.03	0.06	
SA 7	42°16'57.1"N 0°09'01.5"E	Alluvial plain	0.28	2.88	0.23	-0.25	0.07	-0.14	0.08	-11.4
SA 9	42°16'57.1"N 0°09'01.5"E	Alluvial plain	0.13	6.21	0.23	-0.23	0.08	-0.10	0.10	
SA 10	42°16'57.1"N 0°09'01.5"E	Alluvial plain	0.21	3.26	0.08	-0.21	0.07	-0.10	0.04	
SA 11	42°16'57.1"N 0°09'01.5"E	Alluvial plain	0.23	1.74	0.16	-0.20	0.08	-0.12	0.04	
SA 12	42°16'57.1"N 0°09'01.5"E	Alluvial plain	0.13	6.40	0.15	-0.22	0.08	-0.14	0.14	
SA 13	42°16'57.1"N 0°09'01.5"E	Alluvial plain	0.12	6.16	0.15	-0.10	0.08	-0.06	0.04	
SA 15	42°16'57.1"N 0°09'01.5"E	Alluvial plain	0.26	1.90	0.16	-0.35	0.16	-0.18	0.06	-11.4
SA 16	42°16'57.1"N 0°09'01.5"E	Alluvial plain	0.15	4.50	0.16	-0.14	0.04	-0.09	0.03	
SA 17	42°16'57.1"N 0°09'01.5"E	Alluvial plain	0.15	5.27	0.47	-0.20	0.03	-0.12	0.02	-10.6
SA 20	42°16'38.4"N 0°07'46.4"E	Alluvial plain	0.22	3.06	0.18	-0.30	0.13	-0.17	0.11	
SA 21	42°16'38.4"N 0°07'46.4"E	Alluvial plain	0.24	3.80	0.20	-0.15	0.12	-0.07	0.02	
SA 22	42°16'38.4"N 0°07'46.4"E	Alluvial plain	0.39	1.89	0.20	-0.31	0.07	-0.16	0.06	
SA 23	42°16'38.4"N 0°07'46.4"E	Alluvial plain	0.15	6.30	0.17	-0.16	0.09	-0.08	0.06	
SA 30	42°21'52.4"N 0°05'04.4"E	Alluvial plain	0.34	2.99	0.19	-0.35	0.13	-0.18	0.02	
SA 31	42°21'52.4"N 0°05'04.4"E	Alluvial plain	0.25	2.80	0.09	-0.17	0.07	-0.11	0.09	-10.9
SA 32	42°21'52.4"N 0°05'04.4"E	Alluvial plain	0.35	3.04	0.29	-0.38	0.08	-0.20	0.05	
SA 33	42°21'52.4"N 0°05'04.4"E	Alluvial plain	0.17	5.44	0.26	-0.15	0.05	-0.10	0.02	
SA 34	42°21'52.4"N 0°05'04.4"E	Alluvial plain	0.18	4.49	0.15	-0.23	0.08	-0.14	0.07	
SA 35	42°21'52.4"N 0°05'04.4"E	Alluvial plain	0.21	5.47	0.07	-0.22	0.09	-0.14	0.06	
SC 1	42°15'54.3"N 0°11'50.5"E	Delta plain	0.24	1.11	0.12	-0.29	0.08	-0.14	0.08	
SC 2	42°15'54.3"N 0°11'50.5"E	Delta plain	0.21	1.96	0.08	-0.54	0.07	-0.27	0.03	
SC 3	42°15'54.3"N 0°11'50.5"E	Delta plain	0.38	0.86	0.12	-0.71	0.04	-0.34	0.06	
SC 4	42°15'54.3"N 0°11'50.5"E	Delta plain	0.44	0.29	0.12	-0.36	0.08	-0.19	0.12	
SC 5	42°15'54.3"N 0°11'50.5"E	Delta plain	0.19	2.06	0.23	-0.27	0.07	-0.14	0.08	
SC 6	42°15'54.3"N 0°11'50.5"E	Delta plain	0.21	3.81	0.09	-0.18	0.08	-0.09	0.09	-10.0
SC 7	42°15'54.3"N 0°11'50.5"E	Delta plain	0.16	5.06	0.16	-0.23	0.09	-0.12	0.07	
SC 9	42°15'54.3"N 0°11'50.5"E	Delta plain	0.34	-0.44	0.24	-0.35	0.16	-0.13	0.06	

Sample	***Location***	***Type***	***Al/Si***	***$\delta^{7}Li$***	***2 s.d.***	***$\delta^{30}Si$***	***2 s.d.***	***$\delta^{29}Si$***	***2 s.d.***	***εNd***
SC 10	42°16'43.9"N 0°11'03.1"E	Delta plain	0.31	2.19	0.08	-0.31	0.05	-0.17	0.08	
SC 11	42°16'43.9"N 0°11'03.1"E	Delta plain	0.28	2.39	0.16	-0.20	0.08	-0.11	0.10	
SC 12	42°16'43.9"N 0°11'03.1"E	Delta plain	0.39	1.92	0.32	-0.39	0.04	-0.19	0.02	
SC 13	42°16'43.9"N 0°11'03.1"E	Delta plain	0.18	5.97	0.07	-0.19	0.03	-0.10	0.05	
SC 14	42°16'43.9"N 0°11'03.1"E	Delta plain	0.18	6.3	0.12	-0.16	0.09	-0.08	0.06	
SC 20	42°18'48.4"N 0°09'12.6"E	Delta plain	0.23	2.00	0.31	-0.38	0.09	-0.18	0.02	-11.5
SC 21	42°18'48.4"N 0°09'12.6"E	Delta plain	0.42	0.69	0.25	-0.48	0.12	-0.23	0.03	-11.5
SC 22	42°18'48.4"N 0°09'12.6"E	Delta plain	0.21	1.95	0.56	-0.35	0.05	-0.16	0.06	
SC 23	42°18'48.4"N 0°09'12.6"E	Delta plain	0.15	3.10	0.11	-0.16	0.07	-0.07	0.03	
SC 24	42°18'48.4"N 0°09'12.6"E	Delta plain	0.19	3.14	0.18	-0.22	0.09	-0.14	0.06	
SC 25	42°18'48.4"N 0°09'12.6"E	Delta plain	0.17	5.10	0.19	-0.25	0.12	-0.12	0.06	
SD 1	42°16'57.2"N 0°11'47.2"E	Delta front	0.25	0.05	0.15	-0.25	0.10	-0.11	0.07	
SD 2	42°16'57.2"N 0°11'47.2"E	Delta front	0.39	-2.42	0.23	-0.45	0.03	-0.20	0.05	-11.3
SD 3	42°16'57.2"N 0°11'47.2"E	Delta front	0.35	-0.90	0.38	-0.37	0.09	-0.17	0.03	-11.6
SD 4	42°16'57.2"N 0°11'47.2"E	Delta front	0.19	0.31	0.16	-0.22	0.09	-0.10	0.06	
SD 5	42°16'57.2"N 0°11'47.2"E	Delta front	0.2	-0.55	0.09	-0.50	0.04	-0.27	0.03	
SD 6	42°16'57.2"N 0°11'47.2"E	Delta front	0.29	0	0.34	-0.33	0.11	-0.17	0.04	-11.3
SD 7	42°16'57.2"N 0°11'47.2"E	Delta front	0.39	-1.30	0.08	-0.58	0.06	-0.31	0.04	-11.9
SD 8	42°16'57.2"N 0°11'47.2"E	Delta front	0.19	0.60	0.28	-0.16	0.05	-0.09	0.07	-10.8
SD 9	42°16'57.2"N 0°11'47.2"E	Delta front	0.19	1.03	0.10					
SD 10	42°16'57.2"N 0°11'47.2"E	Delta front	0.18	1.60	0.16	-0.17	0.01	-0.08	0.03	-10.7
SD 11	42°16'57.2"N 0°11'47.2"E	Delta front	0.15	1.72	0.14	-0.31	0.06	-0.17	0.01	
SD 12	42°16'57.2"N 0°11'47.2"E	Delta front	0.33	-2.37	0.13	-0.39	0.06	-0.21	0.08	-11.0
SD 20	42°22'17.8"N 0°04'35.2"E	Delta front	0.27	0.50	0.23					-11.2
SD 21	42°22'17.8"N 0°04'35.2"E	Delta front	0.33	3.73	0.27	-0.50	0.08	-0.26	0.05	
SD 22	42°22'17.8"N 0°04'35.2"E	Delta front	0.29			-0.42	0.08	-0.24	0.07	
SD 23	42°22'17.8"N 0°04'35.2"E	Delta front	0.13	6.91	0.24	-0.31	0.08	-0.20	0.01	
SD 24	42°22'17.8"N 0°04'35.2"E	Delta front	0.16	4.19	0.17	-0.28	0.04	-0.17	0.03	-10.3
SD 25	42°22'17.8"N 0°04'35.2"E	Delta front	0.18	3.33	0.30	-0.24	0.04	-0.14	0.07	
SD 26	42°22'17.8"N 0°04'35.2"E	Delta front	0.34	1.99	0.14	-0.41	0.10	-0.24	0.06	
ST 2	42°21'28.0"N 0°09'05.5"E	Pro-delta	0.36	0.10	0.10	-0.52	0.04	-0.30	0.03	
ST 3	42°21'28.0"N 0°09'05.5"E	Pro-delta	0.37	0.84	0.25	-0.41	0.12	-0.20	0.08	-11.3
ST 4	42°21'28.0"N 0°09'05.5"E	Pro-delta	0.18	2.22	0.32	-0.25	0.05	-0.13	0.06	
ST 5	42°21'28.0"N 0°09'05.5"E	Pro-delta	0.37	0.09	0.13	-0.41	0.13	-0.21	0.08	

4.3 Analytical methods

4.3.1 Sample preparation and major and trace element concentrations

Several samples representing different depositional environments and various grain sizes were first chosen for mineralogical observations using thin section profiles. All the collected samples were first dried at 50ºC and then crushed using an agate mortar. Major elements were measured at SARM (Service d'Analyse des Roches et des Minéraux, Vandoeuvre-les-Nancy, France; details of sample preparation analyzing methods are provided at http://helium.crpg.cnrs-nancy.fr/SARM/pages/roches.html). For trace elements, approximately 0.1 g of the crushed samples were dissolved using an HF-HNO_3 mixture. Then the evaporated residuals were repeatedly dissolved in HCl and dried down until the solution was clear. Trace element concentrations were then measured at the Institut de Physique du Globe de Paris (IPGP) using an Inductively Coupled Plasma Quadrupole Mass Spectrometry (ICP-Q-MS).

4.3.2 Selective extraction of Li pools

Selective extractions of Li pools were performed on selected samples to better constrain the controls on the bulk Li isotope composition of the samples. In the “rinsing” experiments, each sample was rinsed with MQ-water for 3 times. First, 5 ml MQ-water were added to ~1 g sample which was then shaken vigorously for 24 hours. Then the sample mixture was centrifuged at a speed of 4,400 rpm, and the top 4 ml were pipetted out and filtered at 0.2 µm. Another 4 ml MQ were then added into the residual and the same procedure was repeated for a second and a third time. In a separate set of “leaching” experiments, the same protocol was followed as for the “rinsing” experiment, but with 0.5 N HCl instead of MQ water. The rinsing solutions were analyzed for Li concentration and for Li isotope composition, and leaching solutions were analyzed for major and trace elements, as well as for Li isotope composition. We emphasize that the H_2O rinsing and HCl leaching experiments were carried out on separate aliquots of sediment

samples, rather than sequentially on the same aliquots. Therefore, the first HCl leaches are likely include solutes that could have been released during H_2O rinse.

4.3.3 Lithium isotope measurements

A double-step separation protocol was performed for each sample in order to separate Li from the sample matrix. In the first step, an 0.5-ml sample aliquot containing 20 ng Li in 1 N HNO_3 was first loaded onto a 1-ml column (BioRad, AG50W–X12, 200–400 mesh) followed by 4 ml of 1 N HNO_3. Collection started right after loading the sample. The whole 4.5 ml eluted volume was collected, evaporated, and the residual was re-dissolved in 0.5 ml of 0.2 N HNO_3. In the second step, the latter solution was loaded onto the same column again, and then eluted with 16 ml of 0.2 N HNO_3. The last 8 ml of the elution volume was collected, evaporated, and then allowed for reacting with 2 ml 6 N HCl for at least 24 hours, in order to destroy potentially remaining organic matter from the resin which would induce matrix effects during the measurements on the mass spectrometer. Each sample was then evaporated again, and the residual was dissolved in 1 ml 0.5 N HNO_3. The summary of the Li separation method is given in Table 2.2 (Chapter 2). To check for the quality of this protocol, during each separation session 5 reference materials were routinely processed together with samples. The five reference materials include basaltic rocks (BHVO-2 and JB-2) and seawater (NASS-6) of known Li isotope composition, in addition to two soil reference materials including SRM-2709a (NIST) and TILL-1 (NRC, Canada). The Li isotope composition of the purified samples was measured at IPGP using a Thermo Fisher Neptune Plus MC-ICP-MS. The Li-pure standard solutions IRMM-016 and SPEC were routinely used to monitor the instrumental stability, while the L-SVEC solution was used as bracketing standard. We obtained accurate and reproducible Li isotope composition of IRMM-016 (δ^7Li=0.13±0.17‰, 2 s.d., n=36), SPEC (δ^7Li=94.32±0.19 ‰, 2 s.d., n=26), NASS-6 (δ^7Li=30.95±0.51 ‰, 2 s.d., n=12), BHVO-2

(δ^7Li=4.66±0.78 ‰, 2 s.d., n=11), and JB-2 (δ^7Li=4.72±0.80 ‰, 2 s.d., n=15), as all the results are in good agreement with values reported in previous studies (e.g. Brand et al., 2014; Dellinger et al., 2014). We obtained reproducible δ^7Li values for the two soil reference materials SRM-2709a (δ^7Li=−0.30±0.58 ‰, 2 s.d., n=13) and TILL-1 (δ^7Li=6.69±0.68 ‰, 2 s.d., n=14).

4.3.4 Silicon isotope measurement

In order to analyze the Si isotope composition, an aliquot of each crushed sample was also digested using alkali fusion in which ~200 mg of NaOH were added to ~10 mg sample in a silver crucible and then heated at 720°C for 12 minutes. The fused samples were then allowed for cooling until room temperature was reached. The crucibles were then transferred into 30-ml Teflon beakers containing ~15 ml of MQ-water. After settling overnight, the samples were sonicated and transferred to pre-cleaned PE bottles. Finally, each sample was then further diluted and weakly acidified to ~100 ml 1% (v/v) HNO_3 solution, the Si concentration of which was analyzed using ICP-Q-MS at IPGP. Then a widely-adopted separation protocol (Pringle et al., 2013a, 2013b, 2014, 2016; Savage and Moynier, 2013; Savage et al., 2013) was used, based on the same resin as the one employed in the Li separation protocol. An aliquot of the fusion solution containing 20 µg Si was loaded onto a column containing 1.8 ml resin and was eluted with 5 ml of MQ water. Sample collection started from the beginning of sample loading. Last, the collected sample was diluted and acidified to a 10 ml 0.2 N HNO_3 solution and its Si isotope composition was measured on a Thermo Fisher Neptune Plus MC-ICP-MS at IPGP within 24 hours after the Si separation. The well characterized reference material BHVO-2 was routinely analyzed as an external standard to check the quality of separation protocol. The quartz sand reference material NBS-28 was also processed through the same digestion and separation method explained above and used as the bracketing standard. A mass-dependent fractionation of Si isotopes across all samples is indicated

by the linear relationship between $\delta^{30}Si$ and $\delta^{29}Si$ across all samples, with a slope value of 0.5153 which is between the slope of kinetic fractionation (0.5092) and that of equilibrium fractionation (0.5178), however, undistinguishable from the theoretical slopes because of instrumental uncertainties. The long-term $\delta^{30}Si$ value of the reference material BHVO-2 used in this study (−0.29±0.05‰, n=21) is in agreement with previously reported values (Zambardi and Poitrasson, 2011; Savage et al., 2011; Savage et al., 2013; Pringle et al., 2016).

4.3.5 Neodymium isotope measurement

To separate Nd from the matrix, we employed a double-column method initially developed by Richard et al. (1976) and further improved by Caro et al. (2006). The HF-HNO_3 digested sample was first evaporated, and an aliquot of the residual was dissolved in a 2 N HNO_3 solution and then loaded onto a first column packed with the TRU-spec resin, which is able to separate rare earth elements from the sample matrix. The solution eluted from the first column was then evaporated and the residual was dissolved in a 0.25 N HCl solution, which was loaded onto a second column packed with the Ln-spec resin, which resulted in the separation of Nd from the rest of the matrix. Finally, the collected Nd was dissolved in a 3% HNO_3 solution and its isotopic composition was measured on a Neptune MC-ICP-MS at IPGP at a concentration of 50 ppb, using a $^{142}Nd/^{144}Nd$ ratio of 0.7218 for the internal correction of instrumental mass fractionation. Well-characterized reference materials were routinely analysed to monitor the quality of Nd measurements. In this study, neodymium isotope composition is expressed in ε-notation:

$$\varepsilon Nd = \left[\frac{(^{143}Nd/^{144}Nd)_{Sample}}{(^{143}Nd/^{144}Nd)_{CHUR}} - 1\right] \times 10000$$

where CHUR stands for chondritic uniform reservoir, and $(^{143}Nd/^{144}Nd)_{CHUR}$ is the value of the ratio in chondrites. The reported results are within uncertainty of ~0.2 εNd units.

4.4 Results

4.4.1 Thin section

We selected samples from the alluvial plain, delta plain, and marine deposits, across a range of grain sizes for mineralogical observation by optical microscopy. The observations are summarized in Table 4.2, and representative images are shown in Figure 4.3. Overall, the thin sections suggest that the sediments of the Ainsa Basin contain a recycled component, meaning that their source rocks are meta-sedimentary rocks. This is in particular shown by the presence of detrital limestone grains in both alluvial and marine sediments. In the coarse fractions (such as sandstones), across all depositional environments, igneous/metamorphic minerals can be observed. Oxides are also a major feature in many samples, in particular in the alluvial plain, deep delta and turbidite environments.

Table 4.2 Summary of thin section examinations

Depositional environment	***Coarse fraction (Sandstone)***	***Fine fraction (Siltstone and claystone)***
Alluvial	Sample: SA 13. The grain size is very coarse. The detrital grains contain some marine carbonates from previous deposition episodes. The large grains are dominated by quartz and calcite, but also contain a significant amount of unweathered primary minerals such as micas. Some detrital oxides/hydroxides are also visible.	Sample: SA 3, SA11, SA15. The grain size is fine. The large grains are dominated by calcite, but also contain some quartz, and a trace amount of micas (<1%). Clays are observed in the matrix. The presence of oxides is suggested (opaques).
Delta plain	Sample: SC6. The grain size is coarse. The main component is calcite. The sample also contains some quartz and micas, and a few other primary minerals.	Sample: SC 2. The grain size is relatively fine. The most important minerals are clays, calcite and quartz, but some detrital oxides/hydroxides are also present (opaques).
Marine	Sample: SD23. The grain size is coarse. Microfossils can be observed. The grains contain considerable amount of quartz. Other grains include some bioclast, mica, calcite, detrital limestone, and some primary minerals. No oxides are observed.	Sample: SD 1, SD2, SD5, SD10, ST2, ST3, and ST5. The grain size is relatively small. The main minerals are quartz and calcite. A significant amount of detrital oxides/hydroxides is observed in the marine deposits. A large amount of clays is observed. Foramineras are visible in some thin sections (SD1 and ST5).

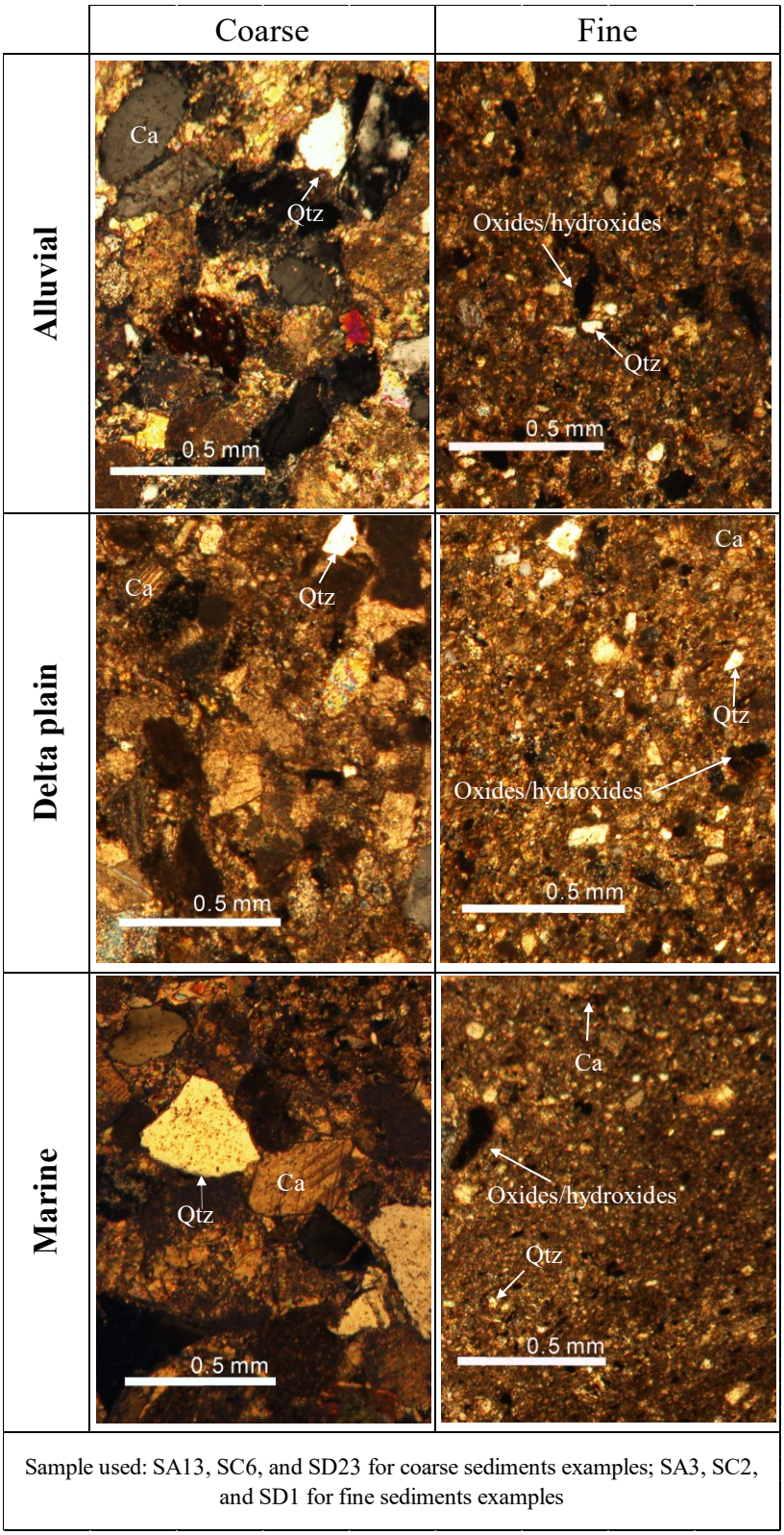

Figure 4.3 Optical microscopy images of the thin sections from selected coarse and fine samples from different depositional environments. Qtz and Ca in the figure respectively represent quartz and calcite.

4.4.2 Major and trace elements

The major and trace element data are reported in Table 4.3 and Table 4.4, respectively. There is little difference in terms of the concentrations of the most of major and trace elements among sediments from the three depositional environments (alluvial plain, delta plain, and delta slope). Samples from all the environments show that the Al and Fe content exert a strong correlation on the Li content (Fig 4.4). As for other elements, no significant enrichment of Li in a particular depositional environment is observed (Fig 4.4), although the distributions of Li/Al and Li/Fe ratios (Fig 4.5) show a marginal difference between continental and marine samples. One exception is Na: sediments which have interacted with seawater (deposited on delta plains or delta slopes) have higher Na than that in the continental sediments. As the Li concentration is correlated with Al and Fe concentrations, a comparison of Na and Li concentrations, both normalized to the sum of Al and Fe concentration, is shown in Figure 4.6. Samples deposited in the delta slope and the delta plain are Na-richer than alluvial samples, indicating that the samples that have interacted with seawater are enriched in Na. At low Na level, the Li content is independent from the Na content, whereas a negative correlation between Li and Na exists when the Na content is elevated (especially in the sediments which were in contact with seawater).

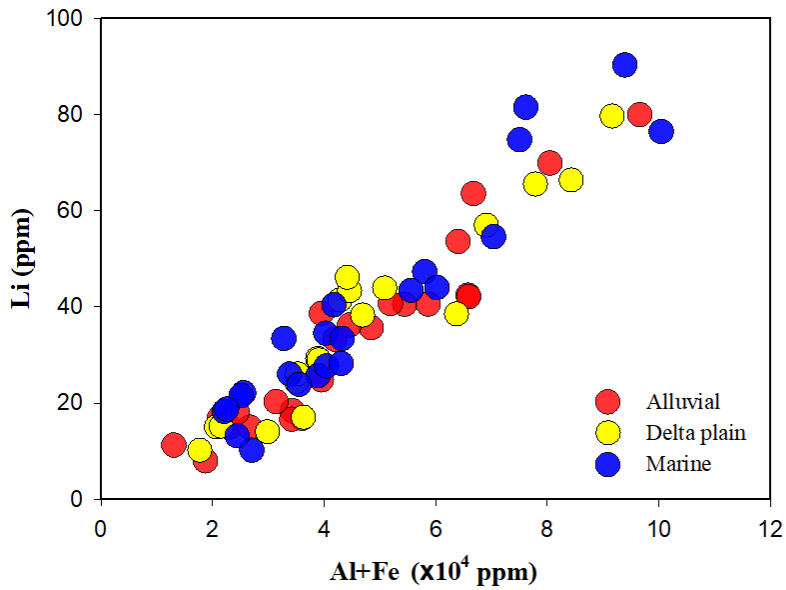

Figure 4.4 Relationship between Li concentration and the sum of Al and Fe concentrations across all samples.

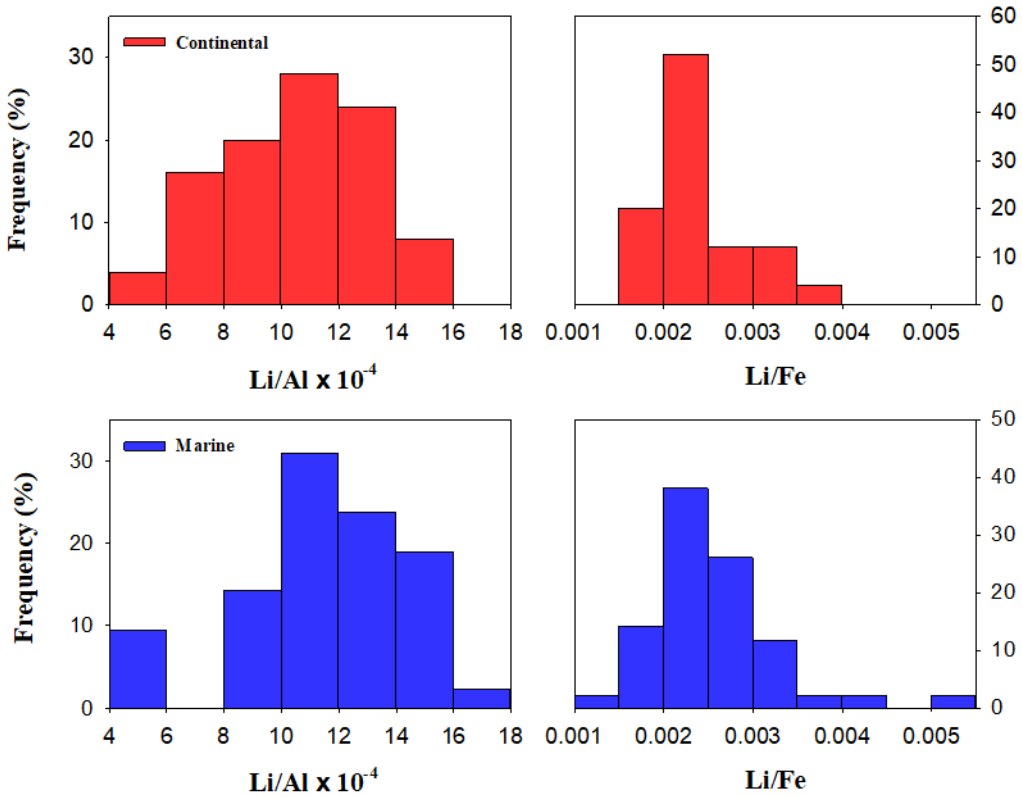

Figure 4.5 Frequency distribution of Li/Al and Li/Fe ratios.

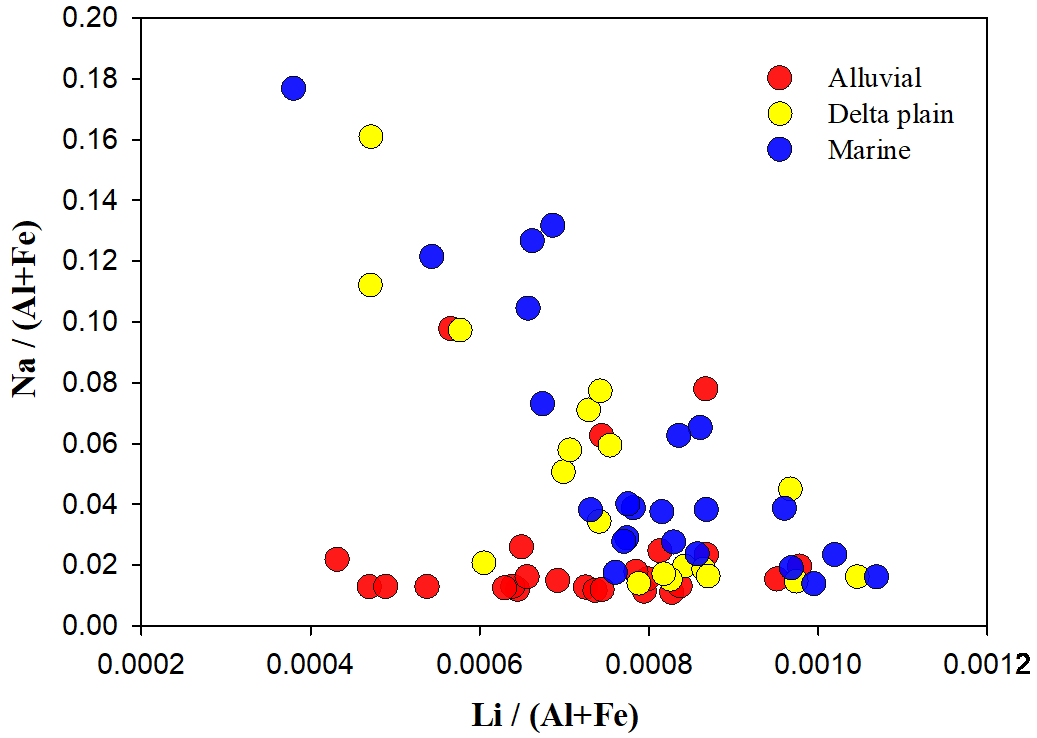

Figure 4.6 Relationship between the Na/(Al+Fe) and Li/(Al+Fe) ratios. The Li content is not correlated to the Na content at low Na level whereas there is a negative correlation between Li and Na when the Na content is higher.

Table 4.3 Major element concentrations in samples from the Ainsa paleo-delta, expressed in weight percent oxides (%)

Sample	SiO_2	Al_2O_3	Fe_2O_3	MnO	MgO	CaO	Na_2O	K_2O	TiO_2	P_2O_5	LOI (1000°C)	Total
Alluvial plain deposits												
SA 1	26.16	4.84	1.95	0.07	2.17	33.68	0.07	1.04	0.31	< D.L.	29.63	99.93
SA 2	25.87	5.05	2.18	0.06	2.41	33.40	0.07	1.03	0.30	< D.L.	29.62	99.99
SA 3	27.31	5.90	2.47	0.06	2.55	31.27	0.08	1.19	0.33	< D.L.	28.43	99.58
SA 4	30.99	11.59	5.04	0.06	4.00	21.96	0.15	2.19	0.45	< D.L.	23.61	100.04
SA 5	29.98	7.94	3.41	0.05	3.65	26.36	0.11	1.53	0.38	< D.L.	26.30	99.71
SA 6	27.91	2.58	0.74	0.03	1.46	36.08	0.06	0.54	0.00	< D.L.	30.91	100.30
SA 7	32.01	8.05	3.34	0.05	3.22	25.32	0.12	1.52	0.42	< D.L.	25.19	99.23
SA 9	44.40	5.17	1.25	0.04	1.99	23.03	0.06	1.44	0.18	< D.L.	22.13	99.69
SA 10	26.72	4.95	1.91	0.07	2.12	33.18	0.07	1.07	0.28	< D.L.	29.15	99.51
SA 11	34.09	6.81	2.63	0.05	3.04	26.03	0.09	1.32	0.40	< D.L.	25.22	99.67
SA 12	42.67	5.01	1.12	0.03	2.03	24.30	0.06	1.28	0.18	< D.L.	22.23	98.91
SA 13	49.18	5.01	1.10	0.03	1.73	20.82	0.06	1.43	0.16	< D.L.	20.38	99.90
SA 15	34.86	7.91	3.17	0.05	3.19	24.40	0.12	1.65	0.44	< D.L.	23.77	99.55
SA 16	20.63	2.76	0.96	0.03	5.01	35.68	0.05	0.67	0.14	< D.L.	33.72	99.64
SA 17	26.41	3.52	0.63	0.04	5.14	31.97	0.05	1.01	0.15	< D.L.	30.73	99.65
SA 20	32.11	6.38	2.60	0.04	2.79	27.96	0.13	1.27	0.36	< D.L.	25.91	99.54
SA 21	26.01	5.47	2.23	0.03	3.33	31.77	0.15	1.13	0.30	< D.L.	29.37	99.79
SA 22	28.31	9.74	4.14	0.05	3.28	26.19	0.26	1.80	0.43	< D.L.	25.73	99.91
SA 23	33.03	4.33	1.22	0.03	2.17	30.48	0.11	1.09	0.18	< D.L.	27.91	100.55
SA 30	24.96	7.54	2.68	0.05	4.22	29.27	0.12	1.55	0.38	< D.L.	28.71	99.48
SA 31	21.78	4.83	2.00	0.04	2.50	36.33	0.11	0.88	0.26	< D.L.	31.47	100.19
SA 32	26.68	8.15	3.38	0.05	3.71	28.45	0.14	1.62	0.40	< D.L.	27.45	100.02
SA 33	28.02	4.14	0.68	0.03	2.23	33.42	0.35	1.18	0.13	< D.L.	28.57	98.74
SA 34	22.71	3.53	0.82	0.04	3.08	36.07	0.21	0.95	0.18	< D.L.	31.39	98.98
SA 35	10.01	1.88	0.45	0.07	1.04	47.14	0.14	0.39	0.00	< D.L.	37.96	98.98
Delta plain deposits												
SC 1	24.80	5.21	2.18	0.04	3.13	33.26	0.26	1.06	0.27	< D.L.	29.68	99.89
SC 2	25.18	4.74	1.96	0.03	3.07	33.60	0.31	1.02	0.25	< D.L.	29.77	99.94
SC 3	27.99	9.42	4.00	0.05	3.86	26.10	0.21	1.80	0.44	< D.L.	26.06	99.92
SC 4	26.28	10.19	4.33	0.05	3.81	26.25	0.16	1.94	0.42	< D.L.	26.39	99.81
SC 5	25.10	4.30	1.75	0.04	2.40	35.03	0.24	0.89	0.25	< D.L.	30.35	100.36
SC 6	12.44	2.31	0.78	0.03	1.94	45.07	0.23	0.34	0.14	< D.L.	37.03	100.30

Sample	SiO_2	Al_2O_3	Fe_2O_3	MnO	MgO	CaO	Na_2O	K_2O	TiO_2	P_2O_5	LOI (1000°C)	Total
SC 7	33.19	4.60	0.78	0.03	2.03	30.97	0.65	1.44	0.00	< D.L.	25.74	99.42
SC 9	27.48	8.14	2.95	0.10	2.87	29.14	0.18	1.48	0.37	< D.L.	27.52	100.22
SC 10	19.74	5.38	2.29	0.03	2.85	36.51	0.09	0.93	0.25	< D.L.	32.38	100.45
SC 11	23.12	5.68	2.01	0.03	3.63	33.46	0.10	1.02	0.29	< D.L.	30.87	100.21
SC 12	23.72	8.17	3.69	0.04	3.45	30.47	0.14	1.45	0.36	< D.L.	29.08	100.55
SC 13	15.52	2.51	1.06	0.03	2.57	42.24	0.20	0.41	0.14	< D.L.	35.76	100.43
SC 14	15.42	2.48	1.20	0.03	2.58	41.64	0.17	0.42	0.15	< D.L.	35.33	99.41
SC 20	32.06	6.39	2.44	0.05	2.24	29.02	0.13	1.27	0.38	< D.L.	25.96	99.91
SC 21	30.25	11.35	4.50	0.05	2.84	23.95	0.20	2.13	0.44	< D.L.	23.89	99.61
SC 22	31.39	5.80	2.31	0.04	2.36	29.54	0.11	1.16	0.35	< D.L.	26.56	99.61
SC 23	44.52	5.87	0.74	0.02	1.66	23.36	0.55	1.88	0.12	< D.L.	21.56	100.27
SC 24	24.56	4.17	1.88	0.04	2.28	35.45	0.16	0.85	0.25	< D.L.	30.57	100.20
SC 25	37.82	5.67	1.30	0.03	1.91	27.02	0.41	1.53	0.19	< D.L.	23.83	99.69
Delta front deposits												
SD 1	10.24	2.31	1.42	0.04	1.67	45.41	0.08	0.51	0.12	< D.L.	37.28	99.07
SD 2	29.76	10.14	3.22	0.04	3.09	25.58	0.17	2.08	0.43	< D.L.	24.99	99.50
SD 3	28.42	8.70	4.15	0.06	2.95	26.46	0.14	1.67	0.42	< D.L.	26.58	99.55
SD 4	25.98	4.46	2.39	0.05	2.78	32.78	0.13	0.94	0.31	< D.L.	28.75	98.57
SD 5	18.07	3.14	1.29	0.06	1.96	40.40	0.13	0.63	0.18	< D.L.	33.33	99.18
SD 6	15.98	4.12	1.58	0.11	1.71	40.44	0.11	0.84	0.20	< D.L.	33.73	98.81
SD 7	40.17	13.67	4.02	0.04	2.07	16.44	0.24	2.78	0.58	< D.L.	18.68	98.69
SD 8	20.25	3.37	1.05	0.05	2.19	38.11	0.22	0.85	0.16	< D.L.	32.32	98.57
SD 9	34.74	5.93	1.09	0.05	1.40	28.78	0.67	1.49	0.12	< D.L.	24.84	99.09
SD 10	38.88	6.35	0.98	0.04	1.12	26.28	0.72	1.75	0.12	< D.L.	22.60	98.84
SD 11	22.40	2.88	1.04	0.06	1.72	38.22	0.19	0.70	0.15	< D.L.	31.60	98.96
SD 12	49.66	14.63	2.36	0.03	2.35	11.09	0.49	2.23	0.35	< D.L.	15.71	98.90
SD 20	30.72	7.40	2.70	0.04	2.75	27.75	0.30	1.39	0.39	< D.L.	25.69	99.12
SD 21	19.23	5.61	1.94	0.03	9.09	28.79	0.17	1.33	0.31	< D.L.	33.12	99.61
SD 22	16.67	4.28	1.61	0.02	8.56	32.28	0.13	1.01	0.25	< D.L.	34.54	99.33
SD 23	36.58	4.17	0.72	0.02	1.42	29.55	0.65	1.38	0.00	< D.L.	24.79	99.27
SD 24	22.12	3.12	1.14	0.03	1.86	38.33	0.40	0.83	0.11	< D.L.	31.82	99.75
SD 25	34.96	5.57	1.95	0.03	2.44	27.77	0.61	1.50	0.25	< D.L.	24.09	99.16
SD 26	17.66	5.27	1.98	0.04	2.13	38.36	0.11	0.92	0.25	< D.L.	32.70	99.42

Sample	SiO_2	Al_2O_3	Fe_2O_3	MnO	MgO	CaO	Na_2O	K_2O	TiO_2	P_2O_5	LOI (1000°C)	Total
Pro-delta deposits (turbidite)												
ST 2	21.95	6.91	2.72	0.05	2.84	32.92	0.29	1.31	0.30	< D.L.	30.07	99.36
ST 3	23.19	7.53	2.92	0.04	2.90	32.39	0.31	1.43	0.32	< D.L.	29.47	100.50
ST 4	26.48	4.12	1.96	0.05	2.16	34.48	0.35	0.79	0.28	< D.L.	29.13	99.81
ST 5	27.49	8.98	3.27	0.04	2.81	28.27	0.38	1.64	0.39	< D.L.	26.87	100.14

Table 4.4 Trace elements concentrations in samples from the Ainsa paleo-delta (in ppm)

Sample	Li	Be	Sc	V	Cr	Co	Ni	Cu	Zn	Ga	Ge	As	Se	Rb	Sr	Y	Zr	Nb	Mo	Cd	Sn	Sb	Cs
SA 1	29	1.5	5	40	29	6	13	8	20	8	0.7	4	0.3	54	229	18	87	9	0.7	0.3	2	1.6	5
SA 2	33	1.3	6	51	34	7	15	10	24	9	0.8	4	2.7	56	345	19	60	9	0.6	0.3	2	1.2	5
SA 3	36	1.2	6	52	37	7	16	13	27	9	0.7	4	1.8	59	283	17	72	8	0.5	0.2	2	1.1	6
SA 4	80	2.5	10	103	75	14	30	24	58	20	1.5	32	2.2	132	234	21	73	12	1.5	0.2	4	2.1	15
SA 5	42	1.6	7	66	42	7	22	13	39	9	0.8	10	1.3	59	262	12	45	7	0.7	0.1	2	1.1	6
SA 6	8	0.4	2	33	11	3	4	3	8	2	0.3	1	1.0	18	447	6	15	1	0.2	0.1	0	0.2	1
SA 7	42	2.0	8	60	44	7	24	10	35	9	0.8	7	1.0	56	229	11	47	7	0.6	0.1	2	1.4	6
SA 9	17	0.8	4	26	22	3	7	4	15	5	0.3	2	0.6	47	200	8	23	3	0.3	0.1	1	0.4	2
SA 10	25	1.3	5	34	24	4	13	6	21	6	0.5	3	1.9	38	223	11	38	5	0.3	0.1	1	0.7	3
SA 11	41	1.8	7	48	38	7	20	11	36	8	0.6	3	2.2	47	301	11	49	7	0.3	0.1	2	0.7	4
SA 12	18	0.7	4	28	26	3	8	4	15	5	0.3	1	1.1	39	244	7	26	3	0.1	0.1	1	0.3	2
SA 13	17	0.8	4	23	20	3	6	4	13	5	0.3	1	0.3	45	251	7	22	3	0.2	0.1	1	0.4	2
SA 15	54	0.6	7	65	47	9	20	15	33	13	1.0	13	0.6	88	275	20	83	12	0.6	0.0	3	1.8	8
SA 16	17	0.0	3	26	21	3	7	4	16	4	0.4	0	0.3	33	216	8	21	4	0.2	0.1	1	0.6	2
SA 17	15	0.2	2	24	16	3	5	3	11	6	0.2	0	0.3	57	152	10	30	5	0.1	0.3	2	0.4	4
SA 20	41	1.2	7	50	39	6	19	10	32	8	0.7	5	1.3	48	329	12	49	7	0.5	0.1	2	0.9	4
SA 21	36	1.0	6	52	32	5	16	10	29	6	1.2	6	0.9	42	512	10	40	5	0.5	0.1	1	0.5	3
SA 22	70	1.9	10	87	59	10	30	18	56	13	1.0	15	1.6	81	856	14	51	8	1.2	0.2	2	1.2	8
SA 23	20	0.6	5	45	36	3	9	5	29	4	0.3	2	1.1	34	482	8	17	3	0.2	0.1	1	0.4	2
SA 30	41	1.6	6	61	43	7	18	14	27	10	0.9	4	1.9	57	476	15	51	9	1.3	0.4	2	1.0	6
SA 31	39	1.0	6	51	35	5	19	12	29	6	0.5	5	1.5	38	457	11	37	5	0.6	0.1	1	0.6	3
SA 32	64	1.2	8	74	60	9	24	18	40	16	1.2	3	0.5	104	471	20	79	12	0.3	0.0	4	1.2	9
SA 33	15	0.0	3	24	21	2	5	3	9	5	0.1	0	0.0	53	432	9	26	3	0.0	0.0	1	0.3	2
SA 34	18	0.6	4	24	22	2	7	4	13	3	0.2	1	1.2	31	357	7	18	3	0.2	0.1	1	0.2	2
SA 35	11	0.0	2	18	16	2	4	2	6	4	0.1	0	0.0	40	325	7	20	2	0.0	0.0	1	0.2	2
SC 1	41	1.0	6	45	33	6	19	12	34	6	1.2	8	1.3	42	549	11	35	6	0.6	0.1	2	0.4	4
SC 2	29	0.8	5	44	29	4	14	10	26	5	0.5	7	1.1	35	1171	9	36	5	0.4	0.1	1	0.4	3
SC 3	66	1.6	9	81	57	9	31	17	57	11	0.9	5	1.2	73	390	13	53	8	0.7	0.1	2	0.5	7
SC 4	66	1.7	9	82	59	9	32	16	62	12	0.9	6	1.3	81	433	12	46	8	0.5	0.1	2	0.5	8
SC 5	24	0.7	5	33	25	4	11	6	23	4	0.5	1	1.2	31	355	10	41	5	0.5	0.1	1	0.2	3
SC 6	10	0.3	3	29	34	2	6	4	12	2	0.2	1	0.7	10	356	6	12	1	0.3	0.1	0	0.1	1
SC 7	14	0.7	3	17	16	2	7	2	11	4	0.4	1	1.0	43	308	6	15	2	0.2	0.1	1	0.2	2
SC 9	39	1.0	5	45	33	9	25	15	33	7	0.4	7	1.6	43	303	8	32	5	0.4	0.1	1	0.4	5
SC 10	43	0.9	6	52	37	5	18	11	29	6	0.6	4	1.0	37	389	9	30	5	0.8	0.1	1	0.5	3

Sample	Ba	La	Ce	Pr	Nd	Sm	Eu	Gd	Tb	Dy	Ho	Er	Tm	Yb	Lu	Hf	Ta	W	Hg	Tl	Pb	Th	U
SA 1	237	24	45	5	21	4	0.9	4	0.7	4	0.7	2	0.3	2	0.3	3.0	1.7	1.8	10.0	0.4	13	8	3
SA 2	279	24	47	6	22	5	1.0	5	0.7	4	0.8	2	0.3	2	0.3	2.2	1.7	1.8	10.0	0.4	14	8	2
SA 3	256	23	46	5	21	4	0.9	4	0.6	3	0.6	2	0.2	2	0.2	2.4	1.0	1.7	3.8	0.3	13	8	2
SA 4	694	34	64	8	28	5	1.2	5	0.7	4	0.9	3	0.3	2	0.3	2.6	1.7	2.7	6.0	0.9	21	13	3
SA 5	249	17	34	4	15	3	0.6	3	0.4	2	0.4	1	0.2	1	0.2	1.3	0.6	1.2	0.5	0.3	9	5	2
SA 6	68	7	14	2	7	1	0.3	1	0.2	1	0.2	1	0.1	0	0.1	0.5	0.1	0.2	0.1	0.1	6	1	1
SA 7	144	18	35	4	15	3	0.6	3	0.4	2	0.4	1	0.2	1	0.2	1.4	0.6	1.2	0.2	0.3	9	6	2
SA 9	168	10	20	2	9	2	0.4	2	0.3	1	0.3	1	0.1	1	0.1	0.8	0.5	0.7	1.1	0.3	8	4	1
SA 10	108	15	29	3	13	3	0.6	2	0.4	2	0.4	1	0.2	1	0.1	1.2	0.6	1.0	0.9	0.2	7	4	1
SA 11	172	16	31	4	14	3	0.6	3	0.4	2	0.4	1	0.2	1	0.2	1.4	0.6	1.0	0.2	0.3	7	5	2
SA 12	178	9	17	2	8	2	0.4	2	0.2	1	0.2	1	0.1	1	0.1	0.8	0.3	0.6	0.3	0.2	6	2	1
SA 13	167	9	19	2	9	2	0.4	2	0.2	1	0.2	1	0.1	1	0.1	0.7	0.4	0.9	2.8	0.2	8	3	1
SA 15	453	32	63	7	29	5	0.9	5	0.5	4	0.5	2	0.0	2	0.0	2.6	1.2	2.0	1.0	0.1	17	12	3
SA 16	147	12	23	3	11	2	0.4	2	0.2	2	0.2	1	0.0	1	0.0	0.6	0.7	0.8	4.3	0.0	11	4	5
SA 17	201	18	35	4	16	3	0.6	3	0.3	2	0.3	1	0.0	1	0.0	1.0	0.7	0.9	1.4	0.2	22	5	8
SA 20	157	17	33	4	15	3	0.7	3	0.4	2	0.5	1	0.2	1	0.2	1.5	0.5	1.4	3.5	0.3	9	6	2
SA 21	133	13	26	3	12	2	0.5	2	0.4	2	0.4	1	0.2	1	0.2	1.2	0.5	1.4	3.6	0.3	7	4	1
SA 22	187	21	41	5	18	3	0.7	3	0.5	3	0.5	2	0.2	1	0.2	1.6	0.7	1.6	2.8	0.5	12	7	2
SA 23	155	10	18	2	9	2	0.5	2	0.3	1	0.3	1	0.1	1	0.1	0.6	0.2	0.8	3.6	0.3	6	3	1
SA 30	170	21	39	5	18	4	0.9	4	0.7	3	0.7	2	0.4	2	0.4	2.0	2.1	2.1	16.8	0.7	13	7	3
SA 31	115	14	26	3	12	2	0.5	2	0.3	2	0.4	1	0.2	1	0.2	1.1	0.4	1.2	3.3	0.2	8	4	2
SA 32	300	32	61	7	27	5	0.9	5	0.5	4	0.6	2	0.1	2	0.1	2.7	1.5	2.2	2.7	0.4	28	11	4
SA 33	356	13	25	3	12	2	0.5	2	0.2	2	0.2	1	0.0	1	0.0	0.8	0.5	0.5	1.1	0.1	12	4	2
SA 34	92	9	18	2	9	2	0.4	2	0.3	1	0.3	1	0.1	1	0.1	0.6	0.2	1.3	4.5	0.2	6	2	5
SA 35	267	10	19	2	9	2	0.4	2	0.1	1	0.1	1	0.0	1	0.0	0.7	0.4	0.4	0.9	0.1	9	3	1
SC 1	99	13	25	3	12	2	0.5	2	0.4	2	0.4	1	0.2	1	0.1	1.2	0.6	1.8	7.8	0.3	9	4	2
SC 2	148	11	22	3	10	2	0.5	2	0.3	2	0.3	1	0.1	1	0.1	1.1	0.5	0.9	0.8	0.2	7	3	2
SC 3	124	19	37	4	16	3	0.7	3	0.4	2	0.5	1	0.2	1	0.2	1.5	0.6	1.3	0.3	0.4	12	6	3
SC 4	125	19	36	4	15	3	0.6	3	0.4	2	0.4	1	0.2	1	0.2	1.4	0.9	1.4	0.4	0.5	12	6	2
SC 5	73	13	26	3	12	2	0.5	2	0.3	2	0.3	1	0.1	1	0.1	1.3	0.4	0.6	0.1	0.2	7	4	1
SC 6	32	6	11	1	5	1	0.3	1	0.2	1	0.2	1	0.1	0	0.1	0.4	0.1	0.2	0.2	0.1	3	1	1
SC 7	165	7	14	2	7	1	0.4	1	0.2	1	0.2	1	0.1	1	0.1	0.5	0.2	0.5	0.6	0.3	8	2	1
SC 9	110	12	25	3	11	2	0.4	2	0.3	1	0.3	1	0.1	1	0.1	1.0	0.6	2.2	9.8	0.3	19	4	2
SC 10	223	12	22	3	10	2	0.5	2	0.3	2	0.3	1	0.1	1	0.1	0.9	0.4	1.3	3.7	0.2	6	4	2

Sample	Li	Be	Sc	V	Cr	Co	Ni	Cu	Zn	Ga	Ge	As	Se	Rb	Sr	Y	Zr	Nb	Mo	Cd	Sn	Sb	Cs
SC 11	46	0.9	6	49	39	6	21	11	34	7	0.5	2	0.7	41	382	10	37	6	0.3	0.1	1	0.3	4
SC 12	57	1.3	8	67	51	7	26	13	44	10	0.8	3	2.2	59	379	11	42	7	0.9	0.1	2	0.7	5
SC 13	15	0.3	4	27	29	2	8	3	13	3	0.3	1	0.7	11	350	6	13	2	0.2	0.1	0	0.1	1
SC 14	15	0.3	5	31	39	3	10	4	14	3	0.3	1	0.9	12	366	6	14	2	0.4	0.1	0	0.2	1
SC 20	44	1.6	7	61	42	8	18	13	32	12	0.9	4	2.2	73	392	20	80	12	0.9	0.4	2	2.0	7
SC 21	80	-	9	83	57	9	28	16	46	15	1.0	10	4.6	87	469	14	-	-	0.8	0.1	2	2.1	9
SC 22	38	0.6	6	50	36	6	14	13	26	10	0.8	4	1.1	63	451	18	72	9	0.5	0.0	2	1.9	5
SC 23	17	0.3	3	24	17	3	6	5	14	7	0.2	0	0.0	77	251	8	26	3	0.0	0.0	2	0.4	3
SC 24	26	0.3	4	40	33	5	11	9	19	7	0.6	3	0.8	40	425	13	37	6	0.4	0.0	1	1.3	2
SC 25	29	0.6	4	31	25	5	9	7	19	9	0.5	1	0.2	76	395	11	32	6	0.1	0.1	3	0.7	4
SD 1	18	0.5	3	23	15	3	9	4	22	3	0.6	9	1.5	20	409	7	15	2	0.7	0.1	1	0.5	2
SD 2	82	1.7	9	85	58	8	23	18	55	14	1.3	10	1.3	114	448	14	55	10	0.6	0.2	3	0.9	13
SD 3	75	1.2	8	83	57	11	27	21	51	16	1.4	10	0.8	115	422	21	76	13	0.7	0.1	3	2.1	17
SD 4	35	1.0	5	41	29	6	20	7	61	6	1.2	8	1.7	38	453	12	46	6	0.8	0.2	1	0.6	4
SD 5	22	0.0	3	27	24	4	10	5	13	4	0.4	1	0.7	30	399	13	30	5	0.2	0.0	1	0.5	2
SD 6	33	0.9	4	41	28	5	13	11	26	7	0.5	3	0.3	52	1148	12	33	6	0.3	0.0	1	0.8	6
SD 7	76	2.0	12	112	68	11	36	22	62	17	1.0	12	2.3	124	259	15	64	11	0.7	0.2	3	1.2	15
SD 8	22	0.6	4	26	22	4	9	5	15	5	0.5	3	0.6	42	322	14	29	5	0.4	0.1	1	0.6	4
SD 9	26	0.0	2	23	15	3	8	3	10	7	0.3	2	0.0	82	293	12	28	4	1.4	0.0	2	0.9	2
SD 10	28	0.8	2	26	15	3	6	3	12	8	0.3	2	0.3	81	250	11	23	4	1.3	0.0	2	0.7	3
SD 11	19	0.6	3	20	20	2	9	3	12	3	0.7	2	0.5	25	356	8	16	2	0.5	0.1	1	0.3	2
SD 12	90	2.6	7	74	62	6	21	14	33	15	0.6	5	0.8	93	207	8	45	7	1.5	0.1	3	0.8	10
SD 20	47	1.1	6	65	42	5	20	10	37	9	0.7	8	1.7	59	453	12	50	7	0.2	0.1	2	1.0	5
SD 21	34	0.8	6	55	38	4	13	8	30	8	0.8	5	0.9	48	308	11	41	6	0.7	0.1	1	0.4	3
SD 22	26	0.7	5	42	30	4	13	7	26	6	0.8	5	0.9	36	380	11	35	5	0.6	0.1	1	0.3	2
SD 23	10	0.7	2	16	13	1	4	1	8	3	0.2	3	1.2	38	306	5	11	1	0.6	0.1	1	0.2	2
SD 24	13	0.5	3	19	17	2	7	2	11	3	0.4	6	0.5	26	499	5	21	2	2.7	0.1	1	0.5	1
SD 25	28	1.2	5	34	27	4	11	4	28	6	0.5	5	1.4	55	422	9	28	4	0.6	0.1	2	0.4	4
SD 26	40	1.1	6	50	35	4	16	11	22	7	0.6	7	0.6	40	430	8	32	5	0.7	0.1	1	0.4	3
ST 2	43	1.2	6	63	41	10	32	10	39	8	0.7	6	1.2	61	480	11	42	6	0.7	0.1	2	0.5	5
ST 3	44	1.2	7	67	42	6	20	10	38	9	0.6	8	2.0	66	469	11	44	6	0.4	0.1	2	0.4	6
ST 4	24	0.6	5	37	25	5	15	4	43	5	0.5	10	1.5	31	631	10	47	5	0.4	0.1	1	0.7	2
ST 5	55	1.4	8	84	53	6	24	12	49	11	0.8	8	1.5	80	504	12	55	8	0.4	0.2	2	0.6	7

Sample	Ba	La	Ce	Pr	Nd	Sm	Eu	Gd	Tb	Dy	Ho	Er	Tm	Yb	Lu	Hf	Ta	W	Hg	Tl	Pb	Th	U
SC 11	116	13	25	3	12	2	0.5	2	0.3	2	0.4	1	0.1	1	0.1	1.1	0.4	1.1	2.1	0.3	7	4	2
SC 12	145	16	30	4	14	3	0.6	2	0.4	2	0.4	1	0.2	1	0.2	1.9	0.6	2.8	21.2	0.4	10	5	4
SC 13	40	8	16	2	9	2	0.4	2	0.2	1	0.2	1	0.1	1	0.1	0.4	0.1	0.5	2.0	0.1	3	2	2
SC 14	42	8	16	2	8	2	0.4	1	0.2	1	0.2	1	0.1	1	0.1	0.6	0.1	1.4	5.8	0.1	4	1	1
SC 20	373	25	50	6	24	5	1.2	5	0.8	4	0.9	2	0.5	2	0.5	3.6	3.5	2.3	11.6	0.8	14	9	3
SC 21	259	24	46	5	20	4	0.7	4	0.5	3	0.6	2	0.2	2	0.2	2.8	-	1.5	-	0.5	17	10	3
SC 22	325	27	54	6	25	5	0.9	5	0.5	4	0.6	2	0.2	2	0.1	2.4	1.0	1.5	1.2	0.2	13	9	3
SC 23	320	14	28	3	13	2	0.5	2	0.2	2	0.2	1	0.0	1	0.0	0.8	0.5	0.7	3.1	0.3	20	6	9
SC 24	286	23	43	5	20	4	0.7	4	0.4	3	0.4	1	0.1	1	0.0	1.2	0.6	0.9	0.7	0.0	11	6	2
SC 25	382	18	34	4	16	3	0.7	3	0.3	2	0.3	1	0.1	1	0.1	1.2	0.8	1.2	2.5	0.4	15	5	2
SD 1	48	9	17	2	8	2	0.4	2	0.2	1	0.3	1	0.1	1	0.1	0.6	0.3	1.5	10.7	0.1	5	2	1
SD 2	197	21	40	5	18	3	0.7	3	0.4	2	0.5	2	0.2	1	0.2	1.6	0.8	1.6	3.4	0.6	14	8	2
SD 3	245	33	63	7	28	5	1.1	5	0.6	4	0.7	2	0.2	2	0.2	2.5	1.3	2.3	2.1	0.5	25	12	4
SD 4	92	14	28	3	13	3	0.6	3	0.4	2	0.4	1	0.2	1	0.2	1.7	0.5	2.9	10.2	0.2	7	4	2
SD 5	251	16	31	4	15	3	0.5	3	0.2	2	0.2	1	0.0	1	0.0	0.8	0.6	0.6	1.0	0.0	8	4	2
SD 6	836	17	32	4	15	3	0.8	3	0.3	2	0.4	1	0.1	1	0.1	1.1	0.7	1.1	2.2	0.2	10	5	2
SD 7	279	28	54	6	23	4	0.8	4	0.5	3	0.6	2	0.2	2	0.2	1.9	0.9	1.8	0.3	0.6	16	9	2
SD 8	124	19	34	4	16	3	0.7	3	0.4	3	0.5	1	0.2	1	0.2	1.0	0.9	1.1	5.7	0.3	9	4	2
SD 9	282	15	29	3	13	2	0.5	2	0.1	2	0.2	1	0.0	1	0.0	0.7	0.6	0.8	0.7	0.1	14	5	2
SD 10	266	14	26	3	13	3	0.8	3	0.4	2	0.4	1	0.1	1	0.1	0.8	0.8	0.8	3.1	0.4	12	5	2
SD 11	81	10	19	2	10	2	0.5	2	0.3	1	0.3	1	0.1	1	0.1	0.5	0.2	1.0	3.8	0.1	5	3	1
SD 12	236	16	31	4	13	2	0.5	2	0.3	2	0.3	1	0.1	1	0.1	1.4	0.7	1.4	1.5	0.5	10	10	2
SD 20	123	17	34	4	15	3	0.6	3	0.4	2	0.4	1	0.2	1	0.2	1.5	0.7	1.2	0.7	0.3	8	5	2
SD 21	112	15	29	4	14	3	0.6	3	0.4	2	0.4	1	0.2	1	0.2	1.1	0.4	0.8	5.6	0.4	6	4	1
SD 22	86	14	27	3	13	3	0.6	2	0.4	2	0.4	1	0.2	1	0.1	1.0	0.3	0.6	2.4	0.2	5	3	1
SD 23	153	6	12	1	6	1	0.3	1	0.2	1	0.2	0	0.1	0	0.1	0.4	0.1	0.2	0.2	0.2	7	2	1
SD 24	83	5	10	1	5	1	0.3	1	0.2	1	0.2	0	0.1	0	0.1	0.6	0.2	0.4	0.2	0.2	5	2	1
SD 25	157	12	24	3	11	2	0.5	2	0.3	2	0.3	1	0.1	1	0.1	1.0	0.4	0.9	1.7	0.3	8	4	1
SD 26	71	11	21	3	10	2	0.4	2	0.3	1	0.3	1	0.1	1	0.1	1.1	0.4	1.6	7.3	0.2	6	4	3
ST 2	117	15	28	3	13	2	0.5	2	0.3	2	0.4	1	0.2	1	0.1	1.2	0.5	1.9	8.1	0.3	12	5	2
ST 3	123	15	29	3	13	2	0.5	2	0.3	2	0.4	1	0.2	1	0.2	1.3	0.3	1.1	0.3	0.3	9	5	2
ST 4	104	12	25	3	12	2	0.5	2	0.3	2	0.3	1	0.1	1	0.1	1.3	0.5	1.0	1.0	0.2	6	4	1
ST 5	131	18	34	4	15	3	0.6	3	0.4	2	0.4	1	0.2	1	0.2	1.6	0.7	1.9	5.3	0.4	11	6	2

4.4.3 Li isotope system

In bulk samples, an overall negative trend (Fig 4.7) is found between the δ^7Li values and the Al/Si ratio, which is used here as a grain size proxy for detrital sediments (Bouchez et al., 2011; Lupker et al., 2011; Dellinger et al., 2014). Heavier Li isotopes are enriched in the coarser fraction, whereas lighter Li isotopes are enriched in the finer part. This observation is in agreement with the previous study on the δ^7Li of river sediments (Dellinger et al., 2014). For the coarse fraction, the δ^7Li values show no significant differences between the various depositional environments. Nevertheless, from the intermediate to fine fractions, the δ^7Li composition of marine sediments are consistently lower than that of continental sediments. Accordingly, the lowest δ^7Li value is 1.70‰ for the alluvial deposits, −0.44 ‰ for delta plain sediments, and −2.42 ‰ for marine deposits.

4.4.4 Silicon isotope system

As observed for the Li isotope system, the δ^{30}Si generally decreases with increasing Al/Si ratio (Fig 4.8). For the coarse fraction, the δ^{30}Si values from all environments are within the range of the upper continental crust (−0.25±0.16‰, Savage et al., 2013). The highest δ^{30}Si value is −0.07‰ for the alluvial deposits, −0.16 ‰ for the delta plain sediments, and −0.16‰ for marine deposits. Similar to the Li isotope system, the δ^{30}Si values of marine sediments are lower than that of alluvial sediments for the intermediate to fine grain sizes. The lowest δ^{30}Si value is −0.38 ‰ for alluvial deposits, −0.71 ‰ for delta plain sediments, and −0.58 ‰ for marine deposits. The range between δ^{30}Si compositions and Al/Si ratios in Ainsa sediments are within the range of sediments from present-day large river systems (Chapter 5), which is defined by primary minerals such as quartz (characterized by low Al/Si ratio and heavy δ^{30}Si) and clays (characterized by high Al/Si ratio and light δ^{30}Si).

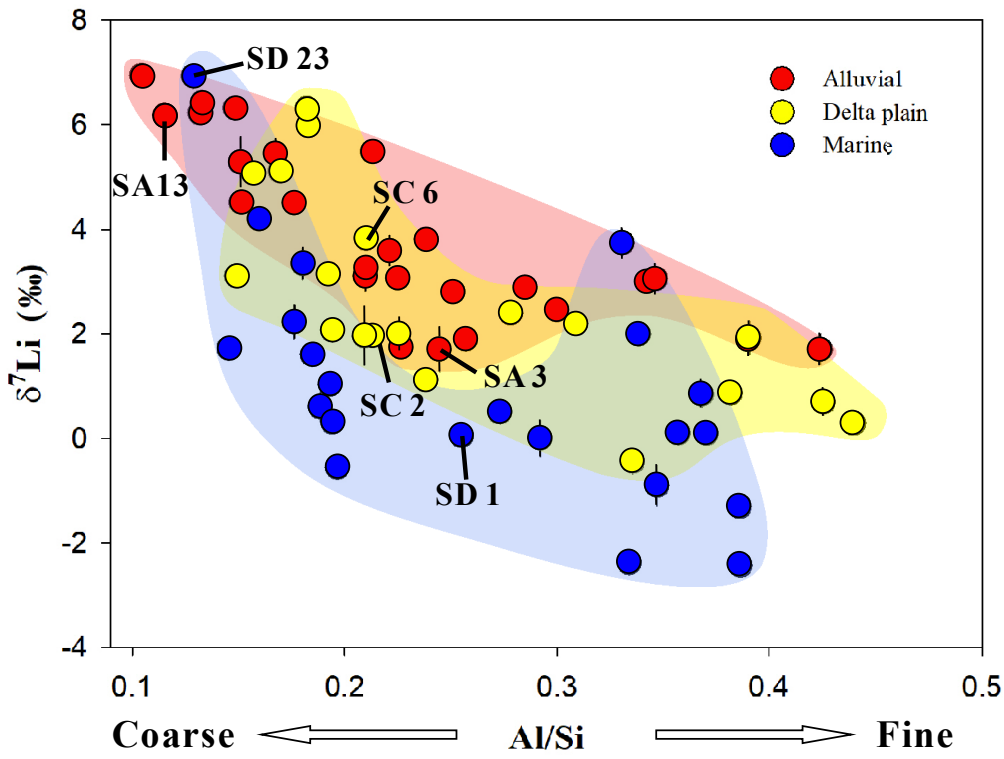

Figure 4.7 Relationship between Li isotope composition (δ^7Li) and grain size (here indexed with the Al/Si ratio; e.g. Bouchez et al., 2011) in Ainsa sediments. Coarse sediments (low Al/Si) are enriched in heavier Li, and finer sediments (high Al/Si) are enriched in lighter Li. The samples from three depositional environments (alluvial plain, delta plain, and marine) have a similar δ^7Li signature for the coarse fraction, whereas the δ^7Li values of marine sediments are isotopically lighter for the fine fractions. The samples selected for thin section observations are labelled. The areas colored in red, yellow, and blue colors represent the sediments deposited in alluvial, delta plain, and marine environments, respectively.

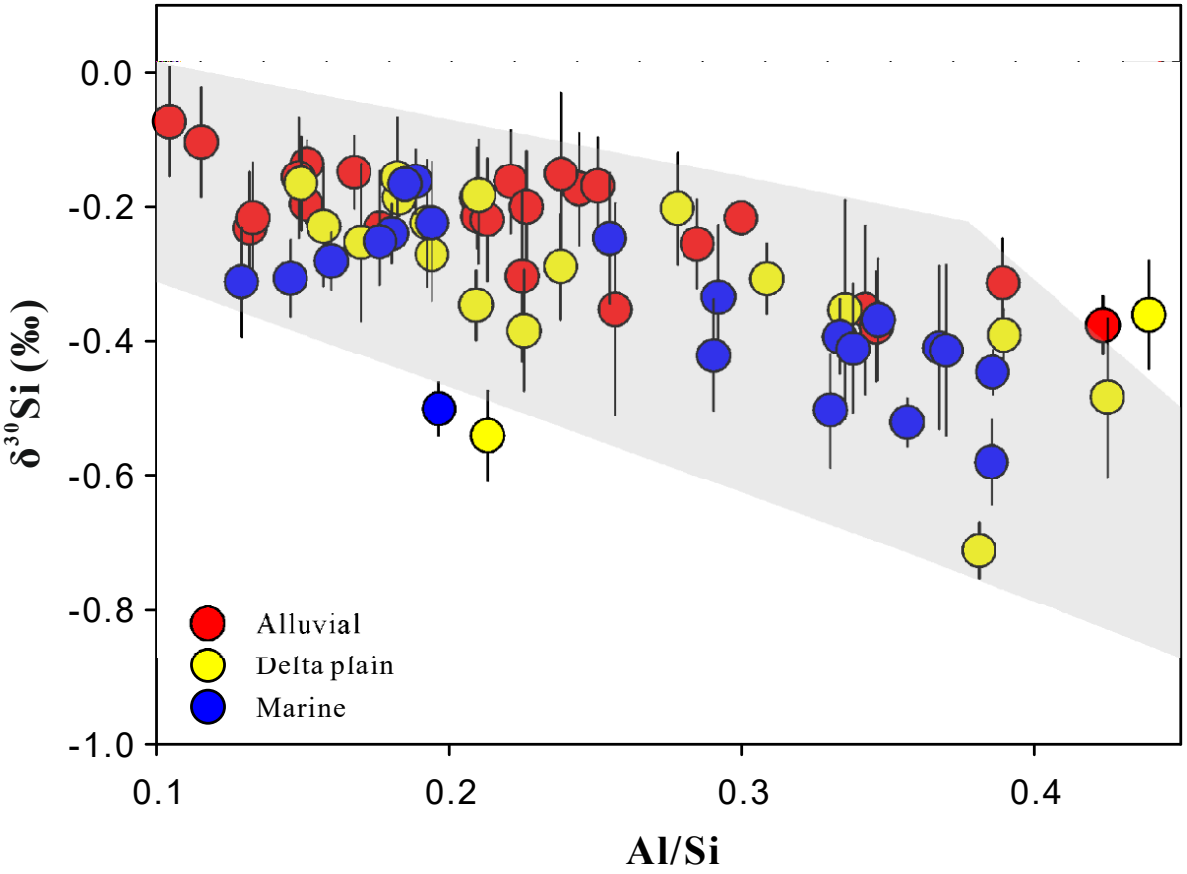

Figure 4.8 Relationship between Si isotope composition (δ^{30}Si) and grain size in Ainsa sediments. Coarse sediments (low Al/Si) are enriched in heavier Si and finer sediments (high Al/Si) are enriched in lighter Si. The alluvial samples are consistently enriched in heavier Si than those sediments which have interacted with seawater (delta plain and marine sediments). Grey area represents the Si isotope compositions of modern river sediments (see Chapter 5).

4.4.5 Neodymium isotopes system

Several samples covering the three depositional environments were selected for Nd isotope measurements. The εNd values from the Sobrarbe system have an average εNd value of −11.1 ± 0.9 (2 s.d), which is close to the estimation of present-day mean global river sediment value (εNd=−10.6; Goldstein and Jacobsen, 1988). Compared to the range of εNd in world river SPM (−42.6<εNd_{SPM}<7.1; Goldstein and Jacobsen, 1988) and in marine sediments (−14.7<$\varepsilon Nd_{Marine-}$

$_{sediment}$<1.9; Othman et al., 1989), εNd values from the studied area are within a limited range (between −11.9 and −10.0), and no systematic variation of εNd amongst different depositional environments has been found.

4.4.6 Water rinsing and HCl leaching experiments

The detailed results from the rinsing and leaching experiments are listed in Appendix i. A small fraction of less than 1% of total Li was extracted from the three-time H_2O rinsing experiment. Overall, as tabulated in Table i.1, 0.32-0.87% of total Li were rinsed in marine samples, whereas this rinseable fraction of Li was 0.17-0.43% in alluvial samples and 0.15-0.35% in delta plain samples. A first-order observation is that the marine samples contain more "rinseable" Li compared to the samples from the other environments (Fig i.1). The isotope signature of this "rinseable" Li was measured except for the alluvial samples, due to a too-low amount of Li in this rinsed fraction, and values range from 1.91 ‰ to 12.84 ‰. On the contrary, significant amounts of cations were extracted during the HCl leaching experiment (Table i.2). In all samples, Ca was significantly extracted during the 3 steps, but with a consistent decrease, and at the end of the leaching experiment a significant fraction of Ca had been leached for all samples (~55% to ~100% of total Ca). In those samples where Ca was significantly extracted (>90%), other metals such as Li, Al, or Fe were also extracted. As for the bulk samples, the Li content in the extracted solution was linked to the amount of Al and Fe extracted (Fig i.2). Therefore, we consider two pools of HCl-extracted Li in our samples: the Li contained in the first leaching solution is representative of "H_2O rinseable" (See appendix i) and "Ca-linked" Li, whereas the Li contained in the solution after Ca exhaustion (the second or the third leaching solution) is termed "Fe/Al associated" (Fig i.3, Fig i.4). The δ^7Li compositions of the first (linked to Ca) and the last (linked to Al and Fe) leaching solutions were measured (Table i.2). The δ^7Li composition of the Li fraction associated

with Ca is characterized by values close to or heavier than the bulk δ^7Li whereas the δ^7Li composition of the Li fraction associated with Al-Fe are characterized by values lighter than the bulk δ^7Li (Fig 4.10).

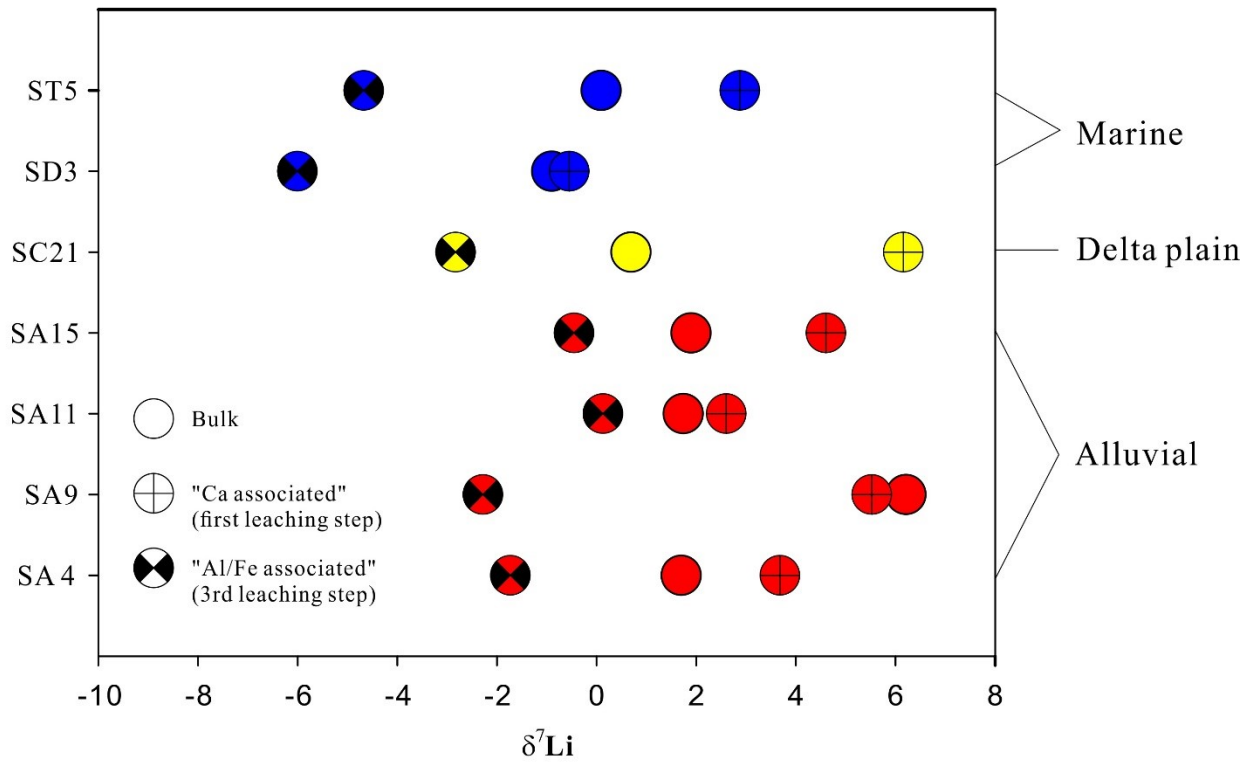

Figure 4.9 δ^7Li composition of the bulk sample, the first step of the HCl leaching procedure ("Ca-associated"), and the third step of the HCl leaching ("Al/Fe associated").

4.5 Discussion

We have observed significant differences in the Li and Si isotope signatures between the sediments deposited in various environments, with and without the influence of seawater. In the following, we will explain why we attribute these differences to processes that can account for "reverse weathering" as proposed from mass balance arguments by various authors in previous studies (Mackenzie and Garrels, 1966; Mackenzie and Kump, 1995; Misra and Froelich, 2012;

Frings et al., 2016). We will then discuss the implications of such processes occurring at estuaries and deltas on the global elemental cycles.

4.5.1 Impact of reverse weathering on the chemical and isotope composition of sediments

As stated earlier, it is difficult to distinguish authigenic clays formed via reverse weathering and detrital clays produced through continental weathering (Fig 4.1), as they have similar chemical compositions. Therefore, an addition of potential authigenic clays into detrital clays will not fundamentally change the chemical properties of a bulk sample, such as major and trace element concentrations. However, as shown in Figure 4.6, one exceptional example is that sediments which have interacted with seawater have higher Na concentrations than alluvial sediments. The mean Na content (represented by Na_2O in total mass, Table 4.3) is 0.12% in alluvial sediments, 0.24% in delta plain sediments, and 0.30% in sediments from delta slopes, indicating that Na concentrations in the seawater-contacted sediments are 200% to 250% times of that in alluvial sediments. During continental weathering, Na is soluble, *i.e.* readily freed from solids and enters the solution. The higher Na concentration in seawater-contacted sediments than in alluvial sediments, shows that processes bring Na from seawater into particulates. This could be attributed to the inclusion of seawater and/or evaporite minerals (halite) in those sediments deposited in the delta plain. Nevertheless, this process can be neglected as the leaching experiments show that the amount of Na being dissolved by 0.5 N HCl are not significantly different among the three depositional environments. In another word, the seawater Na incorporated in the sediments need to be minerals which is able to "survive" the HCl leaching procedure. One possibility for such phases is Na-rich phyllosilicates, which would then correspond to the formation of authigenic clays through reverse weathering. To date, it is still difficult to confirm this hypothesis, but our results do show a small but significant Na enrichment into sediment particles in the marine environment.

This hypothesis is further discussed below based on Si-Li isotope data.

Given the difficulties to distinguish detrital and authigenic clays simply using element concentrations, an alternative approach is to investigate the isotope systems. In theory, detrital clays are precipitated from soil solutions and authigenic clays are formed in the marine environment. The reservoirs supplying the cations in these two types of clays differ in their isotope compositions (Fig 4.1). A good example is the modern Li cycle, the isotope composition of Li in the ocean (31‰) is significantly greater than in continental waters (~23‰). In the case of sediments from the Sobrarbe delta system, systematic differences exist between sediments which have never interacted with seawater (alluvial deposits) and sediments which were influenced by seawater (delta plain and marine deposits). Sediments deposited in marine environment, in particular the fine grain size fraction, are characterized with lower δ^{30}Si and δ^{7}Li values compared to the alluvial sediments (Fig 4.7 and Fig. 4.8). Prior to ascribing the systematic difference to the effect of reverse weathering, other processes which could potentially generate the isotopic difference in alluvial and marine sediments need to be examined.

First, such distinction could in principle be attributed to a difference in the source rocks which supplied the sediments to the deposition system. Nevertheless, the Nd isotope data suggest that the alluvial sediments and the marine sediments have the same source (Table 4.1), and no difference was observed amongst various depositional environments. The Li isotope composition of detrital sediments also depends on grain size (Dellinger et al., 2014), meaning that hydrodynamic sorting alone could in principle generate δ^{7}Li variations between samples from different depositional environments. However, our sampling scheme targets at all grain sizes from each depositional environment (as shown by the over lapping ranges of the grain size proxy, Al/Si ratio, *e.g.* Fig. 4.7 & 4.8) making such effect unlikely.

Alternatively, selective dissolution of detrital minerals characterized by heavy δ^7Li in seawater could also potentially cause a lower δ^7Li in seawater-contacted sediments than alluvial sediments as observed in this study. In general, the δ^7Li values of carbonates is higher than that of silicates (Hathorne and James, 2006; Tang et al., 2007; Misra and Froelich, 2012), and δ^7Li in primary minerals are heavier than in secondary minerals such as clays (Dellinger et al., 2014). A possible scenario is thus that these heavy δ^7Li minerals are present in alluvial minerals whereas they were selectively dissolved in seawater, such that, lower bulk δ^7Li values in marine sediments could be achieved. However, our HCl-leaching experiments show that the Ca-associated Li is relatively small (<1% of bulk Li, close to the rinseable Li), and is therefore not of importance to the bulk δ^7Li composition, although this fraction of Li indeed has a relatively heavier δ^7Li. In principle, carbonate formation in seawater/costal environments could also modify the bulk δ^7Li of sediments. However, the amount of Li associated to carbonates in our sample is too low, as shown by our HCl leaching expeirments (Section 4.4.6). At high temperature (100ºC) $\Delta^7Li_{Calcite/Seawater}$ is ~ −1.9‰ to −3.1‰ and $\Delta^7Li_{Aragonite/Seawater}$ is ~ −10.9 to −12‰ (Marriott et al., 2004). It has also been shown that aragonitic organisms have lower δ^7Li signatures than those with calcite shells (Dellinger et al., 2018).

The microscopic observations show that only a very small amount of primary minerals such as mica are present in some fine alluvial sediments, but these primary minerals are sparse, and clays are much more abundant. Most importantly, the extraction of Li pools shows that in sediments, which have interacted with seawater, a significant portion (4.4% to 41.6% of bulk Li) of light Li (−6.0‰ to −2.8‰) is carried by the Al/Fe-associated phase in seawater-contacted sediments, whereas this portion of Li is relatively smaller (5.3% to 16.3% of bulk Li) and heavier (−2.3‰ to 0.1‰) in alluvial sediments. This clearly shows that the Li in the phase associated with

Fe and Al are controlling the light Li isotope composition, as also suggested by the concentration relationship between Li content and Al+Fe content (Fig 4.4).

Similarly, the δ^{30}Si is lighter in marine sediments than in alluvial sediments. This can be caused either by the loss of heavy Si or by the incorporation of light Si. No significant variations of the Si content can be observed between alluvial and marine sediments. Field studies on DSi (Bien et al., 1958; Conley and Malone, 1992; DeMaster, 2002) and global Si cycle models (Tréguer and De La Rocha, 2013; Frings et al., 2016) suggest that estuarine and deltas are sinks for Si. Our observations are thus compatible with an influx of light Si into detrital particulates in such deltaic environments.

Another potential candidate to modify the δ^{7}Li composition of detrital sediments is the Li sorption onto mineral surfaces. Pistiner and Henderson (2003) showed that Li sorption onto metallic (oxy)hydroxides (gibbsite and ferrihydrite) leads to significant δ^{7}Li fractionation in the ambient solution whereas Li sorption onto smectite does not. Similar sorption experiments have been performed with kaolinite in this work and a remarkable δ^{7}Li fractionation has been observed in the fluids (Chapter 3). This effect could potentially cause an apparent fractionation between alluvial and marine sediments, and the possibility for this process can be examined through the water rinsing experiment. Indeed, although at a very small degree (less than 1% of Li is rinsed out by 3 times water rinsing), more Li is rinsed out from marine sediments than alluvial sediments, suggesting the capacity of Li being taken up through adsorption by detrital sediments in marine environment. Nevertheless, the amount of this rinseable Li (0.15−0.87%) is too small to induce a significant effect on the bulk sediment δ^{7}Li. Additionally, this rinseable Li is isotopically heavier than the bulk Li isotope composition, showing that if the adsorption effect was governing the marine sediment diagenesis, the δ^{7}Li of bulk marine sediments would be higher than that of alluvial

sediments, which is opposite to our observations.

The remaining explanation for the observed difference (lighter Si and Li composition in marine sediments) is therefore the formation of new phases in samples that have interacted with seawater. In this case, the lower δ^7Li signature of marine sediments can be seen as counterintuitive as the seawater δ^7Li composition is heavy compared to continental waters today (Huh et al., 1998; Misra and Froelich, 2012; Dellinger et al., 2015; Henchiri et al., 2016), with modern seawater having a δ^7Li being spatially homogeneous at 31‰. Experimental studies have allowed for the estimation of isotope fractionation factors ($\Delta^7Li_{Min/Fluid} = \delta^7Li_{Min} - \delta^7Li_{Fluid}$) during fluid-mineral partition between seawater and various minerals. For example, at low temperature (25ºC), $\Delta^7Li_{Smectite/Seawater}$ is ~ −10.9‰ (Vigier et al., 2008). In general, the experimental and field data suggest that $\Delta^7Li_{Min/Fluid}$ is <0, meaning that marine authigenic clays having δ^7Li lower than seawater δ^7Li. In addition, it should be reminded that the water that has reacted with the marine sediments in the Ainsa Basin might have had a δ^7Li signature different from that of the modern ocean for different reasons. First, the seawater δ^7Li has changed through geological times. For example, it increased by 9‰ from the Palaeocene to present times. During the formation of Sobrarbe delta complex under study here (approximately 42 Ma ago) the seawater δ^7Li was estimated at ~24‰ by Misra and Froelich (2012), about 7‰ lower than present-day seawater. Second, it should also be noted that the water that has interacted with sediments in the costal context of Ainsa is not "pure" seawater but a mixture between open ocean water and continental water. Finally, the formation of the proposed new phase could also take place in sediment column, such that Li could be taken up from porewater which can have δ^7Li lower than that in seawater (Tomascak et al., 2016).

In addition, according to Misra and Froelich (2012), the variation of δ^7Li in seawater was

mostly due to changes in the style of continental weathering, which in turn affected the global riverine Li flux to the ocean. Most authors have indeed suggested that the global riverine dissolved δ^7Li was low ca. 60 Ma ago (Li and West, 2014; Wanner et al., 2014). The local river dissolved δ^7Li might also have been significantly different from the average riverine δ^7Li. A few constrained can be obtained by investigating the alluvial sediments. Compared to modern large river sediments (Dellinger et al., 2014; Dellinger et al., 2017), the δ^7Li values of the alluvial sediments studied here are relatively high (Fig 4.10). The Ainsa alluvial sediments are consistently ~4-5‰ heavier in δ^7Li across the grain size range compared to modern river sediments from Amazon, Mackenzie, Congo, and Ganga-Brahmaputra rivers (Dellinger et al., 2014), which suggests that (1) the source rock of the Sobrarbe formation had a heavier δ^7Li signature than that of the average crust derived by the large rivers listed above; and/or (2) the contribution of Li carried by the secondary minerals to total detrital Li is low, reflective of highly erosive regimes (Dellinger et al., 2017). A lower degree of clay formation at high erosion rates would indeed result in river δ^7Li being lower than for example global present-day riverine δ^7Li, in line with Misra and Froelich (2012)'s findings that the global river water δ^7Li increased from the Eocene to the present-day. Nevertheless, this interpretation is still difficult to confirm as our sediment samples only represent local conditions, and as no constrains on the source rock δ^7Li signature at Ainsa is available.

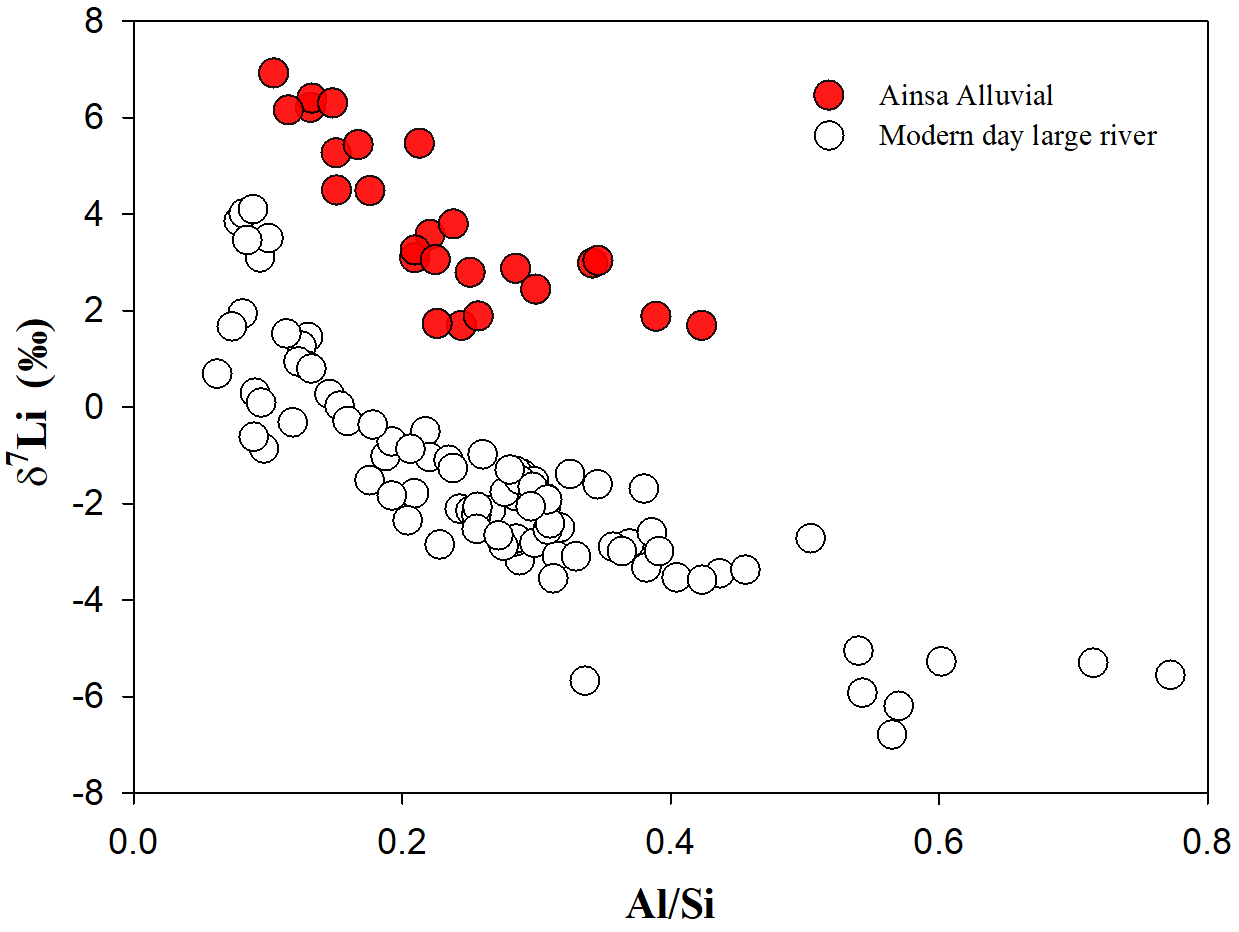

Figure 4.10 δ^7Li vs. Al/Si ratios for alluvial sediments at Ainsa basin and for sediments from modern large rivers (Dellinger et al., 2014; Dellinger et al., 2017).

The experimental study of Michalopoulos and Aller (2004) shows that BSi grains are coated by metals and/or replaced by authigenic clays during diagenesis. Therefore, the Si isotope composition of authigenic clays should depend on the BSi δ^{30}Si. Today, BSi formed in the marine environments usually have δ^{30}Si heavier than detrital sediments (Frings et al., 2016). Assuming the δ^{30}Si of Eocene seawater from Sobrarbe is not different from today, then the δ^{30}Si of BSi should be heavy, and if no δ^{30}Si fractionation is associated with the formation of authigenic clays, then the marine sediments should have a heavier δ^{30}Si than that of alluvial sediments. This is

contradictory with our results where δ^{30}Si in sediments contacted with seawater is slightly lighter than alluvial sediments. Two possible reasons can both explain our observation: (1) As for Li, the δ^{30}Si of the Eocene costal water at Sobrarbe could be lower than present-day seawater δ^{30}Si, and the formation of BSi consequentially have lower δ^{30}Si; (2) A fractionation of δ^{30}Si is associated with authigenic formation from BSi. Although lacking solid evidence from experiments, we would suspect the formation of authigenic clays following the same logics as for clay formation on land: the conversion of BSi to authigenic clays involve Si dissolution from BSi to porewater/seawater, and then precipitation of authigenic clays from porewater/seawater to solids. As for the formation of secondary minerals during weathering, the formation of authigenic clays could also preferentially take up light Si isotopes, such that eventually the marine sediments should be characterized by a lighter δ^{30}Si.

4.5.2 Coupling between Si, Li, and Fe cycles in deltas

Given the chemical species expected to be produced by reverse weathering (*e.g.* clays and oxides, equation 4-1), reverse weathering should mostly affect the finest fraction of sediments. However, low δ^{30}Si and δ^{7}Li compositions (Fig 4.7 and Fig 4.8) do not only characterize fine grains, but also grains of intermediate Al/Si values. This finding is in support of the experimental results of Michalopoulos and Aller (1995), who observed that authigenic clay formation takes place when coarse quartz grains are present in the incubation mixture.

This relative independence of reverse weathering processes on detrital sediment grain size can be attributed to the role of Fe in estuaries and deltas. River estuaries and deltas act as a major sink of riverine dissolved Fe. When river water passes through these environments, dissolved Fe is incorporated into sediments due to colloidal flocculation and adsorption onto particles, and a significant fraction (~90%) of dissolved Fe is removed into sediments (Sholkovitz, 1976; Boyle et

al., 1977). The dissolved Fe transported through subterranean aquifers is also removed due to the redox change (Slomp and Van Cappellen, 2004; Rouxel et al., 2008). This scavenged Fe might play an important role on the formation of authigenic clays at river deltas. Indeed, a common feature of authigenic minerals from experimental results (Michalopoulos and Aller, 1995; Michalopoulos and Aller, 2004) and field studies (Ku and Walter, 2003) is that those clays are Fe-rich.

During continental weathering, the precipitation of amorphous Si is a precursor reaction to clay formation (Oelze et al., 2014; Oelze et al., 2015; Geilert et al., 2014). This may be similar for the formation of authigenic clays in marine environment as well, such that mobile Si is required to be present in pore waters. In sediments, Si supply is limited (Michalopoulos and Aller, 1995; Aller, 2014), and the redissolution of BSi is considered as an important source for Si in the pore water (Van Cappellen and Qiu, 1997; Michalopoulos and Aller, 2004; Aller, 2014). In the deltaic environments, Si supply to solution can be facilitated due to the presence of Fe, as the dissolution of BSi can be promoted by iron oxides (Mayer et al., 1991), and the dissolution of quartz can be enhanced by the redox cycling of Fe (Morris and Fletcher, 1987). Actually, at Ainsa, low δ^{30}Si values in marine samples are found where Si/Fe ratios are also low, suggesting the presence of Fe aids in (Fig 4.11) preferentially taking up lighter Si.

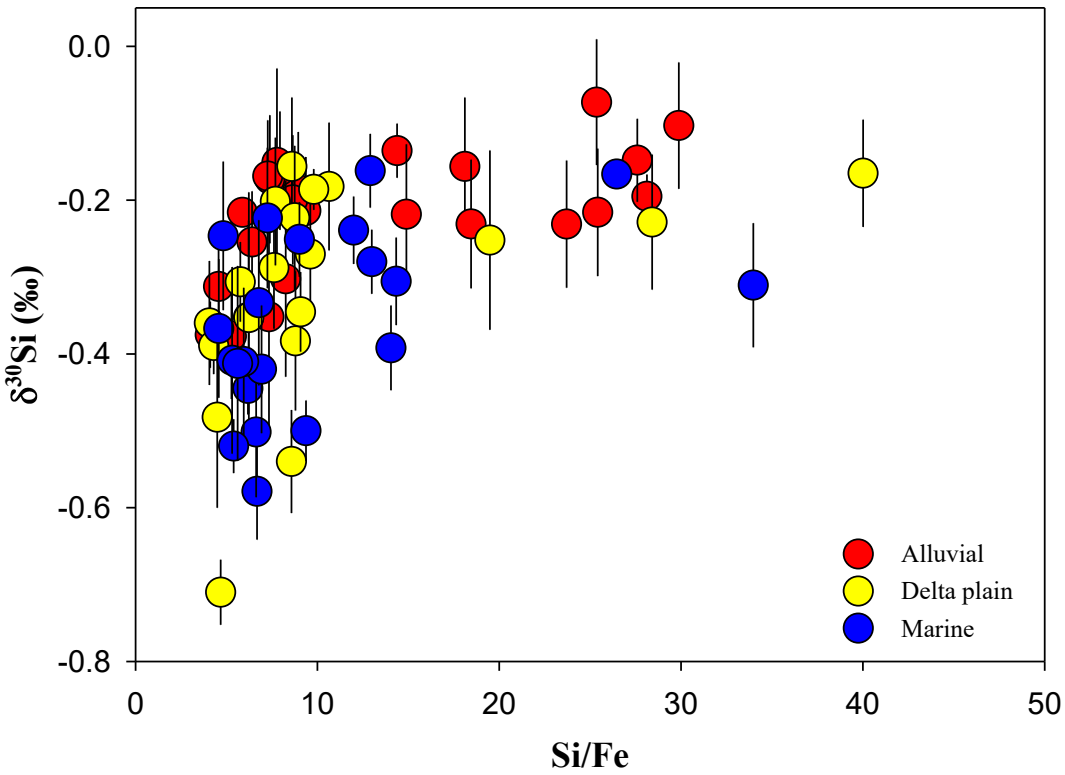

Figure 4.11 Relationship between δ^{30}Si and the Si/Fe in Ainsa sediments.

During continental weathering, low δ^{7}Li values associated with Fe-rich horizons have been observed in weathering profiles on continents too (Kısakürek et al., 2004). In a deltaic environment, with the presence of iron oxyhydroxides, a rapid process of Li sorption (Pistiner and Henderson, 2003) would preferentially take up ^{6}Li. Over larger time scales, early diagenesis allows for the formation of oxides and iron rich aluminosilicates, which could incorporate Li too, as Li^{+} (59 pm, 4-coordinate; 76 pm, 6-coordinate; 92 pm, 8-coordinate) and Fe^{2+} (63 pm, 4-coordinate; 78 pm, 6-coordinate; 92 pm, 8-coordinate) share similar ionic radii (Shannon, 1976).

This involvement of Fe in marine environments provides a suitable explanation of the potential decoupling between δ^{7}Li and grain size in marine sediments (Fig 4.7). During continental weathering, secondary aluminosilicates formation is the major way to incorporate light Li isotopes

in the solids, leading to a correlation between δ^7Li and the Al/Si ratio, which reflects the clay content. In the marine deposits, Fe incorporated into the sediments as iron oxyhydroxides provides another pathway for Li to enter the solids. As shown previously, the Li content in our samples is related to the amount of Al and Fe (Fig 4.4). The control of Al and Fe on δ^7Li is shown by the relationship between δ^7Li and the Li/(Al+Fe) ratio (Fig 4.12a). This relationship is stronger for marine sediments and more scattered for non-marine sediments. No significant differences between alluvial and non-alluvial sediments were observed when only considering the relationship between δ^7Li and the Li/Al ratio (Fig 4.12b), which may be due to the fact that Al is mostly immobile in the estuaries, leading to a lower variation of Al compared to Fe. Additionally, a clear distinction is observed between marine sediments and alluvial sediments when investigating the relationship between δ^7Li and Li/Fe ratios (Fig 4.12c), which is visible for marine sediments only. Such an observation strongly suggests that Li is incorporated and isotopically fractionated by Fe-bearing phases in marine environments.

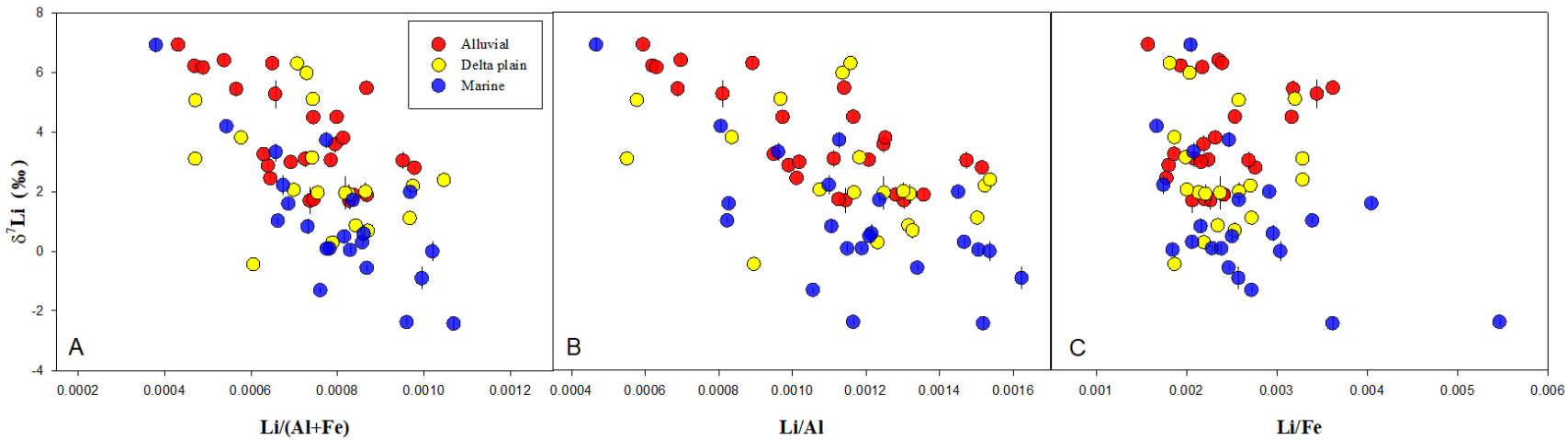

Figure 4.12 Relationship between δ^7Li and the Li/(Al+Fe), Li/Al, and Li/Fe ratios in Ainsa sediments.

Such process is further supported by the HCl-leaching experiment results. A significant fraction of Li was leached out from the solids, together with major metal elements such as Al and Fe (Fig i.2, i.3, and i.4). The analyses of δ^7Li shows that this portion of Li is enriched in ^{6}Li (Fig 4.9). Although this observation is valid for both marine and alluvial sediments, the difference between the δ^7Li of leached, Fe-associated Li, and the bulk δ^7Li are greater in marine sediments than in alluvial sediments which could be due to differences in the "source" dissolved δ^7Li, and/or in the isotope fractionation factor ($\Delta^7Li_{Min/Fluid}$) associated to continental and marine processes. Note that this relationship between δ^7Li and Fe content can also be observed from results reported in some other studies on marine sedimentary rocks and marine sediments dominated by detrital sediments (Fig 4.13). Combining the relationship between δ^7Li and Li/Fe, and the observation that marine sediments having lower δ^7Li than alluvial sediments, we suspect that the formation of Fe-Si rich phases (using Si released from BSi dissolution and Fe scavenged at deltaic environments or Fe released from redox reactions in the sedimentary column) is the cause for the observed spatial variation in δ^7Li and δ^{30}Si at Ainsa.

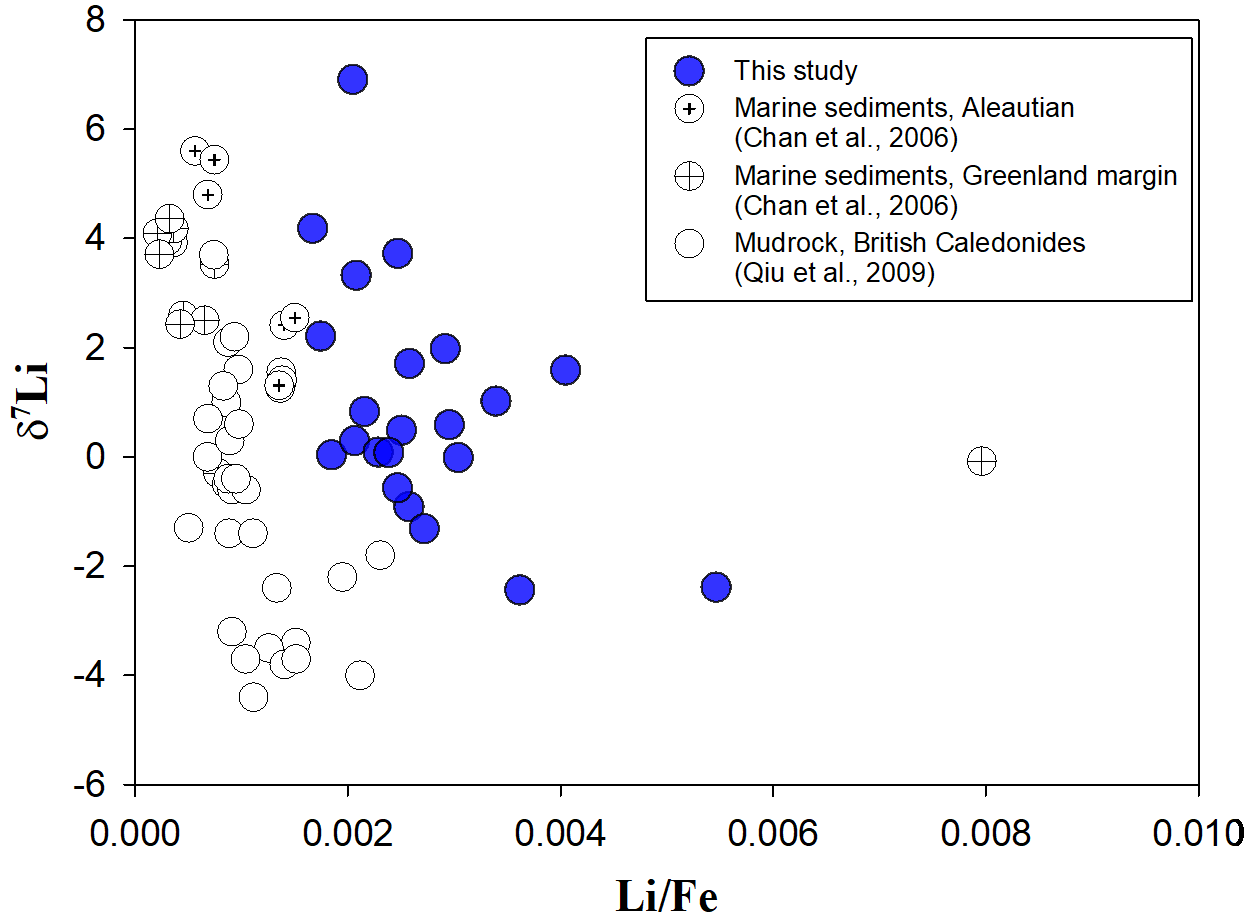

Figure 4.13 Relationship between δ^7Li and Li/Fe in marine sediments (Chan et al., 2006) and marine sedimentary rocks (this study and Qiu et al., 2009).

However, one contradiction remains: on the one hand, the studies on dissolved Li in estuaries (Stoffyn-Egli, 1982; Brunskill et al., 2003; Pogge von Strandmann et al., 2008; Murphy et al., 2014) suggest a conservative behaviour of Li; on the other hand, δ^7Li and Li content in particles do not show the same conservative pattern (Pogge von Strandmann et al., 2008; Murphy et al., 2014). However, it is of importance to point out that the seawater Li concentration is approximately ~100 times greater than the riverine Li concentration. Therefore, in deltas it might be difficult to detect variations in Li concentration outside of those due to mixing. In particular, if dissolved Li is taken up into sediments, the effect of such processes on the Li concentration in the estuarine

zone could be invisible as such variation is small compared to the seawater end-member which has a relatively homogenous Li concentration of 26μM.

4.5.3 Contribution of deltaic processes to the oceanic cycles of Si and Li

At Ainsa, the offset of δ^7Li and δ^{30}Si between marine and alluvial sediments show that light Si and Li are incorporated into marine sediments, which implies in turn that the remaining estuarine/deltaic water is elevated in δ^{30}Si and δ^7Li before entering the open ocean.

For Si, although we are unable to determine the degree of this influx from DSi into sediments, the important implication is that riverine DSi is partially removed at deltas and the remaining DSi is expected to be elevated in terms of δ^{30}Si. This implication qualitatively agrees with the observed behaviour of DSi in the field (Delvaux et al., 2013; Weiss et al., 2015), and further supports the assumptions employed in Si ocean cycle models (e.g., Frings et al., 2016). Furthermore, the marginally lower δ^{30}Si in marine sediments suggest that, if the source of Si for the formation of authigenic clays are BSi, Si isotopes are fractionated which could be occurring during the partial dissolution of BSi or the formation of authigenic clays.

In terms of Li, at this stage, it is still difficult to quantify the effect of the deltaic processes on the global open ocean. However, we can still evaluate the potential effects of these processes based on observation (Section 4.4.3, marine sediments are isotopically lighter than alluvial sediments) and our hypothesis (Section 4.5.3, Li incorporation into authigenically formed Fe-rich aluminosilicate). We can assert that the suspected formation of authigenic clays preferentially takes up light Li isotopes from ambient water and elevate the δ^7Li of seawater. As suggested in Chapter 3, the adsorption of Li onto detrital clays such as kaolinite can effectively elevate δ^7Li in seawater. Based on our observations at Ainsa (marine sediments having lighter δ^7Li than alluvial sediments, and only <1% Li is rinseable in marine sediments), we can state that the effect of

authigenic clay formation on bulk sediment is greater than that of Li adsorption.

Regardless of the process involved in Li incorporation into sediments, we can propose a first-order estimate of its effect on the global ocean δ^7Li signature. Interestingly, Murphy et al. (2014) reported that in an estuarine context dissolved Li was conservative across the mixing zone in terms of concentration but not in terms of isotope signature. This was interpreted as "exchange" between dissolved Li and sediment in the estuaries, with no net effect on the Li fluxes (dissolved vs. particulate) but entailing isotope fractionation. In such a scenario, a simple mass balance on Li fluxes and isotope composition yields that:

$$\Delta^{Li}_{diss} = \frac{(1-f^{Li}_{diss}) \times \phi \times \Delta^{Li}_{sed}}{f^{Li}_{diss}}$$

where Δ^{Li}_{diss} is the difference in δ^7Li between dissolved Li in seawater and dissolved Li in the river (before it enters the estuary); Δ^{Li}_{sed} is the difference in δ^7Li between particulate Li in seawater and particulate Li in the river; f^{Li}_{diss} is the fraction of total Li transported through the estuary as solutes, which goes unchanged through estuarine processes as observed by Murphy et al. (2014); and ϕ is the fraction of total sediments subjected to the exchange process. For example, assuming that at Ainsa, when the delta formed, f^{Li}_{diss} was equal to 0.8 (as inferred for the Eocene by Misra and Froelich, 2012, for the global scale from a mass balance model and the seawater δ^7Li), and noting that Δ^{Li}_{sed} from our measurements of alluvial and marine sediments from the paleo-delta, we can calculate that the seawater would become elevated only by Δ^{Li}_{diss} = 0.75‰ compared to river water if ϕ = 1.

This calculation can be applied for the present time and at a global scale, in order to estimate

the conditions under which an effect such as that observed by Murphy et al. (2014) (exchange of Li at estuaries with no net Li flux effect) could explain the high δ^7Li of seawater. Today Δ^{Li}_{diss} is about 8‰ and in modern rivers f^{Li}_{diss}= 0.2 (Misra and Froelich, 2012). If estuarine/deltaic exchange is controlling the seawater δ^7Li signature elevation (Δ^{Li}_{diss}= 8‰), the minimum δ^7Li difference between modern alluvial and marine sediment can be calculated as Δ^{Li}_{sed} = 2‰ if all riverine Li is subjected to this exchange process (ϕ = 1). Nevertheless, such effect is not being observed in modern marine sediments (Bouman et al., 2004; Chan et al., 2006). Therefore, the involved process need to induce a net flux of Li from the dissolved load to the sediments to explain the Li isotope cycle in the ocean - reverse weathering and adsorption could offer such a flux.

Lastly, the isotope effect of reverse weathering effect observed here would be stronger than previously estimated from an oceanic-scale mass-balance only (Misra and Froelich, 2012). Indeed, during the formation of the studied paleo-delta at Ainsa during the Eocene, seawater δ^7Li was around 24‰; at steady state, the authigenic clays would have a δ^7Li signature ~8‰, (16‰ lower than seawater; Misra and Froelich, 2012), hence heavier than the observed alluvial sediments from the paleo-delta. However, we have observed that marine sediments are lighter than alluvial sediments at Ainsa (Fig 4.7), which suggests that the apparent fractionation between seawater and this authigenic clays is much larger than 16‰ in deltaic environments.

4.6 Conclusion

Although we cannot put definite constraints on the Li ocean cycle yet, our results indicate that estuaries play a significant role in regulating the riverine Si and Li isotope signatures delivered to the ocean. We suggest that a significant sink of Li exists in estuarine environments, and that it

is coupled with the scavenging and the diagenesis of Fe in deltaic environments. During the formation Fe-rich authigenic silicate minerals, light Si and Li isotopes are preferentially taken up.

Our results of Si and Li isotope compositions in marine sediments being lighter than in alluvial sediments suggest the formation of Fe-rich authigenic clays. A simplified chemical equation corresponding to this process could be:

$$SiO_2 + Fe^{2+} + 2HCO_3^- = FeO\text{-}SiO_2 \text{ (Fe-Si rich phase)} + H_2O + 2CO_2 \quad \text{(Equation 4-2)}$$

There are two points that need to be emphasised. First, to form these Fe-Si rich phases, the sources of Si and Fe are needed. The original concept of reverse weathering (Mackenzie and Garrels, 1966) was solely established from the seawater chemistry mass balance, leading to the first-order concept where the authigenic clays were formed directly from dissolved cations in the ocean. Recent studies (Van Cappellen and Qiu, 1997; Michalopoulos and Aller, 2004; Aller, 2014; Rahman et al., 2016) have given better constraints on the source of Si, showing that the source of Si is BSi. Iron can be supplied by the dissolution of detrital iron oxides during the redox changes (Michalopoulos and Aller, 2004), and possibly through the scavenging of Fe at deltas. Second, this formation of Fe-Si rich phases, in spite of poor constraints, requires the consumption of alkalinity and produces CO_2.

Our work opens a gate for future studies: in shallow marine environments, sampling along (1) a trajectory from river channel before the mixing zone all the way to the ocean would provide better constraints on Li behaviour in deltas; (2) in the marine environment, deltas are potentially sites for the formation the authigenic silicates due to the abundance of Si (high BSi productivity) and Fe (detrital supply). If the Si and Fe supplies are the prerequisite, then areas where hydrothermal activities take place can also be good candidates for the occurrence of reverse weathering: Fe can be discharged by hydrothermal vents and Si can be provided in the form of

both BSi (radiolarian) or inorganic Si precipitation (DeMaster, 2002; François and Chaussidon, 2006); (3) experimental studies focusing on clay and oxides interaction with Li are required; (4) as the Li and Fe cycles are coupled, Li isotopes may be applied to better understand environments subjected to redox changes and past geological oxic/anoxic events.

Bibliography

Aller, R.C., 2014. 8.11 - Sedimentary Diagenesis, Depositional Environments, and Benthic Fluxes. In: Holland, H.D. and Turekian, K.K., (Eds.). Treatise on Geochemistry (Second Edition). Elsevier, Oxford.

Bien, G., Contois, D., Thomas, W., 1958. The removal of soluble silica from fresh water entering the sea. Geochimica et Cosmochimica Acta 14 (1-2), 35-54.

Bouchez, J., Gaillardet, J., France-Lanord, C., Maurice, L., Dutra-Maia, P., 2011. Grain size control of river suspended sediment geochemistry: Clues from Amazon River depth profiles. Geochemistry Geophysics Geosystems 12, Q03008.

Bouman, C., Elliott, T., Vroon, P.Z., 2004. Lithium inputs to subduction zones. Chemical Geology 212 (1), 59-79.

Boyle, E., Edmond, J., Sholkovitz, E., 1977. The mechanism of iron removal in estuaries. Geochimica et Cosmochimica Acta 41 (9), 1313-1324.

Brand, W.A., Coplen, T.B., Vogl, J., Rosner, M., Prohaska, T., 2014. Assessment of international reference materials for isotope-ratio analysis (IUPAC Technical Report). Pure and Applied Chemistry 86 (3), 425-467.

Brunskill, G.J., Zagorskis, I., Pfitzner, J., 2003. Geochemical mass balance for lithium, boron, and strontium in the Gulf of Papua, Papua New Guinea (Project TROPICS). Geochimica et Cosmochimica Acta 67 (18), 3365-3383.

Caro, G., Bourdon, B., Birck, J., Moorbath, S., 2006. High-precision 142 Nd/144 Nd measurements in terrestrial rocks: constraints on the early differentiation of the Earth’s mantle. Geochimica et Cosmochimica Acta 70 (1), 164-191.

Chan, L., Leeman, W.P., Plank, T., 2006. Lithium isotopic composition of marine sediments. Geochemistry, Geophysics, Geosystems 7 (6).

Chan, L., Gieskes, J.M., You, C., Edmond, J.M., 1994. Lithium isotope geochemistry of sediments and hydrothermal fluids of the Guaymas Basin, Gulf of California. Geochimica et Cosmochimica Acta 58 (20), 4443-4454.

Conley, D.J., Malone, T.C., 1992. Annual cycle of dissolved silicate in Chesapeake Bay: implications for the production and fate of phytoplankton biomass. Marine Ecology Progress Series , 121-128.

De Federico, A., 1981. La Sedimentacion De Talud En El Sector Occidental De La Cuenca Paleogena De Ainsa. Universidad Autónoma de Barcelona.

Dellinger, M., Bouchez, J., Gaillardet, J., Faure, L., Moureau, J., 2017. Tracing weathering regimes using the lithium isotope composition of detrital sediments. Geology 45 (5), 411-414.

Dellinger, M., Gaillardet, J., Bouchez, J., Calmels, D., Louvat, P., Dosseto, A., Gorge, C., Alanoca, L., Maurice, L., 2015. Riverine Li isotope fractionation in the Amazon River basin controlled by the weathering regimes. Geochimica et Cosmochimica Acta 164, 71-93.

Dellinger, M., West, A.J., Paris, G., Adkins, J.F., von Strandmann, Philip AE Pogge, Ullmann, C.V., Eagle, R.A., Freitas, P., Bagard, M., Ries, J.B., 2018. The Li isotope composition of marine biogenic carbonates: Patterns and Mechanisms. Geochimica et Cosmochimica Acta .

Dellinger, M., Gaillardet, J., Bouchez, J., Calmels, D., Galy, V., Hilton, R.G., Louvat, P., France-Lanord, C., 2014. Lithium isotopes in large rivers reveal the cannibalistic nature of modern continental weathering and erosion. Earth and Planetary Science Letters 401, 359-372.

Delvaux, C., Cardinal, D., Carbonnel, V., Chou, L., Hughes, H., André, L., 2013. Controls on riverine δ30Si signatures in a temperate watershed under high anthropogenic pressure (Scheldt—Belgium). Journal of Marine Systems 128, 40-51.

DeMaster, D.J., 2002. The accumulation and cycling of biogenic silica in the Southern Ocean: revisiting the marine silica budget. Deep Sea Research Part II: Topical Studies in Oceanography 49 (16), 3155-3167.

Dreyer, T., Corregidor, J., Arbues, P., Puigdefabregas, C., 1999. Architecture of the tectonically influenced Sobrarbe deltaic complex in the Ainsa Basin, northern Spain. Sedimentary Geology 127 (3-4), 127-169.

Dunlea, A.G., Murray, R.W., Ramos, D.P.S., Higgins, J.A., 2017. Cenozoic global cooling and increased seawater Mg/Ca via reduced reverse weathering. Nature Communications 8 (1), 844.

François, R., Chaussidon, M., 2006. A palaeotemperature curve for the Precambrian oceans based on silicon isotopes in cherts. Nature 443 (7114), 969.

Frings, P.J., Clymans, W., Fontorbe, G., De La Rocha, C.L., Conley, D.J., 2016. The continental Si cycle and its impact on the ocean Si isotope budget. Chemical Geology 425, 12-36.

Geilert, S., Vroon, P.Z., Roerdink, D.L., Van Cappellen, P., van Bergen, M.J., 2014. Silicon isotope fractionation during abiotic silica precipitation at low temperatures: Inferences from flow-through experiments. Geochimica et Cosmochimica Acta, 142, 95-114.

Goldstein, S.J., Jacobsen, S.B., 1988. Nd and Sr isotopic systematics of river water suspended material: implications for crustal evolution. Earth and Planetary Science Letters 87 (3), 249-265.

Hathorne, E.C., James, R.H., 2006. Temporal record of lithium in seawater: A tracer for silicate weathering? Earth and Planetary Science Letters 246 (3-4), 393-406.

Henchiri, S., Gaillardet, J., Dellinger, M., Bouchez, J., Spencer, R.G.M., 2016. Riverine dissolved lithium isotopic signatures in low-relief central Africa and their link to weathering regimes. Geophysical Research Letters 43 (9), 4391-4399.

Holland, H.D., 2005. Sea level, sediments and the composition of seawater. American Journal of Science 305 (3), 220-239.

Hughes, H., Bouillon, S., André, L., Cardinal, D., 2012. The effects of weathering variability and anthropogenic pressures upon silicon cycling in an intertropical watershed (Tana River, Kenya). Chemical Geology 308, 18-25.

Huh, Y., Chan, L., Chadwick, O.A., 2004. Behavior of lithium and its isotopes during weathering of Hawaiian basalt. Geochemistry, Geophysics, Geosystems 5 (9).

Huh, Y., Chan, L. H., & Edmond, J. M. (2001). Lithium isotopes as a probe of weathering processes: Orinoco River. Earth and Planetary Science Letters, 194(1-2), 189-199.

Huh, Y., Chan, L., Zhang, L., Edmond, J.M., 1998. Lithium and its isotopes in major world rivers: implications for weathering and the oceanic budget. Geochimica et Cosmochimica Acta 62 (12), 2039-2051.

Kısakürek, B., Widdowson, M., James, R.H., 2004. Behaviour of Li isotopes during continental weathering: the Bidar laterite profile, India. Chemical Geology 212 (1-2), 27-44.

Ku, T., Walter, L., 2003. Syndepositional formation of Fe-rich clays in tropical shelf sediments, San Blas Archipelago, Panama. Chemical Geology 197 (1-4), 197-213.

Li, G., West, A.J., 2014. Evolution of Cenozoic seawater lithium isotopes: Coupling of global denudation regime and shifting seawater sinks. Earth and Planetary Science Letters 401, 284-293.

Lupker, M., France-Lanord, C., Lave, J., Bouchez, J., Galy, V., Metivier, F., Gaillardet, J., Lartiges, B., Mugnier, J., 2011. A Rouse-based method to integrate the chemical composition of river sediments: Application to the Ganga basin. Journal of Geophysical Research-Earth Surface 116, F04012.

Mackenzie, F.T., Kump, L.R., 1995. Reverse weathering, clay mineral formation, and oceanic element cycles. Science 270 (5236), 586.

Mackenzie, F.T., Garrels, R.M., 1966. Chemical mass balance between rivers and oceans. American Journal of Science 264 (7), 507-525.

Marriott, C.S., Henderson, G.M., Crompton, R., Staubwasser, M., Shaw, S., 2004. Effect of mineralogy, salinity, and temperature on Li/Ca and Li isotope composition of calcium carbonate. Chemical Geology 212 (1-2), 5-15.

Mayer, L.M., Jorgensen, J., Schnitker, D., 1991. Enhancement of diatom frustule dissolution by iron oxides. Marine Geology 99 (1-2), 263-266.

Michalopoulos, P., Aller, R.C., 2004. Early diagenesis of biogenic silica in the Amazon delta: alteration, authigenic clay formation, and storage. Geochimica et Cosmochimica Acta 68 (5), 1061-1085.

Michalopoulos, P., Aller, R.C., 1995. Rapid clay mineral formation in Amazon delta sediments: reverse weathering and oceanic elemental cycles. Science, 270 (5236), 614-617.

Misra, S., Froelich, P.N., 2012. Lithium Isotope History of Cenozoic Seawater: Changes in Silicate Weathering and Reverse Weathering. Science 335 (6070), 818-823.

Morris, R., Fletcher, A., 1987. Increased solubility of quartz following ferrous–ferric iron reactions. Nature 330 (6148), 558.

Murphy, M.J., von Strandmann, Philip AE Pogge, Porcelli, D., Ingri, J., 2014. Li isotope behaviour in the low salinity zone during estuarine mixing. Procedia Earth and Planetary Science 10, 204-207.

Oelze, M., von Blanckenburg, F., Hoellen, D., Dietzel, M., & Bouchez, J. (2014). Si stable isotope fractionation during adsorption and the competition between kinetic and equilibrium isotope fractionation: Implications for weathering systems. Chemical geology, 380, 161-171.

Oelze, M., von Blanckenburg, F., Bouchez, J., Hoellen, D., & Dietzel, M. (2015). The effect of Al on Si isotope fractionation investigated by silica precipitation experiments. Chemical geology, 397, 94-105.

Opfergelt, S., Delmelle, P., 2012. Silicon isotopes and continental weathering processes: Assessing controls on Si transfer to the ocean. Comptes Rendus Geoscience 344 (11–12), 723-738.

Othman, D.B., White, W.M., Patchett, J., 1989. The geochemistry of marine sediments, island arc magma genesis, and crust-mantle recycling. Earth and Planetary Science Letters 94 (1-2), 1-21.

Pickering, K.T., Bayliss, N.J., 2009. Deconvolving tectono-climatic signals in deep-marine siliciclastics, Eocene Ainsa basin, Spanish Pyrenees: Seesaw tectonics versus eustasy. Geology 37 (3), 203-206.

Pistiner, J.S., Henderson, G.M., 2003. Lithium-isotope fractionation during continental weathering processes. Earth and Planetary Science Letters 214 (1), 327-339.

Pogge von Strandmann, P.A., James, R.H., van Calsteren, P., Gíslason, S.R., Burton, K.W., 2008. Lithium, magnesium and uranium isotope behaviour in the estuarine environment of basaltic islands. Earth and Planetary Science Letters 274 (3-4), 462-471.

Pogge von Strandmann, P.A., Desrochers, A., Murphy, M., Finlay, A., Selby, D., Lenton, T., 2017. Global climate stabilisation by chemical weathering during the Hirnantian glaciation.

Poitrasson, F., 2017. Silicon Isotope Geochemistry. Reviews in Mineralogy and Geochemistry 82 (1), 289-344.

Pringle, E.A., Savage, P.S., Badro, J., Barrat, J., Moynier, F., 2013a. Redox state during core formation on asteroid 4-Vesta. Earth and Planetary Science Letters 373, 75-82.

Pringle, E.A., Savage, P.S., Jackson, M.G., Barrat, J., Moynier, F., 2013b. Si Isotope Homogeneity of the Solar Nebula. The Astrophysical Journal 779 (2), 123.

Pringle, E.A., Moynier, F., Savage, P.S., Badro, J., Barrat, J., 2014. Silicon isotopes in angrites and volatile loss in planetesimals. Proceedings of the National Academy of Sciences 111 (48), 17029-17032..

Pringle, E.A., Moynier, F., Savage, P.S., Jackson, M.G., Moreira, M., Day, J.M.D., 2016. Silicon isotopes reveal recycled altered oceanic crust in the mantle sources of Ocean Island Basalts. Geochimica et Cosmochimica Acta 189, 282-295.

Qiu, L., Rudnick, R.L., McDonough, W.F., Merriman, R.J., 2009. Li and δ7Li in mudrocks from the British Caledonides: metamorphism and source influences. Geochimica et Cosmochimica Acta 73 (24), 7325-7340.

Rahman, S., Aller, R., Cochran, J., 2016. Cosmogenic 32Si as a tracer of biogenic silica burial and diagenesis: Major deltaic sinks in the silica cycle. Geophysical Research Letters 43 (13), 7124-7132.

Ramos, D.P.S., Morgan, L.E., Lloyd, N.S., Higgins, J.A., 2018. Reverse weathering in marine sediments and the geochemical cycle of potassium in seawater: Insights from the K isotopic composition (41K/39K) of deep-sea pore-fluids. Geochimica et Cosmochimica Acta .

Richard, P., Shimizu, N., Allegre, C., 1976. 143Nd/146Nd, a natural tracer: an application to oceanic basalts. Earth and Planetary Science Letters 31 (2), 269-278.

Romer, R.L., Meixner, A., Hahne, K., 2014. Lithium and boron isotopic composition of sedimentary rocks—The role of source history and depositional environment: a 250 Ma record from the Cadomian orogeny to the Variscan orogeny. Gondwana Research 26 (3-4), 1093-1110.

Rouxel, O., Sholkovitz, E., Charette, M., Edwards, K.J., 2008. Iron isotope fractionation in subterranean estuaries. Geochimica et Cosmochimica Acta 72 (14), 3413-3430.

Savage, P.S., Georg, R.B., Williams, H.M., Burton, K.W., Halliday, A.N., 2011. Silicon isotope fractionation during magmatic differentiation. Geochimica et Cosmochimica Acta 75 (20), 6124-6139.

Savage, P.S., Georg, R.B., Williams, H.M., Halliday, A.N., 2013. The silicon isotope composition of the upper continental crust. Geochimica et Cosmochimica Acta 109, 384-399.

Shannon, R.D., 1976. Revised effective ionic radii and systematic studies of interatomic distances in halides and chalcogenides. Acta crystallographica section A: crystal physics, diffraction, theoretical and general crystallography 32 (5), 751-767.

Sholkovitz, E., 1976. Flocculation of dissolved organic and inorganic matter during the mixing of river water and seawater. Geochimica et Cosmochimica Acta 40 (7), 831-845.

Sillen, L.G., 1967. The ocean as a chemical system. Science (New York, N.Y.) 156 (3779), 1189-1197.

Slomp, C.P., Van Cappellen, P., 2004. Nutrient inputs to the coastal ocean through submarine groundwater discharge: controls and potential impact. Journal of Hydrology 295 (1-4), 64-86.

Stoffyn-Egli, P., 1982. Conservative behaviour of dissolved lithium in estuarine waters. Estuarine, Coastal and Shelf Science 14 (5), 577-587.

Tang, Y., Zhang, H., Ying, J., 2007. Review of the lithium isotope system as a geochemical tracer. International Geology Review 49 (4), 374-388.

Teng, F., McDonough, W.F., Rudnick, R., Dalpé, C., Tomascak, P., Chappell, B.W., Gao, S., 2004. Lithium isotopic composition and concentration of the upper continental crust. Geochimica et Cosmochimica Acta 68 (20), 4167-4178.

Tomascak, P.B., Magna, T., Dohmen, R., 2016. Advances in Lithium Isotope Geochemistry. Springer International Publishing, Springer International Publishing Switzerland.

Tréguer, P., De La Rocha, C., 2013. The world ocean silica cycle. Annual review of marine science 5, 477-501.

Tréguer, P., Nelson, D.M., Van Bennekom, A.J., DeMaster, D.J., Leynaert, A., Quéguiner, B., 1995. The Silica Balance in the World Ocean: A Reestimate. Science 268 (5209), 375-379.

Van Cappellen, P., Qiu, L., 1997. Biogenic silica dissolution in sediments of the Southern Ocean. II. Kinetics. Deep Sea Research Part II: Topical Studies in Oceanography 44 (5), 1129-1149.

Vigier, N., Decarreau, A., Millot, R., Carignan, J., Petit, S., France-Lanord, C., 2008. Quantifying Li isotope fractionation during smectite formation and implications for the Li cycle. Geochimica et Cosmochimica Acta 72 (3), 780-792.

Wanner, C., Sonnenthal, E.L., Liu, X., 2014. Seawater δ7Li: A direct proxy for global CO2 consumption by continental silicate weathering? Chemical Geology 381, 154-167.

Weiss, A., De La Rocha, C., Amann, T., Hartmann, J., 2015. Silicon isotope composition of dissolved silica in surface waters of the Elbe Estuary and its tidal marshes. Biogeochemistry 124 (1-3), 61-79.

Zambardi, T., Poitrasson, F., 2011. Precise Determination of Silicon Isotopes in Silicate Rock Reference Materials by MC-ICP-MS. Geostandards and Geoanalytical Research 35 (1), 89-99.

Appendix i:

1. Water rinsing experiments

Table i.1 Extracted Li by water rinsing experiment (in % of bulk content).

Sample name	1st rinse	2nd rinse	3rd rinse	Total rinsed Li	δ^7Li	2 s.d.
SA3	0.10%	0.04%	0.03%	0.17%		
SA4	0.17%	0.06%	0.04%	0.28%		
SA6	0.23%	0.10%	0.10%	0.43%		
SA9	0.13%	0.05%	0.05%	0.23%		
SA11	0.16%	0.06%	0.05%	0.27%		
SA15	0.11%	0.05%	0.04%	0.20%		
SA22	0.12%	0.06%	0.04%	0.22%		
SC4	0.24%	0.07%	0.04%	0.35%	10.57	0.02
SC11	0.09%	0.04%	0.02%	0.15%	12.34	0.10
SC21	0.15%	0.04%	0.03%	0.22%	12.84	0.13
SD3	0.68%	0.12%	0.07%	0.87%	2.15	0.07
SD7	0.39%	0.08%	0.05%	0.52%	1.91	0.17
SD21	0.23%	0.06%	0.03%	0.32%	2.71	0.11
SD23	0.33%	0.10%	0.05%	0.48%	7.50	0.13
ST5	0.29%	0.17%	0.11%	0.57%	12.14	0.21

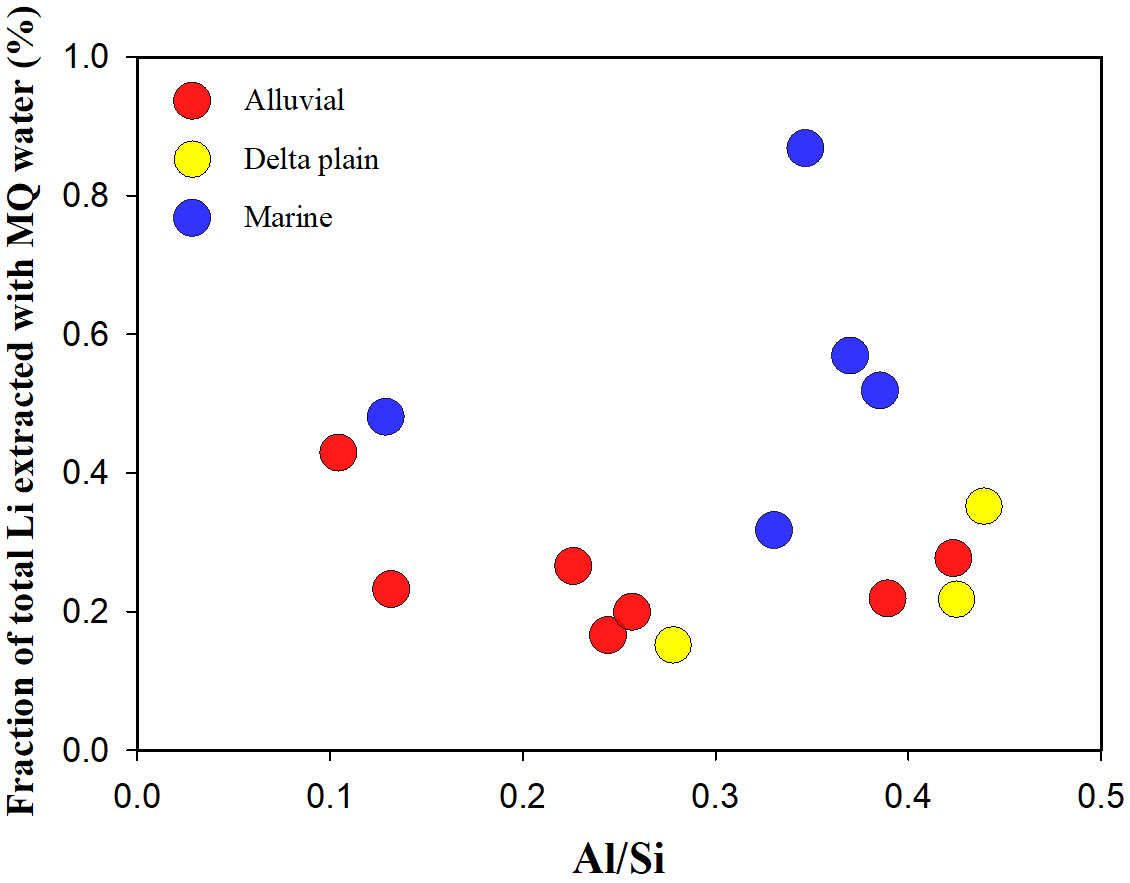

Figure i.1 Relative amount of Li extracted after 3 water rinsing steps (all combined). Across all samples, less than 1% of total Li was extracted with this step. Sediments from marine environments contain the highest fraction of rinseable Li, and no relationship is observed with grain size.

2. Leaching experiments

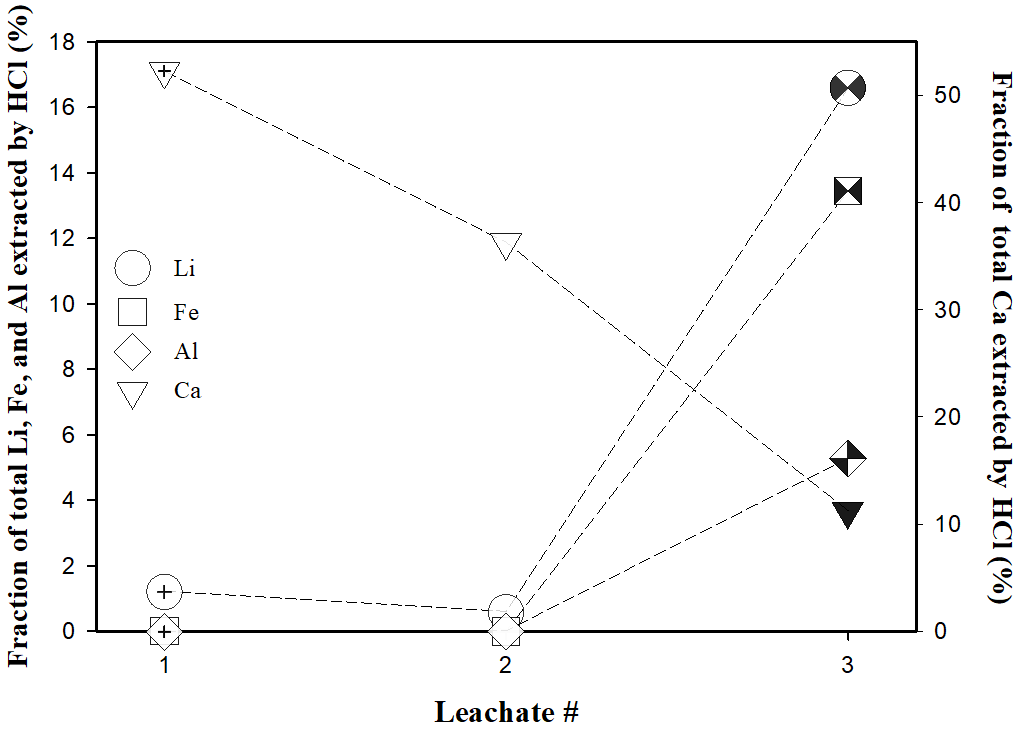

Figure i.2 Example of the stepwise extraction of Li, Fe, Al, and Ca by HCl (sample SD3, a marine deposit sample). The amount of Ca extracted decreases whereas the Li, Al, and Fe extracted amounts were higher after extractable Ca was exhausted.

Table i.2 Extracted cations by HCl leaching experiment (in % of bulk content).

Sample	Li	Na	Al	K	Ca	V	Cr	Mn	Fe	Ni	Cu	Zn	Ga	Ge	As	Rb	Sr	Y	Mo	Sb	Cs
SA3A	0.4	1.4	0.0	0.9	31.6	0.0	0.0	22.0	0.0	0.5	0.4	0.4	0.1	0.3	0.1	0.2	33.0	0.8	1.8	0.2	0.0
SA3B	0.1	0.2	0.0	0.4	32.6	0.0	0.1	23.1	0.0	1.0	0.2	10.2	0.3	1.3	0.4	0.1	31.2	1.6	3.1	0.1	0.0
SA3C	0.2	1.9	0.0	0.2	22.9	0.0	0.0	17.2	0.0	0.2	0.7	1.7	0.6	3.2	0.3	0.1	24.4	5.0	1.2	0.1	0.0
SA4A	0.5	3.1	0.0	0.9	51.9	0.0	0.0	26.6	0.0	0.4	0.1	1.0	0.1	0.3	0.3	0.1	47.8	0.9	1.7	0.1	0.0
SA4B	0.5	0.4	0.0	0.4	37.1	0.0	0.1	23.0	0.0	1.2	0.2	1.5	0.1	0.4	0.4	0.1	26.5	2.5	1.8	0.1	0.0
SA4C	5.8	0.8	3.4	0.9	4.4	2.7	2.9	5.4	3.1	10.4	10.2	13.3	5.0	26.3	2.2	0.4	5.0	26.1	0.0	0.0	0.1
SA6A	1.1	3.4	0.0	0.9	22.8	0.0	0.1	19.1	0.1	1.7	1.0	6.6	0.2	0.9	0.2	0.4	27.6	1.5	3.6	0.7	0.1
SA6B	0.5	0.6	0.0	0.3	18.3	0.0	0.1	16.6	0.1	2.8	0.3	84.3	0.3	0.9	0.4	0.1	19.7	2.0	5.7	1.1	0.0
SA6C	0.9	3.3	0.0	0.3	18.0	0.0	0.1	13.3	0.1	1.0	1.0	9.0	1.4	5.5	0.3	0.2	19.2	7.6	2.9	0.6	0.7
SA9A	0.6	2.8	0.0	0.5	46.3	0.1	0.0	36.4	0.1	1.2	1.1	2.0	0.9	7.5	1.2	0.2	44.9	6.6	3.1	0.5	0.1
SA9B	0.6	1.7	0.0	0.2	34.6	0.1	0.2	19.1	0.0	2.3	0.4	76.8	0.8	4.8	1.1	0.1	34.4	6.2	2.8	0.6	0.0
SA9C	16.3	1.5	4.8	0.6	11.6	12.8	14.5	7.6	16.5	39.4	58.8	29.4	13.0	66.7	7.9	0.9	12.1	35.9	1.0	0.1	0.9
SA11A	0.5	3.9	0.0	1.0	45.5	0.1	0.0	32.1	0.0	0.4	0.4	2.8	0.3	1.5	0.3	0.2	55.6	2.8	4.5	0.3	0.1
SA11B	0.3	0.9	0.0	0.4	40.9	0.1	0.2	26.5	0.0	1.0	0.3	19.6	0.2	0.7	0.2	0.1	35.7	2.4	9.5	0.3	0.0
SA11C	7.4	2.6	3.8	0.9	16.0	6.2	6.3	11.6	6.0	13.8	40.8	14.3	10.1	49.6	5.6	1.2	12.4	38.9	-0.7	0.0	0.5
SA15A	0.2	0.0	0.0	1.4	42.3	0.1	0.1	23.8	0.0	0.9	0.3	1.8	0.0	0.0	0.4	0.1	43.7	0.2	12.9	0.6	0.1
SA15B	0.0	0.6	0.0	1.1	3.2	0.0	-0.1	4.6	0.0	0.1	0.3	9.2	0.2	0.5	-0.2	0.0	-8.5	1.6	-8.8	0.5	0.1
SA15C	5.3	1.8	3.2	0.8	10.7	5.5	4.0	9.3	4.4	12.6	28.4	13.9	6.9	39.0	4.8	0.5	7.2	24.8	-0.2	0.1	0.2
SA22A	0.4	43.2	0.0	0.8	37.0	0.0	0.0	16.7	0.0	0.2	0.1	0.8	0.1	0.2	0.1	0.1	81.0	0.6	1.0	0.1	0.0
SA22B	0.2	2.4	0.0	0.3	28.5	0.0	0.0	16.2	0.0	0.5	0.1	3.5	0.0	0.0	0.2	0.0	38.7	0.1	2.3	0.1	0.0
SA22C	0.4	1.5	0.0	0.3	27.8	0.0	0.0	19.2	0.0	0.5	0.1	-0.5	0.1	0.9	0.2	0.0	12.6	2.3	0.5	0.0	0.0
SD3A	1.2	9.3	0.0	1.6	52.3	0.0	0.0	27.7	0.0	7.2	0.0	6.8	0.2	1.1	0.1	0.7	49.7	1.9	3.7	0.7	0.3
SD3B	0.6	2.7	0.0	0.5	36.3	0.0	0.0	20.1	0.0	4.0	0.1	6.7	0.3	1.5	0.2	0.3	28.8	3.5	3.7	0.5	0.1

Sample	Li	Na	Al	K	Ca	V	Cr	Mn	Fe	Ni	Cu	Zn	Ga	Ge	As	Rb	Sr	Y	Mo	Sb	Cs
SD3C	16.6	2.6	5.3	1.8	11.2	9.3	10.4	10.0	13.4	33.9	3.1	53.0	9.7	28.8	3.3	2.2	9.1	25.4	1.0	0.0	1.8
SD7A	10.0	2.4	2.1	1.2	85.3	4.5	4.1	51.6	9.7	30.4	18.9	45.1	5.8	36.1	12.6	1.0	66.4	33.2	2.6	0.5	0.6
SD7B	23.6	-0.3	4.3	0.9	4.0	4.7	8.5	8.6	16.1	30.6	9.0	38.0	9.3	14.0	7.0	1.5	3.5	3.9	4.9	0.4	2.0
SD7C	8.0	0.0	1.8	0.4	1.2	1.7	3.2	2.9	5.3	10.1	3.0	6.4	3.2	5.1	0.8	0.7	0.8	1.0	2.6	0.1	1.2
SD21A	0.7	9.1	0.0	1.3	35.4	0.0	0.0	16.4	0.1	2.1	0.1	1.7	0.2	0.0	0.2	0.3	30.6	1.1	1.6	0.6	0.1
SD21B	0.8	1.5	0.0	0.4	25.3	0.0	0.0	20.7	0.0	1.5	0.0	2.9	0.2	0.5	0.0	0.2	20.7	1.4	0.6	0.3	0.0
SD21C	1.4	1.7	0.1	0.3	21.5	0.0	0.0	19.8	0.6	2.2	0.3	4.4	1.1	3.9	0.4	0.1	18.8	7.9	0.3	0.0	0.0
SD23A	0.9	0.3	0.0	0.3	28.8	0.1	0.1	18.6	0.1	2.2	0.9	6.8	0.2	2.3	0.2	0.2	33.3	3.3	1.7	1.2	0.1
SD23B	0.3	-0.1	0.0	0.1	15.7	0.1	0.3	10.3	0.0	3.0	0.6	6.6	0.4	0.6	0.2	0.0	18.3	4.4	2.0	1.4	0.0
SD23C	0.7	0.2	0.0	0.1	24.6	0.0	0.0	15.4	0.1	1.2	-0.1	3.7	1.5	9.1	0.6	0.1	27.8	17.7	0.6	0.3	0.0
ST5A	1.1	28.7	0.0	1.8	51.0	0.0	0.0	28.4	0.0	5.8	0.8	4.9	0.2	1.1	0.2	0.7	53.3	2.8	5.4	2.1	0.2
ST5B	0.7	1.6	0.0	0.5	35.7	0.0	0.0	25.3	0.0	5.4	0.7	31.0	0.2	1.2	0.1	0.4	30.5	2.0	4.6	1.3	0.1
ST5C	20.3	1.9	6.9	1.8	11.8	13.0	13.8	15.9	36.1	37.4	38.7	42.7	16.2	72.5	22.7	2.3	10.0	43.5	4.7	0.5	0.6
SC4A	0.7	3.6	0.0	1.1	34.3	0.0	0.0	17.2	0.0	0.4	0.9	0.6	0.0	0.1	0.5	0.2	57.5	0.5	1.3	0.3	0.0
SC4B	0.3	0.9	0.0	0.3	27.1	0.0	0.0	16.0	0.0	0.5	0.1	3.9	0.0	0.0	0.6	0.1	17.0	0.3	3.9	0.5	0.0
SC4C	0.6	1.7	0.0	0.3	27.5	0.0	0.0	21.8	0.0	1.4	0.8	-0.1	0.3	1.7	0.3	0.1	15.8	3.5	0.4	0.4	0.0
SC11A	0.2	1.3	0.0	1.0	24.0	0.0	0.0	19.5	0.0	0.5	0.2	0.8	0.1	0.1	0.4	0.2	24.1	0.8	7.7	0.4	0.0
SC11B	0.1	0.1	0.0	0.3	20.4	0.0	0.1	15.6	0.0	0.6	0.1	12.2	0.1	0.2	0.2	0.1	19.8	1.2	19.3	0.4	0.0
SC11C	0.1	0.8	0.0	0.3	20.7	0.0	0.0	15.3	0.0	0.2	0.1	0.9	0.6	3.2	0.8	0.1	19.2	4.4	-1.7	0.4	0.0
SC21A	0.3	1.3	0.0	0.8	34.6	0.0	0.0	19.8	0.0	0.4	0.5	0.6	0.0	0.4	0.1	0.1	42.7	0.6	1.5	0.1	0.0
SC21B	0.2	0.6	0.0	0.3	34.8	0.0	0.0	22.0	0.0	0.7	0.2	6.2	0.0	0.0	0.2	0.1	24.9	0.7	1.3	0.1	0.0
SC21C	4.4	0.8	2.9	0.8	20.9	3.5	3.6	19.3	3.8	14.1	36.0	17.4	5.6	36.5	2.2	0.4	14.0	40.5	0.1	0.0	0.1

1. The letter (A, B, and C) after the sample name represent the Leachate # 1, 2, and 3.
2. All the numbers are in the unit of % of bulk concentration, representing the fraction of extracted cations in bulk content, and negative numbers are caused by instrumental errors.

Sample	Ba	La	Ce	Pr	Nd	Sm	Eu	Gd	Tb	Dy	Ho	Er	Tm	Yb	Lu	Hf	Ta	W	Tl	Th	U
SA3A	11.1	0.5	0.2	0.2	0.2	0.2	0.9	0.3	0.3	0.3	0.3	0.3	0.3	0.3	0.4	0.0	0.1	5.0	0.3	0.0	4.3
SA3B	8.4	1.3	0.7	0.6	0.7	0.6	1.1	0.8	0.8	0.6	0.7	0.7	0.7	0.5	0.6	0.0	0.1	5.8	0.4	0.0	2.9
SA3C	4.5	3.2	1.9	1.7	1.9	1.6	2.3	2.6	2.5	2.2	2.5	2.3	2.3	1.5	2.0	0.0	0.0	3.1	0.2	0.0	1.1
SA4A	3.7	0.5	0.3	0.3	0.3	0.3	0.7	0.4	0.4	0.4	0.4	0.4	0.3	0.3	0.3	0.0	0.0	4.1	0.1	0.0	3.4
SA4B	2.8	1.1	0.5	0.4	0.5	0.5	1.0	1.0	0.9	0.9	1.0	1.0	0.9	0.6	0.7	0.0	0.2	4.0	0.3	0.0	-0.2
SA4C	16.1	11.2	13.9	16.4	19.3	28.1	29.0	27.9	29.7	27.5	24.4	21.8	21.2	18.2	19.0	0.1	0.0	2.0	0.9	6.8	5.3
SA6A	14.1	0.8	0.4	0.3	0.3	0.3	0.9	0.4	0.5	0.5	0.6	0.7	0.5	0.4	0.7	0.0	0.3	31.5	1.2	0.0	6.3
SA6B	2.5	1.7	0.9	0.7	0.7	0.5	0.7	0.8	0.8	0.8	0.9	0.9	0.6	0.7	0.7	0.1	0.2	25.4	2.7	0.0	3.0
SA6C	1.9	6.3	3.8	3.1	2.9	2.3	2.8	3.5	3.7	3.7	4.2	3.6	3.9	2.7	3.4	0.0	0.0	17.2	4.8	0.2	2.7
SA9A	14.3	5.8	3.5	3.2	3.2	2.6	4.0	4.1	3.4	3.5	3.5	3.4	2.7	2.4	2.6	0.0	0.2	13.6	0.5	0.0	9.2
SA9B	2.4	5.1	3.3	3.1	3.2	2.7	3.2	4.2	3.6	3.4	3.5	3.2	2.4	2.2	2.4	0.1	0.3	11.3	1.3	0.0	7.7
SA9C	2.0	17.3	21.8	26.1	29.0	38.7	40.4	42.0	44.1	44.0	38.7	36.5	35.1	32.5	32.7	0.2	-0.1	5.1	2.2	19.4	12.1
SA11A	14.9	2.2	1.2	1.0	1.1	0.9	2.0	1.4	1.1	1.2	1.3	1.3	1.1	1.0	0.9	0.0	0.1	9.6	0.4	0.0	6.9
SA11B	13.0	1.6	0.7	0.6	0.7	0.6	1.6	1.1	0.9	0.9	1.1	1.0	0.8	0.7	0.8	0.0	0.2	12.7	1.1	0.0	4.2
SA11C	20.8	19.6	22.4	25.6	29.0	38.0	42.7	41.0	43.6	42.9	38.3	35.6	33.1	31.6	29.8	0.2	0.0	2.8	2.6	10.3	6.8
SA15A	5.8	0.1	0.1	0.1	0.1	0.0	0.7	0.1	0.0	0.1	0.1	0.1	2.5	0.1	2.8	0.1	0.4	37.6	0.1	0.0	4.8
SA15B	0.0	1.0	0.5	0.4	0.4	0.4	0.6	0.7	1.1	0.6	1.0	0.6	7.8	0.4	8.9	0.0	0.0	0.9	2.1	0.0	-2.3
SA15C	16.2	11.3	13.2	15.9	17.4	25.3	34.9	26.5	44.1	25.9	33.8	21.9	33.4	18.9	43.7	0.1	-0.1	1.6	6.7	6.2	4.3
SA22A	11.7	0.3	0.2	0.2	0.2	0.2	0.8	0.3	0.3	0.3	0.3	0.3	0.2	0.2	0.2	0.0	0.1	4.3	0.1	0.0	4.9
SA22B	8.3	0.0	0.0	0.0	0.0	0.0	0.5	0.0	0.1	0.0	0.0	0.1	0.0	0.1	0.0	0.0	0.1	3.0	0.4	0.0	4.7
SA22C	4.0	1.0	0.5	0.4	0.5	0.5	0.9	1.0	0.9	0.9	1.1	0.9	0.7	0.6	0.8	0.0	0.0	1.8	0.0	0.0	0.5
SD3A	1.5	1.0	0.6	0.5	0.6	0.6	0.7	0.8	0.9	0.8	1.0	0.9	1.0	0.6	1.0	0.0	0.1	4.5	0.8	0.0	7.3
SD3B	0.8	2.0	1.3	1.2	1.2	1.2	1.3	1.7	1.9	1.6	1.8	1.4	1.7	0.9	1.4	0.0	0.4	3.4	1.5	0.0	3.5

Sample	Ba	La	Ce	Pr	Nd	Sm	Eu	Gd	Tb	Dy	Ho	Er	Tm	Yb	Lu	Hf	Ta	W	Tl	Th	U
SD3C	1.3	10.6	13.5	16.0	18.1	25.7	29.1	26.7	32.9	26.8	27.8	22.6	31.3	19.0	28.5	0.2	-0.1	1.3	3.2	14.2	5.8
SD7A	2.4	9.9	12.0	15.4	19.4	33.6	38.0	38.9	39.1	38.5	33.0	29.6	25.9	24.8	23.3	0.2	0.3	7.8	1.7	9.5	15.6
SD7B	0.5	1.2	1.4	1.8	2.2	3.5	4.0	4.0	4.9	5.1	4.9	4.8	4.5	4.0	4.2	0.0	0.0	2.5	3.2	19.9	4.6
SD7C	0.1	0.7	0.8	0.9	1.0	1.2	1.4	1.2	1.4	1.4	1.3	1.1	1.1	1.1	0.9	0.0	0.0	2.0	0.5	3.6	1.3
SD21A	1.0	1.4	0.7	0.5	0.6	0.4	0.4	0.6	0.5	0.4	0.5	0.5	0.4	0.3	0.4	0.0	0.7	9.6	0.8	0.1	6.4
SD21B	0.4	1.6	0.9	0.7	0.7	0.5	0.5	0.7	0.6	0.6	0.6	0.6	0.5	0.4	0.5	0.0	0.1	1.5	2.0	0.1	1.4
SD21C	0.5	7.0	4.7	4.0	3.9	3.0	3.2	4.8	4.5	4.3	4.5	4.0	3.4	2.9	3.0	0.0	0.0	2.8	-0.2	0.0	0.6
SD23A	0.8	1.8	0.8	0.7	0.7	0.7	0.7	1.0	1.0	1.3	1.5	1.6	1.3	1.3	1.5	0.1	0.2	22.6	0.8	0.0	14.0
SD23B	0.3	3.0	1.5	1.3	1.3	1.0	1.0	1.6	1.5	1.7	2.0	2.0	1.8	1.7	2.0	0.1	0.3	16.4	2.2	0.1	7.9
SD23C	0.4	10.8	6.9	5.8	5.9	4.7	5.0	7.7	7.2	8.0	9.0	9.4	8.1	7.3	7.7	0.1	-0.1	6.2	-0.1	0.0	9.0
ST5A	2.8	1.5	0.9	0.8	0.8	0.9	0.9	1.3	1.2	1.2	1.3	1.2	0.9	0.8	0.8	0.0	0.1	4.6	1.1	0.0	6.0
ST5B	1.6	1.3	0.8	0.7	0.7	0.6	0.6	1.0	0.8	0.9	0.8	0.7	0.5	0.5	0.5	0.0	0.2	2.1	1.4	0.0	0.4
ST5C	2.4	20.2	25.7	30.4	35.4	46.9	48.0	50.0	50.4	50.3	45.0	39.6	35.2	33.0	30.2	0.2	0.0	0.9	2.9	32.3	15.2
SC4A	2.3	0.3	0.1	0.1	0.2	0.1	0.3	0.2	0.2	0.2	0.2	0.3	0.2	0.2	0.2	0.0	0.1	3.6	0.1	0.0	5.6
SC4B	1.0	0.2	0.1	0.1	0.1	0.1	0.1	0.1	0.1	0.1	0.1	0.1	0.1	0.1	0.1	0.0	0.0	3.5	0.6	0.0	5.5
SC4C	0.8	2.4	1.4	1.3	1.5	1.2	1.3	2.0	1.6	1.5	1.6	1.4	1.1	0.7	0.9	0.0	0.0	0.1	0.1	0.1	-0.2
SC11A	22.0	0.4	0.2	0.2	0.2	0.2	1.3	0.4	0.3	0.3	0.4	0.3	0.3	0.3	0.4	0.0	0.1	5.1	0.1	0.0	6.1
SC11B	6.0	0.8	0.4	0.4	0.4	0.4	0.6	0.6	0.5	0.5	0.6	0.6	0.4	0.5	0.5	0.0	0.1	3.8	0.8	0.0	3.5
SC11C	3.0	3.4	2.2	1.9	2.0	1.5	1.9	2.5	2.2	2.0	2.2	1.9	1.7	1.3	1.5	0.0	0.0	0.2	0.0	0.1	2.7
SC21A	3.8	0.2	0.1	0.1	0.2	0.2	0.5	0.3	0.2	0.2	0.3	0.2	0.2	0.2	0.2	0.0	0.0	4.0	0.0	0.0	4.6
SC21B	3.4	0.4	0.2	0.2	0.2	0.2	0.5	0.4	0.3	0.3	0.3	0.2	0.2	0.2	0.2	0.0	0.0	2.8	0.4	0.0	3.1
SC21C	9.9	14.5	18.2	20.7	24.4	37.2	43.6	40.6	43.4	40.5	35.3	31.2	28.2	26.3	24.2	0.2	0.0	-0.1	0.4	4.9	6.2

1. The letter (A, B, and C) after the sample name represent the Leachate # 1, 2, and 3.
2. All the numbers are in the unit of % of bulk concentration, representing the fraction of extracted cations in bulk content, and negative numbers are caused by instrumental errors.

In all samples, the amount of Li extracted before the Ca exhaustion was relatively small compared to the Li being leached after the Ca exhaustion and was of the same magnitude as the “rinseable” Li fraction.

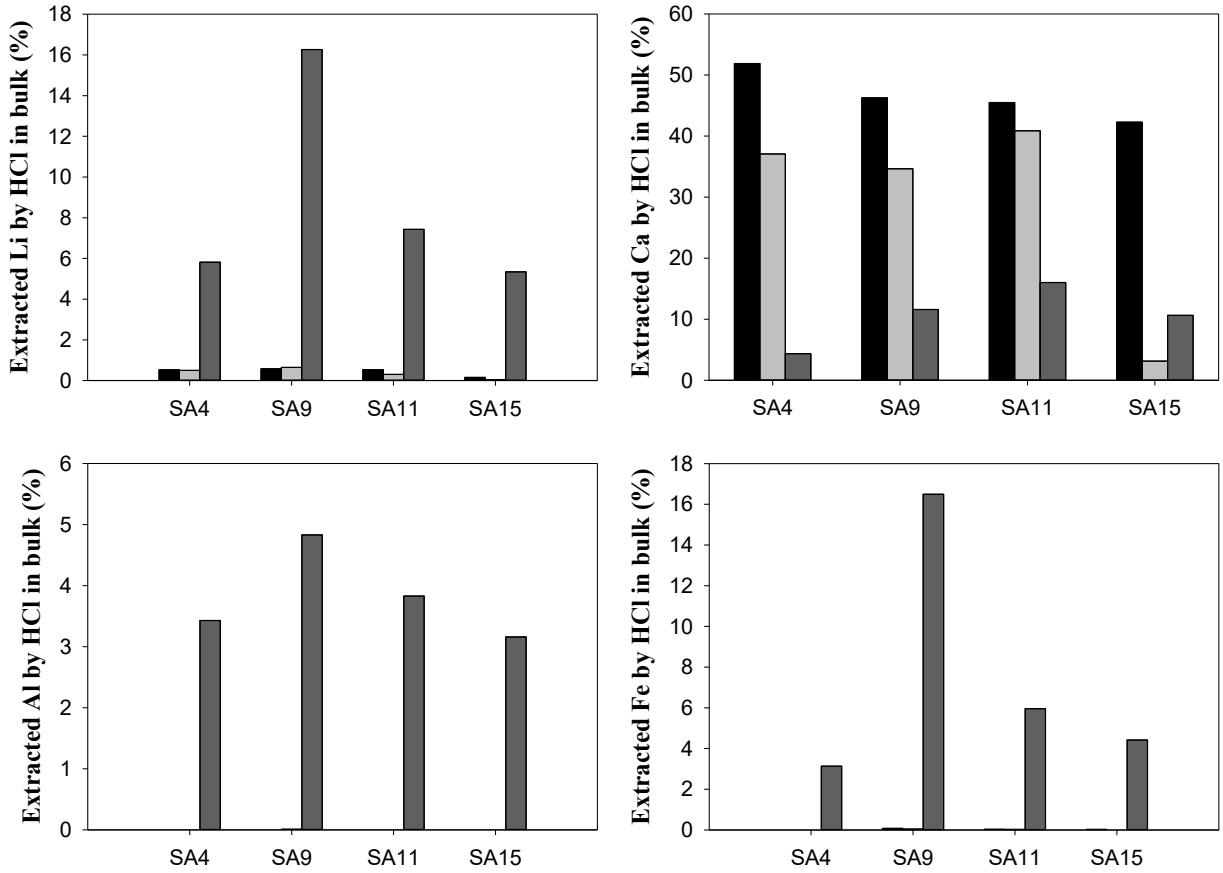

Figure i.3 Extraction of Li, Ca, Al and Fe from continental sediment samples. The first, second, and last leachate are colored by black, grey, and dark grey colors.

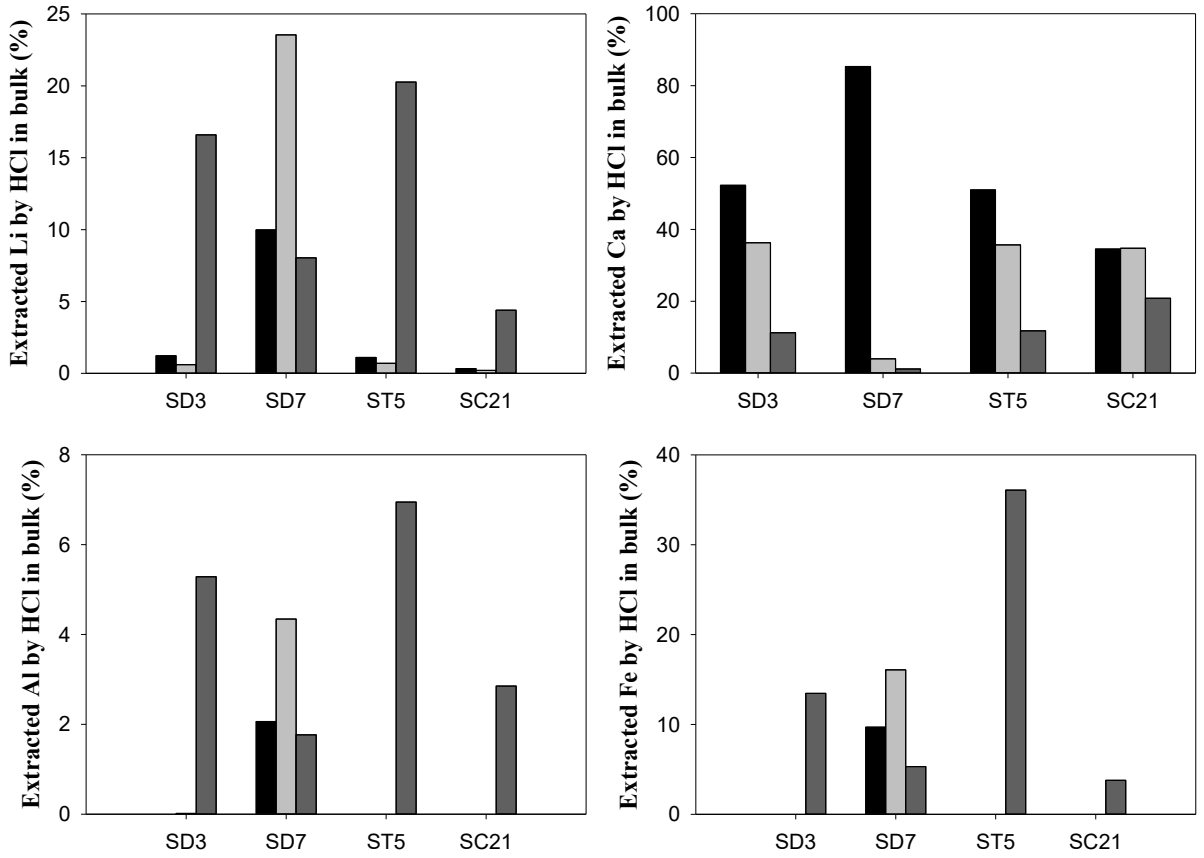

Figure i.4 Extraction of Li, Ca, Al and Fe from marine sediment samples. The first, second, and last leachate are colored by black, grey, and dark grey colors.

Table i.3 Li isotope composition of "Ca-associated" and "Al/Fe associated" Li

Sample	δ^7Li (Ca associated Li)	2 s. d	δ^7Li (Al/Fe associated Li)	2 s.d.
SA 4	3.68	0.24	-1.73	0.20
SA 9	5.52	0.13	-2.28	0.21
SA 11	2.60	0.07	0.13	0.24
SA 15	4.61	0.10	-0.45	0.26
SD 3	-0.55	0.09	-6.01	0.14
SD 7	-6.32	0.08	-3.53	0.27
ST 5	2.88	0.22	-4.67	0.37
SC 21	6.16	0.37	-2.83	0.30

Chapter 5: “Source-to-sink-to-source” effects on the Si isotope composition of detrital sediments

Julien: “The Chinese character ‘川’ means river, right?”.

Xu: “Yep, because it looks like a river, ancient Chinese emoji. But not all characters are pictogram, sometimes it’s the combined meaning of all elements composing that character. For example, ‘海’, it means sea and the combined meaning of its elements means ‘every drop of water’”.

— 26°34'31.8"N 101°42'32.4"E, Panzhihua, China
11/09/2017

5.1 Introduction

Detrital sediments are the solid products of erosion and weathering and are continuously transported from continents to ocean. The geochemistry of suspended sediments thus archives the integrated history of chemical weathering and erosion (Allègre et al., 1996; Dupré et al., 1996; Millot et al., 2004; Dosseto et al., 2006; Viers et al., 2008, 2009; Dellinger et al., 2014), and of the past evolution of the Earth’s surface. As the upper continental crust (UCC) is dominated by silicate minerals, silicon (Si) is the second most abundant element in the Earth crust, after oxygen (Taylor, 1964). The interest to study the behaviour of Si during silicate weathering is severalfold. First, at geological time scales, the weathering of silicate rocks is a pivotal process, which in particular governs the CO_2-climate feedbacks (Walker et al., 1981; Berner et al., 1983). Second, Si is also an essential and regulating nutrient for phytoplanktonic organisms playing an important role in global biogeochemical cycles. For instance, Si-bearing diatoms represent up to half of the marine primary productivity (Egge and Aksnes, 1992; Tréguer et al., 1995; De La Rocha et al., 1998; Mann, 1999; Conley and Carey, 2015). The ultimate source of the dissolved silica (DSi) in the ocean, which is the source of Si for marine ecosystems, originates from the dissolution of silicate minerals by weathering on the continent. Last, Si also provides information of the evolution on the Earth’s lithosphere. For example, DSi released to the ocean by silicate weathering is thought to have been a relatively small flux during the Archean whereas it is a dominant input to the ocean today (Ding et al., 2017).

A powerful approach to study the behavior of Si at the Earth surface is to investigate its stable isotope fingerprints, as these fingerprints can be used to trace the sources of Si and depict the processes behind its transformation during Earth surface processes. Si has three stable isotopes (De Biévre and Taylor, 1993; Poitrasson, 2017): ^{28}Si (92.23%), ^{29}Si (4.67%), and ^{30}Si (3.10%).

The isotope variations of Si are relatively small, as this element is not subjected to redox changes. At the Earth's surface, Si always occurs in the form of SiO_4 tetrahedra in solids, and orthosilicic acid (H_4SiO_4) and its conjugating species in aqueous environments (Poitrasson, 2017). The advent of multi-collector inductively coupled plasma mass spectrometry (MC-ICP-MS) with high mass resolution compared to older generations of techniques, and the improvement of Si purification procedures using cation exchange resins (Georg et al., 2006), have enabled the use of the stable isotope composition of Si as a robust geochemical tracer. The Si isotope composition is expressed in δ-notation in the unit of ‰, related to a reference material, the National Bureau of Standards 28 Sand Quartz (NBS-28, or also called NIST RM-8546):

$$\delta^{x}\mathrm{Si} = \left[\frac{(^{x}\mathrm{Si}/^{28}\mathrm{Si})_{\mathrm{sample}}}{(^{x}\mathrm{Si}/^{28}\mathrm{Si})_{\mathrm{NBS\text{-}28}}} - 1\right] \times 1000, \text{ where } x=29 \text{ or } 30.$$

Only mass dependent fractionation of Si isotopes has been reported, to date, for Earth surface materials, such that the relative variation of the $^{29}Si/^{28}Si$ ratio can be determined from the relative variation of $^{30}Si/^{28}Si$ ratio. Therefore, for the rest of this chapter, the Si isotopic composition is expressed as $\delta^{30}Si$.

In the environment, the isotopic fractionation of Si from abiotic processes favors the incorporation of its lighter isotopes in solid materials whereas heavier isotopes are enriched in the dissolved phase (Ziegler et al., 2005a,2005b; Georg et al., 2006, 2007; Bern et al., 2010; Opfergelt et al., 2010, 2011, 2012; Cornelis et al., 2014; Ameijeiras-Mariño et al., 2017). However, theoretical calculations and experimental results show that equilibrium fractionation in fact favors lighter Si isotopes in aqueous solutions (Dupuis et al., 2015; He et al., 2016). These findings suggest that Si isotopes fractionation in natural weathering systems is controlled by kinetic processes, especially during the formation of secondary weathering products (Oelze et al., 2014,

2015).

Silicon is also an essential trace nutrient for many life forms including diatoms and plants (De La Rocha et al., 1998; Sun et al., 2008; Opfergelt et al., 2008; Tréguer and De La Rocha, 2013), and biogenic Si (BSi) is an important component of the Si cycle. At the Earth surface, BSi displays the largest range of variation of δ^{30}Si due to kinetic effects during the uptake of Si (Frings et al., 2016). On the continents, the estimated annual production of BSi (~84×10^{12} mol/yr) is greater than the riverine flux of Si (~6.3×10^{12} mol/yr) to the ocean (Opfergelt and Delmelle, 2012; Frings et al., 2016). The uptake of Si by plants favors light Si isotopes from the ambient soil solutions, which is what has been observed so far in terrestrial plants including corn, wheat, banana, bamboo, and rice (Ziegler et al., 2005a; Opfergelt et al., 2006; Ding et al., 2008a,b). Processes associated with BSi formation and dissolution are of fundamental importance for the DSi in the ocean, such that the shallow seawater DSi content and its δ^{30}Si are both largely controlled by diatom activity (De La Rocha et al., 2000; Cardinal et al., 2005; Reynolds et al., 2006; De Souza et al., 2012; Fripiat et al., 2012; Grasse et al., 2013; Tréguer and De La Rocha, 2013; Holzer and Brzezinski, 2015). Nevertheless, with the notable exception of Savage et al., (2013), who proposed that marine derived BSi could influence the Si isotope signature of some sedimentary rocks having high δ^{30}Si values, the long-term role of biological activity on the Si signature solids at the Earth surface, in particular in the sedimentary record, has been poorly addressed.

The potential of using Si isotopes in river sediments as a tracer of weathering process has been suggested by Opfergelt and Delmelle (2012). On the one hand, a major fraction of Si in rivers sediments is inherited from the parent rock via physical erosion. On the other hand, Si released in solution by weathering reaction can be taken up during secondary mineral formation. The bulk Si isotope composition of river sediments thus results from a mixture between these two components

and should be related to the erosion and weathering conditions prevailing in the sediment surface areas.

Recently, Bayon et al. (2018) measured the Si isotope composition of sediments from large rivers for different size fractions including silts (4–63 µm) and clays (<4 µm), and reported a negative relationship between the δ^{30}Si and Al/Si ratios for the clay fraction of global river sediments. The authors attribute this relationship to climate, with river basins currently subjected to warmer and wetter climate having a lower δ^{30}Si (and a higher Al/Si ratio) in their sediments’ clay-sized fraction. However, it should first be pointed out that river sediments have a much longer residence time at the Earth surface than the time scale of the current climatic parameters such as annual temperature and precipitation, and climatic variation takes place at a range of time scales (Thompson et al., 2002; Mayewski et al., 2004). This could be a reason why for some large rivers (the Mackenzie River for example) the clay δ^{30}Si signature cannot be explained by climatic parameters (Bayon et al., (2018). In addition, the global effect of lithology on the δ^{30}Si of large river sediments might have been overlooked, as suggested by the shale data of δ^{30}Si (Savage et al., 2013) and by the lithological observations from Bayon et al. (2018) for individual basins of relatively homogeneous climate (Northern Ireland & Congo). In other words, the interpretation of the δ^{30}Si of river clays needs to address the question of when these clays were produced: during the current weathering episode ("soil-hosted" clays) or during ancient weathering episodes ("shale-hosted" clays)?

Indeed, Nd isotopes in sedimentary rocks (Veizer and Jansen, 1979, 1985; Allègre and Rousseau, 1984) show that detrital sediments are largely cannibalistic, meaning that that their source material is already partially sedimentary, or "recycled". During recycling, sedimentary rocks form from the deposition of products from ancient weathering episodes, are uplifted, re-

exposed at the Earth surface, and subjected to erosion/weathering again. Nowadays, more than two thirds of the Earth surface is covered by sedimentary rocks (Amiotte Suchet et al., 2003; Wilkinson et al., 2009; Dellinger et al., 2014). More specifically, a previous study on lithium (Li) isotopes by Dellinger et al. (2014) suggests that lithology, and in particular the presence of recycled, already weathered rocks such as shales or sandstones, strongly influences the Li isotope composition of river sediments. To some extent, Li has isotope properties similar to those of Si at the Earth surface. Li is exclusively hosted in silicate rocks (Kısakűrek et al., 2005; Millot et al., 2010; Dellinger et al., 2014), and the variation of Li and Si isotopes follow similar logics, in which the dissolved species are enriched in heavier isotopes, whereas the lighter isotopes are preferentially incorporated into the solid phase (Huh et al., 1998, 2001; Tomascak et al., 2016) − although it should also be noted that differences exist between the two systems as Li is a trace element and is not significantly involved in biological activity. Dellinger et al. (2014) use the isotopes of Li in large river sediments (from the Amazon, Mackenzie, and Ganges-Brahmaputra rivers) as a tracer of erosion and weathering processes. In particular, this study shows that the “weathered” component of large river sediments is a mixture of solids derived from both (a) the erosion of modern soils which are products of present-day weathering processes and (b) the erosion of detrital meta-sedimentary rocks such as shales, which are products of previous weathering episodes. Therefore, it could be expected that the Si isotope composition of river sediments is also the result of both ancient and modern weathering episodes. Interestingly, Dellinger et al. (2014) made use of the inverse relationship between the Li isotope signature and Al/Si ratio in river sediments, Al/Si being used as a grain size proxy (Bouchez et al., 2011; Lupker et al., 2011; Dellinger et al., 2014). Such relationship is similar to that reported for Si in shales by Savage et al. (2013), who showed that the δ^{30}Si of shales is negatively correlated to their Al/Si ratio. The low δ^{30}Si and high

Al/Si values of some shale samples were suggested to be due to intense or prolonged weathering of the source material, and the high δ^{30}Si and low Al/Si values of some other shale samples were suggested to be due to the addition of marine-derived Si such as BSi. Regardless, these studies suggest that lithology, in particular through the prevalence of meta-sedimentary rocks over most of the continental surface, could play a yet unexplored role on the δ^{30}Si signature of detrital sediments, which might obscure signals pertaining to present-day weathering (Dellinger et al., 2017).

One possibility to address source effects on the isotope composition of detrital sediments is to examine the coarse fraction of these sediments, which is less affected by modern weathering processes (Dellinger et al., 2014). To improve our understanding of the influence of modern weathering (in other words, processes) vs. ancient weathering (in other words, sources) on the Si isotope composition on global river sediment, here we use a range of bulk sediment samples differing in their grain size distribution, ranging from coarse material (River Bed Sediments, RBS) to relatively fine sediments (surface Suspended Particulate Materials, SPM). We use sediments sampled from the world's largest rivers (42 rivers) to answer the following questions: Is biological activity affecting the Si isotopic signature of river sediments? Is the reported variability of δ^{30}Si in shales a manifestation of weathering? Can Si be used as a tracer of modern weathering processes, or does it rather indicate the past weathering processes? More generally, what are the major controls on detrital sediment δ^{30}Si and how we can use this tracer to retrieve information on Earth surface processes?

5.2 Sample material

In this study, we conduct a detailed examination of Si isotope variations over river sediment

“depth profiles” (from channel surface to bed sands) from various sampling locations over the Amazon and Mackenzie basins. Additionally, we also investigated channel surface suspended sediments and bed sands from other world’s large river systems, covering various distinctive geological, climatic, and biological settings (Fig 5.1).

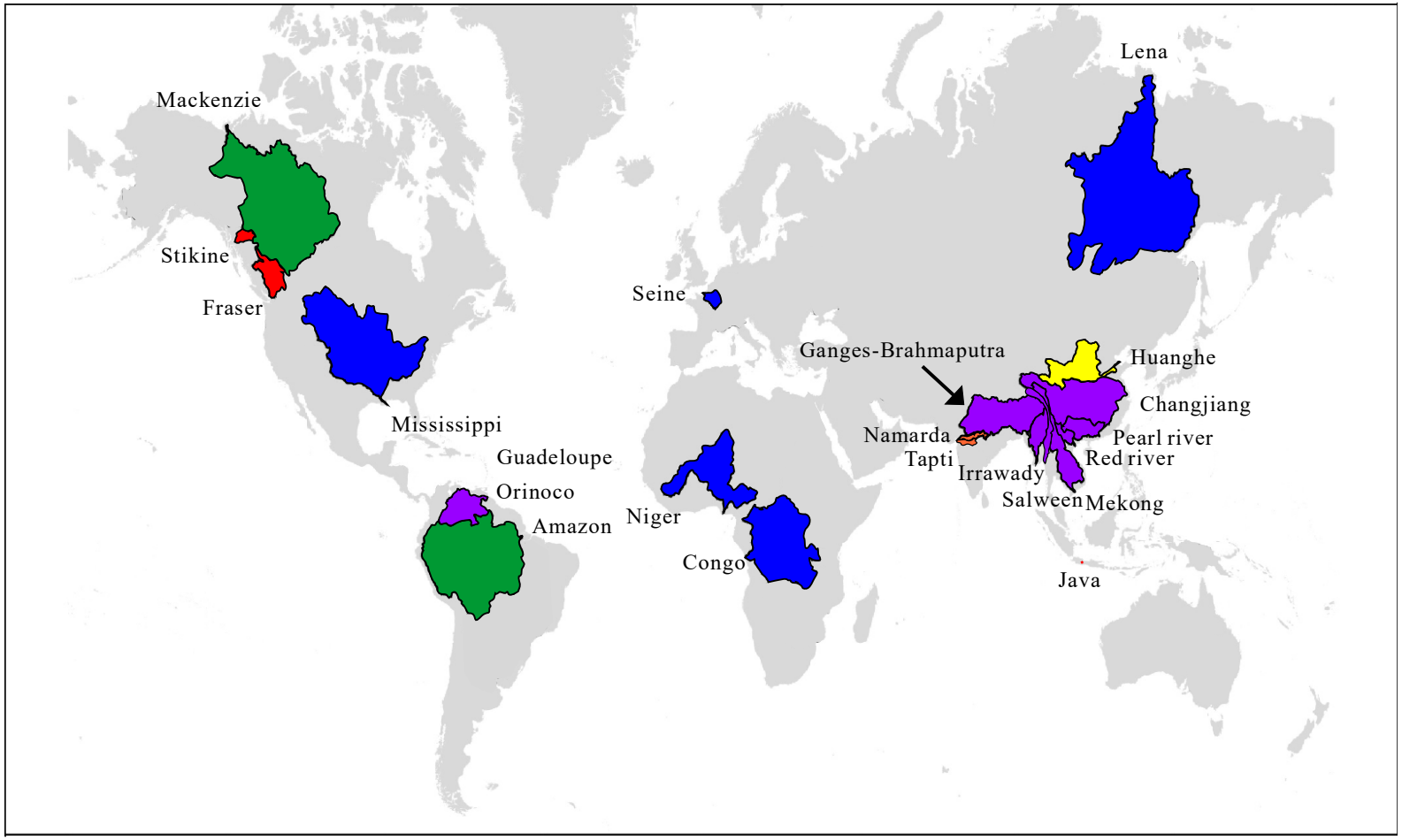

Figure 5.1 Map of rivers whos sediments were investigated in this study. The basins are colored by their geological characteristics: subduction zone (red), sedimentary and cratonic (blue), sedimentary and collisional (purple), loess plateau (yellow), deccan traps (orange), and the Amazon and Mackenzie basins where river depth-profiles were collected are colored in green.

5.2.1 River depth profiles: Amazon and Mackenzie rivers

In order to obtain a representative view of the geochemistry of large river sediments and to address both source and process effects on their isotope signatures, it is necessary to sample the whole range of sediment grain size, which can be accessed through depth profiles. In large river channels, sediments are sorted along the water column by hydrodynamics, resulting in finer particles being enriched near the surface and coarse particles enriched towards the bottom, such that this sorting effect causes variations in the properties of sediments along a given depth profile, including systematic geochemical and isotopic variations (Bouchez et al., 2011; Lupker et al., 2011; Dellinger et al., 2014). In particular, it has been shown that the Si concentration in sediments increases from surface sediments towards RBS (Bouchez et al., 2011). We note that in the study of Bayon et al. (2018), samples from different rivers were collected from a diversity of geomorphological settings, such as river banks, river channels (at unknown depth), or estuaries and submarine deltas, possibly making the interpretation of clay δ^{30}Si because of undocumented mineralogical enrichment effects. This issue does not arise with depth profiles, which represent a mineralogical continuum of a given river at a given time.

Being the world’s largest river regarding basin area (6,300 × 10^3 km^2) and discharge (6,300 km^3/yr), the Amazon River has a sediment flux of 1,200 × 10^6 t/yr to the ocean (Milliman and Farnsworth, 2013). The headwaters of the Amazon drain the Andes on the west side of the basin; the low-relief Central Amazon plain, largely underlain by sediments and covered by the Amazon rainforest; and two cratonic shields (the Guyana and Brazilian shields) are located in the north and south of the basin. The Andes is the main source of sediments to the Amazon River, mainly through two tributaries: the Solimões and Madeira rivers (Gibbs, 1967). Both rivers drain the Andes where sedimentary rocks (shales and sandstones mostly) form the largest contributor to the

outcropping rocks. The Andean part of Madeira tributary system is dominated by sedimentary rocks, such as Ordovician-Silurian shales and Cretaceous-Cenozoic terrigenous sediments (Putzer, 1984). The Andean part of Solimões system also drain ancient sedimentary rocks (Paleozoic-Cenozoic); however, the Solimões basin also features an arc-type igneous bedrock component derived from relatively recent magmatism (Basu et al., 1990), and an active volcanic belt is present within the basins of the Napo and Pastaza rivers (Moquet et al., 2011).

The Mackenzie River is located in the Arctic-sub Arctic area of North America, and discharges 310 km^3/yr of water to the Arctic Ocean from a basin area of 1,800 × 10^3 km^2, with a sediment flux of 100 × 10^6 t/yr (Milliman and Farnsworth, 2013). In terms of suspended particulate flux to the Arctic Ocean, it is the largest Arctic river. The Mackenzie River system is characterized by a Cordillera to the West (Rocky and Mackenzie Mountains), a plain in the center (Mackenzie Interior Platform), and a cratonic shield to the East (Canadian Shield). In the Mackenzie River basin, igneous rocks are sparse, and the lithology is dominated by sedimentary rocks (Reeder et al., 1972; Millot et al., 2003). Because of lower temperature and runoff, the chemical weathering intensity and rates are lower than that of the Amazon (Millot et al., 2003; Dellinger et al., 2014).

Samples from these two major river basins include SPM and RBS for the Amazon (Table 5.1) and Mackenzie basins (Table 5.2). Details about the samples and the sampling procedures are reported in previous publications (Dosseto et al., 2006; Bouchez et al., 2011; Wittmann et al., 2011; Dellinger et al., 2014). It is noteworthy that sediments from the Napo and Pastaza rivers used in this study were sieved at 125 µm (Wittmann et al., 2011).

Table 5.1 Silicon isotope composition of river sediments from the Amazon Basin

Sample name	*River*	*Location*	*Type*	*Depth (m)*	*$\delta^{30}Si$*	*2 s.d.*	*$\delta^{29}Si$*	*2 s.d.*	*Al/Si*
AM06_01	Solimões	Manacapuru	RBS		-0.25	0.03	-0.14	0.03	0.06
AM06_02	Solimões	Manacapuru	RBS		-0.22	0.07	-0.11	0.12	0.09
AM06_03	Solimões	Manacapuru	RBS		-0.19	0.08	-0.13	0.01	0.08
AM06_04	Solimões	Manacapuru	RBS		-0.06	0.03	-0.04	0.03	0.06
AM06_05	Solimões	Manacapuru	RBS		-0.20	0.12	-0.11	0.03	0.13
AM06_06	Solimões	Manacapuru	RBS		-0.27	0.06	-0.16	0.05	0.08
AM05_04	Solimões	Manacapuru	SPM	28	-0.29	0.04	-0.15	0.05	0.22
AM05_06	Solimões	Manacapuru	SPM	14	-0.42	0.04	-0.20	0.04	0.29
AM06_07	Solimões	Manacapuru	SPM	20	-0.30	0.06	-0.17	0.03	0.22
AM06_09	Solimões	Manacapuru	SPM	0	-0.63	0.07	-0.33	0.03	0.37
AM06_10	Solimões	Manacapuru	SPM	22	-0.38	0.04	-0.22	0.01	0.31
AM06_11	Solimões	Manacapuru	SPM	15	-0.39	0.05	-0.20	0.05	0.32
AM06_12	Solimões	Manacapuru	SPM	10	-0.40	0.06	-0.20	0.07	0.31
AM06_13	Solimões	Manacapuru	SPM	5	-0.47	0.03	-0.23	0.02	0.37
AM06_14	Solimões	Manacapuru	SPM	0	-0.62	0.06	-0.32	0.04	0.39
AM06_15	Solimões	Manacapuru	SPM	25	-0.36	0.04	-0.18	0.09	0.27
AM06_16	Solimões	Manacapuru	SPM	18	-0.49	0.06	-0.24	0.05	0.33
AM06_17	Solimões	Manacapuru	SPM	12	-0.61	0.11	-0.33	0.07	0.37
AM06_18	Solimões	Manacapuru	SPM	6	-0.51	0.09	-0.25	0.03	0.38
AM06_19	Solimões	Manacapuru	SPM	0	-0.59	0.07	-0.31	0.04	0.44
AM05_20	Madeira	Foz Madeira	SPM	28	-0.05	0.09	-0.03	0.06	0.09
AM05_24	Madeira	Foz Madeira	SPM	21	-0.38	0.04	-0.20	0.04	0.23
AM06_44	Madeira	Foz Madeira	RBS		-0.20	0.07	-0.09	0.04	0.06
AM05_15	Madeira	Foz Madeira	SPM	23	-0.40	0.02	-0.20	0.03	0.38
AM05_17	Madeira	Foz Madeira	SPM	12	-0.68	0.08	-0.37	0.08	0.40
AM05_18	Madeira	Foz Madeira	SPM	8	-0.66	0.10	-0.33	0.05	0.44

Sample name	*River*	*Location*	*Type*	*Depth (m)*	*$\delta^{30}Si$*	*2 s.d.*	*$\delta^{29}Si$*	*2 s.d.*	*Al/Si*
AM06_33	Madeira	Foz Madeira	SPM	12	-0.38	0.05	-0.20	0.04	0.22
AM06_34	Madeira	Foz Madeira	SPM	6	-0.41	0.06	-0.20	0.04	0.29
AM06_36	Madeira	Foz Madeira	SPM	15	-0.49	0.08	-0.24	0.08	0.28
AM06_37	Madeira	Foz Madeira	SPM	10	-0.40	0.07	-0.22	0.07	0.28
AM06_39	Madeira	Foz Madeira	SPM	11	-0.48	0.06	-0.24	0.08	0.30
AM06_43	Madeira	Foz Madeira	SPM	0	-0.63	0.06	-0.31	0.05	0.36
AM05_44	Amazonas	Obidos	RBS	42	-0.23	0.07	-0.11	0.07	0.08
AM05_46	Amazonas	Obidos	RBS	51	-0.23	0.13	-0.11	0.14	0.07
AM05_35	Amazonas	Obidos	SPM	58	-0.36	0.08	-0.19	0.03	0.20
AM05_36	Amazonas	Obidos	SPM	45	-0.35	0.06	-0.17	0.07	0.21
AM06_55	Amazonas	Obidos	SPM	55	-0.31	0.07	-0.15	0.06	0.21
AM06_58	Amazonas	Obidos	SPM	10	-0.46	0.03	-0.23	0.04	0.33
AM06_60	Amazonas	Obidos	SPM	35	-0.52	0.04	-0.26	0.06	0.29
AM06_63	Amazonas	Obidos	SPM	45	-0.42	0.06	-0.23	0.10	0.31
AM06_64	Amazonas	Obidos	SPM	20	-0.52	0.06	-0.26	0.01	0.36
AM06_65	Amazonas	Obidos	SPM	0	-0.45	0.05	-0.27	0.03	0.42
AM07_05	Beni	Rurrenabaque	RBS		-0.19	0.04	-0.09	0.05	0.10
AM01-14	Beni	Rurrenabaque	SPM		-0.55	0.01	-0.27	0.08	0.42
AM07_01	Beni	Rurrenabaque	SPM	4.5	-0.24	0.12	-0.14	0.08	0.17
AM07_02	Beni	Rurrenabaque	SPM	3	-0.41	0.12	-0.22	0.05	0.31
AM07_03	Beni	Rurrenabaque	SPM	1.5	-0.44	0.06	-0.22	0.05	0.32
AM07_04	Beni	Rurrenabaque	SPM	0	-0.39	0.06	-0.22	0.02	0.33
AM07_06	Beni	Riberalta	SPM	7	-0.27	0.04	-0.16	0.03	0.20
AM07_07	Beni	Riberalta	SPM	5	-0.31	0.04	-0.17	0.01	0.19
AM07_08	Beni	Riberalta	SPM	2.5	-0.34	0.06	-0.16	0.03	0.23
AM07_09	Beni	Riberalta	SPM	0	-0.42	0.09	-0.20	0.02	0.28
AM08_14	Ucayali	Jenaro Herrera	RBS		-0.16	0.04	-0.06	0.03	0.13

Sample name	***River***	***Location***	***Type***	***Depth (m)***	***δ^{30}Si***	***2 s.d.***	***δ^{29}Si***	***2 s.d.***	***Al/Si***
AM08_10	Ucayali	Jenaro Herrera	SPM	23	-0.40	0.06	-0.20	0.04	0.28
AM08_13	Ucayali	Jenaro Herrera	SPM	0	-0.43	0.09	-0.22	0.08	0.31
AM08_17	Ucayali	Jenaro Herrera	SPM	Medium	-0.35	0.06	-0.15	0.03	0.19
AM08_37	Pastaza	Embouchure	RBS		-0.19	0.07	-0.09	0.14	0.27
Napo 3	Napo		RBS		-0.27	0.03	-0.15	0.05	0.35
Napo 4	Napo		RBS		-0.03	0.04	-0.01	0.01	0.34
Coca 1	Napo		RBS		-0.48	0.05	-0.22	0.04	0.33
AM08_36	Pastaza	Embouchure	SPM	0	-0.40	0.07	-0.22	0.01	0.39

Table 5.2 Silicon isotope composition river sediments from the Mackenzie Basin

Sample name	*River*	*Location*	*Type*	*Depth (m)*	*$\delta^{30}Si$*	*2 s.d.*	*$\delta^{29}Si$*	*2s.d.*	*Al/Si*
CAN09_49	Red Arctic	Tsiigehtchic	RBS		-0.23	0.08	-0.13	0.01	0.15
CAN09_53	Red Arctic	Tsiigehtchic	RBS		-0.28	0.08	-0.14	0.03	0.15
CAN09_50	Red Arctic	Tsiigehtchic	SPM	4	-0.39	0.07	-0.20	0.03	0.31
CAN09_51	Red Arctic	Tsiigehtchic	RPM	2	-0.40	0.05	-0.22	0.04	0.31
CAN09_52	Red Arctic	Tsiigehtchic	SPM	0	-0.54	0.06	-0.26	0.05	0.31
CAN09_11	Liard	Fort Simpson	RBS		0.00	0.08	0.02	0.06	0.08
CAN09_12	Liard	Fort Simpson	RBS		-0.24	0.04	-0.15	0.02	0.13
CAN10_50	Liard	Fort Simpson	RBS		0.01	0.09	0.03	0.03	0.07
CAN10_51	Liard	Fort Simpson	RBS		-0.11	0.08	-0.04	0.04	0.10
CAN09_01	Liard	Fort Simpson	SPM	6	-0.22	0.03	-0.11	0.03	0.15
CAN09_02	Liard	Fort Simpson	SPM	4	-0.39	0.04	-0.21	0.02	0.23
CAN09_03	Liard	Fort Simpson	SPM	2	-0.27	0.07	-0.14	0.04	0.19
CAN09_04	Liard	Fort Simpson	SPM	0	-0.36	0.03	-0.18	0.11	0.24
CAN10_46	Liard	Fort Simpson	SPM	4.8	-0.16	0.06	-0.11	0.08	0.11
CAN10_48	Liard	Fort Simpson	SPM	1.5	-0.10	0.08	-0.05	0.04	0.16
CAN10_49	Liard	Fort Simpson	SPM	0	-0.28	0.10	-0.10	0.02	0.28
CAN11_03	Liard	Fort Simpson	SPM	6.5	-0.23	0.03	-0.11	0.01	0.20
CAN11_04	Liard	Fort Simpson	SPM	5	-0.13	0.07	-0.06	0.04	0.19
CAN11_05	Liard	Fort Simpson	SPM	3.5	-0.37	0.11	-0.12	0.04	0.20
CAN11_06	Liard	Fort Simpson	SPM	1.5	-0.32	0.09	-0.20	0.03	0.21
CAN11_07	Liard	Fort Simpson	SPM	0	-0.39	0.01	-0.20	0.05	0.22
CAN09_54	Mackenzie	Tsiigehtchic	RBS		-0.06	0.06	-0.03	0.03	0.13
CAN09_43	Mackenzie	Tsiigehtchic	SPM	19.8	-0.43	0.07	-0.22	0.03	0.29

Sample name	*River*	*Location*	*Type*	*Depth (m)*	*$\delta^{30}Si$*	*2 s.d.*	*$\delta^{29}Si$*	*2s.d.*	*Al/Si*
CAN09_44	Mackenzie	Tsiigehtchic	SPM	15	-0.28	0.03	-0.11	0.06	0.28
CAN09_45	Mackenzie	Tsiigehtchic	SPM	10	-0.37	0.05	-0.18	0.03	0.30
CAN09_46	Mackenzie	Tsiigehtchic	SPM	5	-0.38	0.06	-0.21	0.07	0.29
CAN09_47	Mackenzie	Tsiigehtchic	SPM	0	-0.25	0.10	-0.14	0.01	0.30
CAN11_65	Mackenzie	Tsiigehtchic	SPM	13	-0.07	0.06	-0.02	0.02	0.13
CAN11_66	Mackenzie	Tsiigehtchic	SPM	10	-0.25	0.08	-0.17	0.03	0.17
CAN11_67	Mackenzie	Tsiigehtchic	SPM	5	-0.26	0.06	-0.13	0.10	0.21
CAN10_23	Middle Channel	Inuvik	RBS		-0.13	0.04	-0.07	0.06	0.18
CAN10_27	Middle Channel	Inuvik	RBS		-0.23	0.05	-0.10	0.07	0.10
CAN10_22	Middle Channel	Inuvik	SPM	15	-0.23	0.06	-0.07	0.01	0.21
CAN10_26	Middle Channel	Inuvik	SPM	0	-0.36	0.07	-0.17	0.01	0.33
CAN10_28	Middle Channel	Inuvik	SPM	19	-0.25	0.06	-0.16	0.01	0.21
CAN10_29	Middle Channel	Inuvik	SPM	17	-0.42	0.05	-0.23	0.03	0.31
CAN10_30	Middle Channel	Inuvik	SPM	12	-0.47	0.05	-0.23	0.05	0.32
CAN10_31	Middle Channel	Inuvik	SPM	6	-0.42	0.04	-0.22	0.06	0.32
CAN10_32	Middle Channel	Inuvik	SPM	0	-0.30	0.07	-0.13	0.05	0.38
CAN10_34	Middle Channel	Inuvik	SPM	8	-0.51	0.05	-0.22	0.08	0.27
CAN10_35	Middle Channel	Inuvik	SPM	6	-0.48	0.11	-0.19	0.02	0.26
CAN10_36	Middle Channel	Inuvik	SPM	3	-0.23	0.08	-0.10	0.02	0.28
CAN10_37	Middle Channel	Inuvik	SPM	0	-0.52	0.07	-0.24	0.06	0.35
CAN09_32	Peace	Peace_Point	RBS		-0.36	0.10	-0.14	0.02	0.16
CAN09_33	Peace	Peace_Point	RBS		-0.22	0.07	-0.10	0.01	0.10
CAN09_31	Peace	Peace_Point	SPM	0	-0.37	0.03	-0.18	0.04	0.31
CAN09_41	Peel	Fort McPherson	RBS		-0.13	0.07	-0.06	0.01	0.12

Sample name	*River*	*Location*	*Type*	*Depth (m)*	*δ^{30}Si*	*2 s.d.*	*δ^{29}Si*	*2 s.d.*	*Al/Si*
CAN09_42	Peel	Fort McPherson	RBS		-0.40	0.10	-0.20	0.01	0.18
CAN10_07	Peel	Fort McPherson	RBS		-0.19	0.06	-0.09	0.01	0.09
CAN09_37	Peel	Fort McPherson	SPM	9	-0.36	0.03	-0.18	0.03	0.25
CAN09_38	Peel	Fort McPherson	SPM	6	-0.44	0.04	-0.22	0.02	0.26
CAN09_39	Peel	Fort McPherson	SPM	3	-0.33	0.08	-0.18	0.04	0.26
CAN09_40	Peel	Fort McPherson	SPM	0	-0.49	0.05	-0.26	0.04	0.30
CAN10_03	Peel	Fort McPherson	SPM	8.5	-0.34	0.02	-0.22	0.03	0.19
CAN10_04	Peel	Fort McPherson	SPM	5.5	-0.44	0.06	-0.25	0.03	0.26
CAN10_05	Peel	Fort McPherson	SPM	2.5	-0.48	0.03	-0.25	0.06	0.27
CAN10_06	Peel	Fort McPherson	SPM	0	-0.43	0.10	-0.15	0.03	0.27
CAN11_77	Peel	Fort McPherson	SPM	6	-0.14	0.05	-0.09	0.03	0.20
CAN11_78	Peel	Fort McPherson	SPM	3	-0.35	0.07	-0.16	0.03	0.21
CAN11_79	Peel	Fort McPherson	SPM	0	-0.41	0.05	-0.21	0.03	0.27
CAN09_30	Slave	Fort Smith	RBS		-0.18	0.07	-0.07	0.06	0.09
CAN10_66	Slave	Fort Smith	RBS		-0.06	0.09	0.03	0.02	0.09
CAN09_28	Slave	Fort Smith	SPM	0	-0.22	0.06	-0.08	0.04	0.28
CAN10_65	Slave	Fort Smith	SPM	0	-0.21	0.08	-0.09	0.02	0.28

5.2.2 Sediments from other large rivers

In this study we also report and interpret the δ^{30}Si of sediments (both channel surface SPM and RBS) from other rivers. These samples (Table 5.3) provide complementary information on the Si isotope cycle in various geological settings, which likely result in different patterns because of distinctive source materials (e.g. igneous vs. sedimentary rocks), and/or varying weathering intensity. These settings include subduction zones (Stikine and Fraser rivers, and small rivers of the volcanic island of Guadeloupe), large igneous provinces (rivers draining the Deccan Trap: Tapti, Purna, and Narmada rivers), Chinese loess plateau (Huanghe), sedimentary basins and cratonic settings (Congo, Niger, Lena, and Seine rivers) or collisional zones (Brahmaputra, Ganga, Orinoco, Irrawady, Salween, Mekong, Red, Xijiang, and Changjiang rivers). These samples are from the sample repository of the Institut de Physique du Globe de Paris (IPGP). We note that sediments from small rivers in Guadeloupe were sieved, and only the clay fraction (<63µm) is used in this study.

Table 5.3 Silicon isotope composition of river sediments across the world

Sample name	*River*	*Sample type*	*$\delta^{30}Si$*	*2 s.d.*	*$\delta^{29}Si$*	*2 s.d.*	*Al/Si*	*Setting*
JAVA19	Java	SPM	-0.42	0.09	-0.19	0.02	0.38	Subduction
LEZARDE	Lezarde (Guadeloupe)	Clay	-1.07	0.15	-0.5	0.03	0.56	Subduction
Capesterre 10/9/2007	Capesterre (Guadeloupe)	Clay	-0.76	0.07	-0.4	0.03	0.46	Subduction
La Perle 10/9/2007	La Perle (Guadeloupe)	Clay	-0.70	0.11	-0.37	0.02	0.42	Subduction
CAN99-39	Stikine	SPM	-0.16	0.15	-0.08	0.04	0.23	Subduction
CAN99-21	Fraser	SPM	-0.34	0.03	-0.14	0.06	0.30	Subduction
G0211691	Congo	RBS	-0.04	0.09	-0.07	0.06	0.01	Cratonic / Sedimentary
C89-65	Congo	SPM	-1.06	0.11	-0.58	0.03	0.57	Cratonic / Sedimentary
C89-63	Congo	SPM	-1.19	0.08	-0.63	0.07	0.54	Cratonic / Sedimentary
PK520	Congo	RBS	-0.10	0.05	-0.05	0.07	0.01	Cratonic / Sedimentary
KASAI2	Congo	RBS	-0.14	0.11	-0.06	0.06	0.01	Cratonic / Sedimentary
StanleyPool	Congo	RBS	-0.10	0.08	-0.06	0.06	0.00	Cratonic / Sedimentary
SANGHA1	Congo	RBS	-0.15	0.09	-0.05	0.02	0.01	Cratonic / Sedimentary
LENA94-17	Lena	RBS	-0.13	0.11	-0.06	0.03	0.15	Cratonic / Sedimentary
BP37	Seine	SPM	-0.56	0.11	-0.31	0.01	0.32	Cratonic / Sedimentary
NIGERS95	Niger	SPM	-0.80	0.05	-0.39	0.10	0.42	Cratonic / Sedimentary
NIGERM95	Niger	RBS	-0.13	0.06	-0.07	0.07	0.05	Cratonic / Sedimentary
91M-1	Mississippi	RBS	-0.30	0.16	-0.16	0.06	0.16	Cratonic / Sedimentary
IND98-8	Tapti	SPM	-0.80	0.07	-0.37	0.03	0.35	Decan Trap
IND98-18	Purna	SPM	-0.45	0.02	-0.25	0.05	0.35	Decan Trap
IND98-28	Namarda	SPM	-0.78	0.10	-0.35	0.05	0.37	Decan Trap
CAN96-31	Yellowknife	RBS	-0.11	0.07	-0.05	0.03	0.17	Glacial flour
CH93-5	Huanghe	RBS	-0.19	0.15	-0.06	0.03	0.19	Loess plateau
CH94-5	Huanghe	SPM	-0.25	0.08	-0.15	0.04	0.29	Loess plateau

Sample name	*River*	*Sample type*	*$\delta^{30}Si$*	*2 s.d.*	*$\delta^{29}Si$*	*2 s.d.*	*Al/Si*	*Setting*
CH93-6	Huanghe	SPM	-0.31	0.05	-0.17	0.05	0.34	Loess plateau
CH94-6	Huanghe	SPM	-0.20	0.07	-0.12	0.02	0.31	Loess plateau
VIET92-1	Mekong	SPM	-0.28	0.11	-0.15	0.05	0.28	Collisional / Sedimentary
OR46	Orinoco	SPM	-0.43	0.03	-0.23	0.02	0.24	Collisional / Sedimentary
BIR99-3	Irrawady	RBS	-0.27	0.11	-0.12	0.04	0.19	Collisional / Sedimentary
BIR99-1	Salween	SPM	-0.43	0.11	-0.23	0.04	0.32	Collisional / Sedimentary
IND99-20M	Brahmaputra	SPM	-0.30	0.07	-0.19	0.05	0.29	Collisional / Sedimentary
IND99-20S	Brahmaputra	RBS	-0.25	0.02	-0.14	0.02	0.21	Collisional / Sedimentary
IND99-19M	Ganges	SPM	-0.40	0.10	-0.19	0.04	0.35	Collisional / Sedimentary
IND99-19S	Ganges	RBS	-0.26	0.08	-0.13	0.03	0.11	Collisional / Sedimentary
CH93-1	Chang Jiang	SPM	-0.45	0.07	-0.2	0.08	0.36	Collisional / Sedimentary
CH94-1	Chang Jiang	SPM	-0.41	0.07	-0.2	0.01	0.35	Collisional / Sedimentary
CH93-4	Chang Jiang	SPM	-0.35	0.04	-0.16	0.04	0.32	Collisional / Sedimentary
CH94-3	Chang Jiang	SPM	-0.40	0.08	-0.18	0.06	0.37	Collisional / Sedimentary
CH97-2	JinshaJiang	SPM	-0.44	0.03	-0.19	0.04	0.35	Collisional / Sedimentary
CH97-13	Dadu He	SPM	-0.33	0.08	-0.16	0.03	0.27	Collisional / Sedimentary
CH93-3A	Jialing Jiang	SPM	-0.29	0.08	-0.14	0.06	0.26	Collisional / Sedimentary
CH94-2	Jialing Jiang	SPM	-0.27	0.06	-0.14	0.08	0.26	Collisional / Sedimentary
CH93-3	Jialing Jiang	RBS	-0.27	0.06	-0.17	0.11	0.34	Collisional / Sedimentary
CH94-4S	Xi Jiang	RBS	-0.25	0.16	-0.13	0.06	0.09	Collisional / Sedimentary
CH94-4	Xi Jiang	SPM	-0.44	0.10	-0.2	0.05	0.37	Collisional / Sedimentary
YenBai	Da River (Vietnam)	SPM	-0.43	0.07	-0.23	0.04	0.37	Collisional / Sedimentary
VIET92-5	Red River	SPM	-0.36	0.13	-0.17	0.06	0.34	Collisional / Sedimentary

5.3 Analytical methods

The precise measurement of the $\delta^{30}Si$ signature of river sediments involves four steps: sample digestion, Si concentration determination, Si purification, and $\delta^{30}Si$ measurement. We adopted the alkaline fusion method (Savage and Moynier, 2013; Savage et al., 2013; Pringle et al., 2013a, 2013b, 2014, 2016) to digest the sediments and a modified version of the protocol from Georg et al., (2006) to purify Si from the matrix. Only a summary is provided here as these methods have been widely employed and discussed elsewhere. Sediment samples were firstly grinded in a mortar. Approximately ~200 mg of NaOH were added as a flux to ~10 mg of each powdered samples in a silver crucible, which was heated at 720°C for 12 minutes afterwards. The fused samples were then cooled to room temperature and transferred into ~15 ml MQ-water in 30 ml Teflon beakers, and were allowed to settle overnight. Afterwards, the samples were sonicated and transferred to pre-cleaned PE bottles, and then further diluted and weakly acidified to ~100 ml 1% (v/v) HNO_3 solution. The Si concentration of the sample solutions were analyzed using ICP-OES (Amazon samples) or Q-ICP-MS (all other samples) at IPGP. Before isotope measurements, Si was purified via column chromatography using 1.8 ml cationic resin (BioRad, AG50W–X12, 200–400 mesh). Twenty µg of each sample were loaded onto the column, followed by an elution step with 5 ml MQ water. The final solution was diluted to a Si concentration of 2 ppm and acidified to 0.2 N HNO_3 for isotope analyses on a Thermo Fisher Neptune Plus MC-ICP-MS at IPGP.

The quartz sand reference material NBS-28 was used as the bracketing standard and the well characterized basalt reference material BHVO-2 was used as an external standard to check the accuracy of the protocol. These two reference materials were treated before analyses following the same protocol described above as for samples. The silicon isotope composition of sediments from large river systems, relative to NBS-28, are reported in Table 5.1, 5.2, and 5.3. Mass-dependent

fractionation is indicated by the linear relationship between δ^{30}Si and δ^{29}Si across all samples, with a slope value of 0.5025 (Fig 5.2). At the current resolution of our measurements, we are unable to distinguish whether our results indicate kinetic fractionation (slope = 0.5092) or equilibrium fractionation (slope = 0.5178). The long-term δ^{30}Si of BHVO-2 from this study (−0.29±0.07‰, n=72) is in agreement with previously reported values (Zambardi and Poitrasson, 2011; Savage et al., 2011, 2013; Pringle et al., 2016; Bayon et al., 2018).

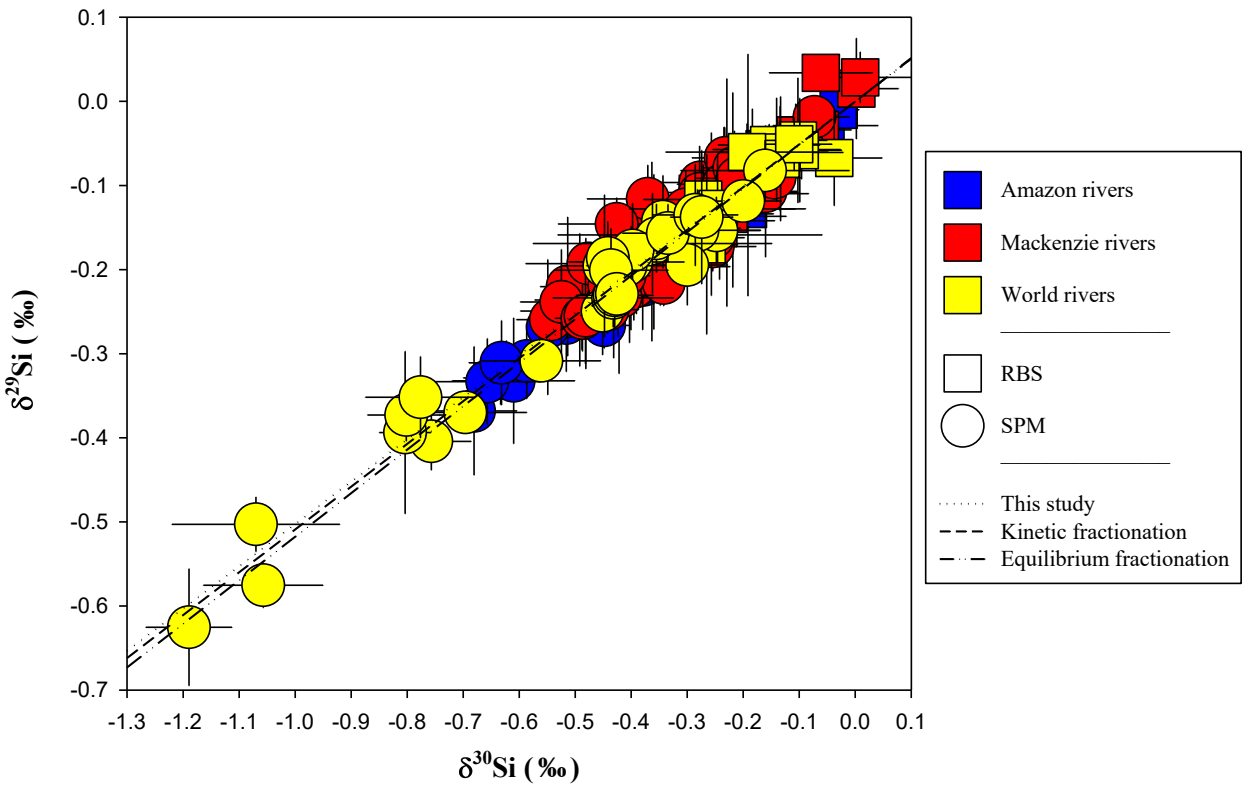

Figure 5.2 "Three-isotope plot" (δ^{29}Si against δ^{30}Si) showing the mass dependent fractionation in large river sediment samples. The measured slope (0.5025) is undistinguishable from the theoretical kinetic (0.5092) and equilibrium (0.5178) relationships.

5.4 Results

Depth-profiles of δ^{30}Si depict a stratification in most of the studied rivers (e.g. Solimões and

Red Arctic, Fig 5.4), whereas in a few rivers it remains invariant along river channel depth. Consistently with the results from Dellinger et al. (2014) for Li, a negative relationship is found (Fig 5.5) between δ^{30}Si and the grain size of sediments, using Al/Si as a grain size proxy (Bouchez et al., 2011; Lupker et al., 2011; Dellinger et al., 2014). In the finer portion of river sediments (high Al/Si), lighter Si isotopes are enriched. In the coarse portion (low Al/Si), there is a significant enrichment of heavier Si isotopes. Notably, this finding is also consistent with the observation from Savage et al. (2013) and Bayon et al. (2018) that the δ^{30}Si value of shales decreases with increasing Al/Si values.

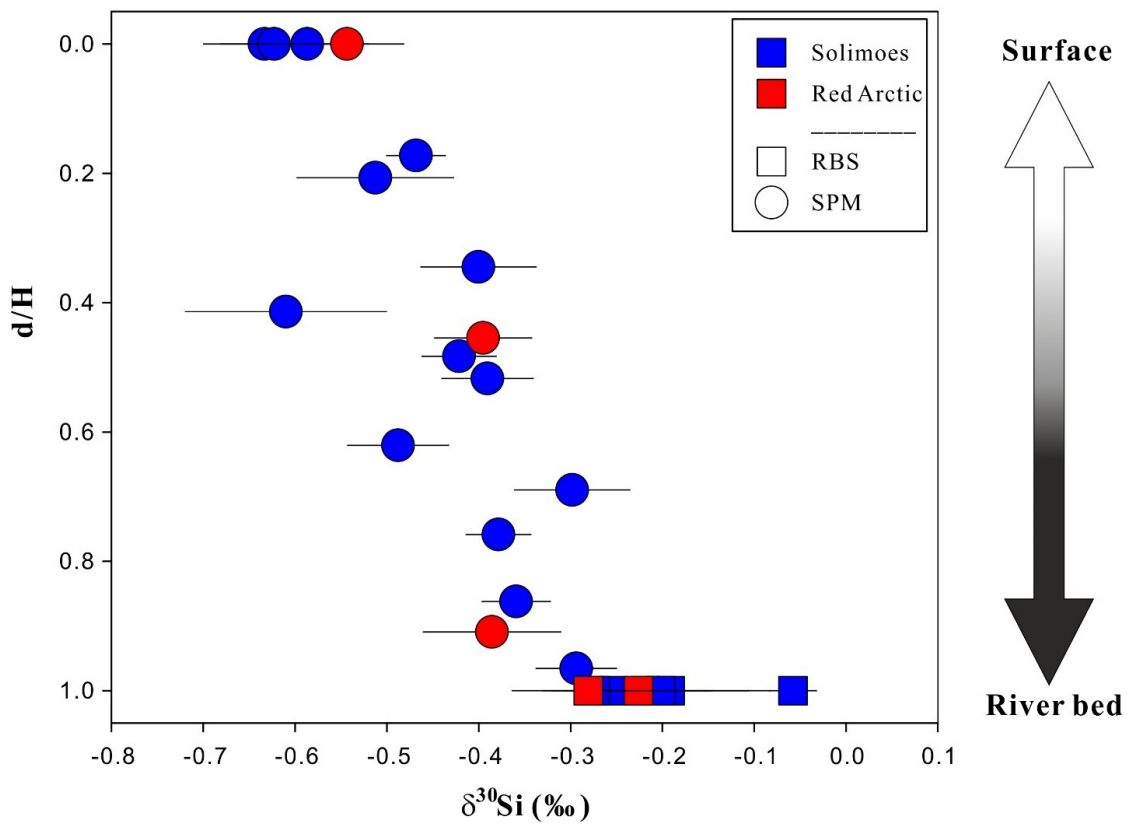

Figure 5.3 Sediment δ^{30}Si in large river depth-profiles: stratification of δ^{30}Si as a function of relative river depth in the water column, d/H – ratio of sampling depth (d) to the river channel depth (H).

For both Si and Li isotope systems, RBS are systematically enriched in heavy isotopes compared

to SPM. In the case of Li, RBS samples plot on a binary mixing trend between igneous rocks and shales (Dellinger et al., 2014). However, RBS have a relatively homogenous δ^{30}Si signature (except for one sieved RBS sample from the Napo river; Fig 5.3). In the following section, we will examine the potential causes for the variations of δ^{30}Si in river sediments and their plausible implications.

The RBS from the world's largest rivers have δ^{30}Si values within the range of the Upper Continental Crust (UCC) composition (−0.25 ± 0.16 ‰; Fig 5.4), which was estimated by Savage et al. (2013) from a weighted average of the four major units composing UCC: sedimentary rocks, felsic intrusive rocks, metamorphic rocks, and gabbros (Wedepohl, 1995). The mean δ^{30}Si value of RBS (excluding the sieved Napo-Pastaza samples) is −0.19 ± 0.19 ‰ (n=44, 2 s.d), matching the mean Si isotope composition in the silt fraction of world river sediments (δ^{30}Si=−0.21± 0.19 ‰, Bayon et al., 2018). The Napo-Pastaza samples have greater Al/Si values compared to other RBS samples, similar to the silt samples from Bayon et al. (2018), because the Napo-Pastaza samples used in our study were sieved at 125 µm (similar to the silt samples used in Bayon et al. (2018), which were sieved at 4–63 µm), such that the coarse component of those samples, which is dominated by quartz whose Al/Si ratio is 0, was discarded. Therefore, these samples plot at higher Al/Si values but still exhibit δ^{30}Si values in a range comparable with that of other RBS.

The δ^{30}Si values of SPM samples are lower than that of RBS samples and UCC. Compared to the clay fraction of river sediments from Bayon et al. (2018) (and considering only the non-marine sediments, as the sediments collected from marine environments may have been subjected to authigenic clay formation, see Chapter 4), SPM have lower Al/Si ratios and higher δ^{30}Si values.

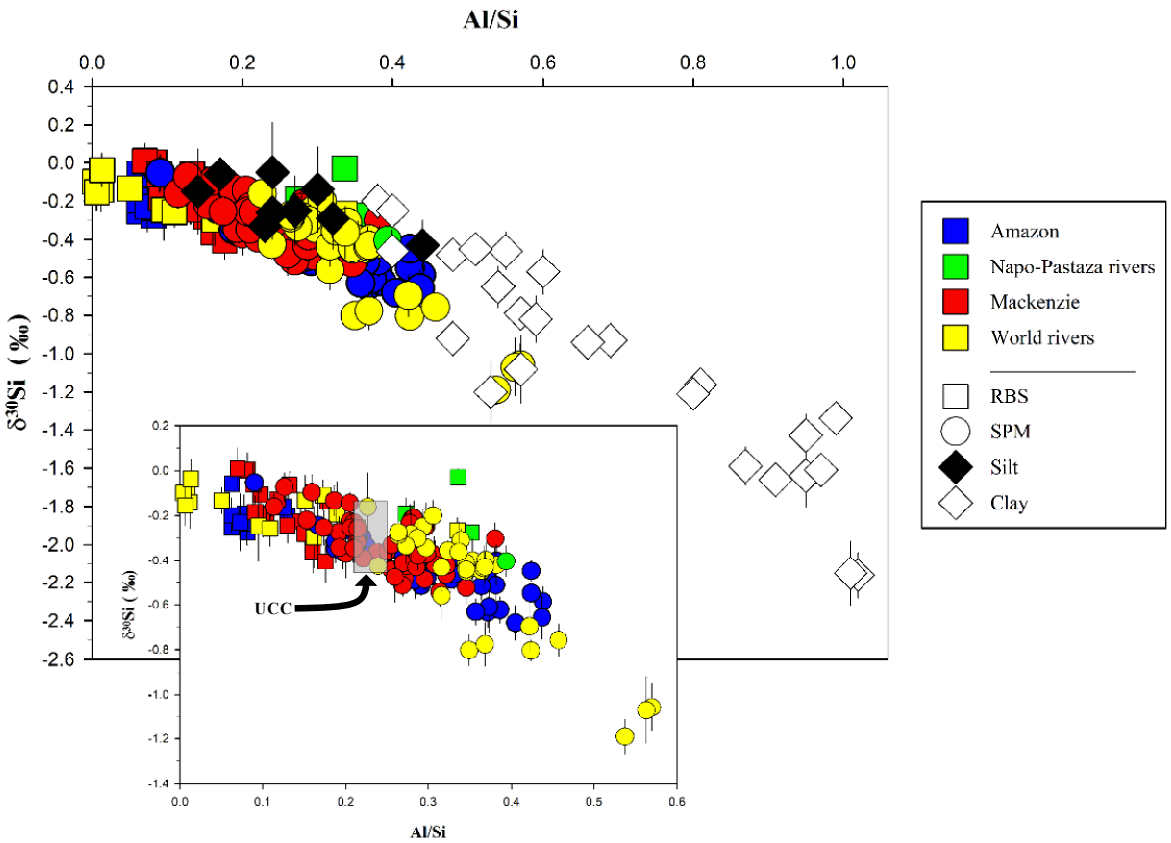

Figure 5.4 Large river sediment δ^{30}Si as a function of their Al/Si ratio, used here as a grain size proxy. Samples with low Al/Si values are river bed sands (RBS, squares) while those with higher Al/Si values are suspended particulate matter (SPM, circles). The grey box in the inset represents the average upper continental crust composition with Al/Si=0.23 ± 0.02, δ^{30}Si=–0.25 ± 0.16 ‰ (Savage et al., 2013). Silt (filled diamonds) and clay (open diamonds) fractions of river sediments are from Bayon et al. (2018).

Compared to Li, the Si isotope composition of large river sediments exhibits a relatively narrow range (Fig 5.3), from −1.2‰ (SPM from Congo river) to 0.0‰ (RBS from the Liard river, Mackenzie system). By contrast, the Li isotope composition of the SPM from the same rivers varies from −6.2‰ to 4.1‰ (Dellinger et al., 2014, 2017). The relative mass difference between ^{6}Li and ^{7}Li (1/6) is approximately 2.3 times that between ^{28}Si and ^{30}Si (1/14). However, the absolute range of δ^{7}Li in SPM (10.3 ‰) observed in river sediments in this study is nearly 9 times larger than that of δ^{30}Si (1.2 ‰). Considering that both elements are not sensitive to redox changes,

and that Si is more strongly involved in biological processes than Li, the limited range of isotopic variation in river sediment of Si compared to Li demands further examination. Meanwhile, δ^{30}Si in the clay fraction of river sediments ($\delta^{30}Si_{Clay}$) also exhibits a greater variation (−0.11‰ to −2.16‰, Bayon et al., 2018), approximately twice the range of δ^{30}Si values in bulk sediments, suggesting that Si geochemistry in river sediment is at least partially controlled by mineralogy.

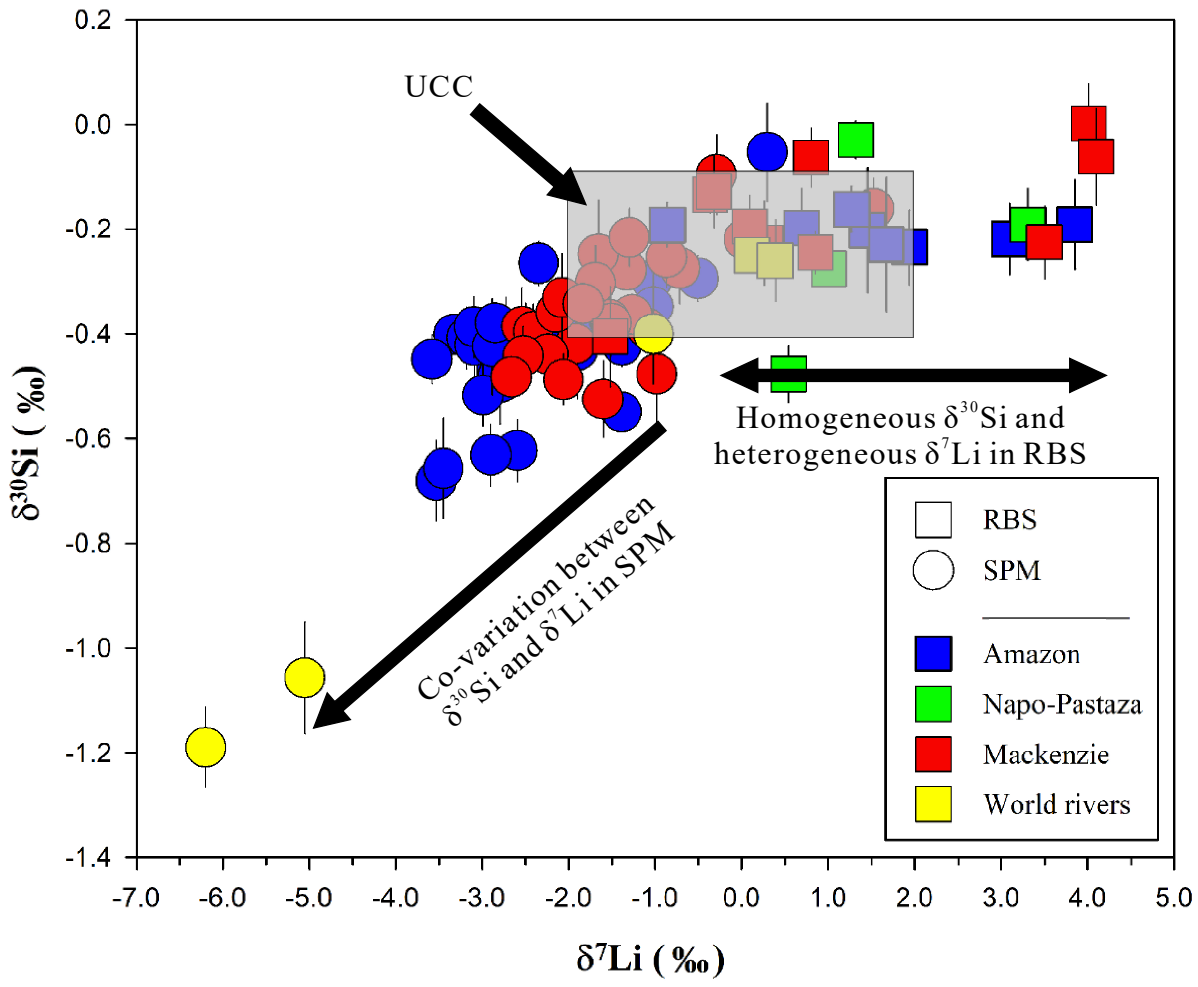

Figure 5.3 Relationship between the δ^{30}Si and δ^{7}Li in river sediments from the Amazon (except Napo-Pastaza), Napo-Pastaza, Mackenzie, and world rivers (Ganga-Brahmaputra and Congo rivers). The grey box represents the average UCC with δ^{30}Si=−0.25 ± 0.16‰ (Savage et al., 2013) and δ^{7}Li=0 ± 2‰ (Teng et al., 2004).

5.5 Discussion

Our results clearly show that the δ^{30}Si of sediments carried by the world's largest rivers is variable, with samples with coarser grain size (lower Al/Si) having higher δ^{30}Si than finer samples (higher Al/Si). This finding is in agreement with the relationships previously reported between Li isotopes and grain size of large river sediments (Dellinger et al., 2014). The relationship between δ^{30}Si and Al/Si ratios also agrees with the observations made from δ^{30}Si in the clay fraction of river sediments (Bayon et al., 2018) and in shales (Savage et al., 2013).

The departure of the SPM δ^{30}Si signature from that of the UCC is due to the fact that during silicate weathering, the partitioning of Si between the solid and dissolved loads entails an isotope fractionation (Ziegler et al., 2005a, 2005b; Georg et al., 2007; Opfergelt et al., 2009, 2011, 2012; Bern et al., 2010; Opfergelt and Delmelle, 2012), and to the enrichment of secondary solids in relatively fine SPM. As a consequence, the δ^{30}Si of SPM from the studied rivers are lower than that of the average global riverine DSi (1.28‰, Frings et al., 2016). Lastly, the comparison between bulk SPM and separated clays from Bayon et al., (2018) suggests that the presence of relatively coarse, unweathered primary minerals in SPM has a strong influence on Si isotope composition in bulk river sediments.

5.5.1 Negligible biological effects on the δ^{30}Si of river sediments

We can first dismiss the influence of biological activity on the δ^{30}Si variation in SPM. First, the BSi fraction in river sediments is small. Frings (2014) estimated that only ~0.6% of the global river SPM is amorphous silica (ASi), which contains some significant proportion of BSi. Second, despite of the fact that Si (unlike Li) is taken up by continental and marine biota, the isotopic variations of Si and Li are broadly correlated (Figure 1.5) with coarser sediments being enriched in heavier isotopes and finer sediments enriched with lighter isotopes, although with smaller

variability for Si than for Li.

However, it should be emphasized that the biological uptake of Si from DSi and the formation of BSi is able to affect the concentration and isotope signature of continental DSi, for example in lake environments where freshwater diatoms sequestrate a significant fraction of influx of DSi (Harrison et al., 2012; Frings et al., 2014b), such that there may be an indirect effect of biological activity on secondary mineral δ^{30}Si that would form from this DSi. The Si isotope signature of the secondary mineral end member is discussed below in this paper (see Chapter 5.5.3).

5.5.2 δ^{30}Si and δ^{7}Li variations in large river bed sands

The fact that biological activity has little effect on the δ^{30}Si of river sediments makes the δ^{30}Si and δ^{7}Li systems comparable. Both isotopic systems are fractionated during weathering processes due to the partition between solids (lighter-isotope enriched) and solution (heavier-isotope enriched). In a δ^{30}Si–δ^{7}Li diagram (Fig 1.5), the trends depicted by SPM and RBS samples are distinct. In SPM, δ^{30}Si and δ^{7}Li are positively correlated, whereas RBS have a homogeneous δ^{30}Si signature comparable to that of the UCC, while their δ^{7}Li displays a large variation from −1.5 ‰ to 4.1 ‰.

At the Earth surface, the isotopic variation of an element can be attributed to different source rock signatures, and/or to chemical transformation on its way from the source rocks. Dellinger et al. (2014) have shown that there is a source effect on δ^{7}Li variation in river sediments, which is displayed in particular by different Li isotope composition of RBS from different rivers. Silicon is contained in all silicate rocks, thus the distinct δ^{30}Si signatures of different parent rocks might explain part of the observed variation in bulk sediment ^{30}Si. The main contrast between potential source rocks is observed (1) between different types of igneous rocks, which have a limited variation in terms of δ^{30}Si (−0.4‰ < δ^{30}Si < −0.1‰, Poitrasson., (2017) and references therein;

for instance the average δ^{30}Si value of granites is δ^{30}Si = −0.23 ± 0.15 ‰ (Savage et al., 2012)); (2) between igneous sedimentary rocks such as shales which exhibit a greater variation of δ^{30}Si towards lower values (−0.8‰ < δ^{30}Si < 0‰, Savage et al., (2013)). Due to its mobile nature and its diffusive behaviour during magmatic processes, Li shows a large δ^{7}Li variation in UCC-type rocks (−5‰ < δ^{7}Li < 15‰) and in continental volcanic rocks (-10‰ < δ^{7}Li < 10‰) (Tomascak et al., 2016). In addition, sedimentary rocks display a large range of δ^{7}Li values (−8‰ < δ^{7}Li < 15‰), towards low values (Tomascak et al., 2016). Altogether, these differences in source rock isotope composition variability could explain the fact that δ^{7}Li displays a larger range than δ^{30}Si in RBS. In addition, the major mineral carrier of Si in most rock types is quartz, which is thought to have a limited range of variation whatever the hosting rock is (−0.20‰, Savage et al., (2013)) and thus would tend to "buffer" variations in δ^{30}Si across a range sediments of relatively coarse grain sizes. In other words, if a river basin was strongly affected by the erosion of meta-sedimentary rocks (shales and sandstones), this would have a strong effect on the δ^{7}Li of RBS exported by this basin (through the erosion of Li-rich, low- δ^{7}Li shales), while this effect would be muted for the δ^{30}Si of RBS (through the erosion of quartz-rich sandstones, quartz having a homogenous δ^{30}Si composition).

By contrast, the δ^{30}Si–δ^{7}Li positive of SPM relationship is likely due to weathering, as during rock-water interactions both systems follow similar logics of fractionation. We discuss below how weathering at all time scales might control the δ^{30}Si composition of river sediments.

5.5.3 Mineralogical controls on the δ^{30}Si of large river sediments

After dismissing the contribution of biological effects, the viable candidates to cause the δ^{30}Si variations in large river sediments are: (1) a source effect resulting from different bedrock sources (chiefly from the contrast between primary rocks and the products of previous weathering

episodes, i.e. metasedimentary rocks; see section 5.5.2) having different δ^{30}Si values; (2) present-day weathering processes through the formation of secondary minerals. It should be noted that both the “source” and “process” isotope effects result from erosion/weathering processes, the question being the time scale (10^3-10^6 yrs vs. 10^8-10^9 yrs) over which weathering effects are integrated within the Si isotope signature of river sediments.

In general, weathering processes dissolve primary minerals such as feldspar and form secondary minerals such as clays. This pattern can be shown when investigating the sodium (Na) content of large river SPM. The most important Na-bearing mineral is feldspar, as Na can only exist as a trace element in clays, and as in quartz there is virtually no Na. The “croissant-shaped” relationship observed between the Na content (expressed as Na/Si) and grain size (Al/Si ratio) for the Solimões River and its tributaries draining terranes in the northern part of the Amazon Basin with a significant contribution of igneous rocks shows that feldspars are enriched in intermediate-Al/Si sediments there (Figure 5.6). This Na/Si “peak” is much lower for rivers draining the southern side of the Amazon Basin (Beni River for example), which almost exclusively drains sedimentary rocks, showing the scarcity of feldspar grains in the SPM of these rivers.

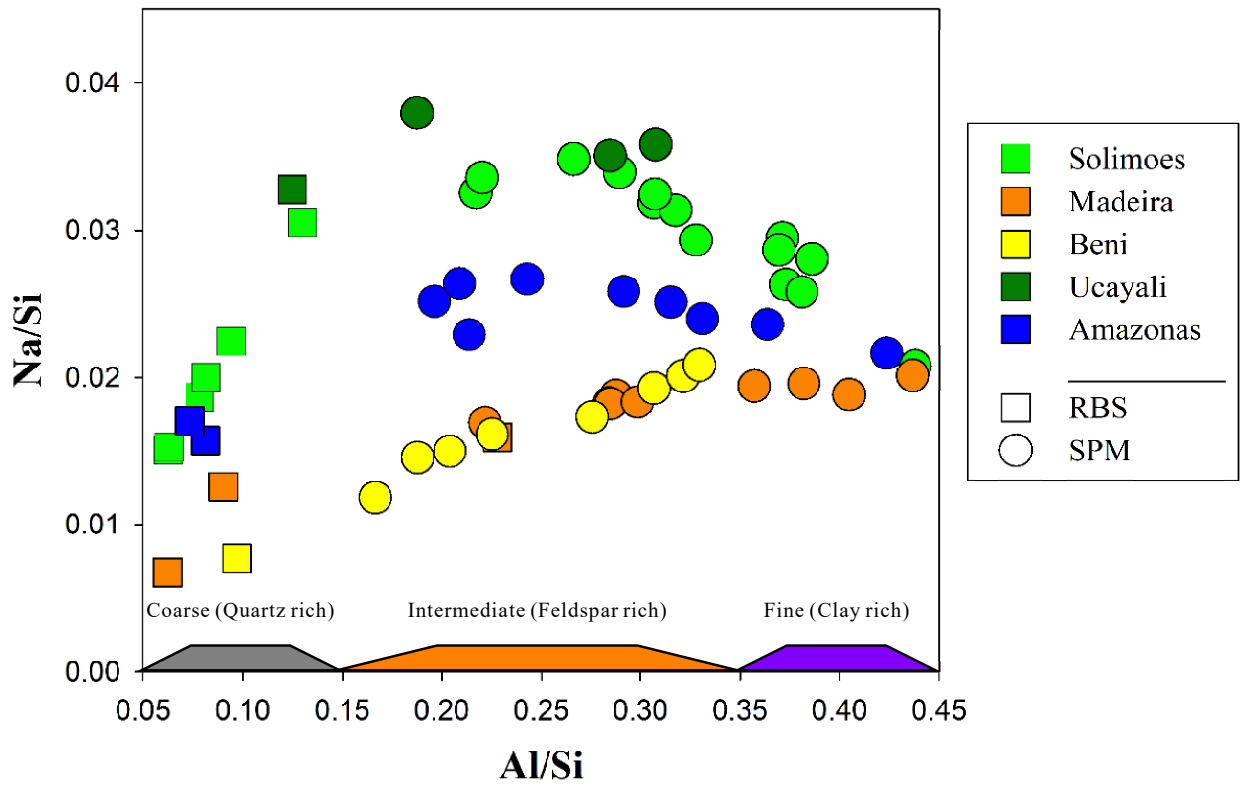

Figure 5.4 Relationship between Na/Si (proxy for feldspar content) and Al/Si (proxy for grain size) for Amazon river sediments.

Given the relationship that exists between Al/Si and Na/Si ratios, our large river sediments δ^{30}Si data set (Fig 5.7) can thus be interpreted in terms of a mixing array amongst three mineralogical endmembers: quartz, weatherable primary minerals (feldspar but also in some settings mafic minerals such as pyroxene), and clays.

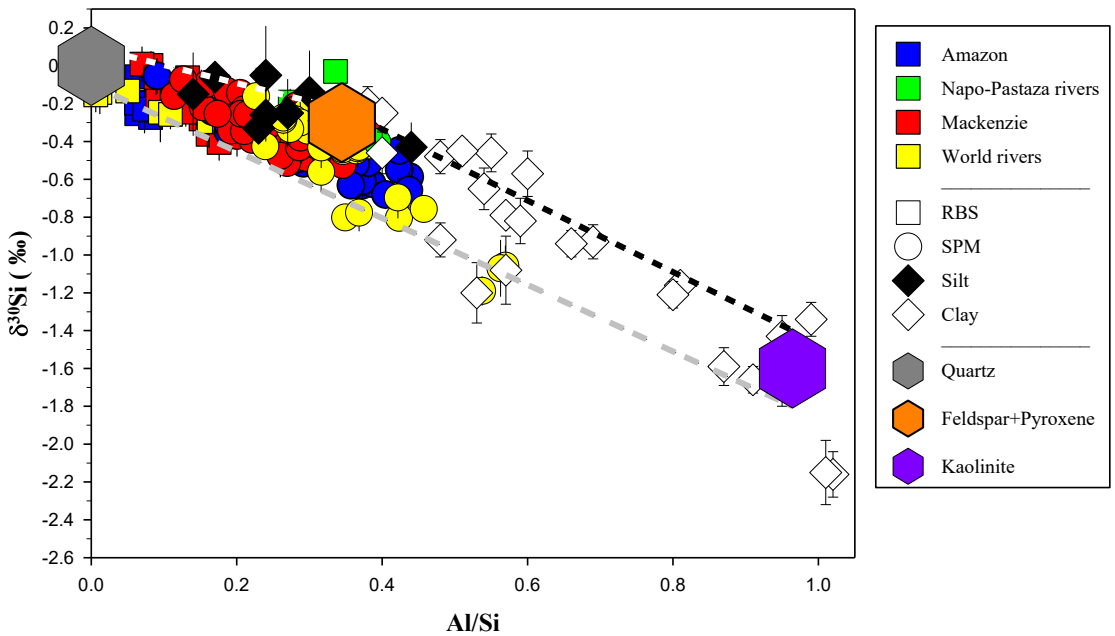

Figure 5.5 Relationship between δ^{30}Si and grain size (Al/Si) for sediments from the world's large rivers showing the solid weathering products as a mixture among three end-members: quartz, feldspar+pyroxene, and kaolinite. See Table 5.4 for explanations about the end-member values.

Whereas previous studies provide constraints on the composition of the quartz and weatherable primary mineral end members, the composition of the clay end member is of particular interest as it is the one which is likely to carry a weathering signal (*e.g.*, Dellinger et al., 2017). We use a simple mass balance based on the mineralogy of river sediments to estimate the δ^{30}Si of this clay end-member, assumed to vary from river to river. First, for a given sediment sample, the Si budget is composed of three end-members:

$$f_{Weatherable} + f_{Quartz} + f_{Clays} = 1 \quad \text{(Equation 5-1)}$$

with $f_{Weatherable}$, f_{Quartz}, and f_{Clays} representing the fraction of Si carried by weatherable minerals (feldspar and pyroxenes), quartz, and clays, respectively.

Additionally, we can establish the mass balance of the Al/Si ratio:

$$\left[\frac{\mathrm{Al}}{\mathrm{Si}}\right]_{Bulk} = \left[\frac{\mathrm{Al}}{\mathrm{Si}}\right]_{Weatherable} \times f_W + \left[\frac{\mathrm{Al}}{\mathrm{Si}}\right]_{Quartz} \times f_{Quartz} + + \left[\frac{\mathrm{Al}}{\mathrm{Si}}\right]_{Clays} \times f_{Clays} \quad \text{(Equation 5-2)}$$

Moreover, the same relationship can also be applied on the Na/Si ratio:

$$\left[\frac{\mathrm{Na}}{\mathrm{Si}}\right]_{Bulk} = \left[\frac{\mathrm{Na}}{\mathrm{Si}}\right]_{Weatherable} \times f_W + \left[\frac{\mathrm{Na}}{\mathrm{Si}}\right]_{Quartz} \times f_{Quartz} + + \left[\frac{\mathrm{Na}}{\mathrm{Si}}\right]_{Clays} \times f_{Clays} \quad \text{(Equation 5-3)}$$

With these three equations, $f_{Weatherable}$, f_{Quartz}, and f_{Clays} can be calculated. For the quartz end-member, a value of 0 is assigned to both Al/Si and Na/Si. For the clay end-member, we use the kaolinite stoechiometry ($Al_2Si_2O_8(OH)_4$) because kaolinite is the Si-bearing mineral representative of the terminal stage of aluminosilicate clay formation during weathering. Further desilication "beyond" kaolinite, would lead to the formation of Si-free phases, such as gibbsite, which would not influence the mixing array of Figure 1.7. This yields an Al/Si ratio of 0.96 and a Na/Si ratio of 0 for the clay end member. It is more difficult to constrain the Al/Si and Na/Si ratios of weatherable minerals end-member, as relative amounts of different types of feldspars (in particular Na-bearing *vs*. K-bearing) or of weatherable minerals (*e.g*. feldpsars *vs*. pyroxenes) (Fig 5.1) might vary from one river system to another. Therefore we use a range of plausible Na/Si ratios for this end member, ranging from the maximum Na/Si ratio observed in each corresponding river depth-profile to 0.274 (stoechiometry of pure Na-feldspar, Table 5.4). As both Al and Si are relatively insoluble, we assume that the Al/Si ratio of the weatherable end-member remains relatively stable during weathering, and we adopt an Al/Si value of 0.34 derived through mass balance using the UCC δ^{30}Si value and normative composition (Table 5.4). Results are presented in Appendix ii Table ii-1. More than 50% of sampled river sediments have a quartz contribution to the Si particulate budget over 40%, showing the prevalence of quartz in setting the bulk δ^{30}Si composition of river

detrital sediments, and as expected, RBS (low Al/Si) have higher f_{Quartz} and lower f_{Clay}, whereas fine SPM (high Al/Si) have lower f_{Quartz} and higher f_{Quartz}.

Then, the δ^{30}Si value of the clay end-member of each river can be estimated by extrapolating the depth-profiles δ^{30}Si *vs.* f_{Clays} trends of to $f_C = 1$. For each river, we obtain a range of δ^{30}Si values for the clay end-member as a range of Na/Si were used for the weatherable mineral end-member (Fig 5.8). Given the resulting uncertainties, it is difficult to observe any significant difference in $\delta^{30}Si_{Clays}$ between different rivers, that could be linked to the prevailing weathering conditions on lithological sources in each basin. Therefore, we use a global average value of $\delta^{30}Si_{Clay}$=−1.60 ± 0.20‰. The range of measured kaolinite δ^{30}Si is around −2.2 ± 0.1‰ for field data (Ziegler et al., 2005b) and −2.0 ± 0.1‰ from our own measurements of the well-studied kaolinite standard KGa-2 (see Chapter 3), which is compatible with the inference derived from the mixing model used here. The value of this end member is lower than that of the pristine continental crust, but the fact that a unique global clay end member, independent from lithology and weathering conditions across very different basins, can be defined in terms of δ^{30}Si signature is somewhat surprising. The possible reasons for this observation are discussed later in this manuscript.

We note that although our approach involves some strong assumptions, extrapolating the depth-profile δ^{30}Si *vs.* f_{Quartz} trends to f_{Quatz}=1 yield $\delta^{30}Si_{Quartz}$ values around −0.0 ± 0.1‰ , which is fully compatible with other estimates of this end member composition. Indeed, the δ^{30}Si value of the quartz end-member can also be determined through extrapolations of depth-profile data in geochemical mixing diagrams (Fig 5.9). When a depth-profile trend of δ^{30}Si vs. Al/Si (or Li/Si) for a given river is projected to 0, the intercept reflects the composition of the quartz (Li-and Al-free) end member in the corresponding river system. We have tested this method using both Al

(Fig 5.9a) and Li (Fig 5.9b) and both element extrapolations yield $\delta^{30}Si_{Quartz}$ = 0.0 ± 0.1‰ for all depth profiles considered here. Interestingly, this relative heavy Si isotope composition of quartz, compared to UCC (−0.25 ± 0.16‰; Savage et al., 2013), is in agreement with the observed relationship between $\delta^{30}Si$ and SiO_2 concentrations in bulk igneous rock samples (Poitrasson, 2017, and references therein) where $\delta^{30}Si$ becomes heavier when SiO_2 concentration increases. The fact quartz $\delta^{30}Si$ is relatively heavier than average UCC, can also be an alternative explanation for some heavy-$\delta^{30}Si$-low-Al/Si sedimentary rocks observed by Savage et al. (2013), who explained such compositions by the incorporation of marine derived BSi. As explained above earlier, BSi most likely plays a subordinate role on the $\delta^{30}Si$ of global detrital sediments. We also emphasize that some of the heavy-$\delta^{30}Si$ rocks reported by Savage et al., (2013) could rather be termed as "sandstones" rather than "shales", as they feature a high abundance of quartz. Additionally, our estimation of $\delta^{30}Si_{Quartz}$ based on river depth profiles is slightly heavier than the one Savage et al. (2013) estimated from mineral-specific analysis (0.0 ± 0.1‰ *vs.* −0.2‰), which would consequentially generate a heavier average value for the sedimentary rocks, assuming sandstone is only composed of quartz, in UCC (−0.19 ± 0.26‰ *vs.* −0.31 ± 0.26‰) using the same mass balance relationship as in Savage et al. (2013). It's unlikely that at Earth surface sandstones only contain quartz, however we emphasize that sedimentary rocks $\delta^{30}Si$ is controlled by the relative abundance of sandstones and shales, which differs from Li whose isotope composition is barely influenced by sandstones.

Finally, our inferred difference between $\delta^{30}Si_{Quartz}$ and $\delta^{30}Si_{Clays}$ is comparable to the silicon equilibrium isotope fractionation farcor between quartz and kaolinite at 300K, estimated at −1.6‰ by theoretical calculation (Méheut et al., 2007) and at −1.5‰ by mass balance calculationd based on field DSi $\delta^{30}Si$ data (Georg et al., 2007).

Table 5.4 Si isotope composition and Al/Si ratio in primary minerals in Upper Continental Crust (UCC). Data from Taylor and McLennan (1995)

Mineral		Stoichiometry	Mineral abundance in UCC (%)	Si content in UCC (%)	Contribution to total UCC Si (%)	Al/Si	δ^{30}Si (‰)
Quartz		SiO_2	16.1	7.5	24.3	0	0±0.1
Feldspar	Orthoclase	$KAlSi_3O_8$	20.1	6.1	63.0	0.34	-0.3±0.1
	Albite	$NaAlSi_3O_8$	33	10.6			
	Anorthite	$CaAl_2Si_2O_8$	13.9	2.8			
Pyroxene	Diposide	$MgCaSi_2O_6$	5.8	1.5	12.7		
	Hypersthene	$(Mg,Fe)SiO_3$	10.0	2.4			
Ilmenite		$FeTiO_3$	1	0.0	0.0		
Total			99.9	30.9	100		

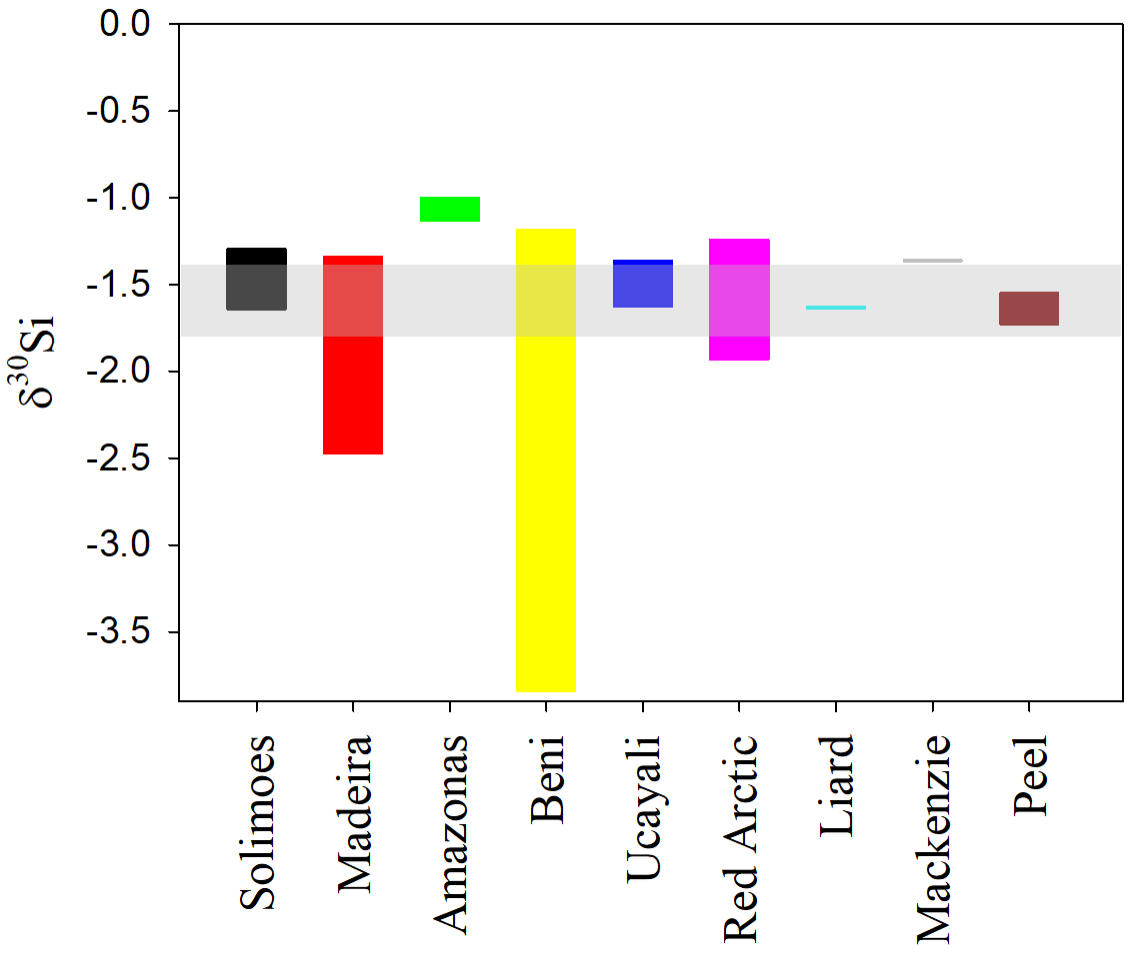

Figure 5.8 Estimation of the Si isotope composition of the clay end-member ($\delta^{30}Si_{Clays}$) for each river using mineralogical mass balances over sediment depth-profiles. The grey area represents the average value over all rivers, at $\delta^{30}Si=-1.60\pm0.20‰$.

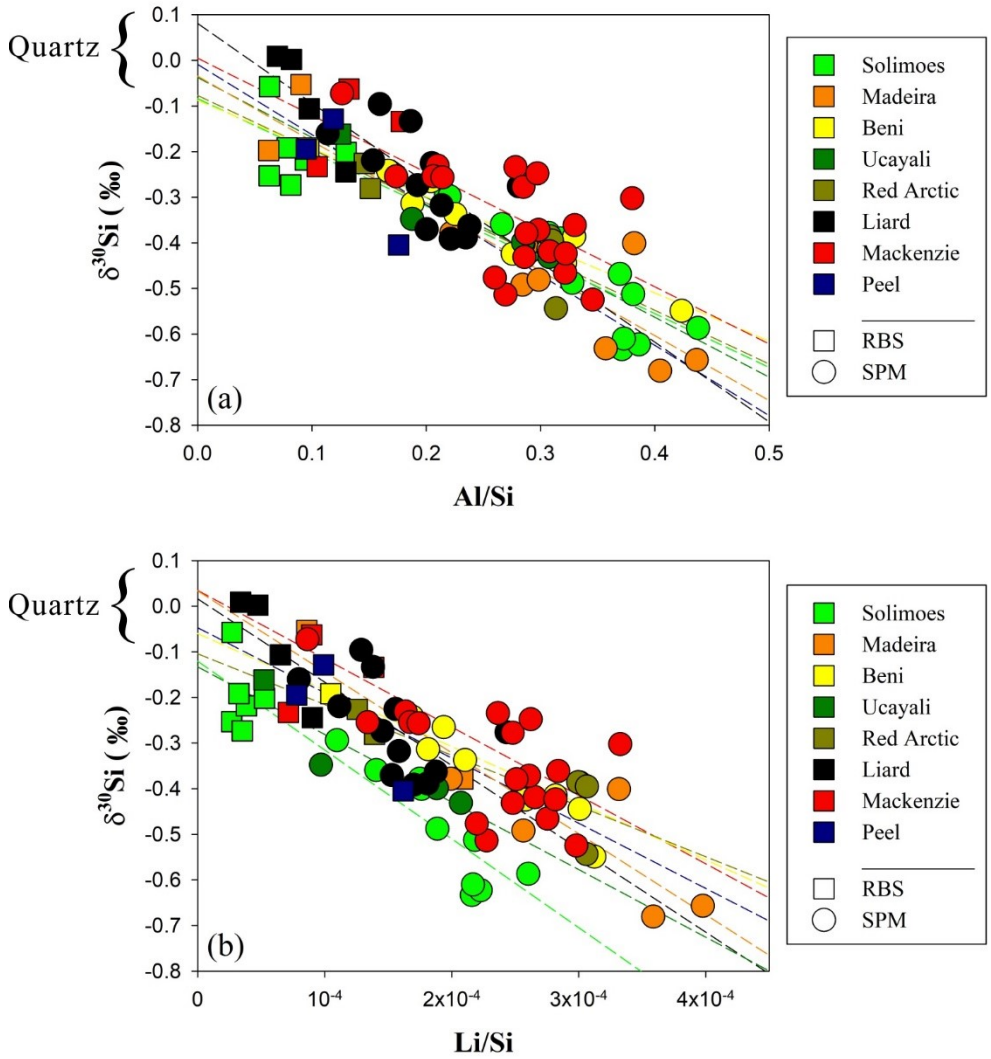

Figure 5.9 Estimation of the Si isotope composition of the quartz end-member ($\delta^{30}Si_{Quartz}$) using sediment depth-profiles from the Amazon and Mackenzie rivers, by intercepting the $\delta^{30}Si$ value at (a) Al/Si = 0 and (b) Li/Si = 0. The stippled lines indicate the linear best-fits for each depth-profile.

5.5.4 Interpretation of large river sediment δ^{30}Si in terms of the geological context

These three endmembers can be placed in a δ^{30}Si-Al/Si diagram, defining a mixing array (Fig 5.7) that can be used to interpret the signature of present river sediments and detrital archives in terms of geological context. At the top of this array, particulates are composed of primary minerals, and contain no clays. Sediments resulting from physical erosion during the weathering of igneous rocks (granite for example) can be found in this part of this array, and most large river RBS and silt samples (Bayon et al., 2018) plot close to this limit. The right edge connects the end-member of “weatherable” primary minerals (feldspars and pyroxenes) and the end-member of clays. This area may be characteristic for the weathering of volcanic islands as quartz is sparse in these settings, and other Si-bearing minerals of basaltic rocks such as olivine dissolve relatively fast (Pokrovsky and Schott, 2000; Oelkers, 2001; Montserrat et al., 2017). We expect this type of sediments to be present only in minor amounts in the sedimentary deposits as at large scales and in particular in continental settings, quartz-free sediments are rare. Consequently, most bulk sediment samples plot relatively “far” away from this limit, except for the sieved samples (quartz-free) from the Napo-Pastaza rivers and the large rivers clays (Bayon et al., 2018). The bottom right limit represents the “congruent” weathering of most rocks featuring the absence of “weatherable” primary minerals, as sediments plotting there are only composed of quartz and clays. For example, the SPM from Congo River plot in this area, illustrating that due to the high weathering intensity of this basin (Gaillardet et al., 1995; Henchiri et al., 2016), weatherable primary minerals are virtually absent.

Altogether, our analysis shows that δ^{30}Si and Al/Si can be used in detrital sediments to retrieve information about the geological and weathering contexts of the sediment source areas. However, we note that Savage et al. (2013) report that the shale δ^{30}Si was not well correlated with

indexes for chemical weathering. This might be due to the effects of "reverse weathering" (Chapter 4), where recycled detrital sediments might have taken up soluble cations during their interaction with seawater before being turned into sedimentary rocks during diagenesis.

Whereas primary minerals such as feldspars are largely consumed during weathering, the position of large river bulk sediment in the δ^{30}Si-Al/Si diagram clearly shows that quartz dominates the particulate Si budget to the ocean, due to its resistance during weathering. As quartz is usually found as coarse grains, the prevalence of quartz should be reflected in the type of sediment transport involved, with possibly a strong contribution of bedload to the total sediment flux of larger rivers, which is discussed in the next section 5.5.5. Finally, the origin of the material forming the third end member (clays) could be both present-day weathering and previous weathering episodes. These possibilities are discussed in section 5.5.6.

5.5.5 Contribution of bedload transport to total sedimentary fluxes of large rivers from Si isotopes

In the following we use a Si isotope mass balance to determine the relative contribution of bedload and suspended sediment flux to the sedimentary export of the Amazon. Indeed, as the Amazon river is the largest river in the world, the geochemical information it carries reflects the integration of erosion and weathering processes over large continental areas. The following Si mass budget can be established among DSi, SPM and RBS:

$$f_{DSi} + f_{SPM} + f_{RBS} = 1 \quad \text{(Equation 5-4)}$$

where f_{DSi} , f_{SPM} , and f_{RBS} represent the fraction of Si carried as DSi, SPM, and RBS in total Si budget. Additionally, for the Si isotope composition:

$$\delta^{30}\mathrm{Si}_{DSi} \times f_{DSi} + \delta^{30}\mathrm{Si}_{SPM} \times f_{SPM} + \delta^{30}\mathrm{Si}_{RBS} \times f_{RBS} = \delta^{30}\mathrm{Si}_{Crust} \quad \text{(Equation 5-5)}$$

Having two equations, we can determine two unknows: f_{SPM}, and f_{RBS}. To obtain a value for f_{DSi}, we compile different global-scale estimates of dissolved and particulate Si fluxes to the ocean (Table 5.5). We assign an approximate Si concentration in solids of 31% (Si abundance in the UCC; Rudnick and Gao, 2003) to calculate the Si mass budget to the total sediment flux. The global estimation yields an approximate fraction of dissolved Si (f_{DSi}) compared total Si (dissolved plus particulate) flux ranging over ~2–5%.

Table 5.5 Dissolved and particulate Si fluxes to the ocean. Data from: a. Meybeck and Ragu (1995); b. Milliman and Farnsworth (2013); c. Frings et al. (2016); d. Opfergelt and Delmelle (2012); e. Tréguer and De La Rocha (2013); and f. Dürr et al. (2011)

	Dissolved Si flux	**Particulate Si flux**
	209×10^6 T/year [a]	5.89×10^9 T/year [b]
	177.24×10^6 T/year [c]	$3.91 \sim 7.44 \times 10^9$ T/year [d]
	202×10^6 T/year [e]	4.12×10^9 T/year [f]
Average	196.08×10^6 T/year	5.23×10^9 T/year

We assume at first-order that the average bedrock within the Amazon should be close to the UCC composition, thus $\delta^{30}Si_{Crust} = -0.25‰$ (Savage et al., 2013). In the Amazon River, the $\delta^{30}Si_{DSi}$ value can be determined as 1.38‰ from a weighted average $\delta^{30}Si_{DSi}$ of the Solimões and Madeira rivers (Hughes et al., 2013). For the value of $\delta^{30}Si_{SPM}$, a grain-size integrated estimate should be used. The main two tributaries of the Amazon River, the Solimões and Madeira Rivers, are responsible for 55% and 45% of the total sediment flux to the Amazon mouth, respectively. The grain-size integrated Al/Si was estimated as 0.25 for Solimões and 0.34 for Madeira (Bouchez et al., 2012). Using the relationship between $\delta^{30}Si$ and Al/Si in the depth-profiles of these two rivers (Appendix ii, Figure ii-1), the averaged $\delta^{30}Si_{SPM}$ of the Amazon rivers can be then calculated at −0.44‰. Finally, the $\delta^{30}Si_{RBS}$ value of −0.20‰ is taken as the average $\delta^{30}Si$ values measured for RBS

samples from the Solimões and Madeira rivers. With these constraints we calculate that f_{SPM} = 53.8% and f_{RBS} = 41.2%.

The sedimentary Si fluxes can also be expressed as a function of total sediment mass fluxes and Si concentration in each flux:

$$\frac{(f_{RBS})}{(f_{SPM})} = \frac{[\mathrm{Si}]_{RBS} \times F_{RBS}}{[\mathrm{Si}]_{SPM} \times F_{SPM}} \quad \text{(Equation 5-6)}$$

Where $[\mathrm{Si}]_{SPM}$ and $[\mathrm{Si}]_{RBS}$ represent the Si concentration in SPM and RBS, and F_{SPM} and F_{RBS} represent the total mass flux of SPM and RBS. The $[\mathrm{Si}]_{RBS}$ can be obtained from the average Si concentration in Solimões and Madeira RBS samples as 39.4%. For the $[\mathrm{Si}]_{SPM}$, the grain-size integrated value (Appendix ii, Fig ii-2) is 31% for the Solimões and 28% for the Madeira, with a weighted average at 30%. Therefore, with equation 5-6, the relative sediment fluxes in the Amazon River can also be estimated. In the Amazon River, the relative flux of bed sands is estimated as 37%. If we consider that bed load is composed of pure quartz ($\delta^{30}\mathrm{Si}_{RBS}$ = 0‰; Fig 5.8; and $[\mathrm{Si}]_{RBS}$ = 46.7%), the relative flux of bed sands s 16.6%. We note that these values are depend on the source rock δ^{30}Si of the draining basin. If we assume a pure sedimentary basin and adopt the value $\delta^{30}\mathrm{Si}_{sedimentary}$= −0.19‰ (quartz dominant, section 5.5.3) or $\delta^{30}\mathrm{Si}_{sedimentary}$= −0.31‰ (Savage et al., 2013), the result of bed load flux will respectively become 28-63% ($\delta^{30}\mathrm{Si}_{sedimentary}$= −0.19‰) or 6-14% ($\delta^{30}\mathrm{Si}_{sedimentary}$= −0.31‰). The Amazon basin is the largest river basin in the world, hence we consider its weight average bed rock δ^{30}Si is close to UCC. The results of these calculations are summarized in Table 5.6.

Table 5.6 Calculation of relative flux of sediments (RBS and SPM)

	RBS	SPM	DSi
Average δ^{30}Si (‰) (Bedrock=UCC)	−0.20 (field data) or 0 (RBS=quartz)	−0.44	1.38
[Si] in sediments (%)	39.4 (field average) or 46.7 (RBS=quartz)	30.0	
Relative Si flux (%) based on field RBS data	41.2	53.8	5
Relative Si flux (%) assuming RBS=quartz	22.5	72.5	5
Sediment flux (F/F_{tot}) based on field data (%)	36.8	63.2	
Sediment flux (F/F_{tot}) assuming RBS=quartz (%)	16.6	83.4	
Relative RBS flux (F/F_{tot}) when $\delta^{30}Si_{bedrock}$= −0.19‰: 28−63%			
Relative RBS flux (F/F_{tot}) when $\delta^{30}Si_{bedrock}$= −0.31‰: 6−14%			

Overall, δ^{30}Si signatures of detrital sediments over depth-profiles show that in the Amazon River, about 16% to 36% of sediments are transported in the form of bed sands. Both results are higher than previously proposed values (10%, Lane and Borland, 1951), but it should be emphasized that direct measurements of bedload fluxes are scarce. Our estimation is similar to that made in a previous study on the Ganges-Brahmaputra river (Galy and France-Lanord, 2001) using ratios of major elements including Al, Si, and Fe.

5.5.6 The evolution of the river sediment Si isotope composition through continental recycling

We show above that the δ^{30}Si signature of fine sediments of large rivers carries information about weathering processes; however, the signal is possibly derived from both long-term processes such as recycling of sedimentary rocks, and relatively "short-term" processes such as modern-day weathering and soil formation. We discuss these two possibilities in the following.

Weathering processes are able to fractionate Si isotopes at two steps: during the release of Si by mineral dissolution and during Si incorporation into secondary phases. We can dismiss the impact of the first step (Frings et al., 2016; Poitrasson, 2017). For example, experimental studies show that the dissolution of basalts preferentially release lighter Si isotopes into the aqueous phase (Ziegler et al., 2005b), but also that this effect is mitigated after the initial steps of the dissolution process. It should also be emphasized that such effect cannot explain field observations showing that aqueous samples are exclusively enriched in heavy Si isotopes compared to solids (Frings et al., 2016).

Significant Si isotope fractionation can occur during the formation of secondary weathering products, clays for instance, which preferably take up lighter Si. Previous studies show that soils have a large range of δ^{30}Si values (from −2.7 ‰ to −0.1‰); (Ziegler et al., 2005a; Opfergelt et al., 2008, 2012; Bern et al., 2010; Steinhoefel et al., 2011; Opfergelt and Delmelle, 2012; Ameijeiras-Mariño et al., 2017). In soils, most secondary Si is hosted by clays, the formation of which results from a series of complex processes. Nevertheless, theoretical calculation and experimental results (Dupuis et al., 2015; He et al., 2016) revealed that at isotopic equilibrium between aqueous H_4SiO_4 solution and kaolinite, lighter Si isotopes are enriched in aqueous phase. The contradiction between the theoretical/experimental findings and field studies suggests that in the environment the fractionation of δ^{30}Si is of kinetic nature, which is probably associated with the precipitation of amorphous silica as an "initial" secondary phase at early stages (Oelze et al., 2014, 2015; Geilert et al., 2014). Sieved soil clays formed on volcanic islands or volcanic ashes (Ziegler et al., 2005a, b; Opfergelt et al., 2010, 2011, 2012; Opfergelt and Delmelle, 2012), or clay fraction of river sediments from Guadeloupe rivers (Table 5.3) have δ^{30}Si signatures at, or even lower than, the bottom range of the large river SPM δ^{30}Si from this study (Fig 5.11a). The low δ^{30}Si observed in

the products of weathering of igneous rocks indicates that the effect of present-day weathering is capable to result in low δ^{30}Si in solid weathering products.

To further explore this hypothesis, it is insightful to compare the δ^{30}Si in river sediments to that of river water, because dissolved δ^{30}Si is dominated by present-day weathering processes. All our samples possess δ^{30}Si values distinctively lower than the average δ^{30}Si of riverine DSi (1.28 ± 0.68‰, Frings et al., 2016). A compilation of δ^{30}Si in river sediments and in continental DSi illustrates that during silicate weathering light Si isotopes are preferentially incorporated in the solids whereas heavy Si isotopes enter the solution (Fig 5.10). An isotopically light counterpart should thus be present in detrital sediments, as shown by SPM data, making our observations compatible with a role of present-day weathering in setting the δ^{30}Si of large river sediments. The proposed role of present-day weathering is also in line with the fact that the lowest δ^{30}Si values of sediments are obtained for the clay-richest samples (highest Al/Si values).

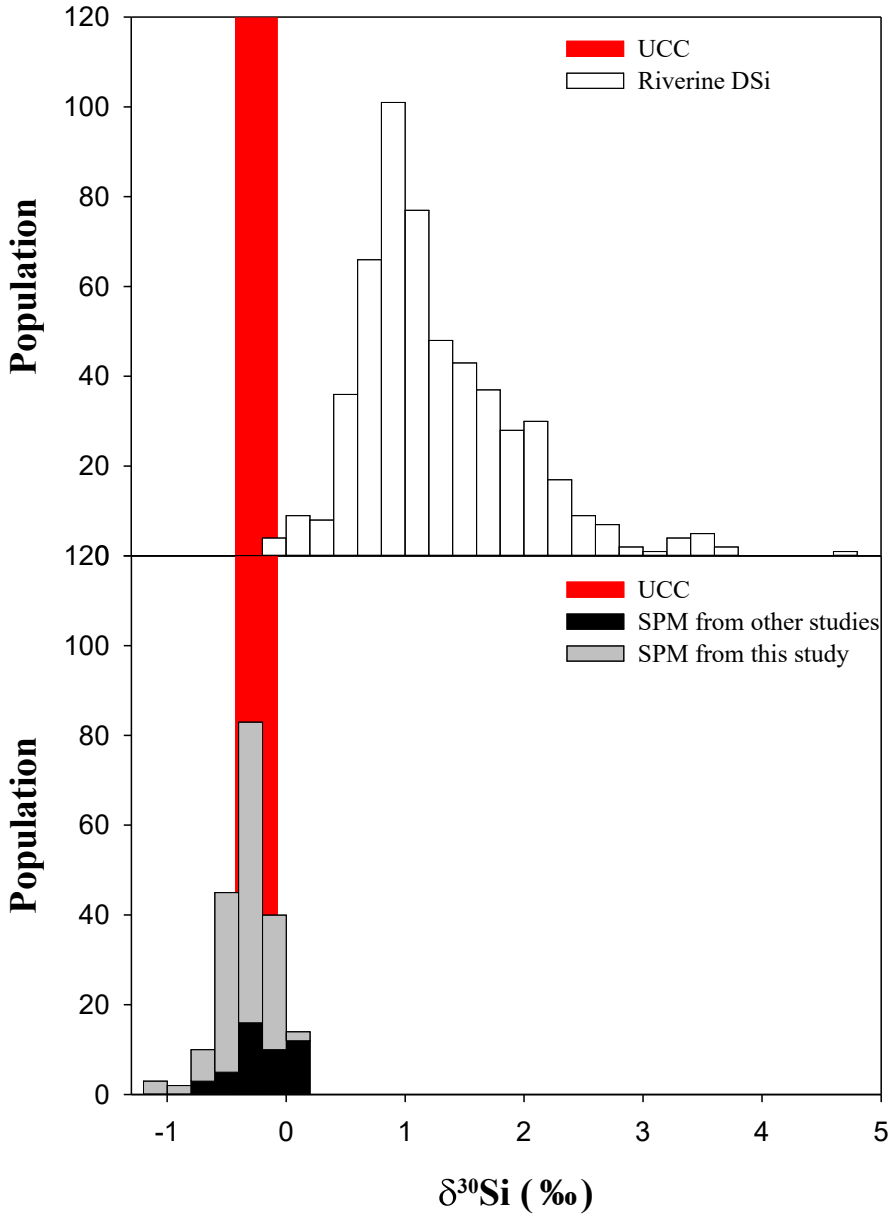

Figure 5.6 Compilation of δ^{30}Si in world's river waters (De La Rocha et al., 2000; Alleman et al., 2005; Ziegler et al., 2005a, b; Georg et al., 2006, 2007, 2009; Opfergelt et al., 2009, 2013; Cardinal et al., 2010; Engström et al., 2010; Engström, 2010; Ding et al., 2011, 2014; Hughes et al., 2011, 2012, 2013; Cockerton et al., 2013; Delvaux et al., 2013; Fontorbe et al., 2013; O. Pokrovsky et al., 2013; Frings et al., 2014a; Mavromatis et al., 2016) and in bulk river sediments: this study and other studies (Ding et al., 2011; Ding et al., 2014). The difference displayed between δ^{30}Si in solution and in solids shows that lighter Si isotopes are preferentially taken up in the solid load whereas heavier Si isotopes are enriched in the dissolved load.

However, low δ^{30}Si value for high Al/Si samples could also be produced with fine clays formed during ancient episodes of weathering and carried by rivers due to present-day erosion. In addition, it should be reminded that the Si isotope composition of the clay end member seems to remain constant from one large river to another (Fig 5.8), independently from the local conditions in terms of weathering regime.

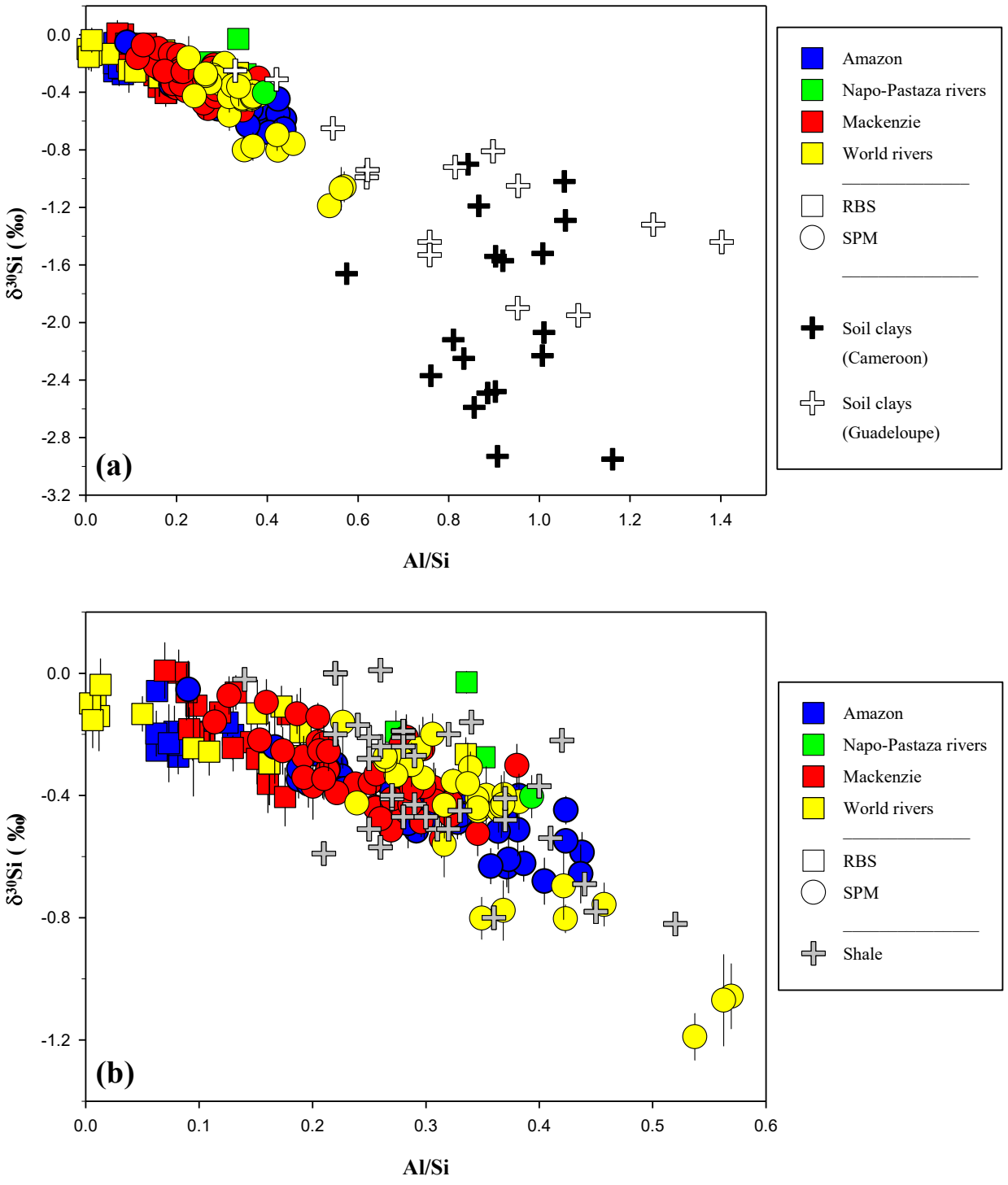

Figure 5.7 Large river sediment δ^{30}Si as a function of grain size (Al/Si), together with (a) present-day products (clays) of the weathering of igneous rocks (Opfergelt et al., 2009, 2010); (b) shales (Savage et al., 2013)

To explore the role of recycling (or in other words of the weathering/erosion of meta-sedimentary rocks) on the δ^{30}Si of large river sediments, we can examine the composition of sedimentary rocks. As shown by Savage et al. (2013), shales (noting that the sample set from Savage et al. (2013) also includes sandstones) exhibit a significant variation in δ^{30}Si, correlated with their Al/Si ratio. When comparing our results on presently transported river sediments with the shale data of Savage et al. (2013) (Fig 5.11b), it is clear that both datasets overlap. If sedimentary rocks (shales, for instance) are one of the lithological components of the considered river basins, those already-weathered sediments are eroded and transported into river systems, and sorting effects in the river channel allow these lighter and finer sediments (shale-derived) to be preferentially transported at the surface of the water column, and heavier and coarser sediments (sandstone-derived) enriched at the bottom. As a result, the depth-profiles of river sediments δ^{30}Si would result from a stratification of eroded grains as a function of their lithological provenance (Bouchez et al., 2011), such that no present-day weathering effect would be required to explain the δ^{30}Si relation to grain size in large river sediments. Such as source rock control on δ^{30}Si in river sediments can explain the similar trends observed in depth profiles of the Mackenzie and Amazon rivers (Fig 5.4), despite different climates prevailing in their respective drainage basins (Bayon et al., 2018).

Nevertheless, if the δ^{30}Si variation is mainly reflecting the variation in source rock δ^{30}Si, meaning that the effect of present-day weathering is small, then how were the shales fractionated from their ultimate source material (which should have had a igneous rock-type δ^{30}Si) in the first place? And why would the weathering of igneous rocks be the only geological possibility for significant Si isotope fractionation? To answer these questions, we can suggest three possible scenarios at this stage:

(a) A cumulated effect of weathering across weathering cycles: the global δ^{30}Si-Al/Si relationship across river sediments (covering a large range of lithological conditions) suggests that the δ^{30}Si of bulk solid weathering products is only slightly different from that of primary rocks. With recycling and repeated weathering cycles, it could be expected that the effects of weathering on the solid δ^{30}Si becomes cumulative with lower and lower δ^{30}Si of the fine end-member corresponding to a greater degree of recycling. According to our calculation based on modern weathering profiles, only a small fraction (<5%) of Si is liberated from rocks to solution in a given episode of weathering, which is accompanied by a relatively small decrease of δ^{30}Si in bulk residual solids. If we assume that the ancient weathering episodes had effects similar to that of today, then it requires at least several cycles to significantly lower the δ^{30}Si of present fine river sediments.

(b) Diagenetic effects: after deposition, detrital sediments undergo diagenesis in contact with seawater. The interaction between the seawater and secondary minerals may further fractionate silicon isotopes; however, this process is still poorly understood (i.e. Michalopoulos and Aller, 1995; Aller, 2014; Rahman et al., 2016). In Chapter 4, it has been shown that in deltaic environments diagenetic effects would further lower the δ^{30}Si of detrital solids, but the importance of this effect on the global Si budget has not been recognized yet. However, the overlap between shales samples and river sediments (Fig 5.9b) suggests that this process either has a similar effect as continental weathering, or that it is not significant.

(c) A mineralogical sorting of secondary minerals during transport: as only a small fraction of the total Si budget is lost to solution as shown above, bulk solid δ^{30}Si is close to that of source rocks, and only fine-grained secondary minerals carry a low δ^{30}Si signature. Fine

secondary minerals are likely to be transported further once delivered to the ocean and to provide the source material for the formation of fine deep clay deposits, that will yield shales after diagenesis and uplift. A hydrodynamic process of clay enrichment is the most plausible scenario to explain the low δ^{30}Si of the shales as only after a single erosion-transport-deposition transfer, the decrease of δ^{30}Si in sediments could be observed.

Regardless of the exact explanation, we can propose a conceptual model for the evolution of the Si particulate reservoirs across weathering cycles (Fig 5.12). During a so-called "first-cycle" weathering of igneous rocks such as basalt or granite, there are no sedimentary rocks/minerals being weathered. Here we use the example of the alteration of granite, as it is representative of the igneous felsic fraction of the upper continental crust. In granite, there are two important Si-carrying minerals: quartz and feldspar (Fig 5.12a). Therefore, here we only consider these two minerals in our source rock. The bulk granite δ^{30}Si composition is estimated at −0.23±0.15 ‰, with a higher δ^{30}Si value for quartz than for feldspar (Savage et al., 2013 and Section 5.5.3 of this study). During weathering, feldspar is more prone to be dissolved than quartz, such that in the particle sink, where the deposition of weathering products occurs, feldspars will be depleted with respect to quartz compared to the source rock. Additionally, Si released to solution during the weathering of granite is precipitated into secondary weathering solids. Depending on the weathering regime, the type of weathering-derived solids will vary. In regimes with moderate weathering intensity, clays with lower Al/Si ratios (such as smectite or illite) are produced. In more advanced weathering regimes, a greater loss of Si occurs and clays with greater Al/Si ratios, such as kaolinite, can be produced. All these weathering products have δ^{30}Si values lower than the source rock granite, as isotope fractionation occurs during their formation, favoring the lighter isotopes in the secondary solids,

and as the isotope fractionation during Si release to solution can be considered as negligible. The Si fractionation in the products characterizing the more advanced weathering regimes (clays such as kaolinite) is greater than that of the solids likely to be found in moderate weathering regimes (clays such as smectite), as shown by theoretical calculations (Méheut et al., 2009; Méheut and Schauble, 2014) as well as measurements in the environment (Ziegler et al., 2005a). In other words, the δ^{30}Si values are thought to be higher in smectite than in kaolinite for a given DSi isotope composition. As rivers integrate weathering processes over their entire basin, the mineralogy of the sedimentary sink of rivers draining geological settings dominated by “first-cycle” weathering is expected to be characterized by unaltered quartz (minor change of abundance), unaltered feldspar (with a loss in abundance compared to parent rock, and the degree of which is dependent on weathering regime), and neo-formed clays with various compositions including Al-rich clays with Al:Si ratios up to 1:1. In the case of the weathering of mafic rocks such as basalts, the mechanism is similar in spite of the difference of the source rock compositions. Notably, a major difference exists between weathering of granite and basaltic rocks: quartz is absent in basaltic rocks. As shown above (Fig 5.7), quartz has a heavy δ^{30}Si signature and exhibits a strong control on river sediments. Additionally, quartz is resistant to weathering. Therefore, during the weathering of basaltic rocks, as the quartz end-member is not present, the δ^{30}Si in river sediments theoretically has a greater potentiality, under the same weathering conditions, to be lowered compared to source rock than during granite weathering. This effect is visible on the SPM from rivers draining Deccan Traps (Table 5.3), the δ^{30}Si signature of which is relatively low (−0.45‰ to −0.80‰) compare to SPM from other geological settings (Fig 5.7).

Tectonic processes not only allow for “source-to-sink” transport from orogenic belts to sediment depocenters, but also permits “sink-to-source” transfer via diagenesis, metamorphism,

and uplift (Fig 5.12b). Here we define the weathering of sedimentary rocks as “secondary-cycle” weathering. In such cycles, the source rock is composed of two parts: fragments of rocks that went unweathered during previous cycles, and “recycled” clays. During this secondary weathering cycle, the unweathered fragments have the same fate as in the first cycle: a loss of Si by the alteration of “weatherable” minerals (feldspars) and a further accumulation of clays (to clays formed in previous weathering episodes) as a result of secondary mineral formation. When comparing rivers draining mostly sedimentary rocks with rivers draining igneous rocks (*e.g.* Madeira *vs*. Solimões, Fig 5.6), a loss of weatherable minerals is observed.

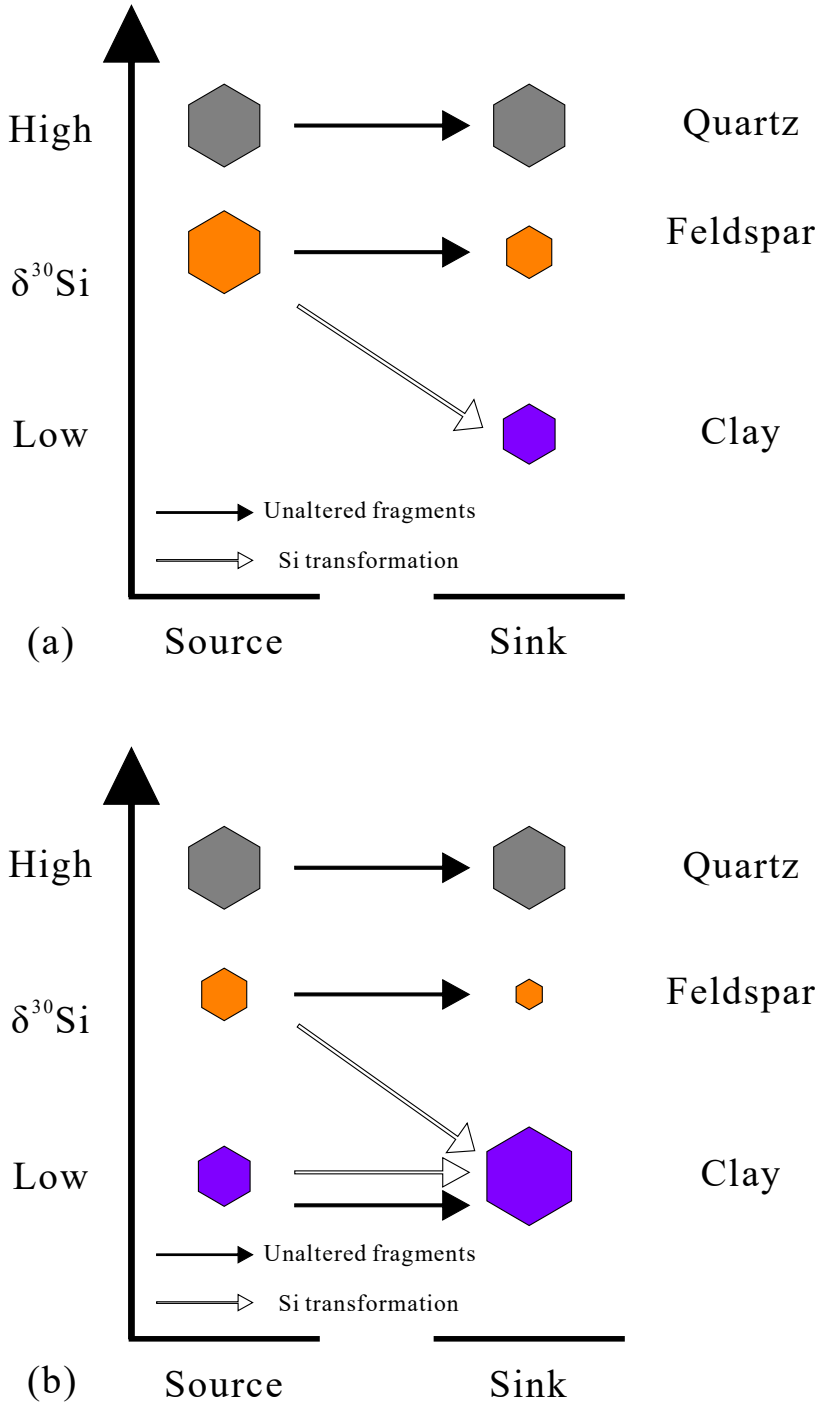

Figure 5.8 Schematic evolution of the mineralogical composition of large river sediment during "first" (a) and "secondary" (b) weathering cycle. The abundance of the primary minerals (quartz and feldspar) and clays at the sediment deposition sites are represented by the size of the polygons. During first cycle weathering (a), primary minerals, in particular feldspar, are subjected to dissolution, and clays are added. During secondary weathering cycles (b), primary minerals are dissolved and accumulation and evolution (e.g. from illite to kaolinite) of clays further lowers the δ^{30}Si composition of bulk sediments.

Regarding clays formed during previous weathering cycle(s), the moderately Al-rich and δ^{30}Si-depleted clays such as smectite and illite may be able to be further weathered to kaolinite, if they are subjected to stronger weathering conditions (longer fluid residence time, higher temperature...) during the current weathering cycle. Therefore, in the secondary weathering cycles, the manifestation of additional weathering on Si is that more primary minerals are weathered to form clays, and low-weathering intensity clays from previous weathering cycle are potentially further altered to form highly weathered products such as kaolinite (Fig 5.10b). The δ^{30}Si values of the bulk of the sedimentary deposits produced from the erosion of areas dominated by secondary-cycle weathering is further reduced compared to that of the first-cycle weathering product. As very intense weathering leads to the release of Si from kaolinite, the bulk δ^{30}Si values of solids cannot be lower than that of kaolinite. It is of importance to emphasize that quartz absolute abundance remains almost unchanged during repeated weathering cycles, such that eventually the bulk solids can be predicted to be dominated by only quartz and clays, and minerals like feldspars to be exhausted. This situation, in fact, is observed in many river systems draining sedimentary basins (Fig 5.6).

Large rivers drain basins underlain by both igneous and sedimentary rocks; the isotope composition of their sediment thus depends on a combination of both first-cycle weathering and secondary-cycle weathering. As the majority of our samples are from large rivers integrating large portions of the upper continental crust, only a minor number of samples are from rivers draining purely igneous basins, but we contend that such situation is representative of large-scale continental weathering. As shown in Figure 5.7, river sediments are globally dominated by quartz and clays due to the recycling of sedimentary rocks. This observation sheds light onto long term changes in the influence of silicate weathering on the C cycle. The uptake of atmospheric CO_2

requires the presence of "weatherable" minerals containing Si and base cations, such as feldspars. In a system where sediment recycling is important the ability of CO_2 uptake through silicate weathering is reduced compared to the weathering of igneous rocks like basalt. This emphasizes the importance of mafic rocks, rich in "weatherable minerals", in regulating atmospheric CO_2 over geological time scales (Louvat and Allègre, 1997)(Gaillardet et al., 1999).

5.5.7 Can we still use the δ^{30}Si composition of detrital sediments to trace weathering regimes?

Bayon et al. (2018) suggest that the variation of Si isotope in large river clays is a result of a climatic effect on present-day weathering, while our data indicate that the role of lithology and sedimentary recycling cannot be neglected. However, for a given river, the lithological effect might be cancelled out if differences in δ^{30}Si between different grain sizes are examined. Here we compare the Si isotope composition difference between surface SPM and RBS of a given river with its weathering intensity proxy W/D (Fig 5.13), which is defined as the ratio of present-day chemical silicate weathering rates (W; Bouchez and Gaillardet, 2014) and the rates of total denudation (D, erosion plus weathering rates). As illustrated in Figure 5.7, weathering effects on Si are shown in (1) enrichment of light δ^{30}Si in the fine sediment fraction (high Al/Si) due to secondary mineral formation; and (2) enrichment of heavy δ^{30}Si in the coarse sediment fraction (Al/Si) due to an increased contribution of quartz resulting from the dissolution of "weatherable minerals". As shown in Figure 5.13, the difference between surface SPM δ^{30}Si and RBS δ^{30}Si increases with increasing W/D. For example, samples plotting in the bottom-left corner of Figure 5.13b (such as the Huanghe River, draining the Chinese loess plateau) have a low weathering intensity and their SPM δ^{30}Si (−0.25‰) is close to that of its RBS (−0.19‰), showing a limited weathering effect. More generally, settings characterized as "cratonic" (*e.g.*, Congo and Niger rivers) and "collisional" (*e.g.*, Ganges and Brahmaputra rivers) differ in their ability to produce

SPM and RBS with different δ^{30}Si signatures. Surface SPM from collisional settings exhibit a small range in δ^{30}Si (−0.44‰ < δ^{30}Si < −0.27‰), whereas surface SPM samples from cratonic settings extends to lower δ^{30}Si values (−1.19‰<δ^{30}Si<−0.30‰). As a consequence, the difference between δ^{30}Si in SPM and RBS is larger in rivers draining cratons than in rivers draining collisional settings.

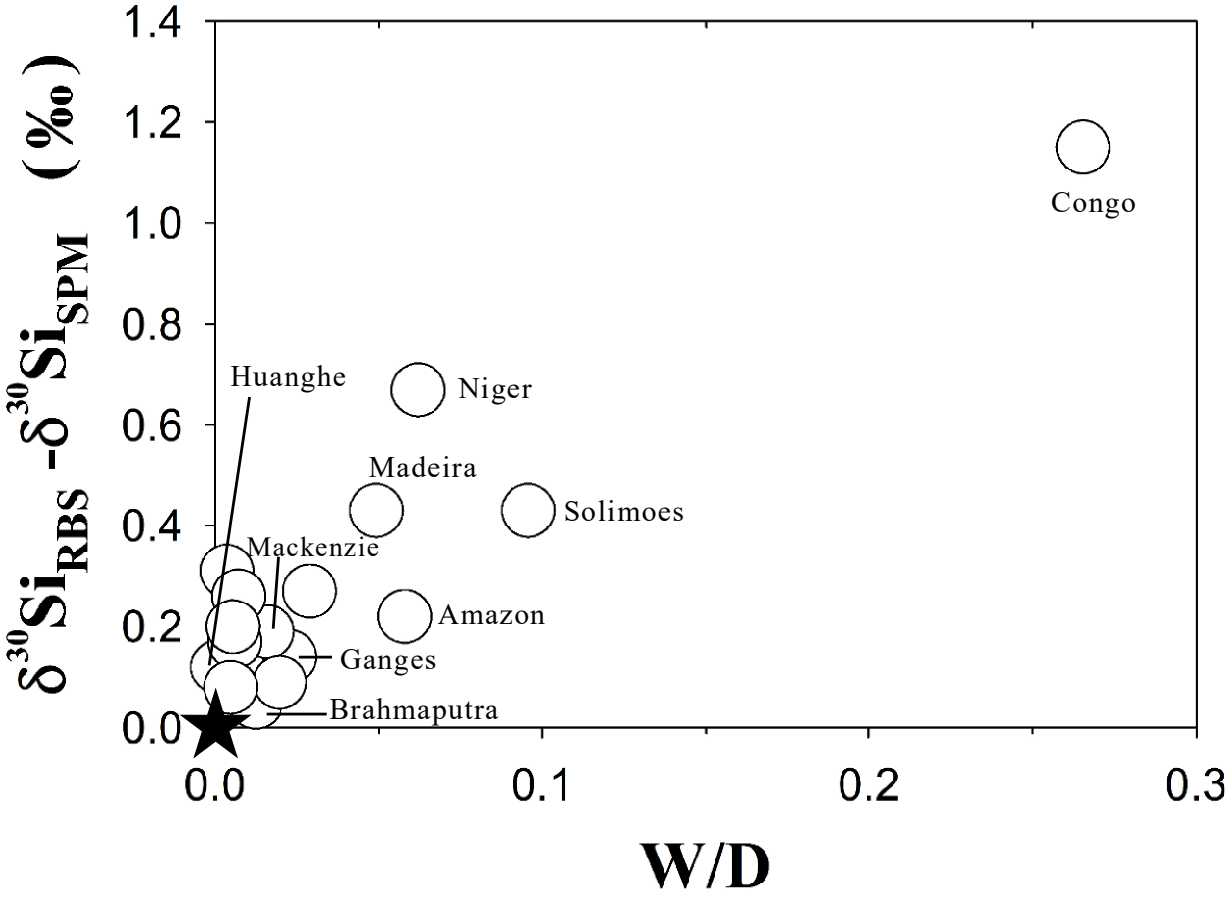

Figure 5.9 Relationship between weathering intensity (W/D) and difference in silicon isotope composition between coarse (river bed sands, RBS) and fine large river sediments (suspended particulate matter, SPM). The star represents a "no chemical weathering" scenario. Large river W data from Gaillardet et al. (1999), D data from Milliman and Farnsworth (2013), and other river W/D data from Dellinger et al. (2015).).

These observations can be explained by the fact that erosion is strong when tectonics are active, and under such conditions the δ^{30}Si in river sediments expected to be close to bed rocks because secondary phases do not have enough time to develop, and result in fine sediments dominated by small rock debris, as explained for Li in Dellinger et al. (2017). By contrast, in cratonic basins, erosion is weaker, leaving more time for clay formation in soils, leading to a lower δ^{30}Si of fine sediments, in this case dominated by clays. At high W/D, RBS is quartz-like and is enriched with heavy Si isotopes, whereas surface SPM is clay-like and is enriched with light Si isotopes.

While the δ^{30}Si-Al/Si relationship is strongly affected by inheritance from previous weathering episodes (Figure 5.11b), the present-day weathering effect drives the difference between SPM and RBS δ^{30}Si signatures. Therefore, considering both coarse and fine material of detrital sediments opens new possibilities for the use of joint δ^{30}Si measurements on contemporaneous shale and sandstone formations, which can provide information on past weathering regimes.

5.6 Conclusion and implications

Here we report the particulate δ^{30}Si signature of the world’s largest rivers. δ^{30}Si in sediments are shown to decrease with increasing Al/Si values along sediment depth-profiles, which is a manifestation of weathering over long time scales. Bulk δ^{30}Si is ultimately controlled by the relative abundance of quartz, clays, and “weatherable” minerals, which in detrital sedimentary formations could be related to the geological setting prevailing in the sediment source area. We also show that the global δ^{30}Si of river sediments is largely influenced by lithological effects, hence sedimentary recycling, athough the relative contribution of "modern-day" weathering vs. ancient weathering episodes (recycling), remains difficult to quantify. However, we suggest a way to use

the difference in δ^{30}Si signature of fine and coarse detrital sediments (*e.g.* in contemporaneous shales and sandstones) to retrieve information about pas weathering conditions. Finally, we also propose an estimate of the bed load flux (16-36%) to the total sediment flux of the Amazon River, using a Si isotope mass balance.

The implications of this study are several folds. First, the range of δ^{30}Si in shales results from long-term processes. Second, hydrodynamic sorting in rivers (and possibly in coastal environments) physically separates clay and quartz, which allows us to observe variable δ^{30}Si values across sedimentary rocks (sandstones *vs.* shales). The result at geological time scales is that weathering of continental crust separates Si from igneous rocks into two major pools: quartz and clays. Third, as weathering of primary minerals such as feldspar or pyroxene is faster than that of clays, and as the difference in δ^{30}Si values between primary minerals and any type clays tends to be greater than that between different types of clays, we suggest that under the same weathering conditions, the δ^{30}Si fractionation between source rock and bulk sediment is maximal during "first-cycle" weathering. More specifically, we suggest that under the same weathering conditions, soils developed over already-weathered materials, shales for example, will have a lower extent of δ^{30}Si fractionation than soils developed over igneous rocks such as basalts and granites. Altogether, Si isotopes in large river sediments emphasize the importance of sedimentary recycling on our planet, in particular through the long-term reduction in the ability of the Earth surface rocks to consume atmospheric CO_2.

Bibliography

Allègre, C.J., Rousseau, D., 1984. The growth of the continent through geological time studied by Nd isotope analysis of shales. Earth and Planetary Science Letters 67 (1), 19-34.

Allègre, C.J., Dupré, B., Négrel, P., Gaillardet, J., 1996. Sr-Nd-Pb isotope systematics in Amazon and Congo River systems: constraints about erosion processes. Chemical Geology 131 (1), 93-112.

Alleman, L.Y., Cardinal, D., Cocquyt, C., Plisnier, P., Descy, J., Kimirei, I., Sinyinza, D., André, L., 2005. Silicon isotopic fractionation in Lake Tanganyika and its main tributaries. Journal of Great Lakes Research 31 (4), 509-519.

Aller, R.C., 2014. Sedimentary Diagenesis, Depositional Environments, and Benthic Fluxes. In: Holland, H.D. and Turekian, K.K., (Eds.). Treatise on Geochemistry (Second Edition). Elsevier, Oxford.

Ameijeiras-Mariño, Y., Opfergelt, S., Schoonejans, J., Vanacker, V., Sonnet, P., de Jong, J., Delmelle, P., 2017. Impact of low denudation rates on soil chemical weathering intensity: A multiproxy approach. Chemical Geology 456, 72-84.

Amiotte Suchet, P., Probst, J., Ludwig, W., 2003. Worldwide distribution of continental rock lithology: Implications for the atmospheric/soil CO2 uptake by continental weathering and alkalinity river transport to the oceans. Global Biogeochemical Cycles 17 (2).

Basu, A.R., Sharma, M., DeCelles, P.G., 1990. Nd, Sr-isotopic provenance and trace element geochemistry of Amazonian foreland basin fluvial sands, Bolivia and Peru: implications for ensialic Andean orogeny. Earth and Planetary Science Letters 100 (1-3), 1-17.

Bayon, G., Delvigne, C., Ponzevera, E., Borges, A., Darchambeau, F., De Deckker, P., Lambert, T., Monin, L., Toucanne, S., André, L., 2018. The silicon isotopic composition of fine-grained river sediments and its relation to climate and lithology. Geochimica et Cosmochimica Acta 229, 147-161.

Bern, C.R., Brzezinski, M.A., Beucher, C., Ziegler, K., Chadwick, O.A., 2010. Weathering, dust, and biocycling effects on soil silicon isotope ratios. Geochimica et Cosmochimica Acta 74 (3), 876-889.

Berner, R.A., Lasaga, A.C., Garrels, R.M., 1983. The carbonate-silicate geochemical cycle and its effect on atmospheric carbon dioxide over the past 100 million years. American Journal of Science 283 (7), 641-683.

Bouchez, J., Gaillardet, J., 2014. How accurate are rivers as gauges of chemical denudation of the Earth surface? Geology 42 (2), 171-174.

Bouchez, J., Gaillardet, J., France-Lanord, C., Maurice, L., Dutra-Maia, P., 2011. Grain size control of river suspended sediment geochemistry: Clues from Amazon River depth profiles. Geochemistry Geophysics Geosystems 12, Q03008.

Bouchez, J., Gaillardet, J., Lupker, M., Louvat, P., France-Lanord, C., Maurice, L., Armijos, E., Moquet, J., 2012. Floodplains of large rivers: Weathering reactors or simple silos? Chemical Geology 332–333, 166-184.

Cardinal, D., Alleman, L., Dehairs, F., Savoye, N., Trull, T., André, L., 2005. Relevance of silicon isotopes to Si-nutrient utilization and Si-source assessment in Antarctic waters. Global Biogeochemical Cycles 19 (2).

Cardinal, D., Gaillardet, J., Hughes, H., Opfergelt, S., André, L., 2010. Contrasting silicon isotope signatures in rivers from the Congo Basin and the specific behaviour of organic-rich waters. Geophysical Research Letters 37 (12).

Cockerton, H., Street-Perrott, F., Leng, M., Barker, P., Horstwood, M., Pashley, V., 2013. Stable-isotope (H, O, and Si) evidence for seasonal variations in hydrology and Si cycling from modern waters in the Nile Basin: implications for interpreting the Quaternary record. Quaternary Science Reviews 66, 4-21.

Conley, D.J., Carey, J.C., 2015. Biogeochemistry: Silica cycling over geologic time. Nature Geoscience 8 (6), 431.

Cornelis, J., Weis, D., Lavkulich, L., Vermeire, M., Delvaux, B., Barling, J., 2014. Silicon isotopes record dissolution and re-precipitation of pedogenic clay minerals in a podzolic soil chronosequence. Geoderma 235–236, 19-29.

De Bievre, P., & Taylor, P. D. P., 1993. Table of the isotopic compositions of the elements. International Journal of Mass Spectrometry and Ion Processes, 123(2), 149-166.

De La Rocha, C.L., Brzezinski, M.A., DeNiro, M.J., Shemesh, A., 1998. Silicon-isotope composition of diatoms as an indicator of past oceanic change. 395 (6703), 683.

De La Rocha, C.L., Brzezinski, M.A., DeNiro, M.J., A first look at the distribution of the stable isotopes of silicon in natural waters. 64, 2467-247781.

De La Rocha, C. L., Brzezinski, M. A., DeNiro, M. J., 2000. A first look at the distribution of the stable isotopes of silicon in natural waters. Geochimica et Cosmochimica Acta, 64(14), 2467-2477.

De Souza, G., Reynolds, B., Johnson, G., Bullister, J., Bourdon, B., 2012. Silicon stable isotope distribution traces Southern Ocean export of Si to the eastern South Pacific thermocline. Biogeosciences 9 (11), 4199-4213.

Dellinger, M., Bouchez, J., Gaillardet, J., Faure, L., Moureau, J., 2017. Tracing weathering regimes using the lithium isotope composition of detrital sediments. Geology 45 (5), 411-414.

Dellinger, M., Gaillardet, J., Bouchez, J., Calmels, D., Galy, V., Hilton, R.G., Louvat, P., France-Lanord, C., 2014. Lithium isotopes in large rivers reveal the cannibalistic nature of modern continental weathering and erosion. Earth and Planetary Science Letters 401, 359-372.

Delvaux, C., Cardinal, D., Carbonnel, V., Chou, L., Hughes, H., André, L., 2013. Controls on riverine δ30Si signatures in a temperate watershed under high anthropogenic pressure (Scheldt—Belgium). Journal of Marine Systems 128, 40-51.

Ding, T., Zhou, J., Wan, D., Chen, Z., Wang, C., Zhang, F., 2008. Silicon isotope fractionation in bamboo and its significance to the biogeochemical cycle of silicon. Geochimica et Cosmochimica Acta 72 (5), 1381-1395.

Ding, T.P., Tian, S.H., Sun, L., Wu, L.H., Zhou, J.X., Chen, Z.Y., 2008. Silicon isotope fractionation between rice plants and nutrient solution and its significance to the study of the silicon cycle. Geochimica et Cosmochimica Acta, 72(23), 5600-5615.

Ding, T., Gao, J., Tian, S., Wang, H., Li, M., 2011. Silicon isotopic composition of dissolved silicon and suspended particulate matter in the Yellow River, China, with implications for the global silicon cycle. Geochimica et Cosmochimica Acta 75 (21), 6672-6689.

Ding, T., Gao, J., Tian, S., Shi, G., Chen, F., Wang, C., Luo, X., Han, D., 2014. Chemical and isotopic characteristics of the water and suspended particulate materials in the Yangtze river and their geological and environmental implications. Acta Geologica Sinica (English Edition) 88 (1), 276-360.

Ding, T.P., Gao, J.F., Tian, S.H., Fan, C.F., Zhao, Y., Wan, D.F., Zhou, J.X., 2017. The δ30Si peak value discovered in middle Proterozoic chert and its implication for environmental variations in the ancient ocean. Scientific Reports 7, 44000.

Dosseto, A., Turner, S.P., Douglas, G.B., 2006. Uranium-series isotopes in colloids and suspended sediments: Timescale for sediment production and transport in the Murray–Darling River system. Earth and Planetary Science Letters 246 (3–4), 418-431.

Dosseto, A., Bourdon, B., Gaillardet, J., Allègre, C.J., Filizola, N., 2006. Time scale and conditions of weathering under tropical climate: Study of the Amazon basin with U-series. Geochimica et Cosmochimica Acta 70 (1), 71-89.

Dupré, B., Gaillardet, J., Rousseau, D., Allègre, C.J., 1996. Major and trace elements of river-borne material: The Congo Basin. Geochimica et Cosmochimica Acta 60 (8), 1301-1321.

Dupuis, R., Benoit, M., Nardin, E., Méheut, M., 2015. Fractionation of silicon isotopes in liquids: The importance of configurational disorder. Chemical Geology 396, 239-254.

Dürr, H., Meybeck, M., Hartmann, J., Laruelle, G., Roubeix, V., 2011. Global spatial distribution of natural riverine silica inputs to the coastal zone. Biogeosciences 8 (3), 597-620.

Egge, J.K., Aksnes, D.L., 1992. Silicate as regulating nutrient in phytoplankton competition. Marine Ecology Progress Series 83, 281-289.

Engström, E., 2010. Fractionation of the stable silicon isotopes studied using MC-ICP-MS: analytical method developments and applications in geochemistry .

Engström, E., Rodushkin, I., Ingri, J., Baxter, D.C., Ecke, F., Österlund, H., Öhlander, B., 2010. Temporal isotopic variations of dissolved silicon in a pristine boreal river. Chemical Geology 271 (3-4), 142-152.

Fontorbe, G., Christina, L., Chapman, H.J., Bickle, M.J., 2013. The silicon isotopic composition of the Ganges and its tributaries. Earth and Planetary Science Letters 381, 21-30.

Frings, P.J., De La Rocha, C., Struyf, E., Van Pelt, D., Schoelynck, J., Hudson, M.M., Gondwe, M.J., Wolski, P., Mosimane, K., Gray, W., 2014a. Tracing silicon cycling in the Okavango Delta, a sub-tropical flood-pulse wetland using silicon isotopes. Geochimica et Cosmochimica Acta 142, 132-148.

Frings, P.J., Clymans, W., Jeppesen, E., Lauridsen, T.L., Struyf, E., Conley, D.J., 2014b. Lack of steady-state in the global biogeochemical Si cycle: emerging evidence from lake Si sequestration. Biogeochemistry 117 (2), 255-277.

Frings, P., 2014. Integrating Fluvial Processes into the Global Si Cycle. Department of Geology, Lund University.

Frings, P.J., Clymans, W., Fontorbe, G., Gray, W., Chakrapani, G.J., Conley, D.J., De La Rocha, C., 2015. Silicate weathering in the Ganges alluvial plain. Earth and Planetary Science Letters 427, 136-148.

Frings, P.J., Clymans, W., Fontorbe, G., De La Rocha, C.L., Conley, D.J., 2016. The continental Si cycle and its impact on the ocean Si isotope budget. Chemical Geology 425, 12-36.

Fripiat, F., Cavagna, A., Dehairs, F., Brauwere, A.d., André, L., Cardinal, D., 2012. Processes controlling the Si-isotopic composition in the Southern Ocean and application for paleoceanography. Biogeosciences 9 (7), 2443-2457.

Gaillardet, J., Dupré, B., Allègre, C.J., 1995. A global geochemical mass budget applied to the Congo Basin rivers: erosion rates and continental crust composition. Geochimica et Cosmochimica Acta 59 (17), 3469-3485.

Gaillardet, J., Dupré, B., Louvat, P., Allègre, C.J., 1999. Global silicate weathering and CO2 consumption rates deduced from the chemistry of large rivers. Chemical Geology 159 (1–4), 3-30.

Galy, A., France-Lanord, C., 2001. Higher erosion rates in the Himalaya: Geochemical constraints on riverine fluxes. Geology 29 (1), 23-26.

Geilert, S., Vroon, P.Z., Roerdink, D.L., Van Cappellen, P., van Bergen, M.J., 2014. Silicon isotope fractionation during abiotic silica precipitation at low temperatures: Inferences from flow-through experiments. Geochimica et Cosmochimica Acta, 142, 95-114.

Georg, R., West, A., Basu, A., Halliday, A., 2009. Silicon fluxes and isotope composition of direct groundwater discharge into the Bay of Bengal and the effect on the global ocean silicon isotope budget. Earth and Planetary Science Letters 283 (1-4), 67-74.

Georg, R., Reynolds, B.C., Frank, M., Halliday, A.N., 2006. Mechanisms controlling the silicon isotopic compositions of river waters. Earth and Planetary Science Letters 249 (3-4), 290-306.

Georg, R.B., Reynolds, B.C., Frank, M., Halliday, A.N., 2006. New sample preparation techniques for the determination of Si isotopic compositions using MC-ICPMS. Chemical Geology 235 (3–4), 95-104.

Georg, R.B., Reynolds, B.C., West, A.J., Burton, K.W., Halliday, A.N., 2007. Silicon isotope variations accompanying basalt weathering in Iceland. Earth and Planetary Science Letters 261 (3–4), 476-490.

Gibbs, R.J., 1967. Amazon river: environmental factors that control its dissolved and suspended load. Science (New York, N.Y.) 156 (3783), 1734-1737.

Grasse, P., Ehlert, C., Frank, M., 2013. The influence of water mass mixing on the dissolved Si isotope composition in the Eastern Equatorial Pacific. Earth and Planetary Science Letters 380, 60-71.

Harrison, J.A., Frings, P.J., Beusen, A.H., Conley, D.J., McCrackin, M.L., 2012. Global importance, patterns, and controls of dissolved silica retention in lakes and reservoirs. Global Biogeochemical Cycles 26 (2).

He, H., Zhang, S., Zhu, C., Liu, Y., 2016. Equilibrium and kinetic Si isotope fractionation factors and their implications for Si isotope distributions in the Earthâ€™s surface environments. Acta Geochimica 35 (1), 15-24.

Henchiri, S., Gaillardet, J., Dellinger, M., Bouchez, J., Spencer, R.G.M., 2016. Riverine dissolved lithium isotopic signatures in low-relief central Africa and their link to weathering regimes. Geophysical Research Letters 43 (9), 4391-4399.

Holzer, M., Brzezinski, M.A., 2015. Controls on the silicon isotope distribution in the ocean: New diagnostics from a data-constrained model. Global Biogeochemical Cycles 29 (3), 267-287.

Hughes, H.J., Sondag, F., Cocquyt, C., Laraque, A., Pandi, A., André, L., Cardinal, D., 2011. Effect of seasonal biogenic silica variations on dissolved silicon fluxes and isotopic signatures in the Congo River. Limnology and Oceanography 56 (2), 551-561.

Hughes, H., Bouillon, S., André, L., Cardinal, D., 2012. The effects of weathering variability and anthropogenic pressures upon silicon cycling in an intertropical watershed (Tana River, Kenya). Chemical Geology 308, 18-25.

Hughes, H.J., Sondag, F., Santos, R.V., André, L., Cardinal, D., 2013. The riverine silicon isotope composition of the Amazon Basin. Geochimica et Cosmochimica Acta 121, 637-651.

Huh, Y., Chan, L. H., & Edmond, J. M. (2001). Lithium isotopes as a probe of weathering processes: Orinoco River. Earth and Planetary Science Letters, 194(1-2), 189-199.

Huh, Y., Chan, L., Zhang, L., Edmond, J.M., 1998. Lithium and its isotopes in major world rivers: implications for weathering and the oceanic budget. Geochimica et Cosmochimica Acta 62 (12), 2039-2051.

Kısakűrek, B., James, R.H., Harris, N.B.W., Li and δ7Li in Himalayan rivers: Proxies for silicate weathering? 237, 387-401112.

Ksakűrek, B., James, R. H., & Harris, N. B., 2005. Li and δ7Li in Himalayan rivers: Proxies for silicate weathering?. Earth and Planetary Science Letters, 237(3-4), 387-401.

Lane, E., Borland, W., 1951. Estimating bed load. Eos, Transactions American Geophysical Union 32 (1), 121-123.

Louvat, P., Allègre, C.J., 1997. Present denudation rates on the island of Reunion determined by river geochemistry: basalt weathering and mass budget between chemical and mechanical erosions. Geochimica et Cosmochimica Acta 61 (17), 3645-3669.

Lupker, M., France-Lanord, C., Lave, J., Bouchez, J., Galy, V., Metivier, F., Gaillardet, J., Lartiges, B., Mugnier, J., 2011. A Rouse-based method to integrate the chemical composition of river sediments: Application to the Ganga basin. Journal of Geophysical Research-Earth Surface 116, F04012.

Mann, D.G., 1999. The species concept in diatoms. Phycologia 38 (6), 437-495.

Mavromatis, V., Rinder, T., Prokushkin, A.S., Pokrovsky, O.S., Korets, M.A., Chmeleff, J., Oelkers, E.H., 2016. The effect of permafrost, vegetation, and lithology on Mg and Si isotope composition of the Yenisey River and its tributaries at the end of the spring flood. Geochimica et Cosmochimica Acta 191, 32-46.

Mayewski, P.A., Rohling, E.E., Stager, J.C., Karlén, W., Maasch, K.A., Meeker, L.D., Meyerson, E.A., Gasse, F., van Kreveld, S., Holmgren, K., 2004. Holocene climate variability. Quaternary Research 62 (3), 243-255.

Méheut, M., Schauble, E.A., 2014. Silicon isotope fractionation in silicate minerals: insights from first-principles models of phyllosilicates, albite and pyrope. Geochimica et Cosmochimica Acta 134, 137-154.

Méheut, M., Lazzeri, M., Balan, E., Mauri, F., 2007. Equilibrium isotopic fractionation in the kaolinite, quartz, water system: Prediction from first-principles density-functional theory. Geochimica et Cosmochimica Acta 71 (13), 3170-3181.

Méheut, M., Lazzeri, M., Balan, E., & Mauri, F. 2009. Structural control over equilibrium silicon and oxygen isotopic fractionation: a first-principles density-functional theory study. Chemical Geology, 258(1-2), 28-37.

Meybeck, M., Ragu, A., 1995. River Discharges to the Oceans: An Assessment of Suspended Solids, Major Ions and Nutrients. UNEP.

Michalopoulos, P., Aller, R.C., 1995. Rapid clay mineral formation in Amazon delta sediments: reverse weathering and oceanic elemental cycles. SCIENCE-NEW YORK THEN WASHINGTON- , 614-614.

Milliman, J.D., Farnsworth, K.L., 2013. River Discharge to the Coastal Ocean: A Global Synthesis. Cambridge University Press.

Millot, R., Vigier, N., & Gaillardet, J. 2010. Behaviour of lithium and its isotopes during weathering in the Mackenzie Basin, Canada. Geochimica et Cosmochimica Acta, 74(14), 3897-3912.

Millot, R., Allègre, C., Gaillardet, J., Roy, S., 2004. Lead isotopic systematics of major river sediments: a new estimate of the Pb isotopic composition of the Upper Continental Crust. Chemical Geology 203 (1–2), 75-90.

Millot, R., Gaillardet, J.é, Dupré, B., Allègre, C.J., 2003. Northern latitude chemical weathering rates: clues from the Mackenzie River Basin, Canada. Geochimica et Cosmochimica Acta 67 (7), 1305-1329.

Montserrat, F., Renforth, P., Hartmann, J., Leermakers, M., Knops, P., Meysman, F.J.R., 2017. Olivine Dissolution in Seawater: Implications for CO(2) Sequestration through Enhanced Weathering in Coastal Environments. Environmental science & technology 51 (7), 3960-3972.

Moquet, J. S., Crave, A., Viers, J., Seyler, P., Armijos, E., Bourrel, L, and Pombosa, R., (2011). Chemical weathering and atmospheric/soil CO2 uptake in the Andean and Foreland Amazon basins. Chemical Geology, 287(1-2), 1-26.

Oelkers, E.H., A. 2001, An experimental study of forsterite dissolution rates as a function of temperature and aqueous Mg and Si concentrations. Chemical Geology, 175(3-4), 485-494.

Oelze, M., von Blanckenburg, F., Hoellen, D., Dietzel, M., & Bouchez, J. (2014). Si stable isotope fractionation during adsorption and the competition between kinetic and equilibrium isotope fractionation: Implications for weathering systems. Chemical geology, 380, 161-171.

Oelze, M., von Blanckenburg, F., Bouchez, J., Hoellen, D., & Dietzel, M. (2015). The effect of Al on Si isotope fractionation investigated by silica precipitation experiments. Chemical geology, 397, 94-105.

Opfergelt, S., Cardinal, D., Henriet, C., Draye, X., André, L., Delvaux, B., 2006. Silicon isotopic fractionation by banana (Musa spp.) grown in a continuous nutrient flow device. Plant and Soil 285 (1), 333-345

Opfergelt, S., Delvaux, B., André, L., Cardinal, D., 2008. Plant silicon isotopic signature might reflect soil weathering degree. Biogeochemistry 91 (2-3), 163-175

Opfergelt, S., De Bournonville, G., Cardinal, D., André, L., Delstanche, S., Delvaux, B., 2009. Impact of soil weathering degree on silicon isotopic fractionation during adsorption onto iron oxides in basaltic ash soils, Cameroon. Geochimica et Cosmochimica Acta 73 (24), 7226-7240.

Opfergelt, S., Georg, R.B., Delvaux, B., Cabidoche, Y.-., Burton, K.W., Halliday, A.N., 2012. Silicon isotopes and the tracing of desilication in volcanic soil weathering sequences, Guadeloupe. Chemical Geology 326–327, 113-122.

Opfergelt, S., Burton, K., von Strandmann, P.P., Gislason, S., Halliday, A., 2013. Riverine silicon isotope variations in glaciated basaltic terrains: Implications for the Si delivery to the ocean over glacial–interglacial intervals. Earth and Planetary Science Letters 369, 211-219.

Opfergelt, S., Cardinal, D., André, L., Delvigne, C., Bremond, L., Delvaux, B., 2010. Variations of δ30Si and Ge/Si with weathering and biogenic input in tropical basaltic ash soils under monoculture. Geochimica et Cosmochimica Acta 74 (1), 225-240.

Opfergelt, S., Georg, R.B., Burton, K.W., Guicharnaud, R., Siebert, C., Gislason, S.R., Halliday, A.N., 2011. Silicon isotopes in allophane as a proxy for mineral formation in volcanic soils. Applied Geochemistry 26, Supplement, S115-S118.

Opfergelt, S., Delmelle, P., 2012. Silicon isotopes and continental weathering processes: Assessing controls on Si transfer to the ocean. Comptes Rendus Geoscience 344 (11–12), 723-738.

Poitrasson, F., 2017. Silicon Isotope Geochemistry. Reviews in Mineralogy and Geochemistry 82 (1), 289-344.

Pokrovsky, O. S., Schott, J. (2000). Kinetics and mechanism of forsterite dissolution at 25°C and pH from 1 to 12. Geochimica et Cosmochimica Acta, 64(19), 3313-3325.

Pringle, E.A., Savage, P.S., Badro, J., Barrat, J., Moynier, F., 2013. Redox state during core formation on asteroid 4-Vesta. Earth and Planetary Science Letters 373, 75-82.

Pokrovsky, O., Reynolds, B., Prokushkin, A., Schott, J., Viers, J., 2013. Silicon isotope variations in Central Siberian rivers during basalt weathering in permafrost-dominated larch forests. Chemical Geology 355, 103-116.

Pringle, E.A., Savage, P.S., Jackson, M.G., Barrat, J., Moynier, F., 2013. Si Isotope Homogeneity of the Solar Nebula. The Astrophysical Journal 779 (2), 123.

Pringle, E.A., Moynier, F., Savage, P.S., Badro, J., Barrat, J., 2014. Silicon isotopes in angrites and volatile loss in planetesimals. Proceedings of the National Academy of Sciences 111 (48), 17029-17032.

Pringle, E.A., Moynier, F., Savage, P.S., Jackson, M.G., Moreira, M., Day, J.M.D., 2016. Silicon isotopes reveal recycled altered oceanic crust in the mantle sources of Ocean Island Basalts. Geochimica et Cosmochimica Acta 189, 282-295.

Putzer, H., 1984. The geological evolution of the Amazon basin and its mineral resources. In: Sioli, H., (Ed.). The Amazon: Limnology and Landscape Ecology of a Mighty Tropical River and its Basin. Springer Netherlands, Dordrecht.

Rahman, S., Aller, R., Cochran, J., 2016. Cosmogenic 32Si as a tracer of biogenic silica burial and diagenesis: Major deltaic sinks in the silica cycle. Geophysical Research Letters 43 (13), 7124-7132.

Reeder, S. W., Hitchon, B., & Levinson, A. A. (1972). Hydrogeochemistry of the surface waters of the Mackenzie River drainage basin, Canada—I. Factors controlling inorganic composition. Geochimica et Cosmochimica Acta, 36(8), 825-865.

Reynolds, B.C., Frank, M., Halliday, A., 2006. Silicon isotope fractionation during nutrient utilization in the North Pacific. Earth and Planetary Science Letters 244 (1), 431-443.

Rudnick, R.L., Gao, S., 2003. 3.01 - Composition of the Continental Crust. In: Holland, H.D. and Turekian, K.K., (Eds.). Treatise on Geochemistry. Pergamon, Oxford.

Savage, P.S., Moynier, F., 2013. Silicon isotopic variation in enstatite meteorites: Clues to their origin and Earth-forming material. Earth and Planetary Science Letters 361, 487-496.

Savage, P.S., Georg, R.B., Williams, H.M., Burton, K.W., Halliday, A.N., 2011. Silicon isotope fractionation during magmatic differentiation. Geochimica et Cosmochimica Acta 75 (20), 6124-6139.

Savage, P.S., Georg, R.B., Williams, H.M., Halliday, A.N., 2013. The silicon isotope composition of the upper continental crust. Geochimica et Cosmochimica Acta 109, 384-399.

Savage, P. S., Georg, R. B., Williams, H. M., Turner, S., Halliday, A. N., Chappell, B. W. (2012). The silicon isotope composition of granites. Geochimica et Cosmochimica Acta, 92, 184-202.

Steinhoefel, G., Breuer, J., von Blanckenburg, F., Horn, I., Kaczorek, D., Sommer, M., 2011. Micrometer silicon isotope diagnostics of soils by UV femtosecond laser ablation. Chemical Geology, 286(3-4), 280-289.

Sun, L., Wu, L., Ding, T., Tian, S., 2008. Silicon isotope fractionation in rice plants, an experimental study on rice growth under hydroponic conditions. Plant and Soil 304 (1-2), 291-300.

Taylor, S. R., 1964,. Abundance of chemical elements in the continental crust: a new table. Geochimica et cosmochimica acta, 28(8), 1273-1285.

Teng, F., McDonough, W.F., Rudnick, R., Dalpé, C., Tomascak, P., Chappell, B.W., Gao, S., 2004. Lithium isotopic composition and concentration of the upper continental crust. Geochimica et Cosmochimica Acta 68 (20), 4167-4178.

Thompson, L.G., Mosley-Thompson, E., Davis, M.E., Henderson, K.A., Brecher, H.H., Zagorodnov, V.S., Mashiotta, T.A., Lin, P.N., Mikhalenko, V.N., Hardy, D.R., Beer, J., 2002. Kilimanjaro ice core records: evidence of holocene climate change in tropical Africa. Science (New York, 298 (5593), 589-593.

Tomascak, P.B., Magna, T., Dohmen, R., 2016. Advances in Lithium Isotope Geochemistry. Springer International Publishing, Springer International Publishing Switzerland.

Tréguer, P., Nelson, D.M., Van Bennekom, A.J., DeMaster, D.J., Leynaert, A., Quéguiner, B., 1995. The Silica Balance in the World Ocean: A Reestimate. Science 268 (5209), 375-379.

Tréguer, P., De La Rocha, C., 2013. The world ocean silica cycle. Annual review of marine science 5, 477-501.

Veizer, J., Jansen, S.L., 1979. Basement and sedimentary recycling and continental evolution. The Journal of geology 87 (4), 341-370.

Veizer, J., Jansen, S.L., 1985. Basement and sedimentary recycling-2: time dimension to global tectonics. The Journal of geology 93 (6), 625-643.

Viers, J., Roddaz, M., Filizola, N., Guyot, J., Sondag, F., Brunet, P., Zouiten, C., Boucayrand, C., Martin, F., Boaventura, G.R., 2008. Seasonal and provenance controls on Nd–Sr isotopic compositions of Amazon rivers suspended sediments and implications for Nd and Sr fluxes exported to the Atlantic Ocean. Earth and Planetary Science Letters 274 (3–4), 511-523.

Viers, J., Dupré, B., Gaillardet, J., 2009. Chemical composition of suspended sediments in World Rivers: New insights from a new database. Science of The Total Environment 407 (2), 853-868.

Walker, J.C.G., Hays, P.B., Kasting, J.F., 1981. A negative feedback mechanism for the long-term stabilization of Earth's surface temperature. Journal of Geophysical Research: Oceans 86 (C10), 9776-9782.

Wedepohl, K.H., 1995. The composition of the continental crust. Geochimica et Cosmochimica Acta 59 (7), 1217-1232.

Wilkinson, B.H., McElroy, B.J., Kesler, S.E., Peters, S.E., Rothman, E.D., 2009. Global geologic maps are tectonic speedometers—Rates of rock cycling from area-age frequencies. Geological Society of America Bulletin 121 (5-6), 760-779.

Wittmann, H., von Blanckenburg, F., Guyot, J.L., Laraque, A., Bernal, C., Kubik, P.W., 2011. Sediment production and transport from in situ-produced cosmogenic 10Be and river loads in the Napo River basin, an upper Amazon tributary of Ecuador and Peru. Journal of South American Earth Sciences 31 (1), 45-53.

Zambardi, T., Poitrasson, F., 2011. Precise Determination of Silicon Isotopes in Silicate Rock Reference Materials by MC-ICP-MS. Geostandards and Geoanalytical Research 35 (1), 89-99.

Ziegler, K., Chadwick, O.A., White, A.F., Brzezinski, M.A., 2005a. d30Si systematics in a granitic saprolite, Puerto Rico. Geology 33 (10), 817-820.

Ziegler, K., Chadwick, O.A., Brzezinski, M.A., Kelly, E.F., 2005b. Natural variations of δ30Si ratios during progressive basalt weathering, Hawaiian Islands. Geochimica et Cosmochimica Acta 69 (19), 4597-4610.

Appendix ii

Table ii-1. Mineralogical contribution of quartz, weatherable minerals, and clays in bulk depth-profile sediments. Respectively, f_Q, f_W, and f_c represent the calculated fraction of quartz, weatherable minerals, and clays. The suffix number shows the results from different scenarios constraining the end-member of weatherable minerals: 1. Na/Si=0.27 (pure albite) and Al/Si=0.35; 2. Na/Si=the highest Na/Si observed in the corresponding river and Al/Si=0.35; 3. Na/Si=0.12 (UCC) and Al/Si=0.32; 4. Na/Si= the highest Na/Si observed in the corresponding river and Al/Si=0.32.

Sample name	*River*	Al/Si	Na/Si	f_Q-1	f_Q-2	f_Q-3	f_Q-4	f_W-1	f_W-2	f_W-3	f_W-4	f_c-1	f_c-2	f_c-3	f_c-4
AM05_04	Solimoes	0.22	0.03	0.70	0.18	0.61	0.18	0.12	0.93	0.26	0.93	0.18	-0.11	0.13	-0.11
AM05_06	Solimoes	0.29	0.03	0.62	0.07	0.52	0.07	0.12	0.97	0.27	0.97	0.26	-0.05	0.20	-0.05
AM06_01	Solimoes	0.06	0.02	0.90	0.66	0.86	0.66	0.05	0.43	0.12	0.43	0.05	-0.09	0.02	-0.09
AM06_02	Solimoes	0.09	0.02	0.85	0.49	0.79	0.49	0.08	0.64	0.18	0.64	0.07	-0.13	0.03	-0.13
AM06_03	Solimoes	0.08	0.02	0.88	0.58	0.82	0.58	0.07	0.54	0.15	0.54	0.06	-0.11	0.03	-0.11
AM06_04	Solimoes	0.06	0.02	0.90	0.65	0.86	0.65	0.06	0.44	0.12	0.44	0.05	-0.09	0.02	-0.09
AM06_05	Solimoes	0.13	0.03	0.79	0.30	0.71	0.30	0.11	0.88	0.25	0.88	0.09	-0.18	0.05	-0.18
AM06_06	Solimoes	0.08	0.02	0.87	0.55	0.81	0.55	0.07	0.57	0.16	0.57	0.06	-0.12	0.03	-0.12
AM06_07	Solimoes	0.22	0.03	0.69	0.15	0.60	0.15	0.12	0.96	0.27	0.96	0.18	-0.12	0.13	-0.12
AM06_09	Solimoes	0.37	0.03	0.55	0.07	0.46	0.07	0.11	0.85	0.24	0.85	0.35	0.08	0.30	0.08
AM06_10	Solimoes	0.31	0.03	0.61	0.09	0.52	0.09	0.12	0.91	0.26	0.91	0.28	-0.01	0.23	-0.01
AM06_11	Solimoes	0.32	0.03	0.60	0.09	0.51	0.09	0.11	0.90	0.25	0.90	0.29	0.01	0.24	0.01
AM06_12	Solimoes	0.31	0.03	0.61	0.08	0.51	0.08	0.12	0.93	0.26	0.93	0.28	-0.01	0.23	-0.01
AM06_13	Solimoes	0.37	0.03	0.55	0.09	0.47	0.09	0.10	0.82	0.23	0.82	0.35	0.09	0.30	0.09
AM06_14	Solimoes	0.39	0.03	0.53	0.08	0.45	0.08	0.10	0.81	0.23	0.81	0.36	0.11	0.32	0.11
AM06_15	Solimoes	0.27	0.03	0.64	0.08	0.54	0.08	0.13	1.00	0.28	1.00	0.23	-0.08	0.18	-0.08
AM06_16	Solimoes	0.33	0.03	0.59	0.12	0.51	0.12	0.11	0.84	0.24	0.84	0.30	0.04	0.26	0.04
AM06_17	Solimoes	0.37	0.03	0.55	0.13	0.48	0.13	0.10	0.76	0.21	0.76	0.35	0.12	0.31	0.12
AM06_18	Solimoes	0.38	0.03	0.54	0.13	0.47	0.13	0.09	0.74	0.21	0.74	0.36	0.13	0.32	0.13
AM06_19	Solimoes	0.44	0.02	0.50	0.16	0.44	0.16	0.08	0.60	0.17	0.60	0.43	0.24	0.40	0.24
AM05_15	Madeira	0.38	0.02	0.56	-0.02	0.50	-0.02	0.07	0.97	0.16	0.97	0.37	0.05	0.34	0.05
AM05_17	Madeira	0.40	0.02	0.54	-0.02	0.48	-0.02	0.07	0.94	0.15	0.94	0.40	0.09	0.37	0.09

Sample name	***River***	**Al/Si**	**Na/Si**	**f_Q-1**	**f_Q-2**	**f_Q-3**	**f_Q-4**	**f_W-1**	**f_W-2**	**f_W-3**	**f_W-4**	**f_c-1**	**f_c-2**	**f_c-3**	**f_c-4**
AM05_18	Madeira	0.44	0.02	0.50	-0.10	0.44	-0.10	0.07	1.00	0.16	1.00	0.43	0.10	0.40	0.10
AM05_24	Madeira	0.23	0.02	0.73	0.26	0.68	0.26	0.06	0.79	0.13	0.79	0.22	-0.05	0.19	-0.05
AM06_33	Madeira	0.22	0.02	0.73	0.23	0.68	0.23	0.06	0.84	0.14	0.84	0.21	-0.07	0.18	-0.07
AM06_34	Madeira	0.29	0.02	0.66	0.10	0.60	0.10	0.07	0.93	0.15	0.93	0.27	-0.04	0.25	-0.04
AM06_36	Madeira	0.28	0.02	0.66	0.12	0.61	0.12	0.07	0.91	0.15	0.91	0.27	-0.03	0.24	-0.03
AM06_37	Madeira	0.28	0.02	0.66	0.12	0.61	0.12	0.07	0.90	0.15	0.90	0.27	-0.03	0.24	-0.03
AM06_39	Madeira	0.30	0.02	0.65	0.11	0.59	0.11	0.07	0.91	0.15	0.91	0.29	-0.02	0.26	-0.02
AM06_43	Madeira	0.36	0.02	0.58	0.01	0.53	0.01	0.07	0.96	0.16	0.96	0.34	0.03	0.32	0.03
AM06_44	Madeira	0.06	0.01	0.92	0.72	0.90	0.72	0.02	0.34	0.05	0.34	0.06	-0.06	0.05	-0.06
AM05_35	Amazonas	0.20	0.03	0.74	0.19	0.67	0.19	0.09	0.94	0.20	0.94	0.17	-0.13	0.13	-0.13
AM05_36	Amazonas	0.21	0.03	0.72	0.15	0.65	0.15	0.10	0.99	0.21	0.99	0.18	-0.14	0.14	-0.14
AM05_37	Amazonas	0.24	0.03	0.69	0.11	0.61	0.11	0.10	1.00	0.22	1.00	0.22	-0.11	0.18	-0.11
AM05_44	Amazonas	0.08	0.02	0.88	0.54	0.83	0.54	0.06	0.59	0.13	0.59	0.06	-0.13	0.04	-0.13
AM05_46	Amazonas	0.07	0.02	0.88	0.51	0.84	0.51	0.06	0.64	0.14	0.64	0.05	-0.15	0.03	-0.15
AM06_55	Amazonas	0.21	0.02	0.72	0.23	0.66	0.23	0.08	0.86	0.18	0.86	0.19	-0.09	0.16	-0.09
AM06_58	Amazonas	0.33	0.02	0.60	0.08	0.53	0.08	0.09	0.90	0.19	0.90	0.31	0.02	0.28	0.02
AM06_60	Amazonas	0.29	0.03	0.64	0.08	0.56	0.08	0.09	0.97	0.21	0.97	0.27	-0.04	0.23	-0.04
AM06_63	Amazonas	0.32	0.03	0.61	0.07	0.54	0.07	0.09	0.94	0.20	0.94	0.29	-0.01	0.26	-0.01
AM06_64	Amazonas	0.36	0.02	0.57	0.05	0.50	0.05	0.09	0.88	0.19	0.88	0.35	0.06	0.31	0.06
AM06_65	Amazonas	0.42	0.02	0.51	0.04	0.45	0.04	0.08	0.81	0.17	0.81	0.41	0.15	0.38	0.15
AM07_01	Beni	0.17	0.01	0.80	0.46	0.77	0.46	0.04	0.57	0.10	0.57	0.16	-0.03	0.14	-0.03
AM07_02	Beni	0.31	0.02	0.64	0.09	0.58	0.09	0.07	0.92	0.16	0.92	0.29	-0.01	0.26	-0.01
AM07_03	Beni	0.32	0.02	0.62	0.05	0.56	0.05	0.07	0.96	0.16	0.96	0.31	-0.01	0.28	-0.01
AM07_04	Beni	0.33	0.02	0.61	0.02	0.55	0.02	0.08	1.00	0.17	1.00	0.31	-0.02	0.28	-0.02
AM07_05	Beni	0.10	0.01	0.88	0.66	0.86	0.66	0.03	0.37	0.06	0.37	0.09	-0.03	0.08	-0.03
AM07_06	Beni	0.20	0.01	0.75	0.33	0.71	0.33	0.05	0.72	0.12	0.72	0.19	-0.05	0.17	-0.05
AM07_07	Beni	0.19	0.01	0.77	0.36	0.73	0.36	0.05	0.70	0.12	0.70	0.18	-0.06	0.15	-0.06
AM07_08	Beni	0.23	0.02	0.73	0.27	0.68	0.27	0.06	0.77	0.13	0.77	0.21	-0.04	0.19	-0.04
AM07_09	Beni	0.28	0.02	0.67	0.18	0.62	0.18	0.06	0.83	0.14	0.83	0.26	-0.01	0.24	-0.01
AM08_10	Ucayali	0.28	0.04	0.62	0.11	0.52	0.11	0.13	0.92	0.28	0.92	0.25	-0.04	0.19	-0.04
AM08_13	Ucayali	0.31	0.04	0.60	0.07	0.49	0.07	0.13	0.94	0.29	0.94	0.27	-0.02	0.22	-0.02

Sample name	***River***	**Al/Si**	**Na/Si**	**f_Q-1**	**f_Q-2**	**f_Q-3**	**f_Q-4**	**f_W-1**	**f_W-2**	**f_W-3**	**f_W-4**	**f_c-1**	**f_c-2**	**f_c-3**	**f_c-4**
AM08_14	Ucayali	0.13	0.03	0.79	0.32	0.70	0.32	0.12	0.86	0.26	0.86	0.09	-0.18	0.04	-0.18
AM08_17	Ucayali	0.19	0.04	0.72	0.16	0.61	0.16	0.14	1.00	0.31	1.00	0.14	-0.16	0.09	-0.16
AM08_36	Pastaza	0.39	0.06	0.44	0.14	0.26	0.14	0.23	0.70	0.52	0.70	0.32	0.16	0.22	0.16
AM08_37	Pastaza	0.27	0.09	0.50	0.07	0.24	0.07	0.34	1.00	0.74	1.00	0.16	-0.07	0.02	-0.07
Napo 3	Napo	0.35	0.00	0.64	0.63	0.63	0.63	0.00	0.00	0.00	0.00	0.36	0.37	0.37	0.37
Napo 4	Napo	0.34	0.00	0.65	0.65	0.65	0.65	0.00	0.00	0.00	0.00	0.35	0.35	0.35	0.35
Coca 1	Napo	0.33	0.00	0.66	0.66	0.66	0.66	0.00	0.00	0.00	0.00	0.34	0.34	0.34	0.34
CAN09_49	Red Arctic	0.15	0.01	0.82	0.26	0.79	0.26	0.04	0.92	0.09	0.92	0.14	-0.18	0.12	-0.18
CAN09_50	Red Arctic	0.31	0.01	0.65	0.07	0.62	0.07	0.04	0.95	0.09	0.95	0.30	-0.02	0.29	-0.02
CAN09_51	Red Arctic	0.31	0.01	0.65	0.04	0.61	0.04	0.04	1.00	0.10	1.00	0.31	-0.04	0.29	-0.04
CAN09_52	Red Arctic	0.31	0.01	0.65	0.07	0.61	0.07	0.04	0.95	0.09	0.95	0.31	-0.01	0.29	-0.01
CAN09_53	Red Arctic	0.15	0.01	0.82	0.32	0.79	0.32	0.04	0.82	0.08	0.82	0.14	-0.14	0.13	-0.14
CAN09_01	Liard	0.15	0.02	0.80	0.30	0.76	0.30	0.06	0.85	0.13	0.85	0.14	-0.14	0.11	-0.14
CAN09_02	Liard	0.23	0.02	0.72	0.24	0.68	0.24	0.06	0.80	0.12	0.80	0.22	-0.04	0.20	-0.04
CAN09_03	Liard	0.19	0.02	0.76	0.26	0.72	0.26	0.06	0.84	0.13	0.84	0.18	-0.10	0.15	-0.10
CAN09_04	Liard	0.24	0.02	0.72	0.23	0.67	0.23	0.06	0.82	0.13	0.82	0.23	-0.05	0.20	-0.05
CAN09_11	Liard	0.08	0.02	0.88	0.35	0.83	0.35	0.06	0.87	0.13	0.87	0.06	-0.23	0.04	-0.23
CAN09_12	Liard	0.13	0.02	0.82	0.27	0.77	0.27	0.06	0.92	0.14	0.92	0.11	-0.20	0.08	-0.20
CAN10_46	Liard	0.11	0.02	0.84	0.31	0.79	0.31	0.06	0.89	0.14	0.89	0.10	-0.20	0.07	-0.20
CAN10_48	Liard	0.16	0.02	0.80	0.31	0.75	0.31	0.06	0.82	0.13	0.82	0.14	-0.13	0.12	-0.13
CAN10_49	Liard	0.28	0.01	0.68	0.23	0.63	0.23	0.05	0.74	0.11	0.74	0.27	0.03	0.25	0.03
CAN10_50	Liard	0.07	0.02	0.89	0.33	0.84	0.33	0.06	0.93	0.14	0.93	0.05	-0.26	0.02	-0.26
CAN10_51	Liard	0.10	0.02	0.86	0.35	0.81	0.35	0.06	0.86	0.13	0.86	0.08	-0.21	0.05	-0.21
CAN11_03	Liard	0.20	0.02	0.74	0.15	0.69	0.15	0.07	0.99	0.15	0.99	0.19	-0.14	0.16	-0.14
CAN11_04	Liard	0.19	0.02	0.76	0.17	0.71	0.17	0.07	0.99	0.15	0.99	0.17	-0.16	0.14	-0.16
CAN11_05	Liard	0.20	0.02	0.75	0.17	0.70	0.17	0.07	0.97	0.15	0.97	0.18	-0.14	0.16	-0.14
CAN11_06	Liard	0.21	0.02	0.73	0.14	0.68	0.14	0.07	1.00	0.15	1.00	0.20	-0.14	0.17	-0.14
CAN11_07	Liard	0.22	0.02	0.73	0.13	0.67	0.13	0.07	1.00	0.15	1.00	0.20	-0.13	0.18	-0.13
CAN09_54	Mackenzie	0.13	0.02	0.83	0.31	0.78	0.31	0.06	0.87	0.12	0.87	0.12	-0.17	0.09	-0.17
CAN09_43	Mackenzie	0.29	0.01	0.67	0.17	0.63	0.17	0.05	0.83	0.12	0.83	0.28	0.00	0.26	0.00
CAN09_44	Mackenzie	0.28	0.01	0.67	0.18	0.63	0.18	0.05	0.82	0.12	0.82	0.28	0.00	0.25	0.00

Sample name	***River***	**Al/Si**	**Na/Si**	**f_Q-1**	**f_Q-2**	**f_Q-3**	**f_Q-4**	**f_W-1**	**f_W-2**	**f_W-3**	**f_W-4**	**f_c-1**	**f_c-2**	**f_c-3**	**f_c-4**
CAN09_45	Mackenzie	0.30	0.01	0.66	0.18	0.62	0.18	0.05	0.79	0.11	0.79	0.29	0.03	0.27	0.03
CAN09_46	Mackenzie	0.29	0.01	0.67	0.18	0.63	0.18	0.05	0.82	0.12	0.82	0.28	0.01	0.26	0.01
CAN09_47	Mackenzie	0.30	0.01	0.66	0.16	0.61	0.16	0.05	0.83	0.12	0.83	0.29	0.01	0.27	0.01
CAN11_65	Mackenzie	0.13	0.02	0.83	0.23	0.78	0.23	0.06	1.00	0.14	1.00	0.11	-0.23	0.08	-0.23
CAN11_66	Mackenzie	0.17	0.02	0.78	0.18	0.73	0.18	0.06	0.99	0.14	0.99	0.16	-0.18	0.13	-0.18
CAN11_67	Mackenzie	0.21	0.02	0.74	0.17	0.69	0.17	0.06	0.95	0.14	0.95	0.20	-0.12	0.17	-0.12
CAN10_22	Middle Channel	0.21	0.01	0.75	0.20	0.70	0.20	0.05	0.91	0.12	0.91	0.20	-0.11	0.18	-0.11
CAN10_23	Middle Channel	0.18	0.02	0.78	0.17	0.73	0.17	0.06	1.00	0.13	1.00	0.16	-0.17	0.14	-0.17
CAN10_26	Middle Channel	0.33	0.01	0.62	0.09	0.58	0.09	0.05	0.89	0.12	0.89	0.32	0.02	0.30	0.02
CAN10_27	Middle Channel	0.10	0.02	0.86	0.29	0.81	0.29	0.06	0.94	0.12	0.94	0.09	-0.23	0.06	-0.23
CAN10_28	Middle Channel	0.21	0.02	0.75	0.18	0.71	0.18	0.06	0.94	0.12	0.94	0.19	-0.12	0.17	-0.12
CAN10_29	Middle Channel	0.31	0.01	0.65	0.11	0.60	0.11	0.05	0.89	0.12	0.89	0.30	0.00	0.28	0.00
CAN10_30	Middle Channel	0.32	0.01	0.63	0.10	0.59	0.10	0.05	0.88	0.12	0.88	0.31	0.02	0.29	0.02
CAN10_31	Middle Channel	0.32	0.01	0.63	0.10	0.59	0.10	0.05	0.88	0.12	0.88	0.32	0.02	0.29	0.02
CAN10_32	Middle Channel	0.38	0.01	0.57	0.07	0.53	0.07	0.05	0.84	0.11	0.84	0.38	0.09	0.36	0.09
CAN10_34	Middle Channel	0.27	0.01	0.69	0.14	0.64	0.14	0.05	0.90	0.12	0.90	0.26	-0.04	0.24	-0.04
CAN10_35	Middle Channel	0.26	0.01	0.70	0.15	0.65	0.15	0.05	0.91	0.12	0.91	0.25	-0.06	0.23	-0.06
CAN10_36	Middle Channel	0.28	0.01	0.68	0.13	0.63	0.13	0.05	0.90	0.12	0.90	0.27	-0.03	0.25	-0.03
CAN10_37	Middle Channel	0.35	0.01	0.61	0.06	0.56	0.06	0.05	0.91	0.12	0.91	0.34	0.03	0.32	0.03
CAN09_31	Peace	0.31	0.01	0.65	0.30	0.62	0.30	0.04	0.59	0.10	0.59	0.30	0.11	0.28	0.11
CAN09_32	Peace	0.16	0.02	0.79	0.24	0.74	0.24	0.07	0.93	0.15	0.93	0.14	-0.17	0.11	-0.17
CAN09_33	Peace	0.10	0.02	0.85	0.25	0.79	0.25	0.07	1.00	0.16	1.00	0.08	-0.25	0.05	-0.25
CAN09_37	Peel	0.25	0.01	0.71	0.22	0.68	0.22	0.04	0.81	0.10	0.81	0.24	-0.03	0.23	-0.03
CAN09_38	Peel	0.26	0.01	0.71	0.23	0.67	0.23	0.04	0.79	0.10	0.79	0.25	-0.02	0.23	-0.02
CAN09_39	Peel	0.26	0.01	0.71	0.24	0.67	0.24	0.04	0.77	0.09	0.77	0.25	-0.01	0.23	-0.01
CAN09_40	Peel	0.30	0.01	0.66	0.18	0.63	0.18	0.04	0.81	0.10	0.81	0.29	0.02	0.27	0.02
CAN09_41	Peel	0.12	0.01	0.86	0.54	0.84	0.54	0.03	0.52	0.06	0.52	0.11	-0.06	0.10	-0.06
CAN09_42	Peel	0.18	0.01	0.79	0.24	0.75	0.24	0.05	0.89	0.11	0.89	0.16	-0.14	0.14	-0.14
CAN10_03	Peel	0.19	0.01	0.77	0.33	0.74	0.33	0.04	0.73	0.09	0.73	0.19	-0.06	0.17	-0.06
CAN10_04	Peel	0.26	0.01	0.70	0.19	0.67	0.19	0.05	0.85	0.10	0.85	0.25	-0.04	0.23	-0.04
CAN10_05	Peel	0.27	0.01	0.69	0.17	0.65	0.17	0.05	0.85	0.10	0.85	0.27	-0.02	0.25	-0.02

Sample name	***River***	**Al/Si**	**Na/Si**	**f_Q-1**	**f_Q-2**	**f_Q-3**	**f_Q-4**	**f_W-1**	**f_W-2**	**f_W-3**	**f_W-4**	**f_c-1**	**f_c-2**	**f_c-3**	**f_c-4**
CAN10_06	Peel	0.27	0.01	0.69	0.18	0.65	0.18	0.05	0.83	0.10	0.83	0.27	-0.01	0.25	-0.01
CAN10_07	Peel	0.09	0.01	0.88	0.55	0.86	0.55	0.03	0.55	0.07	0.55	0.09	-0.10	0.07	-0.10
CAN11_77	Peel	0.20	0.01	0.76	0.24	0.72	0.24	0.05	0.85	0.10	0.85	0.20	-0.09	0.18	-0.09
CAN11_78	Peel	0.21	0.01	0.75	0.22	0.71	0.22	0.05	0.88	0.11	0.88	0.20	-0.10	0.18	-0.10
CAN11_79	Peel	0.27	0.02	0.68	0.08	0.64	0.08	0.06	1.00	0.12	1.00	0.26	-0.08	0.24	-0.08
CAN09_28	Slave	0.28	0.02	0.67	0.30	0.63	0.30	0.06	0.63	0.12	0.63	0.27	0.06	0.25	0.06
CAN09_30	Slave	0.09	0.02	0.85	0.26	0.78	0.26	0.09	1.00	0.20	1.00	0.06	-0.26	0.02	-0.26
CAN10_65	Slave	0.28	0.02	0.67	0.25	0.62	0.25	0.06	0.71	0.14	0.71	0.27	0.04	0.24	0.04
CAN10_66	Slave	0.09	0.02	0.86	0.35	0.80	0.35	0.08	0.88	0.17	0.88	0.06	-0.22	0.03	-0.22

Figure ii-1 Determination of integrated δ^{30}Si in Solimões and Madeira river sediments

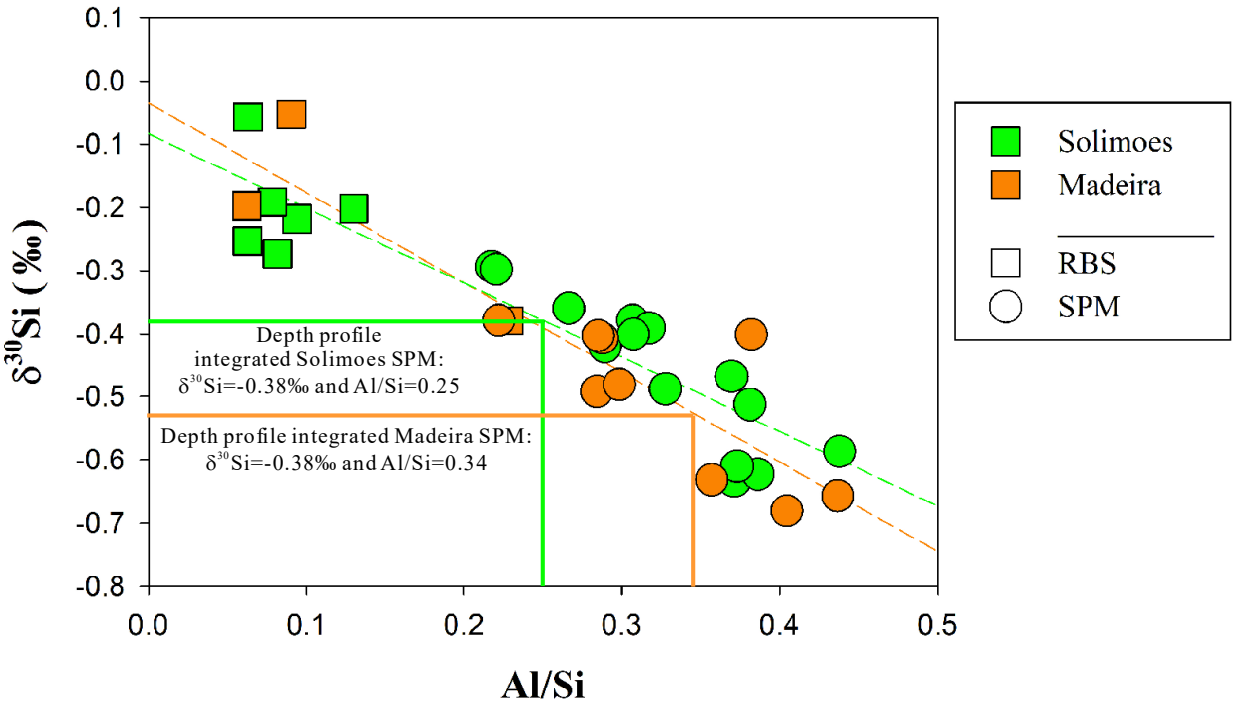

Figure ii-2 Determination of integrated δ^{30}Si in Solimões and Madeira river sediments

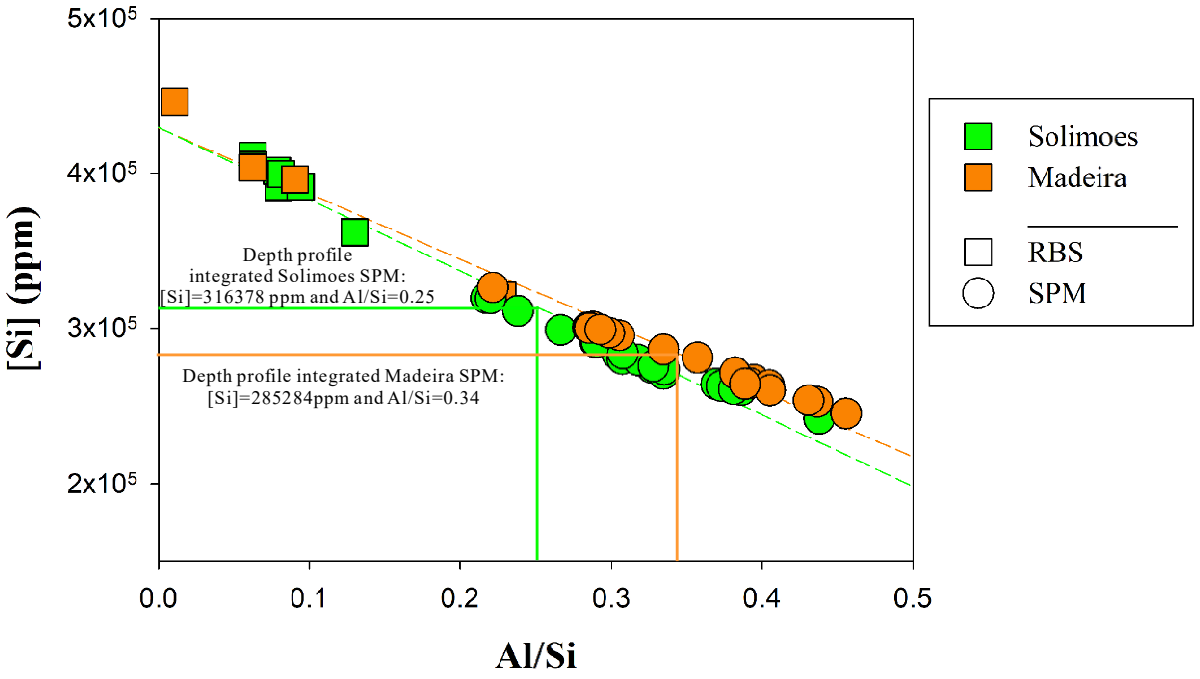

Chapter 6: Conclusions and perspectives

In this thesis, we mainly investigate the coupled interaction between rock cycle and water cycle at the Earth surface throughout geological time. More precisely, recall Figure 1.12, we emphasize the importance of cannibalistic recycling of sedimentary rocks: detrital sediments produced from weathering show great potential to remain at Earth surface if they can escape from subduction zones, and these sediments can be recycled back to sub-aerial environment and incorporated with water cycle to be weathered again. This effect tends to perpetuate the geochemical nature of the Earth surface (Mackenzie and Garrels, 1971; Allègre and Rousseau, 1984; Veizer and Mackenzie, 2013). Moreover, we also highlight the effect of diagenesis and reverse weathering processes, in-between weathering and sedimentary recycling, on the chemical composition of seawater. These objectives were achieved by using non-traditional isotope systems (Si and Li) through various approaches including a set of well controlled experiments, a field examination of a paleo-deltaic system, and a global survey of sediments from world's large rivers. The main conclusions of this thesis are summarized below.

The experimental study showed the great capacity of highly weathered product clays such as kaolinite to take up Li mobilised from the alteration of rocks, which can further regulate the Li isotope composition in the ocean. The fractionation of Li isotopes by the adsorption of kaolinite follows a Rayleigh-like fractionation, matching the results from a previous study (Zhang et al., 1998). As the clay minerals produced during continental weathering can significantly elevate the Li isotope composition in seawater, therefore the evolution of seawater δ^7Li (Hathorne and James, 2006; Misra and Froelich, 2012) could be, at least partially, explained by the variation of clay production on the continents. From Palaeocene, δ^7Li in seawater has rose by 9‰ (Misra and Froelich, 2012), and meanwhile the global seawater level has been falling (Haq et al., 1987; Miller et al., 2005). The falling of sea-level is able to expose the epicontinental land mass. Over these

new surface, geological features such as alluvial plains could develop, and the residence time of weathering would be prolonged. Consequentially, riverine dissolved δ^7Li could be elevated and clays could be matured. The combined effect on dissolved Li and clays transported to the ocean further elevate the δ^7Li signature of seawater.

In the paleo-deltaic system in the Ainsa basin, a systematic difference of Si and Li isotope signatures exists between sediments deposited in alluvial environment and in marine environment: marine sediments have consistently lower δ^{30}Si and δ^7Li than alluvial sediments in intermediate to fine grain size fractions. These differences are thought to be caused by the coupling of Si and Li with Fe cycle in deltaic environment, where Fe-rich minerals (clays and oxides) can be formed. During the formation of these minerals, lighter Si and Li are preferentially taken up. In terms of Si, our data suggest a sink of light Si isotopes in deltas, confirming the results from mass balance models (Frings et al., 2016). Regarding to Li, our observation shows that in delta environments, the Li behaves similarly with that in continental weathering, and it is on contrary with results suggested by Teng et al. (2004) that δ^7Li in fine sediments increase during the interaction with seawater.

The survey of world's large rivers' sediments showed that lithology has a primary control on Si isotope composition. Globally, river sediments inherit the signature of δ^{30}Si from the end-member of sedimentary rocks. However, the weathering during "first-cycle" weathering is a main contributor of the δ^{30}Si variation as primary minerals such as feldspars have relatively higher δ^{30}Si than that in secondary minerals such as clays. The effect of present-day weathering can be investigated by examining both surface sediment and river bed sand, in those rivers with high weathering intensities such as Congo. Using δ^{30}Si and depth profile, an estimation of bed sand load in Amazon river is made to be 16 to 36% of total sediments transported to the ocean. Due to

the cannibalism of sedimentary rocks, present-day sediments are dominated by quartz and clays, suggesting that the source-to-sink-to-source cycle separate Si derived from igneous rocks into two major Si pools. As Si in these two reservoirs, quartz and clays, are relatively stable during weathering, thus at a sedimentary rocks-dominated Earth surface, atmospheric CO_2 uptake by silicate weathering is chiefly achieved by the weathering of igneous rocks such as basalt.

In this thesis, we also raise some questions and give a few perspectives for future studies. First, the status quo of the relationship between physical and chemical weathering is considered to be positive: high chemical weathering rates is maintained by high physical erosion rates (Gaillardet et al., 1999). This relationship is derived from dataset from present-day large rivers. On the one hand, as shown in Li isotopes (Dellinger et al., 2015) in Amazon and Sr isotopes (Derry and France-Lanord, 1996) in Himalayas, the weathering of large rivers are mostly taken place in their low land areas such asa floodplains. On the other hand, as proposed in Chapter 3, during the evolution of Earth surface topography a considerable fraction of the low land areas could have been submerged under sea-level. Hence, if the weathering of large rivers are coupled between weathering in the mountains (characterized by high erosion rates) and weathering in floodplains (characterized by high chemical weathering rates), the variation of global sea-level could de-couple these two processes by prohibiting the weathering in low land areas. Therefore, the question becomes to which extend the correlation between physical and chemical weathering would be hold valid?

In terms of process occurring at estuaries and deltas, our data clearly shows a manifestation of Si and Li isotopes. Nevertheless, the exact mechanism is still unknown. To date, most studies on dissolved Li show a conservative behaviour during mixing between river water and seawater. However, errors could have been made since seawater has a much higher (~100 times) Li

concentration than river water. Few studies have investigated the variation of Li concentration from river transect to river mouth. Additionally, results from Chapter 3 and Chapter 4 shows that the adsorption of seawater Li by detrital clay minerals and the formation of Fe-rich minerals both can elevate the seawater Li isotope signatures, and the relationship between these two processes are still unknown. In Ainsa, the isotope behaviour of Si and Li is thought to be coupled with Fe, whereas in some rivers Fe can escape the scavenging in mixing zones (Powell and Wilson-Finelli, 2003; Opfergelt et al., 2017), such as Mississippi river. In the meantime, authigenic clay formation can also take place in these areas (Presti and Michalopoulos, 2008), and the behaviour of Si and Li isotopes there is unknown. Lastly, the compilation of δ^7Li and Li/Fe in sediments and sedimentary rocks have shown that the coupling between the geochemical cycle of these two elements, which may provide a new approach to study the anoxic/oxic changes.

Our results of Si isotope in world large rivers show the importance of both source effect and present-day weathering, nevertheless, these two effects are not well resolved. More precisely, the accumulation effects of previous weathering episodes were at different degrees (*e.g.* shales display a δ^{30}Si range of −0.80 to 0‰) and the present-day weathering profile of world rivers varies (*e.g.* Congo *vs.* Huange). In both cases, the key factor is the residence time: how long a particle has been weathered in the past and now. In order to understand the relationship between ancient weathering and present-day weathering, it is necessary to obtain the information of both bedrock and river sediment. Moreover, as indicated in Chapter 5, rivers draining basins characterized by basalts has a pivotal role regulating atmospheric CO_2. We are still lacking knowledge on parameters controlling these rivers. For example, whether the mineralogical chemistry of Si is more important than temperature and climate? A systematic study of this type of rivers such as Yenisei (Siberian traps), Columbia (Columbia traps), Parana (Parana large igneous providence),

and Tapti (Deccan traps) may be insightful.

Bibliography

Allègre, C.J., Rousseau, D., 1984. The growth of the continent through geological time studied by Nd isotope analysis of shales. Earth and Planetary Science Letters 67 (1), 19-34.

Dellinger, M., Gaillardet, J., Bouchez, J., Calmels, D., Louvat, P., Dosseto, A., Gorge, C., Alanoca, L., Maurice, L., 2015. Riverine Li isotope fractionation in the Amazon River basin controlled by the weathering regimes. Geochimica et Cosmochimica Acta 164, 71-93.

Derry, L.A., France-Lanord, C., 1996. Neogene Himalayan weathering history and river87Sr86Sr: impact on the marine Sr record. Earth and Planetary Science Letters 142 (1-2), 59-74.

Frings, P.J., Clymans, W., Fontorbe, G., De La Rocha, C.L., Conley, D.J., 2016. The continental Si cycle and its impact on the ocean Si isotope budget. Chemical Geology 425, 12-36.

Gaillardet, J., Dupré, B., Louvat, P., Allègre, C.J., 1999. Global silicate weathering and CO2 consumption rates deduced from the chemistry of large rivers. Chemical Geology 159 (1–4), 3-30.

Haq, B.U., Hardenbol, J., Vail, P.R., 1987. Chronology of fluctuating sea levels since the triassic. Science (New York, N.Y.) 235 (4793), 1156-1167.

Hathorne, E.C., James, R.H., 2006. Temporal record of lithium in seawater: A tracer for silicate weathering? Earth and Planetary Science Letters 246 (3-4), 393-406.

Mackenzie, F.T., Garrels, R., 1971. Evolution of Sedimentary Rocks. Norton.

Miller, K.G., Kominz, M.A., Browning, J.V., Wright, J.D., Mountain, G.S., Katz, M.E., Sugarman, P.J., Cramer, B.S., Christie-Blick, N., Pekar, S.F., 2005. The Phanerozoic record of global sea-level change. Science (New York, N.Y.) 310 (5752), 1293-1298.

Misra, S., Froelich, P.N., 2012. Lithium Isotope History of Cenozoic Seawater: Changes in Silicate Weathering and Reverse Weathering. Science 335 (6070), 818-823.

Opfergelt, S., Williams, H., Cornelis, J., Guicharnaud, R., Georg, R., Siebert, C., Gislason, S., Halliday, A., Burton, K., 2017. Iron and silicon isotope behaviour accompanying weathering in Icelandic soils, and the implications for iron export from peatlands. Geochimica et Cosmochimica Acta 217, 273-291.

Powell, R.T., Wilson-Finelli, A., 2003. Photochemical degradation of organic iron complexing ligands in seawater. Aquatic Sciences 65 (4), 367-374.

Presti, M., Michalopoulos, P., 2008. Estimating the contribution of the authigenic mineral component to the long-term reactive silica accumulation on the western shelf of the Mississippi River Delta. Continental Shelf Research 28 (6), 823-838.

Teng, F., McDonough, W.F., Rudnick, R., Dalpé, C., Tomascak, P., Chappell, B.W., Gao, S., 2004. Lithium isotopic composition and concentration of the upper continental crust. Geochimica et Cosmochimica Acta 68 (20), 4167-4178.

Veizer, J., Mackenzie, F., 2013. Evolution of Sedimentary Rocks.

Zhang, L., Chan, L., Gieskes, J.M., 1998. Lithium isotope geochemistry of pore waters from Ocean Drilling Program Sites 918 and 919, Irminger Basin. Geochimica et Cosmochimica Acta 62 (14), 2437-2450.